BRNO UNIVERSITY OF TECHNOLOGY
VYSOKÉ UČENÍ TECHNICKÉ V BRNĚ

FACULTY OF MECHANICAL ENGINEERING
FAKULTA STROJNÍHO INŽENÝRSTVÍ

ENERGY INSTITUTE
ENERGETICKÝ ÚSTAV

DISC FRICTION LOSS IN CENTRIFUGAL PUMPS AND HYDRAULIC TURBINES
DISKOVÉ ZTRÁTY ODSTŘEDIVÝCH ČERPADEL A VODNÍCH TURBÍN

DOCTORAL THESIS
DIZERTAČNÍ PRÁCE

AUTHOR Ing. Lucie Zemanová
AUTOR PRÁCE

SUPERVISOR doc. Ing. Pavel Rudolf, Ph.D.
ŠKOLITEL

BRNO 2022

Abstract

The thesis deals with an experimental and numerical study of the flow in sidewall gaps of hydraulic machines with a focus on low specific speed pumps. Although the fluid which fills the sidewall gaps represents only a very small portion of the whole volume of the machine, it can have a great impact on the flow in the whole domain. It can significantly influence the behavior, characteristics, and overall performance, especially in the case of low specific speed machines since it determines disk friction. The flow field in sidewall gaps also influences the pressure distribution inside a machine and thus generates axial thrust. The understanding of the flow in these regions is limited since it is based on the theory obtained for simplified geometry and its application in turbomachinery is questionable. In order to investigate the flow in the sidewall gaps of centrifugal pumps, a test rig including a real impeller has been designed and built up. It enabled observation of the flow in the backside wall gap for various operational regimes including optical measurement of velocity profiles, measurement of axial thrust, and frictional torque. A method for precise numerical simulation of such type of flow was developed to help reveal phenomena, which are not observable in the experimental apparatus and to extend the research to a wider range of operating conditions.

Keywords

Sidewall gap flow, Disk friction losses, Rotating cavity, Instability, Axial thrust, CFD, Centrifugal pumps, Turbines, Hydraulic machines, Turbomachinery

Rozšířený abstrakt

Disertační práce se zabývá experimentálním výzkumem a numerickým modelováním proudění v mezidiskových prostorách hydraulických zařízení se zaměřením na čerpadla s nízkými specifickými otáčkami. Navzdory tomu, že mezidiskové prostory představují pouze zlomek z celkového objemu tekutiny v čerpadle, proudění v těchto oblastech může ovlivnit charakter proudění v celém stroji a tím jeho chování, charakteristiku a celkový výkon. Významný je tento vliv zejména u strojů s nízkými specifickými otáčkami, kde velkou roli hrají diskové ztráty vznikající právě v těchto prostorách.

Předchozí teoretické práce staví na zjednodušujících předpokladech, že proudění v mezidiskových prostorách hydraulických strojů lze přibližně modelovat rovnicemi, které byly odvozeny pro proudění v okolí disku rotujícího ve válcové spáře. Takový případ byl dobře popsán teoreticky a později byly poznatky validovány a rozšířeny celou řadou experimentálních studií. Nicméně použití takového zjednodušení pro reálná zařízení je značně diskutabilní.

Různí autoři průběžně zdokumentovali proměnné, které hrají v případě skutečných hydraulických zařízení nezanedbatelnou roli, a pokusili se korigovat rovnice pro stanovení účinků významných pro praxi (diskových ztrát a axiální síly) tak, aby výsledky lépe odpovídaly reálným provozním pozorováním. Objevují se různé korekce zahrnující vliv různých podmínek (otáčky, průtok), konstrukčních prvků, drsnosti povrchu atd. Tyto empirické modely možná přibližují sledované veličiny blíže realitě, ale stále poskytují pouze hrubý odhad a neříkají nic o tom, co se s prouděním v mezidiskových prostorách ve skutečných strojích odehrává.

Do jisté míry neprobádaná je i oblast numerických simulací tohoto typu proudění. Kombinacemi různého průměru disku (oběžného kola), otáček a šířkou spáry lze dosáhnout kromě 4 základních režimů také řadu přechodových stavů. Část domény obsahuje laminární režim proudění, který jinde může různými mechanismy přecházet v turbulentní proudění. To je doprovázeno nestabilitami, které jsou numericky poměrně obtížně zachytitelné.

Na základě analýzy současného stavu poznání a testování na zjednodušené geometrii, pro kterou existuje řada publikovaných experimentálních prací pro validaci, bylo ověřeno, že jednodušší modely turbulence nejsou schopny podchytit nestability vznikající v přechodových režimech. Většina RANS modelů predikuje dobře rychlostní profil ve střední oblasti spáry, mezní vrstvy v blízkosti stěn však neodpovídají experimentálním pozorováním. Vznik a šíření vírových struktur bylo možné zachytit pouze při použití přístupu Large Eddy Simulation. LES je možné s úspěchem použít pro modelování proudění na zjednodušeném příkladu proudění v samotné spáře, simulovat však celý stroj

z hlediska výpočetní náročnosti možné není. Z tohoto důvodu byla na dalším postupném kroku odzkoušena metodika, kdy je doména čerpadla rozdělena na několik dílčích zón spojených rozhraními (interfacy). Pouze zóny mezidiskových prostor byly řešeny LES přístupem, ve zbytku čerpadla byl použit RANS model. Tento postup umožnil zachycení nestabilních vírových struktur při zachování dosažitelné výpočetní náročnosti. Byl použit pro veškeré následující CFD simulace v rámci dizertační práce.

Pro studium režimů proudění v mezidiskových prostorách hydraulických strojů a pochopení vyplývajících důsledků pro diskové ztráty a vznikající axiální sílu bylo navrženo a vyrobeno experimentální zařízení. To umožňuje realizovat výzkum proudění ve spáře za reálným oběžným kolem, čímž překonává dosud používané koncepty redukované na rotující disk v jednoduché válcové spáře. Proudění vytvořené v nově navrženém zařízení je bližší provozním podmínkám reálných strojů. Pomocí změny otáček oběžného kola, vkládáním distančních podložek a možností vytvořit průtok je umožněno dosáhnout a studovat širokou škálu režimů proudění.

Ústředním prvkem experimentálního zařízení je reálné oběžné kolo z čerpadla s nízkými specifickými otáčkami $n_s = 33$. Spirála a zadní část za oběžným kolem je průhledná (vyrobena z plexiskla), což umožňuje použití optických metod (LDA nebo PIV) pro měření rychlostního pole v zadní mezidiskové spáře. Ponechává to také prostor pro experimentální vizualizaci proudění, např. reflexními částicemi rozptýlenými v kapalině. Snímatelný zadní disk oběžného kola byl do budoucna plánován pro případný výzkum vlivu prvků pro potlačení vznikající axiální síly (je na něj jednoduše možné umístit zadní lopatky nebo realizovat vrtání). Změna šířky zadní mezidiskové spáry je zajištěna vkládáním distančních podložek s definovanou tloušťkou. Kromě šířky zadní spáry lze měnit otáčky oběžného kola a pro protékané varianty nastavovat průtok. Kombinací zmíněných veličin je možné dosáhnout a popsat celou řadu režimů proudění včetně vlivu na vznikající diskové ztráty a axiální sílu.

Pro 4 různé šířky zadní mezidiskové spáry byly provedeny série měření, kdy se pro rozsah otáček (0-320)/min sledovala velikost axiální síly a krouticího momentu. Pro jednu šířku bylo realizováno detailnější měření rychlostních profilů v různých místech spáry pomocí LDA. Dále byl na zvolené variantě studován vliv průtoku. Pomocí CFD modelu byla experimentální měření rozšířena o provozní podmínky, které by bylo obtížné studovat experimentálně. Numerické simulace také poskytují detailní vhled do proudového pole v zadní mezidiskové spáře a umožňují sledovat řadu parametrů a odvozených veličin, čímž vhodně doplňují měření.

Výsledky práce odhalily, že použití zjednodušeného modelu odvozeného pro disk rotující ve válcové spáře není pro reálné aplikace v hydraulických strojích příliš použitelné. Proudění v zadní mezidiskové spáře je silně ovlivněno lopatkami oběžného kola. V důsledku jejich přítomnosti vznikají periodické jevy vázané na pozici lopatkových kanálů. Počet vznikajících spirálních vírových struktur je celočíselným násobkem právě počtu lopatek oběžného kola. Jsou vytvářeny v důsledku různého směru proudění (do/ze spáry) v různých místech po obvodu. Postupný vývoj těchto struktur se zvyšujícími se otáčkami oběžného kola je také složitější v porovnání s případem hladkého disku rotujícího ve válcové spáře.

Dalším faktorem, který významně ovlivňuje charakter proudění je šířka spáry. Bylo zjištěno, že čím širší spára, tím větší prostor pro vývoj nejrůznějších vírových struktur a tím větší variabilita vznikajících jevů proudění. Pro střední šířku spáry je celý příčný průřez (od statoru k rotoru) vyplněn vírovými strukturami. V případě širší spáry se proudění v blízkosti statoru vytváří do jisté míry nezávisle na proudění kolem rotoru. Také šíření struktur v radiálním směru do středu mezidiskové spáry je pro větší šířku omezeno. Naproti tomu úzká spára způsobuje potlačování vírů už na vstupu do domény a proudění je tak stabilnější i pro vyšší otáčky.

Komplexita proudění v zadní mezidiskové spáře má za důsledek posun hranic mapy režimů získaných pro zjednodušený případ rotujícího disku. Jak experimentálně, tak numericky, byly detekovány celkem 3 různé režimy a přechody mezi nimi (I – laminární režim se spojenými mezními vrstvami, III – turbulentní režim se spojenými mezními vrstvami, IV – turbulentní režim s oddělenými mezními vrstvami). Pro daný rozsah otáček a šířek spáry nebyl zaznamenán výskyt režimu II (laminární s oddělenými mezními vrstvami). Pro jeho dosažení by bylo pravděpodobně třeba rozšířit výzkum o spáru s ještě větší šířkou.

Studium vlivu průtoku neodhalilo v analyzovaném rozmezí otáček a s tím souvisejících průtoků významné změny ve stavu proudění v zadní mezidiskové spáře. Průtok není dostatečně velký, aby měl za následek vznik nesymetrie proudění nebo změnil vznikající struktury. Destabilizační efekt průtoku byl pozorován pouze jako o něco dřívější přechod z režimu III do režimu IV.

Ačkoli byla pozorována celá řada změn charakteru proudění včetně přechodů mezi režimy, jejich projevy není možné zaznamenat na průběhu krouticího momentu nebo axiální síly. Jak měřené, tak simulované průběhy jsou hladké křivky bez viditelných zlomů. Potenciálně nebezpečné stavy pro provoz čerpadel a turbín, kdy dochází ke změně směru působení axiální síly, se ve studovaném rozsahu otáček nevyskytují. Pro vyšší otáčky zase nesouvisí se změnou režimu proudění, která tam nenastává.

Ve sledovaném rozmezí byl pozorován nárůst krouticího momentu s otáčkami nezávisle na šířce spáry. Přítomnost průtoku také nemá na velikost krouticího momentu vliv. CFD simulace jsou ve shodě s experimentálním měřením.

Velikost axiální síly také narůstá s rostoucími otáčkami, a to strměji v porovnání s krouticím momentem, závislost na otáčkách je kvadratická. Závislost na šířce spáry není jednoznačná a bude vyžadovat další zkoumání. Z měřených výsledků pro šířky spáry h_1–h_4 je pozorovatelný nárůst axiální síly s rostoucí šířkou spáry až po dosažení jisté šířky, kde se charakter obrací a s dalším zvyšováním šířky vznikající síla klesá. Z CFD vyplývá monotónní nárůst s rostoucí šířkou spáry, nicméně z časových důvodů byl analyzován pouze rozsah šířek h_1–h_3. Je možné, že pro širší spáru by se průběh obrátil, ale stejně tak by se mohla projevit chyba v důsledku nejistoty měření. S určitostí lze však konstatovat, že na rozdíl od krouticího momentu, na velikost axiální síly má zásadní vliv přítomnost průtoku.

Přítomnost, byť malého, průtoku snižuje velikost axiální síly. Závislost není nijak jednoduchá, pro specifickou kombinaci otáček a průtoku je pokles síly napříč studovaným rozsahem různý. Příčinou je změna tlakových poměrů na nosném a krycím disku oběžného kola po připojení do experimentální trati. Celkový tlak v celém systému vzrostl, nicméně výsledná axiální síla není daná absolutní hodnotou tlaku, ale rozdílem mezi přední a zadní mezidiskovou spárou. Rozložení tlaku působící na krycí disk (v přední mezidiskové spáře) se kvalitativně neliší napříč analyzovaným rozmezím otáček a rozdíl není patrný ani mezi uzavřenou konfigurací a stavem s průtokem. Rozdíl nastává v tlakových poměrech na nosném disku (zadní mezidisková spára), kde se projevuje změna jak s nárůstem otáček, tak v odlišnosti mezi případy s průtokem a uzavřeným stavem. Důsledkem je nižší celková síla a složitější průběh, který je vidět z měření.

Zjištění závislosti pro vyšší otáčky a průtoky a tím prozkoumání dalších režimů blízkým provozním podmínkám reálných strojů, je dobrým tématem pro budoucí studium. Dalším námětem směřujícím k praktickému využití by mohlo být studium vlivu prvků používaných k potlačení axiální síly (otvory v nosném disku, zadní lopatky).

Citation

ZEMANOVÁ, Lucie. Disc Friction loss in Centrifugal Pumps and Hydraulic Turbines. Brno, 2022. Available at: https://www.vutbr.cz/studenti/zav-prace/detail/137920. Doctoral thesis. Brno University of Technology, Faculty of Mechanical Engineering, Energy institute. Supervisor Pavel Rudolf.

Declaration of Compliance

By signing this declaration, I confirm that the Ph.D. thesis submitted by me was done, to the best of my belief, in accordance with good scientific practice and that I am aware of and agree that a finding of serious violations of good scientific practice will be handled according to the faculty guidelines and will preclude a positive assessment of the thesis and/or possibly result in the revocation of the degree awarded to me.

Ing. Lucie Zemanová
22nd February, 2022
Brno

Acknowledgements

I would like to express gratitude to my supervisor, doc. Ing. Pavel Rudolf, Ph.D., that let me continue my Ph.D. journey in his department. I would like to thank him for his willingness to guide me through the study leading to this thesis, for being a source of inspiration and constructive criticism.

Many thanks belong to the laboratory crew for help with the experimental part of the thesis. Namely to Ing. Martin Hudec, Ph.D., Bronislav Kusý, Karel Večeřa and also to doc. Ing. Vladimír Habán, Ph.D. for his advice on experiments.

Last but not least I thank Pavel for his help with manufacturing drawings.

I thank also my Norwegian supervisor, prof. Pål-Tore Selbo Storli, who hosted me, although for a short period of time, at NTNU, Vannkraftlaboratoriet, Norway. It was an enlightening experience from both a professional and personal point of view.

Finally, I am grateful to the team of Ph.D. students at Viktor Kaplan Dept. of Fluid Engineering for kindly accepting me and for a nice working environment, and to all of my friends who supported me and believed that this will ever become real.

Contents

Introduction

Despite the sidewall gaps of hydraulic machines are tiny spaces and the volume of the fluid inside it is orders of magnitude smaller compared to the other dimensions of a pump or a turbine, the character of the flow in their interiors can significantly influence the flow in the machine in general. It consequently impacts its operation, efficiency, and reliability. Moreover, the theoretical description of the flow near rotating disks as well as its numerical simulation is a challenging task and has drawn the attention of researchers in the past for its relevance to many, but not only, industrial problems.

The first publication focused on the flow near a rotating disk was from the oceanography field issued in 1905 by Ekman [1] and dealt with the impact of the rotation of the Earth on wind-driven ocean currents. He was followed by Von Kármán [2] and Bödewadt [3]. A few alterations of the problem including rotating disk in stationary fluid, stationary disk in rotating fluid, and rotating disk in rotating fluid were studied. The authors described specific types of boundary layers developed under specific conditions and hence they have been named after them: Von Kármán boundary layer, Bödewadt boundary layer, and Ekman boundary layer. A solution of Navier-Stokes equations for the mentioned flows was proposed and further extensively studied both numerically and experimentally, e.g., in [4–7]. Later on, configurations with finite dimensions were introduced to apply the derived theories to some industrial applications.

Disk-shaped cavities filled with fluid are common in applications, such as torque converters of an automatic gearbox, magnetic storage devices, or semiconductor manufacturing processes with rotating wafers in electronics. Nevertheless, the most important industrial application is associated with flow in sidewall gaps in turbomachinery.

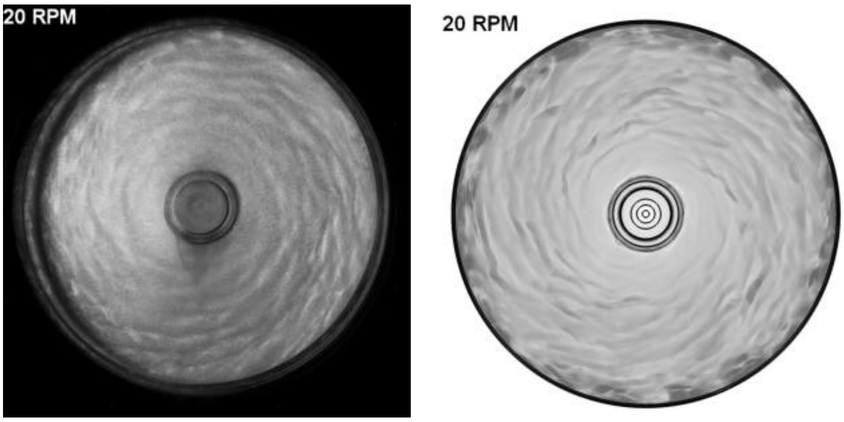

Figure 0.1. Experimental and numerical visualization of the flow in rotating disk cavity

With the increasing knowledge in fluid mechanics as well as in turbomachinery, it became evident that the flow in the sidewall gaps is a quite complex problem. Even the solution of the flow in a simple cylindrical cavity is not trivial and involves a wide variety of regimes and structures, as illustrates experimental and numerical visualization in Figure 0.1. Moreover, the geometry of the gaps in hydraulic machines is not as simple as in reported research studies. Furthermore, it is complicated by the presence of throughflow, which is not negligible, since it has certain consequences in various related phenomena. The most important issues that are directly governed by the flow inside the sidewall gaps are disk friction and axial thrust.

Increasing demands on the performance of all devices are undoubtedly connected with understanding the phenomena occurring inside these systems. Description of the underlying physics and prediction of possible conditions may lead to machine design optimization, an increase of performance, cost reduction, better reliability, and in the final consequence, to higher efficiency.

However, the understanding of the flow in sidewall gaps of hydraulic machines is limited, since it is based on the theory and observations obtained for very simplified assumptions. Its applicability in turbomachinery is doubtful. Experiments on rotating cavities, which are by its shape closer to the real pumps or turbines, are missing, there are also unanswered questions about the appropriate approach to numerical modeling.

The thesis aims to bring better insight into the flow in sidewall gaps of centrifugal pumps, study the impact of the flow on phenomena significant for its operation and find a suitable approach to numerical simulations of such types of problems.

The first part of the thesis gives an overview of the current theoretical knowledge. Chapter one offers a review on the flow in rotating cavities, its link to a flow in sidewall gaps of hydraulic machines, the theoretical description, and analysis of possible approaches to numerical computations. The second and the third chapters deal with phenomena resulting from its presence (disk friction losses and axial thrust). The second part of the thesis specifies the objectives of the thesis and outlines the intended approach to the research. The third part summarizes the material and methods, which have been used within the dissertation research. It covers the path to finding a suitable CFD methodology, the design of the experimental apparatus, its features, options, and limitations. The overview of performed measurements and simulated cases are also covered. The last part consists of experimental and numerical results, conclusions, and prospects of the research.

Part I

Theoretical background

CHAPTER 1

Flow inside rotating cavities

A solution of the flow near a rotating disk is a quite challenging task. Flow structures emerging inside such cavities can be very complex and despite many studies, a complete understanding of the transition and the turbulent breakdown process has not been achieved yet. The state of the flow in a rotating cavity is determined by the shape and dimensions of the gap and by the operating conditions.

1.1 Parameters for the description of flow

In order to characterize the geometry of the rotor-stator cavity and operating conditions, several parameters are defined according to the following equations and Figure 1.1. The regime of the flow can be described by a combination of two nondimensional variables: aspect ratio G and rotational Reynolds number Re. The aspect ratio expresses the influence of the geometry, while the rotational Reynolds number involves the effect of operating conditions.

$$G = h/b, \tag{1.1}$$

where h is the width of the gap and b is the outer radius, as is shown in Figure 1.1.

$$Re = \left| \frac{\vec{v} \cdot \nabla \vec{v}}{\nu \Delta \vec{v}} \right| = \frac{UL}{\nu} = \frac{\Omega b^2}{\nu}, \tag{1.2}$$

where L is a typical length scale (in the case of enclosed cavity outer radius), U circumferential velocity, Ω is rotational speed and ν is the kinematic viscosity of the fluid.

For easier comparison of the studies performed by different authors, the curvature parameter of the cavity is defined as:

$$R_m = \frac{b+a}{b-a} \tag{1.3}$$

Operating conditions, which play an important role in the behavior of the fluid, are often expressed by means of dimensionless numbers. Rotational Reynolds number Re and Rossby number Ro, are relevant for the description of the flow near rotating disks.

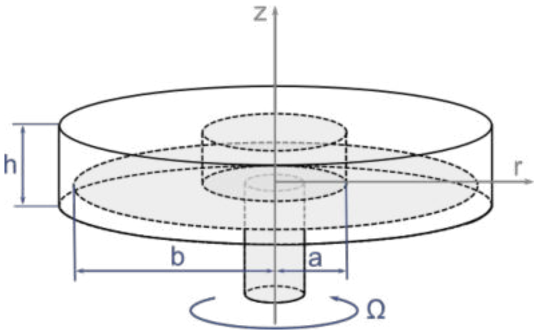

Figure 1.1. Designation of variables for characterization of the flow in sidewall gap

The Reynolds number quantifies the ratio of advection and viscous diffusion, whereas the Rossby number describes the importance of the Coriolis effect (force) over the inertial force. It is defined as:

$$Ro = \left| \frac{\vec{v} \cdot \nabla \vec{v}}{2\vec{\Omega} \times \vec{v}} \right| = \frac{U}{L\Omega}, \tag{1.4}$$

where L is a typical length scale, U velocity, Ω is rotational speed and ν is the kinematic viscosity of the fluid.

The flow in rotor-stator cavities, in general, is to a large extent influenced by the effects taking place in the boundary layers. Characteristic length appearing in the definition of dimensionless numbers is in many cases related to the rotating boundary layer thickness δ, which can be expressed as [8]:

$$\delta = \sqrt{\frac{\nu}{\Omega}} \tag{1.5}$$

For considering the boundary layer effects, it is necessary to distinguish the fluid rotational speed (outside the boundary region) Ω_f and the disk rotational speed Ω_d. The Reynolds number of the rotating boundary layer near the disk can be then defined according to [8]:

$$Re_\delta = \frac{(\Omega_f - \Omega_d) r \delta}{\nu} = \frac{r}{\delta} Ro_\delta, \tag{1.6}$$

where:

$$Ro_\delta = \frac{(\Omega_f - \Omega_d)}{\Omega} \tag{1.7}$$

and:

$$\Omega = \frac{(\Omega_f + \Omega_d)}{4} + \sqrt{\frac{(\Omega_f + \Omega_d)^2}{16} + \frac{(\Omega_f - \Omega_d)^2}{2}} \tag{1.8}$$

The presence of throughflow in the rotating cavity can make a dramatic difference in the flow regime. Therefore, to express its influence, a variable named flow rate coefficient C_w was introduced:

$$C_w = \frac{Q}{\nu b} \tag{1.9}$$

1.2 Flow regimes and patterns in rotor-stator cavity

1.2.1 Types of rotating boundary layers

Several types of boundary layers, typical for specific operating conditions (depending on the values of Ω_f and Ω_d) can be distinguished. They are named after researchers that historically contributed to the research of a particular type of boundary layer:

- Von Kármán boundary layer ($Ro = -1$)
- Ekman boundary layer ($Ro = 0$)
- Bödewadt boundary layer ($Ro = 1$)

Von Kármán boundary layer

(infinite rotating disk + infinite stationary fluid)

In the case of a rotating disk surrounded by a fluid, which is stationary at infinity ($\Omega_f = 0$), the disk acts as a pump. The fluid comes axially and is forced to leave in the radial direction. The Reynolds number varies with radius, nevertheless, a constant boundary layer thickness develops [8]. The situation is schematically shown in Figure 1.2 left. The right graph shows the velocity components.

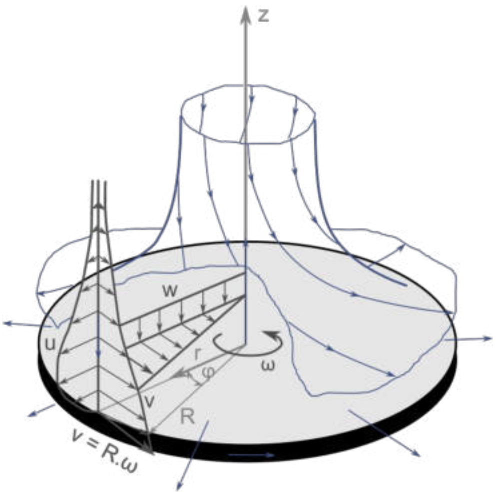

Figure 1.2. Von Kármán boundary layer [9]

Von Kármán [2] presented an exact solution of the Navier-Stokes equations for a steady-state, laminar, axially symmetric viscous flow induced by an infinite disk rotating steadily with constant angular velocity. The problem can be reduced to a set of ordinary differential equations and solved using an approximate integral method. Later on, the solution was revised by other authors [6], [7]. Theoretical, numerical, and experimental work focused on the flow at higher Reynolds numbers followed. Obtained results were significantly different among the authors, which led to further investigation and discovery of the instability phenomenon.

Von Kármán layer became a prototype for the research of instability in theoretical, experimental, and numerical ways [10]. It was noticed that some disturbances (waves or vortices) occur for particular Reynolds numbers. It is the first evidence of a transition to the turbulent regime.

The topic was for the first time published by Smith [11], who carried out a series of experiments focused on the laminar boundary layer of a rotating disk. He observed fluctuations that appear in a narrow range of Reynolds numbers below the transition. Measurements were performed using a hot wire placed in the rotating disk boundary layer near the disk surface. The existence of sinusoidal waves excited by random disturbances was observed. This instability is referred to as Type 1, Type B, or crossflow instability.

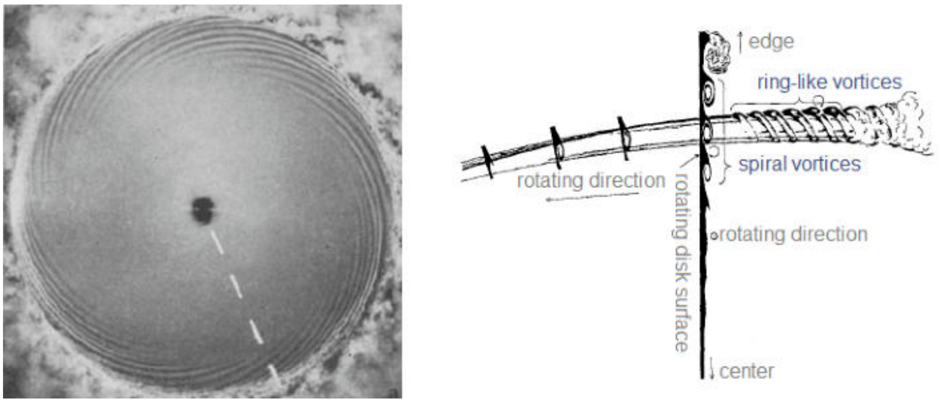

Figure 1.3. Spiral vortices during transition to turbulence [12]

Kohama [12] visualized the structures generated in the boundary layer using titanium tetrachloride and multi-strobe light. Figure 1.3 left shows the visualization of the flow near the disk rotating anticlockwise. During the transition to turbulence, various structures were observed and documented schematically in Figure 1.3 right.

Faller and Kaylor [13] described the existence of a second instability, which is denoted Type 2 or Type A. It is also visible in the form of spiral vortices. In [10] possible mechanisms of the second instability generation appearing in lower values of Reynolds number are described. Type 1 instability is characteristic of stationary spiral vortices with positive azimuth angle relative to circles, while spiral vortices of Type 2 instability have an opposite angle and move rapidly outward. The Type 1 disturbances can be described as almost stationary waves due to their relatively small values of wave speed. On the contrary, the disturbances of Type 2 can be quickly amplified as moving spirally outward with high wave speed and thus transit to an unstable region.

Bödewadt boundary layer

(infinite stationary disk + infinite rotating fluid)

Analogous problem to Von Kármán boundary layer arises when the fluid at infinity (large distance) rotates with uniform angular velocity. Centrifugal force acting on the fluid is in equilibrium with the radial pressure gradient. However, the circumferential velocity of the fluid near the stationary wall decreases, and therefore, the centrifugal force is lower. Fluid particles are under the same pressure gradient of the inward direction, which leads to a radial inward flow. As a consequence of continuity, flow in the axial direction, so-called secondary flow, occurs as shows Figure 1.4.

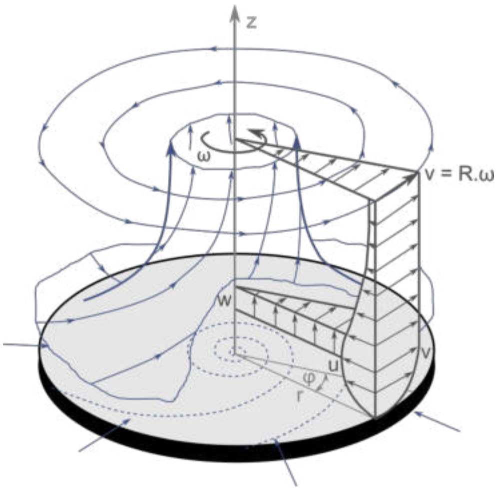

Figure 1.4. Böedewadt boundary layer [9]

The situation was extensively studied by Bödewadt [3], who proposed a solution of the flow, thus this type of boundary layer was named after him. Batchelor [4] and Stewartson [5] discussed the similarity solution obtained by Bödewadt. They questioned the possibility of the occurrence of such a flow in real conditions. As a coincidence of axial outflow, the boundary layer loses the fluid, and therefore on the axis, the radial velocity vanishes. They reached the conclusion that the flow could be physically attainable, however, the solution should take into consideration how the boundary layer was created.

Faller [10] investigated the numerical solution obtained for the Bödewadt layer. He noticed the same two types of instabilities as for the Von Kármán boundary layer. He pointed out that in this case, the critical Reynolds number for Type 2 instability is very low ($Re = 15.1$). However, it is necessary to mention that the simplifying assumptions are stronger than for the Von Kármán boundary layer and thus, there can be more pronounced errors. Type 1 instability appears for $Re = 25$ and has a larger growth rate than Type 2. It was also experimentally confirmed that Type 2 instability occurs very rarely and Type 1 dominates.

An experimental study by Savaş [14] revealed a new type of unstable structures observed in the Bödewadt boundary layer. Initial angular velocity was set and then a spindown test was performed. Instability in the form of concentric circles was observed when a specific angular velocity was achieved, as can be seen in Figure 1.5. It started around the outer edge of the disk and moved towards the center. Cross-sectional observations also confirmed azimuthal vortices. The field of disturbance filled up the disk layer and then disappeared.

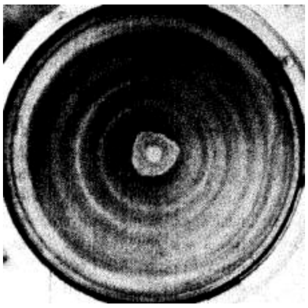

Figure 1.5. Circular shaped waves [14]

Ekman boundary layer

(infinite rotating disk + fluid rotating at infinity with the same angular velocity)

Ekman boundary layer appears when the angular velocity of the fluid at infinity approaches the angular velocity of the disk ($\Omega_d = \Omega_f$), thus $Ro = 0$. The fluid is driven outwards as a result of centrifugal forces and consequently, a downwards axial flow is developed. The boundary layer is named after Ekman, who first published the evidence of the existence of such a phenomenon in connection with oceanography and flow in the atmosphere. He focused on the analytical solution of the flow assuming a steady, homogeneous horizontal flow including friction.

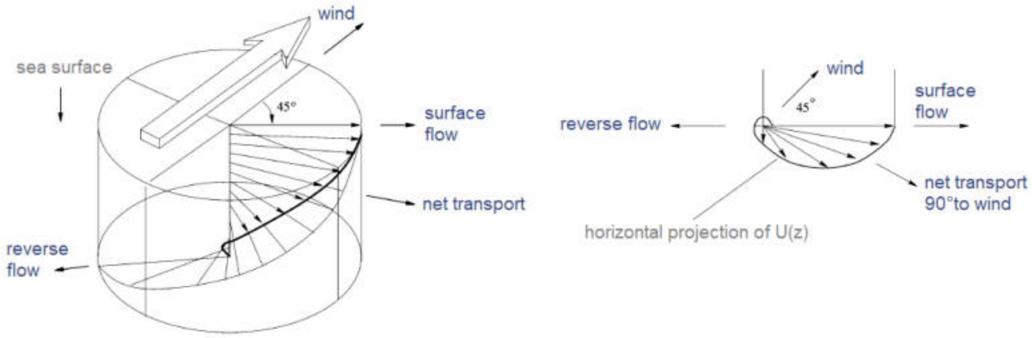

Figure 1.6. Ekman spiral [15]

His solution is known as Ekman spiral, because of the vertical distribution of currents, as can be seen in Figure 1.6. The analytical solution presumes laminar flow and constant dynamic viscosity, however, it is known that the boundary layer flow in the atmosphere is mostly turbulent. Ekman proposed a description of this type of flow including time-averaged Navier-Stokes equations and Reynolds stress modeled by eddy viscosity [8].

The stability of the Ekman boundary layer was studied by Lilly [16] numerically. He predicted the same two types of instabilities as in Von Kármán and Bödewadt boundary layers. It was experimentally confirmed by Tatro and Mollo-Christensen [17]. The Type 2 instability always appears first, taking the form of spiral vortices oriented approximately 15° clockwise. It belongs to the critical Reynolds number around $Re = 56$ and according to [18], it extracts the energy from the component of the mean flow parallel to the instability roll axis. Unlike that, Type I instability extracts the energy from the component of the mean flow perpendicular to the instability roll axis. Critical Reynolds number belonging to Type I is approximate $Re = 125$. It was also found out that Type II vortices are able to suppress the development of Type I instability.

1.2.2 Types of flow inside rotating cavities with finite dimensions

Although the findings obtained for basic types of boundary layers can be to some extent applied to two disks with infinite radius separated by a finite thickness of the fluid, the application to industrial problems is questionable, since the rotor-stator cavities are not infinite in the radial direction. Experimental results are always influenced by finite dimensions and the presence of edges. With the growth in demand for the performance and efficiency of hydraulic machines, the need for understanding such type of flow has gained its importance.

Brady and Durlofsky [19] investigated how the finite dimensions influence the validity of the similarity solution using numerical analysis. They found out that the effect of finite disks increases with increasing Reynolds number. The larger Re is, the bigger part of the domain has a different flow field from the similarity solution. Near the disk edge, the similarity solution is not valid, closer to the axis of rotation the solution approaches the similarity. Thus, the deviations are not only local, but influence a significant area of the domain. For arbitrary but finite disks, the similarity solution is a good qualitative and quantitative approximation only for low Re. When $Re > 200$, good quantitative agreement was restricted over only a fraction of the domain. Open ends lead to approaching the Stewartson solution while the closed ends resemble the Batchelor solution. Another mismatch with the similarity solution is connected with instabilities, which originate at the edges of the disks.

Daily and Nece [20] studied the problem of flow in enclosed cavities experimentally. They proved the existence of four different regimes. The flow can be laminar or turbulent and the boundary layers can be either separated or merged, as demonstrates Figure 1.7.

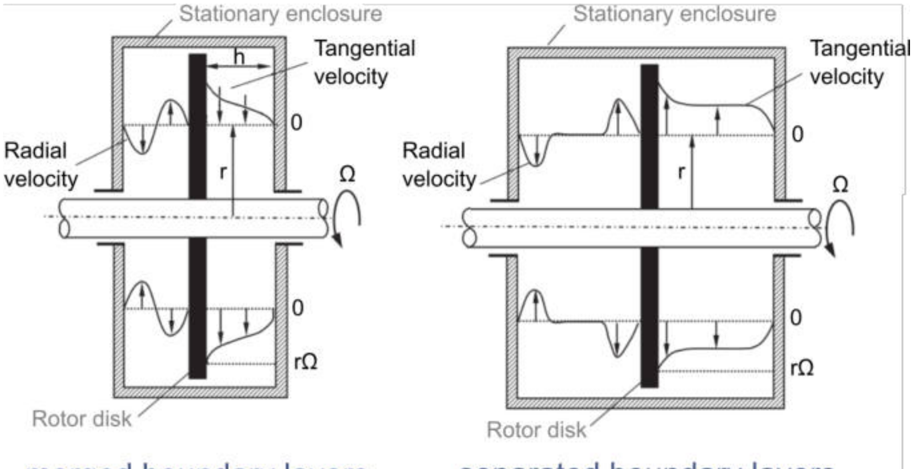

merged boundary layers separated boundary layers

Figure 1.7. Schematic visualisation of flows with merged and separated boundary layers [21]

The state of the flow is governed by a combination of dimensions of the cavity and the operating conditions given by the nondimensional variables *Re* and *G*, which were defined in the first section of this chapter. Four different regimes according to Figure 1.8 are then possible:

- Regime I (laminar flow, merged boundary layers)
- Regime II (laminar flow, separate boundary layers)
- Regime III (turbulent flow, merged boundary layers)
- Regime IV (turbulent flow, separate boundary layers)

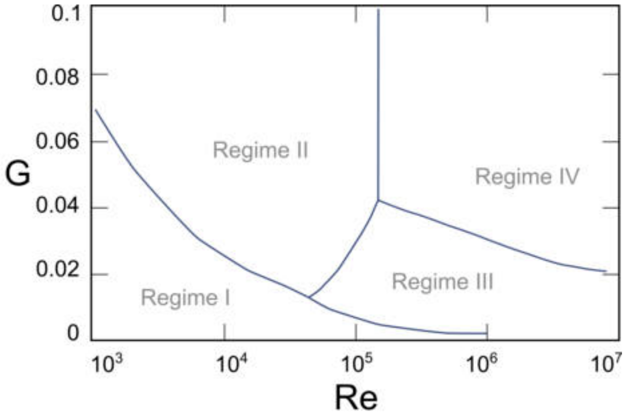

Figure 1.8. Map of regimes [22]

Regimes I and III

Those regimes are often denoted as small clearance cases and can be described as torsional viscous Couette-type of flow. The radial velocity profile is an S-shaped curve with a flow of outward direction along with the rotor and inward flow near the stator. The tangential component of velocity varies linearly across the gap, as shows the following figure. For large aspect ratios of the cavity, these regimes may never exist. For industrial applications, regime III is usually more relevant due to higher *Re*. The frictional resistance for those regimes decreases with increasing gap width as a consequence of the reduced velocity gradient [23].

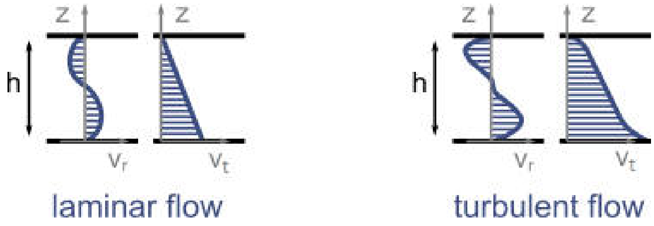

Figure 1.9. Velocity profiles of small clearance regimes [24]

Regimes II and IV

The flow is usually referred to as Batchelor type or a large clearance flow. For those regimes, the boundary layers along the rotor and stator are separated by an inviscid rotating core. The rate of difference from the similarity solution due to the finite dimensions is characterized by an entrainment coefficient K [25]:

$$K = \frac{\Omega_f}{\Omega_d} \tag{1.10}$$

The flow is inhomogeneous in the radial direction, K increases with local radius r. The boundary layer on the rotor is termed the Ekman layer, while the boundary layer on the stator is the Bödewadt layer. The radial component of the flow at the rotor is positive (outward direction) and is compensated by the inward radial velocity at the stator. The tangential component of velocity in the Ekman layer changes between the speed of the disk $\Omega_d r$ and the core speed $K\Omega_d r$. In the Bödewadt layer, the tangential velocity ranges between $K\Omega_d r$ and 0. The radial velocity component approaches zero in a major part of the domains except for the regions near the confining cylinders as shows the following figure.

Cheah et al. [26] observed boundary layers and reported that the rotor boundary layer near the cavity center is laminar and with increasing radial coordinate becomes turbulent. On the contrary, the stator boundary layer is turbulent for all Reynolds numbers (on the whole geometry). However, the character of the turbulence is different from that on the rotor side. It can be illustrated, e.g., by measurements carried out

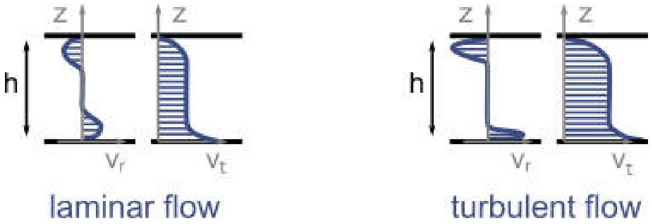

Figure 1.10. Velocity profiles of large clearance regimes [24]

by Gauthier et al. [27]. They found out that both the Ekman layer on the rotor and the Bödewadt boundary layer on the stator decrease with increasing *Re*. For a given angular velocity, the Ekman boundary layer thickness is constant, independent of the radial coordinate. The thickness of the Bödewadt boundary layer decreases from the center to the periphery, as documents Figure 1.11. This dependence is directly connected with the finite dimensions of the cavity. In the case of one disk or infinite disks, this behavior was not observed.

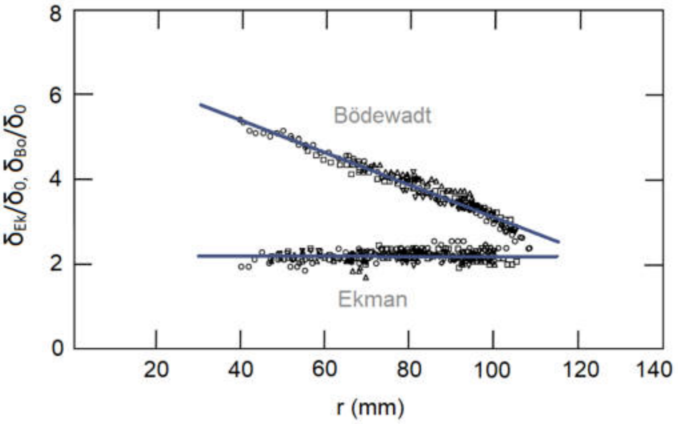

Figure 1.11. Thickness of boundary layers [27]

For the separated boundary layer cases, the frictional resistance increases with increasing gap width due to the braking influence of the outer cylindrical shroud [23].

Regime IV is generally considered relevant for most of the applications in hydropower or pumping and thus most of the later mentioned studies deal with it [21]. However, regime III was also reported in [28] and laminar regimes in the pump for oil with high viscosity were studied by Li [29].

1.2.3 Instabilities and transitions

A wide variety of unstable structures and transition scenarios among all previously described flow regimes may occur. The stability is principally governed by the boundary layers of the disks. Additionally, the presence of the hub and shroud influences the global stability as well and causes a difference between theoretical results for infinite disks and experiments with real geometry. An occurrence of various structures was observed depending, again, on the geometry and operating conditions.

San'kov and Smirnov [30] observed instabilities in regimes with merged boundary layers. They are characterized by localized turbulent structures in the form of spots or of solitary waves. The structures are usually superimposed on a short-wavelength spiral pattern, and its number increases with increasing Reynolds number [31].

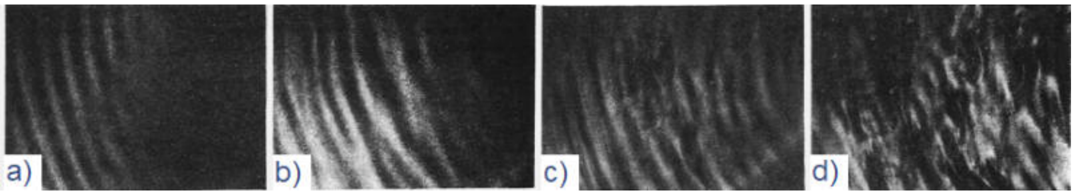

Figure 1.12. Type B transition to turbulence [30]

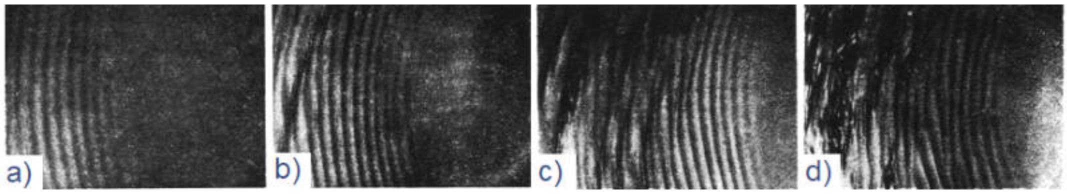

Figure 1.13. Type A transition to turbulence [30]

For $G = 0.0267$ at a particular value of angular velocity, regular steady vortices, which are oriented along a spiral twisting towards the center when moving in the direction of rotation as shows Figure 1.12 a), are developed. After the transition, the form is independent of the acceleration conditions. In the area near the hub, the vortices are less pronounced due to boundary effects. This type of normal supercritical bifurcation of the basic flow, which produces a new steady laminar regime, is called Type B vortices (waves), analogously to the one disk case. As the angular velocity increases, the vortices occupy gradually more space, consequently reducing the central region of the basic flow. Simultaneously, the waves bifurcate at the periphery, and further vortices at individual places begin to execute weak oscillatory displacements (Figure 1.12 b). The flow pattern becomes more complex, however, still keeps a regular structure. The formation of solitary strong perturbations in the peripheral region can be observed at distinct angular velocities. It travels to the center along the spiral trajectory dissipating in the region of basic flow (Figure 1.12 d). The core of the perturbations moves with a significant component of vorticity parallel to the axis of rotation. As the angular velocity increases, the number of perturbations increases as well and tends to group. In the end, the whole fluid domain is occupied by turbulent pulsations, see Figure 1.12 d).

In the narrower gap ($G = 0.01$), a regular steady system of waves oriented as concentric circles appears at a certain angular velocity. These vortices are denoted Type A and occupy the whole flow domain except the narrow hub area, as can be seen in Figure 1.13 a). The system of vortices can be described as a normal bifurcation since acceleration conditions and recovery after the introduction of perturbations were also observed. At a specific angular velocity, single solitary waves start to appear (Figure 1.13 b).

The fronts of these vortices form a spiral traveling in the direction of rotation. The structure movement has a locally lower velocity than the surface of the rotating disk. As the angular velocity rises, the number of solitary waves increases, gradually turning into narrow "plaits" with a clearly turbulent character (Figure 1.13 c). With further increasing angular velocity, the width of the plaits rises (Figure 1.13 d) until they begin to merge and complete turbulence is achieved.

For particular geometries ($G = 0.017$), a combination of structures A and B can be observed. Waves occupy an internal annular region, while B vortices appear at the periphery.

Cross and Le Gal [32] focused on the instabilities in Regime I and based on the experimental visualization, different forms of instabilities and the region of their occurrence were identified. A summary of their findings is presented in Figure 1.14. The angular velocity of the rotating disk was gradually increasing, whereas the stable torsional Couette flow becomes distorted by the appearance of periodic roll instability called spiral rolls (SR III). It is apparently generated by the combined effects of viscosity and Coriolis force and corresponds to so-called Type II waves in [30]. At higher angular velocity Ω, some dislocations appear and a structure called turbulent spirals replaces SR III. With increasing Ω the width of the spirals increases as well, however, their number decreases simultaneously until it completely disappears. For particular Re, structures called spots occur and coexist with the turbulent spirals. Their number increases until it invades the whole domain, leading to a fully turbulent state. Origination of turbulent spirals for small aspect ratios ($G < 0.016$) takes place on the SR III waves, in contrast with $G > 0.016$, where the turbulent spots originate at the boundaries of the flow field and propagate along spiral trajectories towards the centre [33].

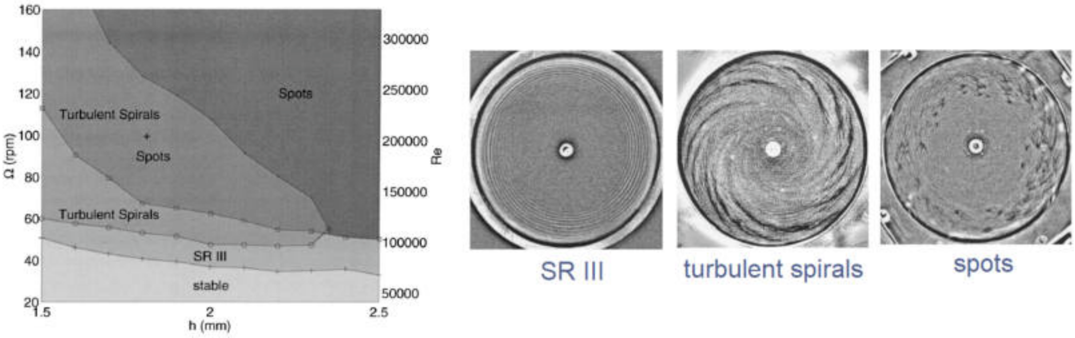

Figure 1.14. Transition diagram [32]

Schouveiler et al. [34] focused on the instabilities for regimes with separated boundary layers. The study confirmed that the stator (Bödewadt) boundary layer is more unstable than the rotor (Ekman) boundary layer. The unstable vortices are firstly formed near the periphery of the disk in the form of circles moving towards the center, as can be seen in Fig. 1.15 left. When the angular velocity Ω is large enough, the second wave system consisting of spiral vortices develops. These two patterns can coexist in a way that circular waves are visible near the axis of rotation, as shows Fig. 1.15 right. These spiral waves are unsteady and travel outwards unlike the circular ones.

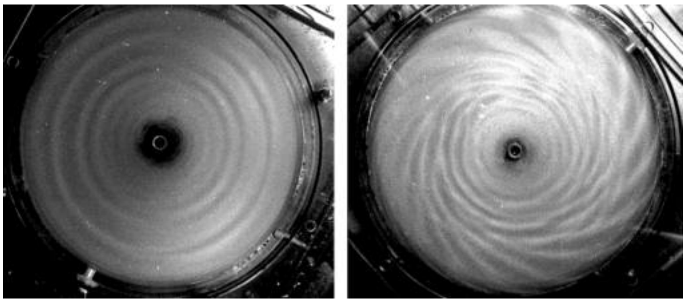

Figure 1.15. Visualisation of two types of instabilities [34]

Schouveiler et al. [31] expanded the study of transition scenarios to all of the four possible regimes of base flow. They used an experimental apparatus, which enabled a continuous change of angular velocity Ω as well as the gap height and thus aspect ratio G. A wide variety of structures was detected and summarized in a transition map, which can be seen in Figure 1.16. Particular flow regimes are denoted by initials: BF for basic flow, CR for circular rolls, SR for spiral rolls, SW for solitary waves, and SP for spots. The authors distinguish 3 types of basic flow designated as BF_j for joined boundary layers, BF_s for separated boundary layers, and BF_m for the situation, when in a part of the domain the boundary layers are separated and in the rest of it are merged.

For relatively large aspect ratios ($7.14 \times 10^{-2} \leq G \leq 14.29 \times 10^{-2}$), curve 1 describes the loss of stability leading to the origination of circular rolls. When increasing the angular velocity, the second bifurcation breaks the axisymmetry of the flow. It leads to the formation of spiral rolls (SRI) appearing in the peripheral region of the domain. They travel in an outward direction and coexist with CR. On the contrary to the circular waves, their frequency is not linked to the disk rotation frequency. Depending on the initial conditions, a flow with 16 to 24 arms can be obtained. In Figure 1.16 curve 2 describes this transition. With a further increase of the angular velocity, the flow resulting from the coexistence of these two modes becomes more complex without any apparent development of new instability. Wave turbulence emerges by the interaction between the two kinds of vortices.

For small aspect ratios ($0.71 \times 10^{-2} \leq G \leq 1.79 \times 10^{-2}$), the transition differs significantly. The primary bifurcation is associated with the destabilization of the purely viscous basic flow. The first instability generates a network of spiral vortices (SR III) with a small angle $-3° \leq \alpha \leq -5°$. The wavelength of the vortices is the order of the gap thickness h and they propagate with a small radial phase velocity which can be either positive or negative. Their appearance is in Figure 1.16 described by curve 1". The occurrence of solitary waves (SW) is associated with curve 2". These structures are superimposed on the SR III network and more tilted (the angle α is about $-20°$). They rotate in the same direction as the disk, however, their angular velocity is different. The structures do not exhibit periodicity, either spatial or temporal. Over a curve 3" another structure appears. It is formed locally at the periphery in the form of spots (SP)

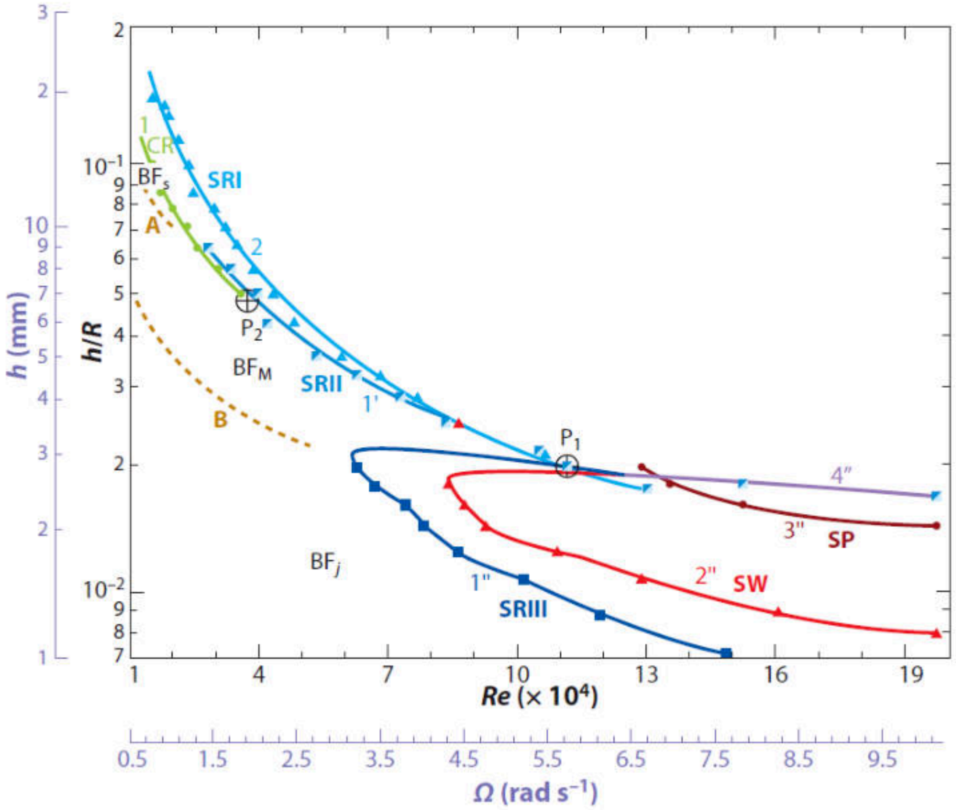

Figure 1.16. Transition diagram for merged (BF_J) and separated (BF_S) boundary layers [25]

moving towards the center of spiral trajectories while passing through the SR III rolls and solitary waves. Above curve 4”, the spiral structure and the solitary waves disappear, and simultaneously the number of spots increases until it penetrates the whole domain and the flow becomes turbulent.

For intermediate aspect ratios ($1.79 \times 10^{-2} \leq G \leq 7.14 \times 10^{-2}$), there is one more mode of instability. It appears while the parameters corresponding to curve 1’ are achieved. The waves take the form of a stationary network of spiral structures (SR II) having a positive angle $12° \leq \alpha \leq 15°$ with azimuthal direction. The typical wavelength of the spirals corresponds to the gap thickness h. Under certain conditions, it is possible to observe the coexistence of three types of structures (CR, SR I, and SR II). SR I rolls propagate radially outwards, while in the central area, stationary rolls (SR II) can be observed, and simultaneously, circular rolls (CR) are distinguishable.

1.2.4 Rotating cavities with throughflow

The effect of the presence of throughflow on the flow patterns inside the rotating cavities was studied due to its relevance to turbomachinery, e.g., in [35–38].

Hide [35] came with an estimated analytical solution for a rotating cavity including throughflow for a regime with laminar flow. He expected that the basic steady flow is axisymmetric and symmetric with respect to the middle height of the cavity. The flow in the core is geostrophic and its extent depends on the mass flow rate of the throughflow. It was noted that even a very slight increase in the mass flow rate results in instability.

Later on, it was studied by Owen and Pincombe [36] who modified the theory and extended it also for the turbulent flow. A series of experimental measurements revealed that with increasing flow rate, the width of the central flow grows and as a consequence, the depth of the Ekman boundary layer decreases. It is in agreement with the earlier formation of instabilities. They studied also the effect of the throughflow direction (whether the fluid enters the cavity axially or radially) as illustrates Figure 1.17. The major difference was described in the size and nature of the flow in the immediate vicinity of the inlet. In the case of the radial inlet, the flow is gradually destabilized by large-scale instabilities occurring as a consequence of Ekman layer onset while increasing *Re*. Contrarily, the axial inlet forces recirculation and the occurrence of Ekman layer instability and/or vortex breakdown in the central region causing unsteady flow despite the value of *Re*, under all observed conditions.

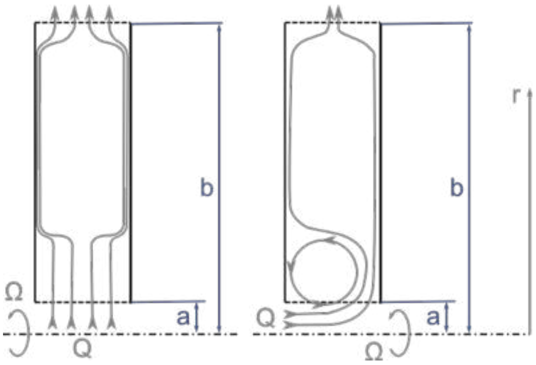

Figure 1.17. Different directions of inflow [36]

Crespo et al. [37] described the exact mechanism of the creation of instabilities in a rotating cavity with the presence of a throughflow. In the case of the weakly forced throughflow, the flow is steady at the beginning, nevertheless, an increase in mass flow rate causes a chaotic temporal behavior, which is changing through several bifurcations perturbing the basic spatial configuration of the flow. The process starts by breaking the symmetry with respect to the midheight of the cavity. It is followed by a wavy motion starting from the inlet, moving alternately towards the top and bottom Ekman layers, despite the boundary layers are not disturbed. Provided an increasing flow rate, a periodic oscillatory instability with vortices along with the Ekman boundary layers and horizontal waves in the core region is developed. The oscillations have a frequency close to the rotation rate frequency of the whole cavity. With further increases in the throughflow rate, a transition to quasiperiodicity characterized by larger amplitudes and shorter wavelength emerges. Another periodic behavior comes up followed by the final transition to chaotic flow.

Serre et al. [38] found out a three-dimensional solution of an unstable flow in a rotating cavity with throughflow. The first instability was formed as pairs of counter-rotating axisymmetric rolls traveling radially outward in the Ekman layer, as can be seen in Figure 1.18 top. The instabilities appear mainly at the border between the Ekman layer and the geostrophic core. The second observed instability was not axisymmetric but emerges as a set of spirals, see Figure 1.18 bottom. The shape of the spiral and the number of its arms is influenced by the curvature of the cavity. Once formed, instabilities of both types remain to stay stable unless further disturbances occur.

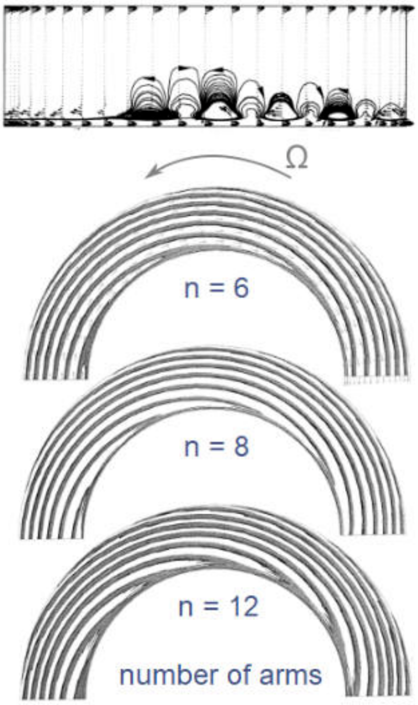

Figure 1.18. Axisymmetric and non-axisymmetric instability patterns [38]

Many other experimental studies describing the characteristics of the instabilities can be found, e.g., [39], [40] or [41]. Other authors focused on the effects of boundary conditions, e.g., the influence of the edge [42], throughflow [43] or types of flow patterns in co- and counter-rotating pair of disks [42], [44], [45].

1.2.5 Sidewall gaps of hydraulic machines

Sidewall gaps are the areas separating the rotor and the stator of the machine, that can be found in front of the rotor shrouds. Fig. 1.19 shows it with the examples of centrifugal pump and Francis turbine. Axial clearances between the shrouds of a closed impeller and the casing are a necessary requirement from the mechanical design point of view. Their dimensions and inner geometry differ among hydraulic machines as it is given by aspects of mechanical design, standardization of particular components, manufacturing, and material costs.

For centrifugal pumps, the ratio of the mean width of the gap to the outer radius of the impeller is usually about 0.09 [29]. The reason is the possibility to accommodate the

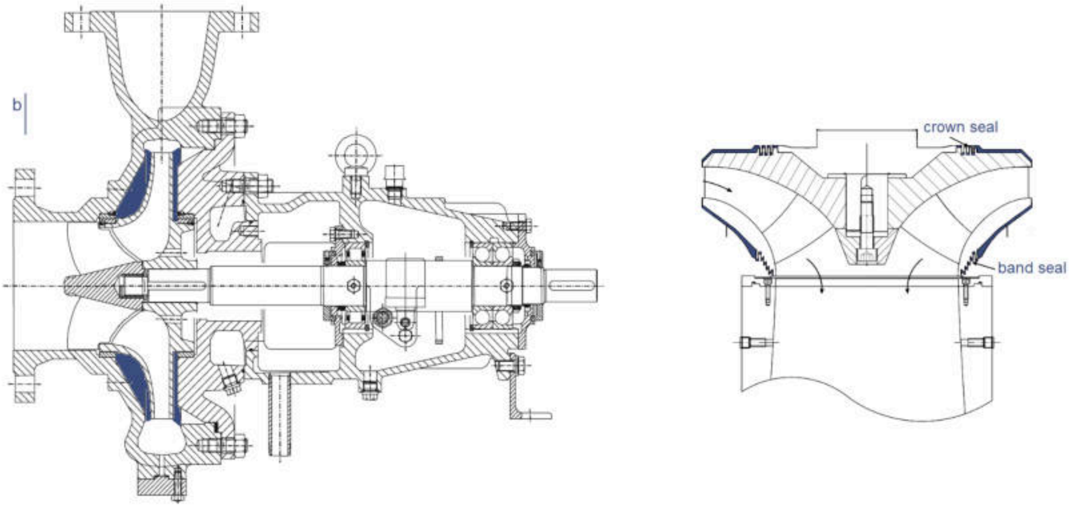

Figure 1.19. Sidewall gaps in a pump [46] and turbine [47]

casing with different impeller sizes. According to Gülich [46], the ratio should be kept between 0.03–0.08 since large volumes of fluid could increase turbulent dissipation and thus disk friction losses. The general advice is to avoid complex contours and shapes such as ribs, which decrease the rotation of the fluid. It leads to a trade-off between the disk friction losses and axial thrust. The design of the volute should ensure that the fluid of low velocity flowing from the volute into the sidewall gap does not interfere with the pumping action of the shrouds. It is necessary to enable the transfer of the energy from the fluid in the boundary layers to the main flow. In high-energy pumps, wide impeller sidewall gaps open to the volute should be avoided. The sidewall gaps should be always designed respecting eventual additional elements of the impeller, e.g., for axial thrust balancing. Auxiliary vanes on the shrouds increase the rotation of the fluid inside the sidewall gaps, while the balance holes make the flow conditions in the back sidewall gap more similar to the front one.

In the case of turbines, the design process of the sidewall gaps should secure the proper function of the labyrinth seals. The seal consists of two parts: a static seal connected to the stationary cover and a rotating part connected to the runner. The counterparts are coupled in a crested manner where wider and narrower channels take turns in order to lower the fluid velocity. The gaps influence the volumetric efficiency of the turbine, therefore, they are manufactured as narrow as possible. In low-head turbines, the gaps are machined directly into the runner and the achieved clearances are usually about 1–2 mm. For larger head turbines, there are special gap counterparts made of bronze or stainless steel enabling even tighter clearance. As the seals wear, the gap width increases, causing the leakage to increase [48].

The potential influence of the clearance on the performance and efficiency of hydraulic machines is demonstrated in [49–51]. Aly et al. [49] showed how the characteristic of the centrifugal pump is shifted for different gaps. As can be seen in Figure 1.20, the head and efficiency decrease with increasing side clearance. The optimums were found in lower flow rates.

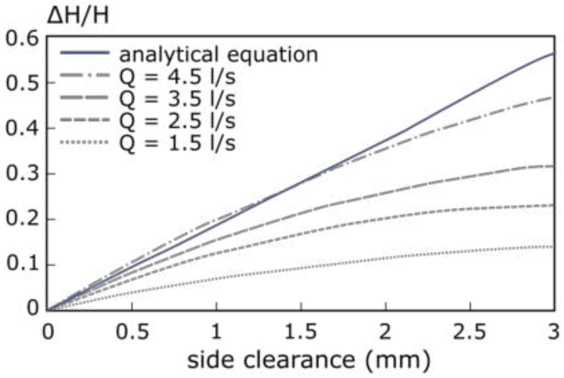

Figure 1.20. Change of the pump head with increasing the side clearance width [49]

Special attention requires the design of the clearances in hydraulic machines which can operate as pumps as well as turbines (reversible Francis turbines and pump-as-turbine = PAT), as shows [51]. The width and shape of the wear-ring clearance, in general, affect the volumetric efficiency and the performance of the pump-turbine significantly. The design of the sealing plays a decisive role in the overall efficiency as well. Yan et al. [51] investigated the effect of different designs of sealing. They compared the performance of PAT with a flat seal ring to the same PAT closed by labyrinth seals. Different clearances were also taken into consideration. The efficiency characteristics differed in both pump and turbine modes. It was observed that with increasing clearance the efficiency decreases, regardless the machine works as a pump or a turbine. Such a conclusion is in agreement with other studies dealing with the topic [49, 50]. The performance of the labyrinth seal is generally considered better than that of the flat ring seal.

The designers of hydraulic machines have to keep in mind also the strong influence of the gaps on the dynamics of the rotor. Surface-to-surface contact between the stationary and rotating parts of the seal may cause damping and significantly lower natural frequency [52].

The topic of flow inside the sidewall gaps of turbines and pumps stood a long time at the edge of interest. However, it turns out that in spite of their small dimensions, the flow in these spaces can significantly influence the flow field inside a hydraulic machine in general. It can have consequently an impact on the prediction of the efficiency and cause associated phenomena, such as disk friction losses, axial thrust, and rotordynamics.

Due to the tiny dimensions and deceptive separation from the main flow field in a hydraulic machine, the flow in those regions tends to be neglected. However, this turned to be not a correct assumption. Although most of the published numerical studies focusing on modeling the flow in hydraulic machines completely neglect the sidewall gaps geometry, some authors [47, 50, 53–56] showed that the flow in those domains can have a remarkable impact on the whole flow pattern [57–59].

Čelič and Ondračka [57] studied the difference between CFD of Francis turbine with and without considering sidewall gaps and reported an acceptable 3 % difference for the best efficiency point (BEP). Nevertheless, in off-design conditions, the discrepancies greatly rise. Feng et al. [60] published the discrepancy as a result of neglecting disk friction in the CFD model of Francis turbine about 10 %. Significant errors in computed efficiency while neglecting sidewall flow in the same turbine described also Jošt et al. [58] and Mössinger et al. [59]. Losses related to the flow inside sidewall gaps are the most pronounced while operating at low specific speed as can be seen in Figure 1.21.

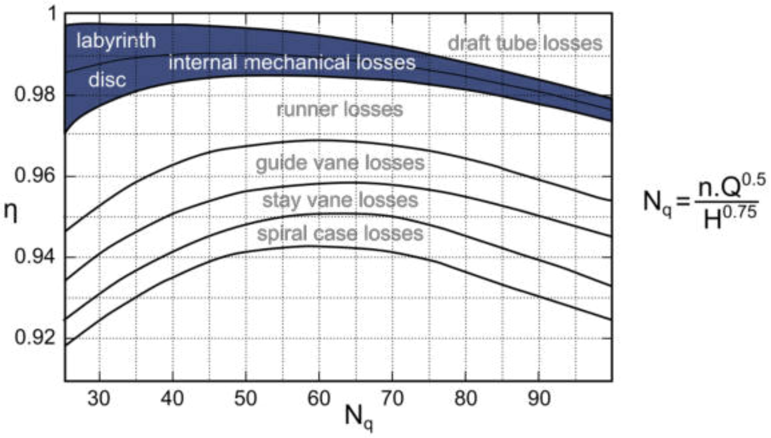

Figure 1.21. Losses related to flow in sidewall spaces of Francis turbine as function of specific speed [57]

Casartelli et al. [61] reported that for the computation of global characteristics (head and efficiency) of Francis turbine, neglecting the sidewall gaps can be a reasonable assumption. However, it has to be kept in mind that the flow in the near-wall region is affected considerably. It results in a completely different flow pattern, which can be significant for the correct solution of the flow field in the draft tube. Local flow patterns created due to the presence of sidewall inflow are advected and persist downstream influencing the boundary layer. Accordingly, the computed components of the flow entering the draft tube differ between the cases with and without considering the sidewall gap flow. It is a potential source of errors since the diffusing flows such as those found in draft tubes are very sensitive to inlet conditions.

The authors [62] showed how is the calculation of the flow in the draft tube influenced by neglecting the flow from side gaps for BEP as well as for off-design operating conditions: part-load (PL) and high load (HL). Although unsteady behavior was obtained for both PL calculations, a significantly lower rise of the pressure between the inlet and the outlet for the case with leakage flow was found. Moreover, the amplitudes of the pressure fluctuations caused by unsteady swirl were lower by 16 %, suggesting the damping effect of the mixing process in the near-wall region due to the presence of leakage inflow. Contrarily to [57], the biggest discrepancy was obtained for BEP. The presence of the sidewall gap flow changed the character of the overall flow field completely. Involving the sidewall gaps resulted in unsteady flow, while the simplified simulation led to a steady flow field, probably as a consequence of increased damping and generation of losses due to the presence of side inflow. HL conditions produced steady results for both settings. In contrast to the PL, the case involving sidewall inflow exhibited a higher growth of the calculated pressure. The different flow fields at BEP demonstrates Fig. 1.22. In both cases, the backflow zone in the elbow region of the draft tube was found, however, the extension is different. It is larger for the case without sidewall gap inflow and begins further upstream. On the contrary, the area of recirculation in the axial direction is of a larger extent for the case with gap inflow.

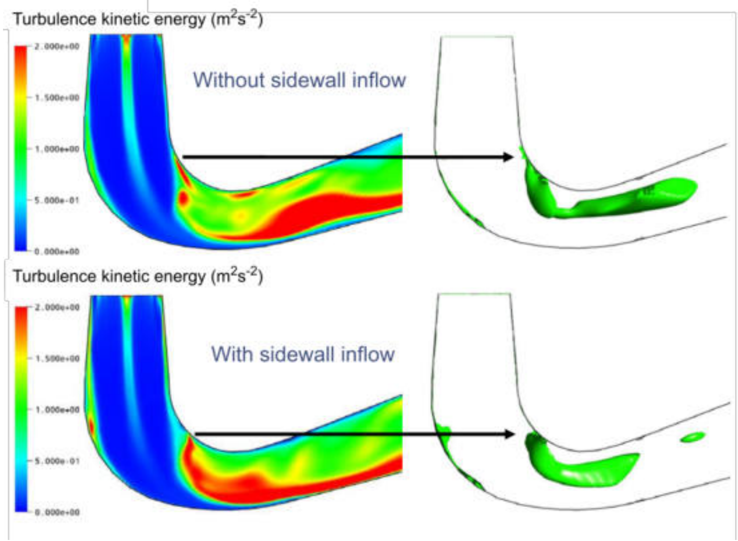

Figure 1.22. Discrepancies in turbulent kinetic energy and recirculating zones in draft tube of Francis turbine [62]

Feng et al. [60] studied the propagation of the leakage through the crown seal gap downstream. The meridional velocity in the vicinity of the crown is reduced by through-flow and therefore, the velocity gradient along with the blade height increases. Then it causes significant changes in the flow pattern even inside the draft tube.

Trivedi [47] found a complete breakdown of the boundary layer at the junction of the runner and the draft tube by CFD simulation of the complete domain of the Francis turbine. It is induced by jet-type flow from the labyrinth (band) seal gap, where a collapse of turbulence layers and the shear layer between the viscous and turbulent layers results in the adverse pressure gradient and recirculating flow between the runner outlet and the elbow.

Aly et al. [49] observed the effect of neglecting the sidewall gaps in a centrifugal pump with a semi-open impeller. As well as in turbines, the sidewall gap flow leads to the generation of the secondary vortex, which strongly impedes the core flow in the impeller. The width of the sidewall gap alters the pressure near the connection to the main flow and therefore, influences the calculated efficiency of the pump.

Will et al. [28] reported an essential difference in the evolution of the radial pressure distribution in the sidewall gap of a centrifugal pump. A non-negligible axial velocity occurs in the back sidewall gap with weak leakage flow, which is connected to uneven velocity directions at different tangential positions. The asymmetry of the volute casing plays a vital role in establishing a region with low static pressure behind the cutwater. The radial pressure force is not able to counterbalance the acceleration of the fluid in the tangential direction, resulting in recirculation. The fluid is centrifuged out of the sidewall cavity into the volute and then mixed with the main flow. Oppositely, the fluid before the cutwater is sucked into the sidewall gap due to the radial pressure gradient. Besides that, the flow evolves in time as the position of rotor channels changes as was outlined by Su et al. [63].

Wu et al. [55] dealt with the flow in the front sidewall gap of the pump, where leakage dominates. Asymmetric effects were found in the front chamber as well. As shows Figure 1.23, the uneven effects are stronger in off-design points. The secondary flow from the front sidewall gap is a significant source of vorticity, affecting the flow field at the impeller inlet and a source of energy loss.

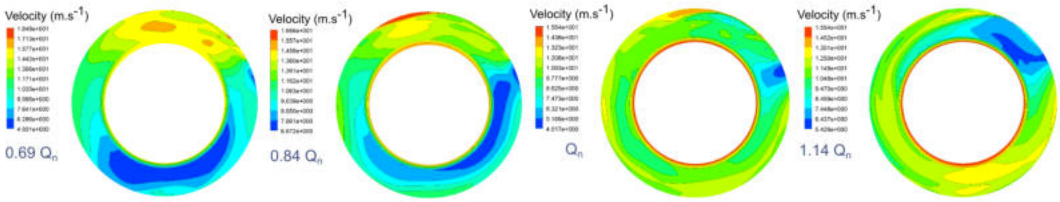

Figure 1.23. Velocity in the middle section of the front pump sidewall gap for off-design and nominal flow rate [55]

Zhou et al. [56] studied the flow in the front sidewall gaps of Francis turbine under transient conditions. A change of the guide vanes angle leads to the periodic variation of leakage flow, producing strong pressure pulsations in labyrinth seals.

Gautam et al. [64] observed erosion of Francis turbine in an inlet near hub-shroud region and towards the trailing edge of the runner blade. It is likely caused by vortices traveling from the clearance gaps. It hits the inlet of the turbine runner and moves out with a very high velocity.

The flow through various sealings was the scope of a number of studies, e.g., [65–71]. Yan et al. [51] compared the flow in the sidewall gaps of the pump-turbine realized by labyrinth seal and flat ring seal, considering different clearances as well.

When operating in turbine mode, the direction of the outflow from the sidewall gap is the same as the main flow, therefore, the influence is minor. In pump mode, the mixing area plays a more important role. The leakage flow rate through the labyrinth seal is lower, so the main flow is less affected than with the flat ring. The same trend is observable for enlarging the flat ring with clearance.

1.3 CFD simulation of the flow in rotor-stator cavities

1.3.1 CFD simulation approaches

With the development of computer technology, computational fluid dynamics (CFD) became a common tool for the analysis of flows. New challenges are connected with the accuracy of modeling of the flow using CFD. Different approaches exist and the choice of an appropriate model means usually a compromise between the accuracy and computational resources. Possible approaches sorted in descending order according to their complexity:

- Direct numerical simulation (DNS)
- Large eddy simulation (LES)
- Hybrid models
- Reynolds stress model (RSM)
- Reynolds-averaged Navier-Stokes equations (RANS)

Direct numerical simulation (DNS)

The method representing the best achievable accuracy is a direct numerical simulation (DNS), where Navier-Stokes equations are solved at all length scales and timescales. From that fact results also a disadvantage, since the computational domain has to be large enough to include the largest naturally occurring eddies, while the computational grid has to be fine enough to fully resolve all dissipation scales. It limits this approach to relatively low Reynolds numbers ($Re < 10^4$), which are unfortunately orders of magnitude smaller than in common industrial applications. Moreover, these methods are not implemented in commercial software, and they require the deployment of special numerical schemes, as described [72], or [73].

Large eddy simulation (LES)

One level lower model is large eddy simulation (LES), which takes into consideration the turbulence as a composition of a large number of various size vortices. Eddies of large scale are solved directly using Navier-Stokes equations, while the small scale (sub-grid) eddies are modeled. Using this approach, a significant reduction of the computational cost compared to DNS is achieved while the high accuracy of the solution is retained. The large eddies computed directly carry most of the turbulent energy and are responsible for most of the momentum transfer. Sub-grid scale eddies are by their nature more isotropic and homogeneous, therefore the modeling is sufficient to obtain the solution with high accuracy [74]. Still, quite high computational demands remain, since the time resolution orders of magnitude smaller in comparison with RANS needs to be used. Strict requirements apply also to the spatial resolution of the grid. The integration up to the walls means the appropriate quality of elements in boundary layer regions [75].

Reynolds-averaged Navier-Stokes equations (RANS)

Engineering applications often involve flows with higher Re, therefore a simpler approach enabling solutions in a reasonable time is often used. It is based on averaging the turbulence in time instead of the description of the instantaneous flow field. So-called Reynolds-averaged Navier–Stokes (RANS) equations are solved. It is a result of Reynolds decomposition, which divides the variables into time-averaged and fluctuating components. However, this leads to additional variables, which makes the system of equations unsolvable. This is referred to as the closure problem and to overcome it, some equations (turbulence models) are added in a way that RANS can be solved. There are many types of turbulence models usually classified according to the number of added equations, (0-4)-equation models are distinguished. Among them, the two-equation models based on Boussinesq eddy viscosity hypothesis, e.g., k-ε or k-ω, are most commonly used in practical applications [76].

The most frequent k-ε model offers a good trade-off between the computational cost and accuracy. It adds two transport equations for turbulence kinetic energy k and turbulence dissipation rate ε. It is a so-called high-Reynolds model, suggesting that it is suitable for flows with high turbulence Reynolds numbers. Turbulence Reynolds number is a measure of the level of turbulence. In the regions, where the viscous effects prevail (e.g., near-wall regions), high-Reynolds models are not suitable and other approach needs to be engaged. The common practice for k-ε model is to use wall functions. The integration is not carried out up to the wall, but it is replaced by empirically obtained equations in the near-wall regions. Modifications enabling k-ε to resolve the flow field also close to the walls without the wall-functions were developed later (low-Reynolds version of k-ε model). However, the wall functions as well as the mentioned integration up to the wall are based on the empirical relationships, which were derived for boundary layers developed during the steady flow over a flat plane. Consequently, the validity in cases of complex flow involving boundary layer separation, pressure gradient, suction, blowing, roughness, etc. is questionable [77].

More accurate results in the regions of boundary layers provide low-Reynolds two-equation k-ω model. Two transport partial differential equations for k and ω (rate of energy dissipation) are added to solve the closure problem. It gives good results for flows with adverse pressure gradients and in the cases, where the integration through the viscous sublayer is preferred (e.g., for solving boundary-layer transitions) [78]. Modification, which is often implemented in commercial software was introduced by Menter [79]. SST k-ω offers an effective combination of high- and low-Reynolds approach in a way that the k-ω is used in the regions of boundary layers and it switches to the k-ε in the core.

Reynolds stress model (RSM)

A more advanced option for turbulence modeling is Reynolds Stress Model (RSM). In contrast to the eddy viscosity models, it takes into consideration the anisotropy of the turbulence. It is possible to solve more complex turbulent interactions such as strongly swirling flows since the individual components of the Reynolds stress tensor are directly computed. Both the wall function and the low-Reynolds approach can be applied connected to RSM [76].

Hybrid models

In order to gain more accuracy than offers RANS modeling and to overcome the computational demands of LES for higher Reynolds numbers, so-called hybrid models were developed. It combines the advantages of both LES and RANS approaches.

Detached eddy simulation (DES) solves the detached eddies (separated regions) far from the boundaries by LES and uses the RANS model for the flow near walls. It provides good results in solving large separation regions, cavities with simple geometry, or coupled simulations of flow and acoustics. Nevertheless, it is weak in the description of curved streamlines and the results are strongly dependent on the mesh quality accomplishment [80]. Thus, the regions which are solved by LES, where the separation of the flow is expected, should be known prior to the simulation and provided with the mesh of appropriate quality, as described [81].

A slightly different technique, which brings dynamic behavior to the model, provides the scale-adaptive simulation (SAS) method. It introduces the Von Kármán length scale into the scale-determining equation of RANS turbulence models, which enables automatic balancing of the contributions of modeled and resolved parts of the turbulent stresses. As a result, in unstable flows, the model changes smoothly from LES through diverse stages of eddy resolution to steady RANS [82].

1.3.2 Modelling of flow in rotor-stator cavity

It should be emphasized that modeling the flow between stationary and rotating disks is a quite challenging task for CFD. The flow structures can be very complex, involving laminar, transitional, and turbulent regions at the same time. Moreover, as a consequence of rotation effects, the turbulence is inhomogeneous and anisotropic. Many different approaches to modeling can be found in the literature.

Chew [83] performed a calculation of the rotating cavity flow using the most simple approach: RANS equations and high Reynolds eddy viscosity model k-ε with wall functions approximation. He found out that this model is not able to predict at least the major flow characteristics obtained by measurement, as documents Figure 1.24.

Chew and Vaughan [84] obtained more satisfactory results with low Reynolds mixing-length models, which use the integration of flow equations over the wall sublayer region. The boundary layer thickness was in good agreement with the experimental results and

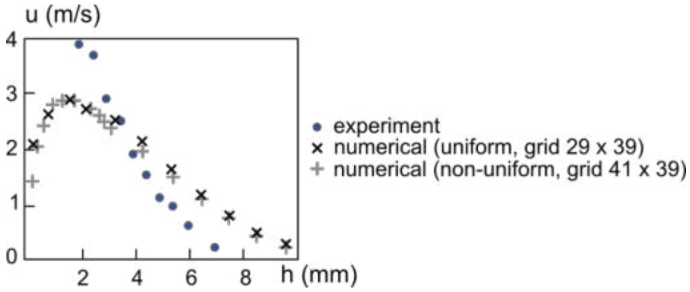

Figure 1.24. Radial velocity profile obtained numerically and experimentally [83]

the predicted velocity is (3-4) % below the measured value, thus it is sufficiently accurate for many engineering purposes. The authors suggested that the approach without wall functions could also work together with k-ε model. It led other authors to use the zonal modeling approach: a high Reynolds model in the core of the fluid, i.g. k-ε or algebraic stress model (ASM), in cooperation with low Reynolds mixing length models near walls.

Elena and Schiestel [85] compared the low Reynolds k-ε, zonal approach with ASM in the core and k-ε for the wall treatment, low Reynolds stress model (RSM) and their proposed modified (RSM2, RSM3) models for the rotating-stationary cavity configuration. Obtained results were compared with the experimental data in order to assess the model accuracy. Refinement of the mesh grids near the walls was specified to acquire steep velocity variations across the boundary layers. The resulting mean velocity profiles can be seen in Figure 1.25.

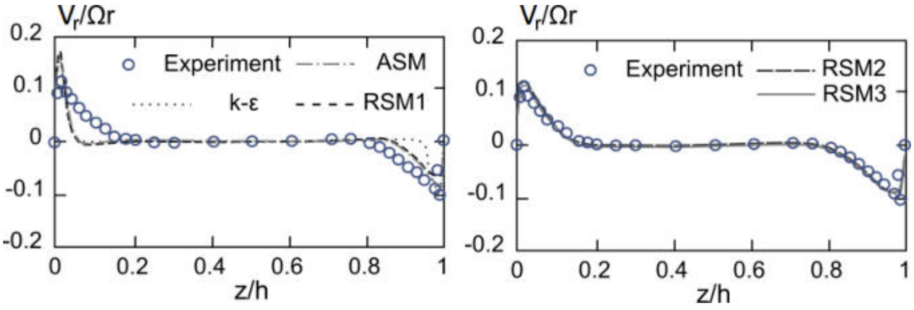

Figure 1.25. Radial velocity profile for different models [85]

All models are able to predict the velocity in the cavity center precisely, differences can be seen in the boundary layer areas. Original models (k-ε, ASM and RSM1) underestimate the Ekman boundary layer thickness on the rotating disk. ASM and RSM model gives at least better results on the stator side, while the modified RSM2 and RSM3 provide better agreement with the experiment on both sides. The same situation is when comparing the components of Reynolds stress. New models are closer to the measurement, however, the results especially near the rotating disk are not quantitatively satisfactory and improvement in numerical modeling near the walls is needed.

Promising results with RSM model achieved also Poncet et al. [86] for a rotating cavity with centrifugal and centripetal throughflow. They found out that RSM gives realistic results for velocity components as well as for Reynolds stresses. Unlike k-ε

model, which overestimates the stress and fails to predict correct velocity profiles, the RSM ensures better results even in the boundary layers. This was again proved by the same group of authors in numerical studies for the regime with two separate boundary layers [43] and by Haddadi and Poncet [87] for the regime of flow with merged boundary layers.

Poncet et al. [88] carried out a study to compare the capabilities of k-ω model introduced by Wilcox [89] and SST k-ω model developed by Menter [79] with k-ε and RSM. The main advantage of k-ω is its robustness and accurate formulation for near-wall regions, however, the original version of the model suffers from the strong free stream sensitivity. This problem was overcome by Menter's extension, which combines k-ω model for boundary layers and k-ε model for the flow in the core of the fluid, which also means that in these regions it is not sensitive to rotation and curvature. They found out that two-equation models overestimate the tangential velocity in the core region. This can be seen in both radial and axial components in Figure 1.26. For higher radii, a better agreement is achieved using RSM. Nevertheless, all tested models failed to predict the thickness of boundary layers. It can be explained by the presence of three-dimensional instabilities which affect even the mean flow.

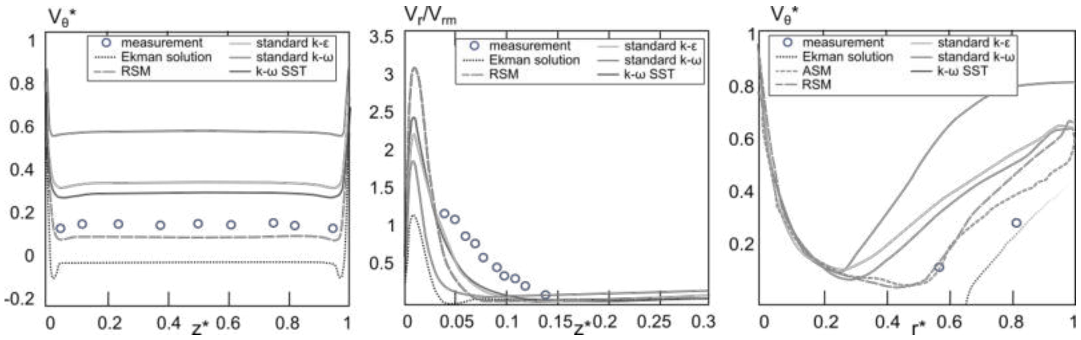

Figure 1.26. Comparison of velocity profiles [88]

Soghe et al. [90] focused in detail on the differences between high- and low-Reynolds approaches. A set of experiments using the same experimental apparatus as Poncet [86] was performed and then solved numerically. RSM, k-ε, and variations of k-ω models were compared. Special attention was paid to the quality of the mesh. The different approaches to the wall region treatment for high- and low-Reynolds models shows Figure 1.27.

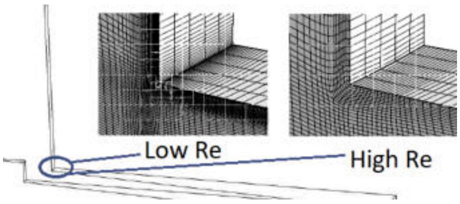

Figure 1.27. Mesh near walls [90]

For a closed cavity, all of the tested models were able to catch the velocity and pressure profiles with reasonable accuracy regardless of the low- or high-Reynolds approach. A different situation occurs for centrifugal and centripetal throughflow. The models were successful in the description of the tangential component of the velocity, however, the predicted radial velocity differs especially in the area near the axis of rotation. The farther from the axis, the closer the models are to each other. RSM provides the most accurate velocity description in the boundary layer. RANS models overestimate the outward flow along the rotor and on the contrary, underestimate the outward flow along the stator. Even though the RANS models provide a reasonable overview of the base flow inside rotating cavities, they are not able to describe the behavior in the boundary layers precisely and even though an unsteady algorithm is applied, the instabilities are not predicted. For these reasons, studies based on DNS such as [91], [92] or [93] appeared. This approach did not allow to solve more complex cases based on real geometry and flow with higher Re, hence it was substituted by a slightly simpler LES.

Lo et al. [94] solved the flow using LES with the Smagorinsky model for computing subgrid stress. The grid size was used as a filtering criterion for the vortices that are solved directly and for those which are modeled. Based on the mesh size sensitivity analysis, the ideal mesh size for the calculations was selected as 80 × 80 × 80. No-slip boundary condition was applied to the walls, the cavity was considered closed, thus no inlet or outlet was defined. Angular velocity corresponding to rotational $Re = 6.9 \times 10^5$ was set due to comparison with the previously done measurement. Comparison of radial and tangential velocity profiles confirmed that the LES model gives results much closer to the experimentally obtained data than the laminar solution or k-ε turbulence model. The azimuthal vorticity contours can be seen in Figure 1.28. Structures aligned with the tangential direction can be observed. The vorticity contours are more coherent near the rotating disk (solid lines), while on the stator, the pattern is more chaotic. It indicates the higher turbulence intensity along the stator increasing with the radial coordinate.

Figure 1.28. The azimuthal vorticity [94]

LES method was further used by Pasquetti et al. [95]. They utilized the spectral vanishing viscosity (SVV) method instead of the Smagorinsky subgrid-scale model. SVV is able to stabilize the computations without losing exponential convergence by completing the momentum, and eventually combines the transport–diffusion equations with SVV dissipation terms. This artificial dissipation is sufficiently large to suppress oscillations, nevertheless small enough to preserve the accuracy. The authors tested the capabilities of LES-SVV to solve the rotor-stator transitional flow and compared the results with DNS. Reynolds number was increased up to $Re = 7 \times 10^4$. DNS calculations were performed using $101 \times 200 \times 65$ grid in (r, θ, z) directions and time step $\Delta t = 5 \times 10^{-4}$. On the contrary, LES-SVV mesh needed only $33 \times 64 \times 23$ elements and $\Delta t = 4 \times 10^{-3}$, which is 3.7% of the DNS resolution. Positive spirals were observed, 4 pairs of rolls in the radial direction can be seen in DNS results as well as in LES-SVV, as shows Figure 1.29. The difference can be seen in the azimuthal wavenumber, which is at the outer radius almost three times smaller in the SVV–LES solution (23 spiral arms) than in the DNS solution (37 spiral arms). It is caused by the fact that the azimuthal wavelength of the spiral pattern is smaller than the azimuthal grid size for LES-SVV. Nevertheless, the overall agreement in velocity components was good, and the method was found to be applicable for higher Reynolds numbers than DNS.

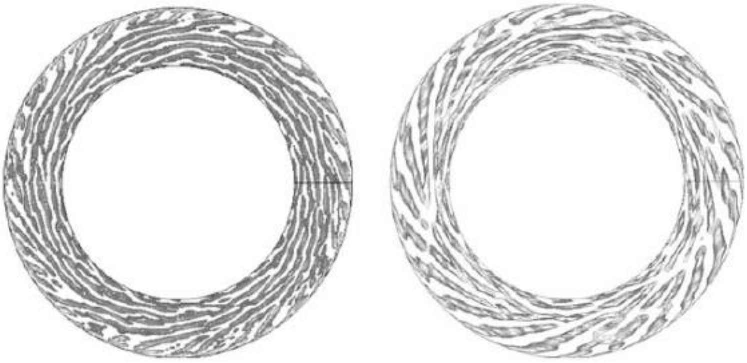

Figure 1.29. DNS (left) and LES-SVV (right) results [95]

The study was expanded by Severac and Serre [96], who carried out mesh sensitivity analysis, and a finer mesh was used for LES. The flow was analyzed for $Re = 7 \times 10^4$ and $Re = 7 \times 10^5$, thereafter, the numerical solution of the velocity components was compared with the experimental results obtained by LDA. They use Q-criterion for visualization of unstable structures. According to Q-criterion, the vortex is a spatial region where the Euclidian norm of the vorticity tensor dominates over the rate of strain. It can be expressed as [96]:

$$Q = \frac{1}{2}(\Omega_{ij}\Omega_{ij} - S_{ij}S_{ij}) \tag{1.11}$$

where Ω_{ij} is the vorticity tensor and S_{ij} is the rate-of-strain tensor. As can be seen in Fig. 1.30, the flow for $Re = 7 \times 10^5$ consists of co-rotating vortices created near the shroud and traveling radially inwards on the stator side (outwards on the rotor). The inner cylinder was considered as rotating as well as the outer one, which has a strong destabilizing effect. Vortices move from Bödewadt to Ekman boundary layer and they are accelerated and strengthened. Satisfying agreement between measurements and LES calculation was achieved in terms of both radial and azimuthal velocity profiles, the thickness of the boundary layers also correspond. The comparison of experimental

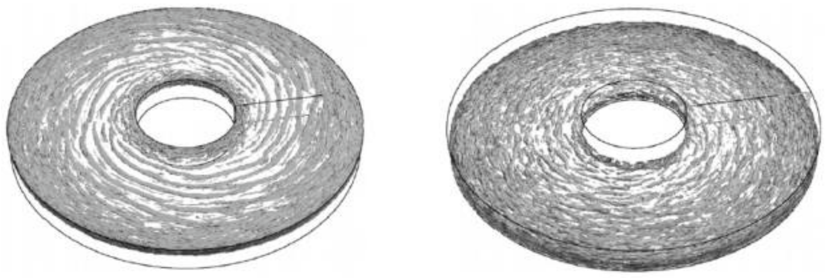

Figure 1.30. Flow structures in rotor and stator boundary layer, iso-surface of $Q = 0.3$ [96]

data and simulations can be seen in Figure 1.31. Furthermore, the calculated Reynolds stress components agree with the measurements, which confirms the capability of LES to perform highly accurate computations.

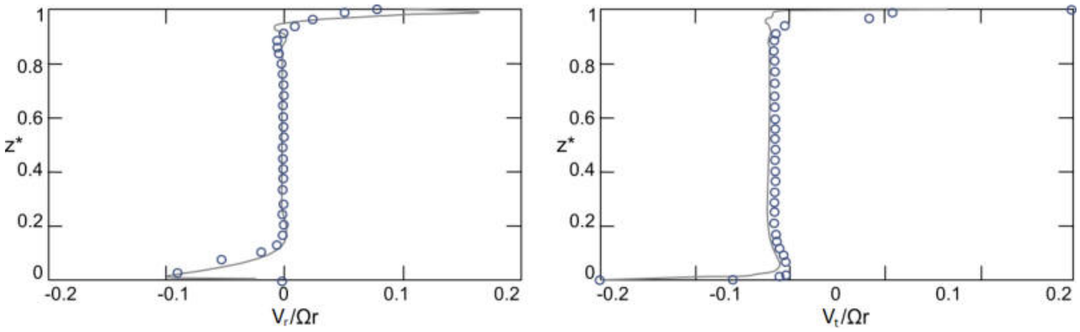

Figure 1.31. Comparison of experimental and numerical results of velocity components [96]

CHAPTER 2

Disk friction losses

Disk friction losses appear on a shroud and a hub of an impeller rotating in the fluid. It has a significant impact on the overall efficiency, especially in the case of centrifugal machines with low or moderate specific speeds. According to Gülich [97], at a specific speed, $n_q = 10$, the power losses due to the disk friction reach typically about 50 % of the useful power. This applies also to low specific speed turbines, especially when operating in off-design conditions, as described Trivedi [98]. Disk friction losses can rapidly rise as a result of corrosion or sediment erosion. The decrease in efficiency up to 50 % due to the increase of disk friction was reported [99]. Thus, there is a need to be able to estimate the disk friction losses during the design phase.

2.1 Calculation of disk friction losses

An estimation of the disk friction is based on a simplified case of the plain disk rotating in an enclosed cylindrical casing. The shear stress due to the local friction coefficient c_f generated on the surface of a rotating disk can be calculated as [46]:

$$\tau = \frac{1}{2}\rho c_f u^2, \tag{2.1}$$

where u is the circumferential velocity:

$$u = \omega r, \tag{2.2}$$

friction force acting on the surface of the disk is then:

$$dF = 2\pi\tau r dr, \tag{2.3}$$

torque caused by the friction can be expressed:

$$dM = rdF = \pi\rho c_f \omega^2 r^4 dr, \tag{2.4}$$

and the friction power on one side of the disk is calculated as:

$$P_{RP} = \omega\int_a^b dM = \frac{\pi}{5}\rho c_f \omega^3 b^5 \left(1 - \frac{a^5}{b^5}\right). \tag{2.5}$$

This approach could not be valid for a disk rotating in a casing, since the velocity profile between the stationary and rotating disk depends on the clearance. The velocity of flow in the core can approximate as [46]:

$$u = \frac{1}{2}\omega r \tag{2.6}$$

and thus, the power consumed by the disk in the stationary casing is calculated as half of the power of a free disk rotating in a stationary fluid.

A detailed explanation of the influence of the established flow regime was published by Daily and Nece [100]. By experimental measurement of friction torque, they quantified the effect of a particular flow regime using a variable called moment coefficient c_m:

$$M = c_m \frac{1}{2}\rho\omega^2 b^5. \tag{2.7}$$

For different Re representing different flow regimes (I-IV) the friction torque M was measured and equations describing the moment coefficient were derived:

$$c_m{}^{I} = \frac{2\pi}{(s/b)\cdot Re}, \tag{2.8}$$

$$c_m{}^{II} = \frac{3.7\cdot(s/b)^{\frac{1}{10}}}{Re^{\frac{1}{2}}}, \tag{2.9}$$

$$c_m{}^{III} = \frac{0.08}{(s/b)^{\frac{1}{6}}\cdot Re^{\frac{1}{4}}}, \tag{2.10}$$

$$c_m{}^{IV} = \frac{0.0102\cdot(s/b)^{\frac{1}{10}}}{Re^{\frac{1}{6}}}, \tag{2.11}$$

where s is the axial gap between rotating and stationary disk and b is the outer radius of the cavity.

Nece and Daily [100] studied also the influence of surface roughness. They found out that for laminar regimes I and III, the roughness does not affect the friction torque. The characteristics were the same regardless of the smooth or rough surface of the disk. On the contrary, in turbulent regimes II and IV the effect of relative surface roughness b/k even dominates over the effect of axial gap width. Moreover, it was reported that even the roughness of the disk casing affects the transition to turbulence and consequently the value of c_m. The combination of rough disk and rough stator exhibits a constant c_m no matter which Re, s/b, and b/k were. For the combination of rough disk and smooth casing, c_m does not show a trend to stabilize on a constant value and is proportional to $Re^{-1/10}$. An alternative equation for the estimation of the moment coefficient considering surface roughness valid for turbulent regimes was derived:

$$\frac{1}{\sqrt{c_m}} = 3.8 log\left(\frac{b}{k}\right) - 2.4\left(\frac{s}{b}\right)^{1/4}. \tag{2.12}$$

Poullikkas [101] confirmed the roughness effect and determined a variant of the equation for the estimation of c_m:

$$c_m = \left(\frac{k}{b}\right)^{0.25} \cdot \frac{(s/b)^{0.1}}{Re^{0.2}}. \tag{2.13}$$

Moreover, he addressed a possible effect of throughflow on the value of the moment coefficient. So-called throughflow parameter λ for assessment of the importance of the throughflow over the rotational flow in the fluid core of the cavity was introduced by Daily et al. [102]. They found out that if λ takes the value over 0.219, the flow becomes rotationally to radially dominated.

$$\lambda = \frac{C_w}{Re^{0.8}}, \tag{2.14}$$

where Re is rotational Reynolds number and C_w is the throughflow Reynolds number (sometimes denoted also as flow rate coefficient or throughflow coefficient), see eq. 1.9. Increasing throughflow forces boundary layers to compress and despite the decrease in tangential velocity in the stator boundary, the gradient of tangential velocity governing the shear stress in the rotor boundary layer becomes close to ωr, and therefore, the value of c_m increases.

Chew and Vaughan [84] related the effect of throughflow to c_m . The results are summarized in Figure 2.1, which shows the ratio of moment coefficient of the cavity with throughflow c_m to moment coefficient of equivalent configuration with no throughflow c_{m_0} plotted against the throughflow parameter λ.

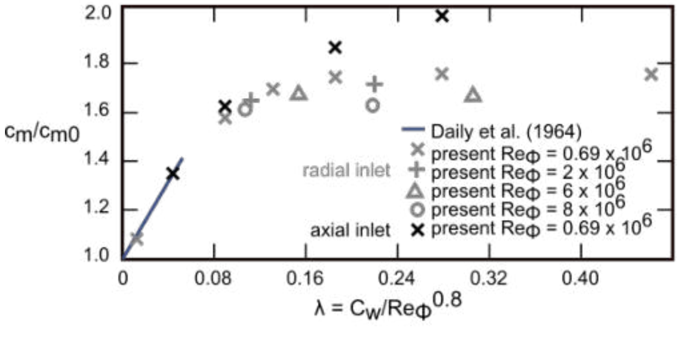

Figure 2.1. Effect of throughflow on moment coefficient [84]

Owen [103] described the influence of the direction of the inflow (radial vs. axial, see Figure 2.2 on the value of c_m numerically. The different parts of the domain are affected differently: the source flow is mainly given by the inlet boundary conditions, while the rest is not affected.

Hu et al. revised the influence of throughflow and its flow direction (centripetal [22] vs centrifugal [104] flow). A modified map of regimes was introduced by expanding the existing 2D diagram to 3D by adding the throughflow coefficient on the third axis.

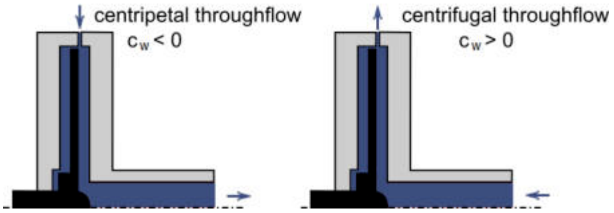

Figure 2.2. Centripetal vs centrifugal throughflow [22]

Special attention due to practical applications was paid to the turbulent regimes and identifying the transition between them. Obtained results are summarized in Figure 2.3 right.

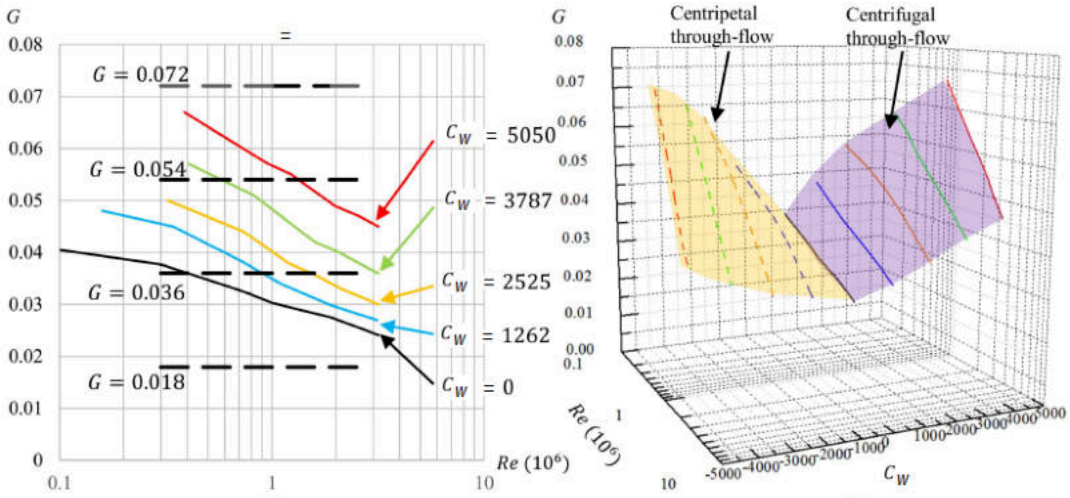

(a) (b)

Figure 2.3. Distinguishing lines and surface between regimes III and IV [104]

It was found out that for a particular aspect ratio G, both radial and tangential velocity decrease with increasing value of throughflow coefficient C_w. Especially the tangential velocity is much lower for the high value of C_w. It is a result of the impact of the jet flow which becomes even greater for smaller G. By closer examination of the tangential velocity profiles, it was possible to detect the change of the flow pattern from Regime III to Regime IV. For $G = 0$ the distinguishing line is identical to the 2D diagram published in [20]. The lines become steeper with increasing throughflow, as can be seen in Figure 2.3 left. The change of throughflow coefficient C_w also directly influences the friction represented by moment coefficient c_m. The value of c_m increases with increasing c_D, whilst with increasing Re it tends to decrease. For large Re, the impact of throughflow becomes less pronounced. The value of c_m in regimes III and IV can be approximated by the following equations [22]:

$$c_m{}^{III} = 0.011 G^{-\frac{1}{6}} \cdot Re^{-\frac{1}{4}} \cdot e^{10^{-4}|C_w|}, \tag{2.15}$$

$$c_m{}^{IV} = 0.014 \cdot G^{\frac{1}{10}} \cdot Re^{-\frac{1}{5}} \cdot e^{0.610^{-4} \cdot |C_w|}, \tag{2.16}$$

During the transition from regime III to IV, it is possible to use both equations leading to a very similar prediction of c_m. The values of the moment coefficient for the centrifugal throughflow case exceed those for centripetal throughflow at the same value of C_w.

The problem of experimental data correlation was discussed, since the obtained values for the same Re strongly depend on the design and setup of the particular experimental apparatus, despite the derived equations are based on the same theoretical background. The agreement of previously performed experiments with new measurements was about 10 %. Moreover, there is questionable applicability of those findings for real hydraulic machines. Most of the experiments were performed on simple annular geometry with steady operating conditions, which is not always true in turbomachinery applications. As a result of optimization and years of development, complex shapes of sidewall gaps or features such as labyrinth seals are commonly used in hydraulic machines. Further uncertainty presents the presence of throughflow and requirements for a wide range of operating conditions leading to unsteady flows. About 40 to 70 % higher losses than expected based on the estimations for plain disk in a cylindrical casing were obtained by measurements in volute casings [105].

Gülich [97] investigated the effects determined by real shapes of an impeller, which influence the disk friction. He derived equations considering the true geometry of a pump impeller without simplification, as illustrates Figure 2.4. For $\gamma < 45°$ and $Re > 10$, the friction power is [97]:

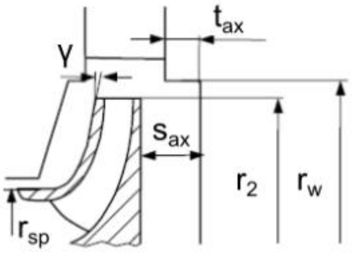

Figure 2.4. Designation of the variables for real impeller geometry [46]

$$P_{RR} = \frac{k_{RR}}{cos\gamma}\rho\omega^3{r_2}^5\left[1-\left(\frac{r_1}{r_2}\right)^5\right], \tag{2.17}$$

where k_{RR} is friction coefficient (annalogy of c_m for plain disks). The coefficient is possible to express by the multiplication of terms representing single effects. A formula for estimation of the friction coefficient valid for all flow regimes can be calculated [97]:

$$k_{RR} = \frac{\pi}{2Re\ s^*_{ax}} + \frac{0.0625}{Re^{0.2}}(1-k_o)^{1.75}f_{R,imp}f_l, \tag{2.18}$$

where s^*_{ax} is ratio of axial gap to impeller outer radius $s^*_{ax} = s_{ax}/r_2$, $f_{R,imp}$ expresses the roughness effect, f_l poses influence of leakage and k_o is rotation factor of the flow with zero leakage Q_{sp}. Rotation factor is given by the ratio of fluid velocity to impeller circumferential velocity:

$$k = \frac{c_u}{u}. \tag{2.19}$$

For zero leakage, it is given as [97]:

$$k_0 = \frac{1}{1 + (\frac{r_w}{r_2})^2 \cdot \sqrt{(\frac{r_w}{r_2} + 5\frac{t_{ax}}{r_2})\frac{c_{f,case}}{c_{f,imp}}}}, \tag{2.20}$$

where $c_{f,case}$ and $c_{f,imp}$ are the friction coefficients of the casing wall and impeller. Factors taking into account surface roughness and leakage flow by influencing the value of friction coefficient are formulated as [97]:

$$f_{R,imp} = \frac{k_{RR}(\epsilon)}{k_{RR}(\epsilon = 0)} = \left[\frac{log\frac{12.5}{Re}}{log\left(0.2\frac{\epsilon}{r_2} + \frac{12.5}{Re}\right)}\right]^{2.15}, \tag{2.21}$$

where ϵ is the equivalent sand roughness of the impeller side.

$$f_l = \frac{k_{RR}(Q_{sp})}{k_{RR}(Q_{sp} = 0)} = exp\left\{-350\varphi_{sp}\left(\left[\frac{r_2}{r_{sp}}\right]^l - 1\right)\right\}, \tag{2.22}$$

where φ_{sp} is the leakage coefficient including the direction of the leakage flow. If it aims radially inwards, φ_{sp} is positive and $l = 1$, if the direction is outwards, φ_{sp} is negative and $l = 0.75$. The value of the leakage coefficient can be expressed as [97]:

$$\varphi_{sp} = \frac{Q_{sp}}{\pi r_2^2 u_2}. \tag{2.23}$$

2.2 Factors influencing the disk friction losses

Numerous studies deal with the effects of individual variables influencing the disk friction significantly. Most important conditions are:

- Reynolds number
- Axial gap
- Surface roughness
- Boundary layer
- Shape of the stator and sidewall gap
- Leakage flow
- Partload recirculation
- Exchange of momentum

2.2.1 Reynolds number

The friction coefficient, and therefore the friction losses, increases with increasing *Re*. The character of the flow is in most cases turbulent. When the flow becomes laminar, the disk friction rises significantly. The share of disk friction losses in the power consumption of a pump decreases exponentially with increasing specific speed. In the case of low specific speeds, the disk friction is the main source of loss [97]. It is shown in the study of Mikhail et al. [106], where a set of experiments on centrifugal pumps revealed that the disk friction coefficient increases parabolically with increasing specific speed and decreases with increasing pump capacity, see Figure 2.5.

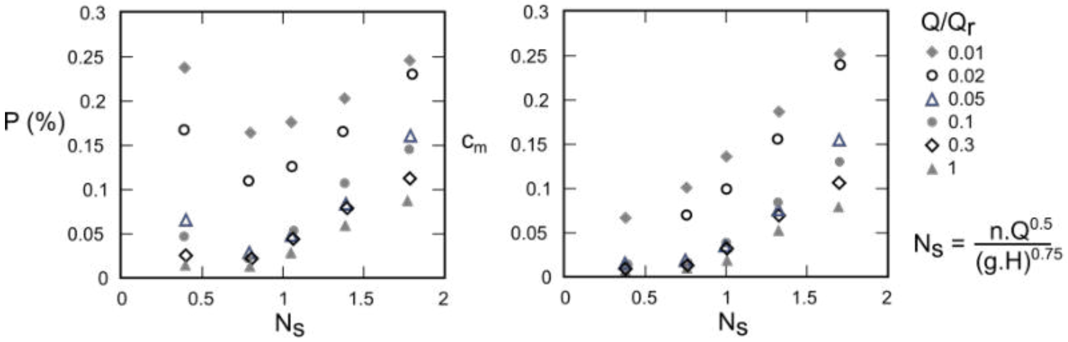

Figure 2.5. Disk friction efficiency and disk friction coefficient for different specific speed and different capacity ratio [106]

2.2.2 Axial gap

Gülich [46] reported that the effect of the axial gap is most pronounced in laminar regimes and plays a minor role in a turbulent flow. When the gap is thinner than the thickness of the boundary layers, the value of c_m is extremely high. With increasing clearance, it increases towards its theoretical minimum. According to [107], the disk friction losses decrease with an increasing axial gap until it reaches $s/r = 0.032$, which corresponds to the theoretical boundary layer thickness. The rise of c_m is presumably caused by increased recirculation area due to increments in axial clearance. At the same time, if the region of recirculation diminishes to less than the border of the boundary layer thickness, c_m increases due to the viscous effect of the wall. Hence, a theoretically optimal design with minimum disk friction should have an axial gap similar to the theoretical boundary layer thickness. It is not achievable in hydraulic machines and so the disk friction losses increase until the turbulent flow regime is reached.

The disk friction in the turbulent regime was treated by Nemdilli and Hellmann [108]. They found out that the value of c_m steadily decreases with the increasing axial gap. The finding agrees with [109], where it is explained by the decreasing difference between the fluid and shroud angular velocity. With decreasing ratio of impeller diameter to the axial clearance r_2/s_1 the dependency of c_m on the pump flow rate increases. Nevertheless, the role of axial clearance in a turbulent regime is minor, set side by side with other effects, especially surface roughness, as documents Figure 2.6.

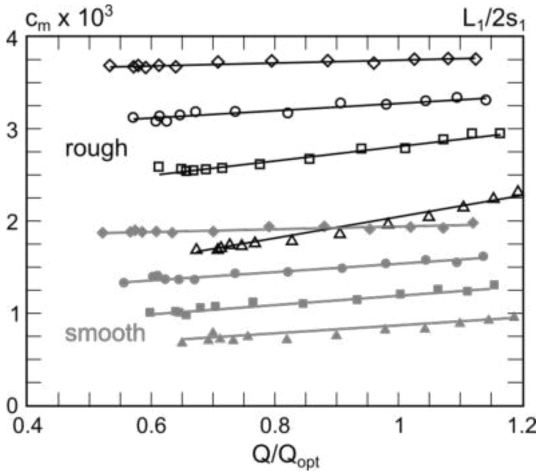

Figure 2.6. Disk friction coefficient for different specific speed and different capacity ratio in centrifugal pumps [109]

Feng et al. [60] reported the decrease in disk friction when increasing the axial gap in the Francis turbine. They found out that the effect is stronger near the runner band than close to the crown. However, it is necessary to point out that such a change results in a decrease in overall efficiency given by a significant increase in leakage flow. Since the drop in efficiency is bigger than the disk friction loss decrease, it is not applicable.

2.2.3 Surface roughness

Both, the surface roughness of the impeller, and the roughness of the casing affect the disk friction. It can be minimized by achieving hydraulically smooth surface conditions. An increase in the friction power occurs when the roughness peaks extend above the viscous sublayer. Structured roughness resulting from machining does not have such a negative impact, e.g., machined disks with equivalent sand roughness $\epsilon = 120\ \mu m$ exhibit similar disk friction as polished disks with $\epsilon \approx 0\ \mu m$. Rotation of the fluid in the sidewall gap does not depend on the roughness, if $\epsilon_{impeller} = \epsilon_{casing}$. When $\epsilon_{impeller} > \epsilon_{casing}$, the rotation rises, contrarily to $\epsilon_{impeller} > \epsilon_{casing}$, when it drops. As a result, the disk friction losses change [46].

However, Tamm and Stoffel [109] showed by measurement of c_m that the disk friction for a rough surface is approximately twice higher than for a smooth surface. If only the casing surface is rough, the lowest angular velocity of the fluid is achieved, which leads to the lowest pressure drop in the sidewall gap and the highest throughflow. It lowers the disk friction more than when smooth casing and disk are taken into account.

Fukuda [110] dealt with the effect of the roughness of the runner on the disk friction losses and efficiency of the Francis turbine. A runner with 6 different values of equivalent sand roughness and 1 hydraulic smooth were tested. As expected, the turbine efficiency decreased proportionally to the frictional resistance of its equivalent sand roughness. Besides, the observation revealed a shift of BEP to lower speed and lower discharge for the runners with higher roughness.

Gülich described how the roughness modification can change the flow in impeller channels and secondary flow. It can lead to a change of the slip factor and theoretical head. The lower the hydraulic efficiency of the original pump is, the higher is the improvement from an enhancement of its surface. The benefit caused by the improvement of surface quality is increasing with increasing Re. However, the surface roughness should be related to the size of the machine (ϵ/r_2), whereas an increase in the surface quality of small pumps results in higher efficiency improvement than for the large pumps.

Gülich [111] pointed out that along with the exact value of the surface roughness, the geometry of the roughness plays an essential role. Parameters such as height, pitch, density, and direction of roughness elements should be taken into account since the structure interacts with near-wall turbulence. These effects limit the accuracy of disk friction prediction because it is of a statistical nature.

2.2.4 Boundary layer

Theoretically, it is possible to influence the turbulence structure of the boundary layer in order to reduce the disk friction. Fine grooves can have such an effect in the direction of the flow, as reported by Brodersen [112]. Tiny V-shaped grooves parallel to the flow direction led to a reduction of friction by 8 %. The described modification, however, is expensive and hardly feasible for hydraulic machines. Moreover, an increase in the friction losses by inconvenient intervention to the boundary layer was achieved as well [111].

2.2.5 Shape of the stator and sidewall gap

The shape of the casing influences the rotation of the fluid and has an effect on the disk friction losses in a similar way as surface roughness. The rotation can be influenced by the shape of the stator itself or by the presence of structures (e.g. ribs), which reduce the fluid rotation [46]. Moreover, it was found out, that the disk friction coefficient of a disk rotating inside the volute casing is up to 70 % higher than that of a disk in a cylindrical casing. The reason for that is reduced k_o and increased k_{RR} resulting from decreased whirl velocity due to friction on the large volute surface. However, this is not true for an impeller inside the volute casing. Strong circumferential velocity in the channels accelerates the side room flow and thus the disk friction decreases [111].

2.2.6 Leakage flow, part-load recirculation, exchange of momentum

The effect of leakage was studied by Kurokawa and Toyokura [113], who described the impact of the different designs of the diffuser of impeller outlet on the disk friction, as shows Figure 2.7 right. The flow in the outer region is determined mainly by the shape of the impeller outlet in the case of type-A design. In the type-B design, the exchange of the angular momentum and the friction on the casing wall are the decisive influences. As shows the trend in Figure 2.7 left, the disk torque decreases with increasing inward leakage flow rate, same for both types. However, for the design of type-B, it increases also with the axial gap. The influence is small for radial inward leakage, on the contrary to the radial outward leakage flow rate, where the torque coefficient strongly rises.

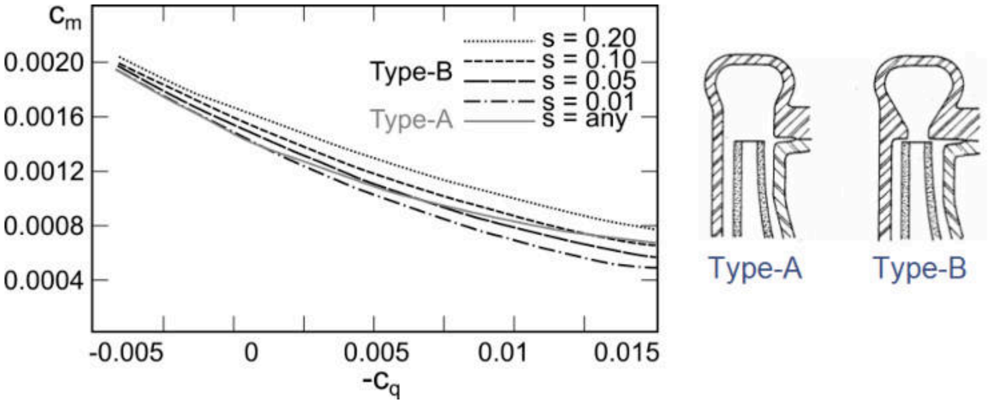

Figure 2.7. Type of the design and their torque coefficient [113]

Gülich [111] dealt with different leakage flow rate Q_{SP} and pre-rotation of the fluid given by the rotation factor at the side-room inlet $k_E = c_{2u}/u_2$. He found out, that for the inward direction, leakage flow through the impeller sidewall gap induces an angular momentum, which can increase or decrease the disk friction depending on the rotation factor k_E. If $k_E > k_o$, the inward leakage accelerates the rotation and the disk friction is reduced, otherwise the outward leakage leads to an increase of disk friction losses. Part load recirculation entering the sidewall gap with low circumferential velocity causes slower fluid rotation and thus the disk friction increases. Radially outward leakage decreases the fluid rotation and therefore increases the disk friction regardless of the value of pre-swirl k_E.

Not only the geometry of the impeller but also the spiral casing can affect the disk friction losses. According to [97], the influence can be specified by r_w/r_2 ratio. The experimental setup with a simple disk in the cylindrical casing has this ratio slightly lower than 1, while the disk in the real spiral casing has a ratio usually about 1.3–1.4. It results in rotation factor k_0 (see eq. 2.20) and higher k_{RR} (see eq. 2.18). Due to the large volute surface, the whirl velocity c_u is lower and thus, friction losses are higher [105]. If the impeller of real shape is taken into account, the flow leaving the impeller channels has high circumferential velocity and therefore, accelerates the flow inside sidewall gaps, which leads to the reduction of disk friction losses.

Exchange of momentum generated by an interaction between main flow, impeller sidewall gap flow, leakage flow, and part load recirculation can crucially impact the disk friction losses and bring huge uncertainty to the loss estimation. Gülich [46] mentions that the calculation tolerance of disk friction losses according to empirical equations is about ±25%, which is the reason for recent authors to prefer CFD for the determination of disk friction rather than an empirical approach, e.g., [105, 107, 114, 115].

CHAPTER 3

Axial thrust

Axial thrust in a centrifugal pump is a result of unbalanced forces acting on the rotor of the pump in the axial direction. The resulting force is a sum of sub forces caused by the pressure distribution on the impeller shrouds F_{DS} and F_{TS}, the momentum F_I, unbalanced axial forces F_w acting on the shaft and the rotor weight in case of vertical pumps, as illustrates Figure 3.1 [46]. As it is given by the flow field in the hydraulic machine, it is closely connected with the flow inside sidewall gaps.

The force F_I is associated with the change of the flow direction and it depends on the shape of the impeller. F_I is significantly lower than F_{DS} and F_{TS}. For the most frequently used radial hydrodynamic pumps, it contributes usually between 3-11 % to the overall axial thrust. Forces caused by uneven pressure distribution on the shrouds are influenced by many various effects, such as type of the pump, type of diffuser, flow rate, design of the impeller, and the pump body [116].

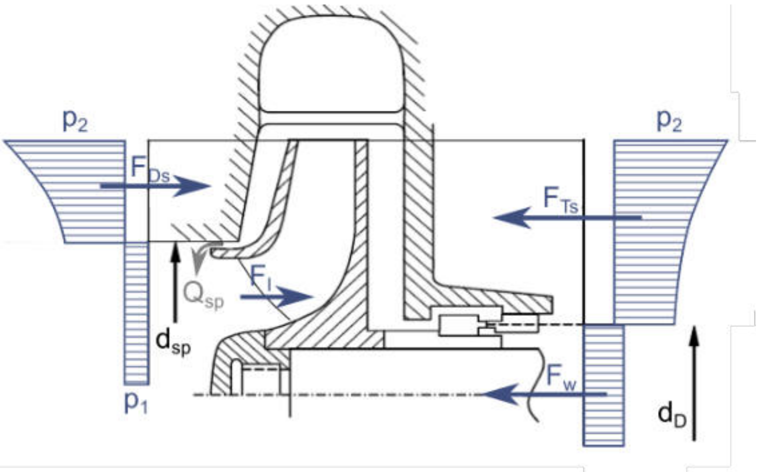

Figure 3.1. Pressure distribution and axial forces acting on an impeller [46]

From the design point of view, it is crucial to consider the axial thrust in the choice of bearings. Many failures due to the axial movement of the rotor are known, leading to complete damage of a pump or turbine. Possible imbalances influence the stability of the operation and the dynamics of the whole system. Periodical loading can cause wearing if the bearings are not chosen properly with respect to axial forces. Since the reliability and service time is determined by this factor, there is a strong need to estimate the value of axial thrust.

3.1 Calculation of axial thrust

There are equations to determine the particular components of axial thrust, however, they were derived considering many simplifying assumptions. Therefore, they provide results, which can be significantly different from measurements. The general assumption is that the liquid in the impeller sidewall gaps has a velocity equal to half of the circumferential speed of the impeller. The next assumption states that the pressure distribution on the impeller outer diameter is uniform. This results in a parabolic distribution of the pressure in the impeller sidewall gaps [116]. Following variables can be affected by inaccuracies [46]:

- Inlet swirl to the impeller sidewall gap (given by the velocity distribution at the impeller outlet)
- Differences between p_2 on the hub and the shroud (especially in the case of radial impellers of high specific speeds and semi-axial pumps)
- Impeller losses and consequently p_2
- Rotation factors k and magnitudes of leakages
- Geometric tolerances (annular seal clearances, axial rotor position, casting tolerances of the impeller)

According to Gülich [46], the force acting on the hub F_{DS} can be expressed:

$$F_{DS} = \pi {r_2}^2 \left\{ \left[1 - \left(\frac{d_{sp}}{d_2} \right)^2 \right] \Delta p_{La} - \frac{\rho}{4} {u_2}^2 k^{-2} \left[1 - \left(\frac{d_{sp}}{d_2} \right)^2 \right]^2 \right\}, \tag{3.1}$$

F_{TS} acting on the shroud:

$$F_{TS} = \pi {r_2}^2 \left\{ \left[1 - \left(\frac{d_D}{d_2} \right)^2 \right] \Delta p_{La} - \frac{\rho}{4} {u_2}^2 k^{-2} \left[1 - \left(\frac{d_D}{d_2} \right)^2 \right]^2 \right\}, \tag{3.2}$$

where Δp_{La} is static pressure above the impeller inlet ($\Delta p_{La} = p_1 - p_2$), u_2 is the outlet circumferential velocity, k is the rotation factor of the fluid in the impeller sidewall gap, which is given by the ratio of the tangential fluid velocity to the rotational speed. Other geometrical variables are given by the dimensions described in Figure 3.1. These equations are appropriate when there is none or only a small leakage. Otherwise, it is advised to use another way of calculation, where the forces are calculated using the former equations first, then the thrust reduction coefficient is determined, and finally, the following equations are used:

$$F_{DS} = \pi {r_2}^2 \left\{ \left[1 - \left(\frac{d_{sp}}{d_2} \right)^2 \right] \Delta p_{La} - \frac{\rho}{4} {u_2}^2 k^{-2} c_A \right\}, \tag{3.3}$$

$$F_{TS} = \pi {r_2}^2 \left\{ \left[1 - \left(\frac{d_D}{d_2} \right)^2 \right] \Delta p_{La} - \frac{\rho}{4} {u_2}^2 k^{-2} c_A \right\}, \tag{3.4}$$

where c_A is the axial thrust reduction coefficient on the impeller shroud due to the fluid rotation. It takes into consideration reduction of the axial force caused due to the rotation of the fluid compared to the case when $p = p_2 =$ constant (then $k = 0$). The reduction is related to a force corresponding to a pressure distribution acting on a surface $\pi {r_2}^2$ ($k = 1$). The change in the flow direction produces a momentum force F_I, which acts away from the suction and can be calculated as:

$$F_I = \rho Q (c_{m1} - c_{m2} cos(\epsilon_2)), \tag{3.5}$$

where Q is flow rate, c_{m1} is meridional velocity at the inlet, c_{m2} is meridional velocity at the outlet, ϵ_2 is the angle between the mean streamline at the impeller outlet and the rotor axis. Determination of unbalanced axial forces F_w, which act on the shaft differs for each type of pump. In single-stage pumps, according to Figure 3.1 it can be calculated using the following equation:

$$F_w = \frac{1}{4} \pi {D_2}^2 (p_{atm} - p_1). \tag{3.6}$$

The resulting axial thrust is given by:

$$F_A = F_{TS} - F_{DS} - F_I + F_w. \tag{3.7}$$

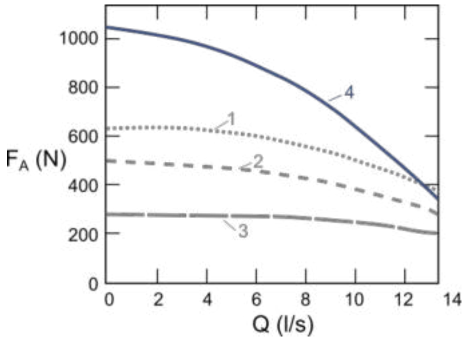

Figure 3.2. Measured (4) and predicted (1-3) axial thrust [116]

Besides the described calculation, there exist many other analytical and empirical relationships. A simplified calculation of axial force was presented, e.g., by Kurokawa and Toyokura [117] or an extended version including more variable parameters by the same authors [113]. Evgen'ev et al. [118] designed a calculation based on measurements for semi-open impellers. The complexity of the flow inside the pump and various internal and external effects do not enable a precise determination of the axial thrust. Analytical or empirical equations are always an only approximation and the real generated axial force may differ significantly, as shown by Gančo [116]. He compared the measured axial force of a particular pump with 3 different empirical models. In Figure 3.2 the measured axial force is the blue curve (4), (1-3) represent the empirical equations derived by different authors. Great discrepancies can be observed, hence there is a need to analyze the factors causing the axial thrust in detail. It was found out that for a precise determination of the axial thrust, it is crucial to consider the proper character of the flow in the impeller sidewall gap and the exact pressure distribution at the impeller outlet.

3.2 Factors influencing axial thrust

3.2.1 Character of flow in the impeller sidewall gap

Flow structures appearing in the front and the back-sidewall gap can be fairly complex, as was described in the first section. For most turbomachinery applications, turbulent flow with separated boundary layers (regime IV) is developed. The fluid adheres to the wall of the shroud which results in the velocity $c_u = \omega \times r$. The fluid also adheres to the wall of the casing, where $c_u = 0$. Centrifugal forces act on the fluid in the rotating boundary layer, which consequently moves radially outwards. To preserve the mass, fluid near the casing wall is forced to flow radially inwards. The circumferential component of the velocity usually dominates over the radial. The circumferential velocity in the core region determinates the pressure distribution and the frictional resistance of the rotor. The resulting torque is influenced by the circumferential velocity gradient in the axial direction, and the pressure is given by the magnitude of the circumferential velocity [28]. Because of the seal leakage, the net flow through the impeller sidewall gap can be added to the circulating flow induced by rotation. The leakage brings the angular momentum into the impeller sidewall gap and therefore accelerates the rotation of the fluid [46].

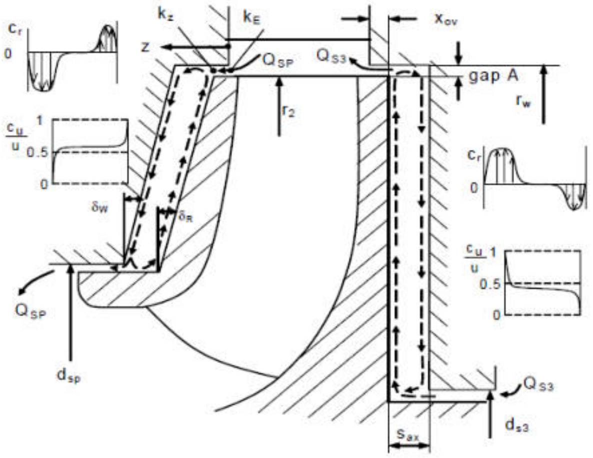

Figure 3.3. Velocity profiles in the impeller sidewall gaps [46]

The main flow at the impeller outlet and the flow in the impeller sidewall gap can be more or less coupled. If gap A is small, and the overlap x_{ov} is large, the flows do not influence each other very much. If the impeller sidewall gaps are open to the main flow, the flow in the impeller sidewall gap is significantly connected to the main flow by the exchange of momentum. It accelerates or retards the fluid rotation dependently on the ratio of the local tangential velocity near the shroud at the impeller outlet to the outlet velocity. Shear stresses in the fluid on the rotating shroud act as a driving moment, while the friction effects decrease with increasing Reynolds number and increase with the roughness. On the other hand, fluid friction on the casing causes a retarding moment. It increases with the casing surface adjacent to the sidewall gap and with the roughness, while it decreases with Reynolds number [46]. Another phenomenon, which influences the flow, is the turbulent dissipation in the impeller sidewall gap, in other words, disk friction losses, leading to the fall of the fluid rotation [46].

Iino et al. [119] noted the importance of the possible axial displacement of the impeller. It affected the pressure distribution in both front and back sidewall gaps and the flow field. By shifting the impeller backward, the front-sidewall gap is wider and the fluid angular velocity decreases. On the contrary, the angular velocity in the back sidewall gap increases. The same behavior was observed by Yamashita et. al [120]. As a result, the axial thrust rises. However, according to [120], the change due to axial shift is not significant for the range of normal operating conditions and plays an important role only for low flow rates. Pehlivan and Parlak [121] reported only a slight increase in axial thrust when only the backside clearance was widened without change of the front sidewall gap.

Gantar et al. [122] pointed to the problem of increased wear ring radial clearance. It causes a reduction of the pressure in the front sidewall gap, which increases the fluid angular velocity and leakage. The character of the flow in the front side wall gap changes and the axial thrust increases.

Another example of a rapid transformation of the flow in sidewall gaps occurs in hydraulic turbines during transient conditions, such as load rejection when unsteadiness of the rotational flow due to acceleration and deceleration of the runner are present [123]. It was found out that a stable velocity field and thus axial force are not formed immediately, which causes pressure pulsations. In addition, during load rejection, a strong swirl emerges at the runner outlet. It leads to a pressure drop along the runner cone and the maximum thrust in the upward direction. It can be equal to the weight of the runner and there is a danger of lifting the rotor. A few lifting accidents of Francis turbines are known [124, 125].

The problem of unsteady axial thrust due to time-dependent conditions is crucial in pump turbines (PAT), where a wide variety of operating conditions have to be taken into account. During the generating mode, PAT serves at least in three working zones: the turbine zone, the turbine brake zone, and the reverse pump zone. Moreover, special features such as fewer blades, higher rotating speed, high water head, cause higher hydraulic forces. Flow conditions differ also among guide vane openings. Li et al. [126] reported that in pump mode, the resulting axial thrust varies slightly with increasing flow rate. However, in turbine mode, the axial force is dominant and special attention has to be paid to it.

3.2.2 Pressure distribution at impeller outlet

Pressure distribution along the impeller outlet, eventually the pressure difference between the hub and shroud, has a direct impact on the resulting axial force. It can be influenced by the radial flow in the sidewall gap or by the volute casing [116]. As was described before, the pressure distribution is influenced by the magnitude of the circumferential velocity in the sidewall gap. In the case of centrifugal pumps, the pressure in the impeller side gaps decreases with decreasing radial coordinate [28].

Shi et al. [127] studied the influence of impeller surface roughness on axial thrust. Modified pressure distribution at a given radius was recognized. As a result, the decrease of axial force with increasing roughness was observed. The higher hydraulic loss led to the reduced head and to lower axial thrust.

3.3 CFD calculation of axial thrust

Since the possibilities of analytical and empirical models to predict the axial thrust are limited, with the development of computational technology, the determination of the axial thrust using CFD is commonly used.

An example could be the work of Harada et al. [128]. They followed the calculation outlined by Gülich [46], however, instead of approximation of the pressure acting on particular parts of the impeller, numerical results from CFD were considered. Moreover, the resulting axial thrust for the analyzed pump was measured experimentally. The simulation was solved as steady-state with SST k-ω turbulence model. Particular components and the total axial thrust obtained from CFD simulation can be seen in Figure 3.4. It

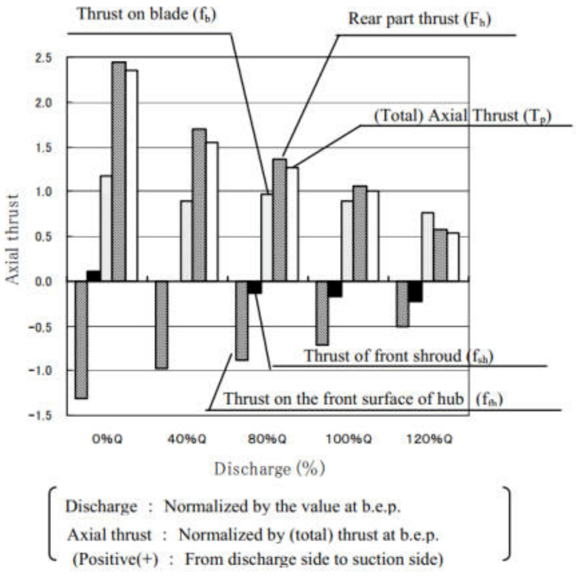

Figure 3.4. Components of axial thrust [128]

can be seen that the thrust acting on the front part of the hub f_{fh} and the thrust of the front shroud f_{sh} are outweighed by the thrust on the blade f_b. It results in the total thrust T_p caused mainly by the rear part. Numerical simulations were performed for different specific speeds. By comparison with the experimental results, it was verified that the CFD method for the determination of the axial thrust is applicable.

Determination of the axial thrust by CFD is in more detail described, e.g., in the study by Wei-Dong et al. [129]. Their aim was to overcome the inaccurate empirical approximation of the axial thrust by solving the problem numerically. According to the measurements, they were able to predict the axial force with an error of less than 10 %. At the inlet area, the velocity was specified, whereas the outflow boundary condition was applied to the outlet. A No-slip boundary condition was used on the walls. Wall roughness was taken into account with a value of 0.1 mm given by the manufacturer. The calculation was set as steady with the second order of accuracy. Multiple Reference Frame model was used for coupling rotating and stationary parts. Different models of turbulence were tested (standard k-ε , RNG k-ε, standard k-ω and SST k-ω). Obtained axial forces were different in the order of units, therefore the least computationally demanding model was chosen. Hence, k-ε turbulence model with wall functions was used for modeling the turbulence in all subsequent calculations. The total axial thrust was calculated as the sum of the partial forces acting on particular parts of the pump, as shows Figure 3.5.

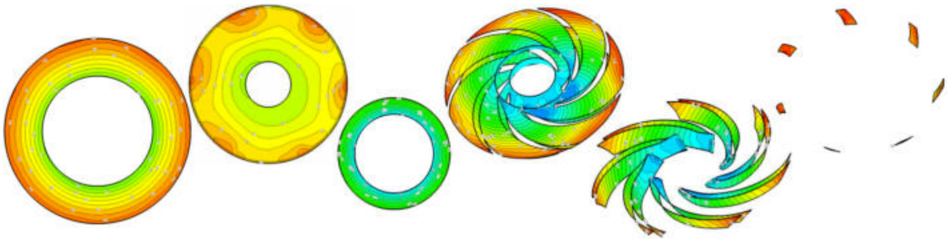

Figure 3.5. Contours of pressure on particular pump parts [129]

As shows Fig. 3.6, the axial thrust is reduced with increasing flow rate, which is in agreement with the previous study [128]. For all analysed flow conditions, the maximum error in comparison with experimental data does not exceed 6 %.

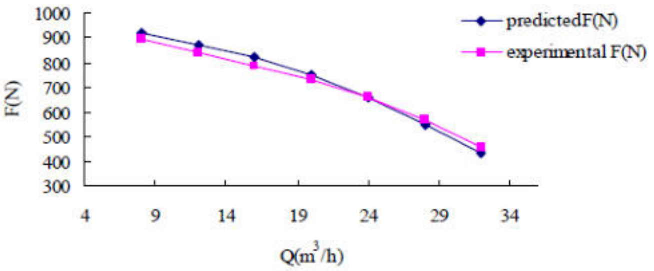

Figure 3.6. Comparison of measured and calculated axial thrust [129]

Pehlivan and Parlak [121] used a CFD simulation verified by experiments for the investigation of the influence of design parameters on the resulting axial thrust of a centrifugal pump. Low-Reynolds approach with attention to mesh quality in near-wall regions and k-ω turbulence model was used. By the described approach, the difference between measurement and simulation in the range of 2.3% to 11.1 % was achieved. Ji et al. [125] described that CFD simulation agrees the best at BEP. The further from BEP, the larger the discrepancy.

Li et al. [126] used a CFD for calculation of the axial thrust in PAT turbine in generating mode. Different guide vane openings belonging to particular operating modes were investigated. Besides the precious determination of axial thrust, a solution of the complete flow field inside the machine by CFD enables a deeper understanding of the phenomena. The axial force reaches its maximum in turbine mode, while in the runaway and turbine brake modes, the component perpendicular to the shaft gains on importance.

3.4 Reduction of axial thrust

Proper design of bearings is an inevitable assumption of the long and reliable service life of a hydraulic machine. Since an uneven pressure acting on the sides of the impeller and therefore nonzero axial thrust can not be avoided, there are efforts at least to minimize the unbalanced force. The symmetry of the pressure distribution on the impeller shrouds is desired, however, the complete symmetry is not possible to obtain. Thus, only a partial balance of force occurs and it is necessary to capture the remaining force in the bearings. In order to minimize the captured thrust, additional hydraulic equipment is also included. There are various ways to balance the axial force, the most commonly used are:

- Double suction impeller
- Balancing piston (drum)
- Balancing disc
- Balance holes and wear rings
- Back vanes
- Grooves on casing wall

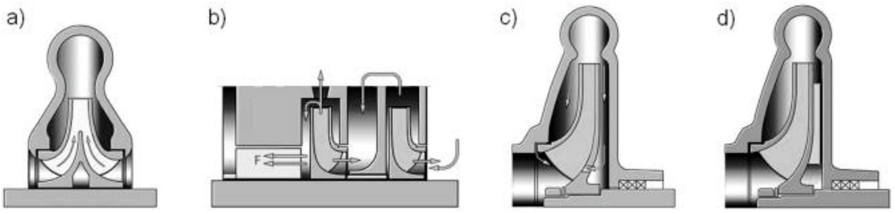

Figure 3.7. Different measures to balance axial thrust: a) double suction impeller, b) balancing drum, c) balance holes, d) back vanes [130]

Part II

Thesis objectives

CHAPTER 4

Objectives

The purpose of the thesis is to extend the current state of the art in the flow inside sidewall gaps of hydraulic machines by obtaining a better understanding of its consequences on the phenomena of disk friction losses and axial thrust.

Experimental studies are limited to the cases with simplified geometry (a plain disk rotating in a cylindrical casing). Such an approach gives only a limited idea of the flow and is not capable of capturing undoubtedly significant effects caused by blades of the impeller and complex shapes of real geometry in general. Despite we are aware of the existence of various unstable flow structures and the conditions under which they occur, the applicability of those findings in real turbomachinery problems is uncertain.

The impact of the presence of unstable flow structures in sidewall gaps on disk friction losses and axial thrust is also unclear. The presence of a real impeller with a certain number of blades can possibly disturb the flow field in the backside wall gap and makes the applicability of previous findings even more doubtful.

The aim of the thesis is to describe the possible regimes and flow structures appearing in the sidewall gaps of the real shaped impeller and to put it into the context of disk friction losses and axial thrust.

Particular objectives of the doctoral thesis:

- Methodology of CFD for flow in rotor-stator gaps capable of capturing all possible flow regimes
- Design of an experimental apparatus with inner geometry close to the real pump, which enables simultaneous observation of flow regimes and measurements of disk friction losses and axial thrust
- Experimental measurements supported by CFD simulations
- Summary of new findings and conclusions applicable in turbomachinery

Part III

Numerical and experimental techniques

CHAPTER 5

CFD methodology

5.1 Finding a suitable turbulence model

Since CFD is one of the main methods in the research of the flow in sidewall gaps of hydraulic machines in this thesis, therefore, it is crucial to find the optimal approach for the numerical simulations. Correctly resolved pressure and velocity fields (including possible instabilities) enable the precise calculation of the disk friction losses as well as the determination of axial thrust.

As was described in Section 1.3.2, the problem of numerical simulation of the flow field in rotor-stator cavities introduces a number of challenges due to the high complexity of the flow. Laminar, transitional, and turbulent regions can coexist, the rotation causes inhomogeneous and anisotropic turbulence.

As was mentioned in the theoretical part, different authors have different approaches to the problem of modeling flow in sidewall gaps. A wide variety of turbulence models from eddy viscosity (both low- and high- Reynolds) [83, 84, 90] through RSM [85, 86] to LES [94–96] and DNS [91–93] can be found. Unfortunately, a complex comparison of those approaches is missing. Although the simpler models are apparently sufficient for the determination of velocity profiles in good agreement with experimental measurements, the authors generally do not consider unstable structures. Since a lot of them do not deal with operating regimes, where it can be expected, it does not necessarily mean that this approach is wrong. However, it is not possible to conclude whether those models are capable of capturing it or not. The only approaches, which explicitly mention the successful simulation of instabilities in this type of flow are DNS and LES.

Since LES is quite computationally demanding and DNS is not integrated into any commercial CFD software, the question, whether it is not possible to reliably simulate the flow by any other model, arises. A promising way could represent one of the hybrid models combining RANS with LES. As it is a relatively new method, publications of its application to the rotating cavity flow are missing. The capability of capturing unstable structures by simpler RANS models is also unclear. The initial aim is therefore to summarize the potential of the particular approach and find the model which represents a good trade-off between accuracy and computational demand.

Based on the literature review, the use of the following models seems to be reasonable and thus will be tested and compared:

- LES
- SAS
- DES
- SBES
- RSM
- SST k-ω

5.1.1 Geometry and mesh

The testing case for the optimization of CFD methodology is based on the geometry of the simple enclosed rotating cavity without throughflow. The geometry and dimensions were taken over from the research of Severac et al. [131, 132], in order to be able to compare the numerical results with any available experimental measurements. The experiments were performed using an apparatus equipped with two parallel disks, one of them is stationary, while the second is rotating. The outer cylinder (shroud) is connected to the stator, the inner cylinder (the hub) is rotating with the rotating disk. The height of the gap is fixed, therefore the operating conditions are governed only by the change of rotating speed. The dimensions of the fluid domain are shown in Figure 5.1. Considering the symmetry of boundary conditions and the resulting flow, it is possible to reduce the domain to a fraction and save computational resources, as was shown in [132].

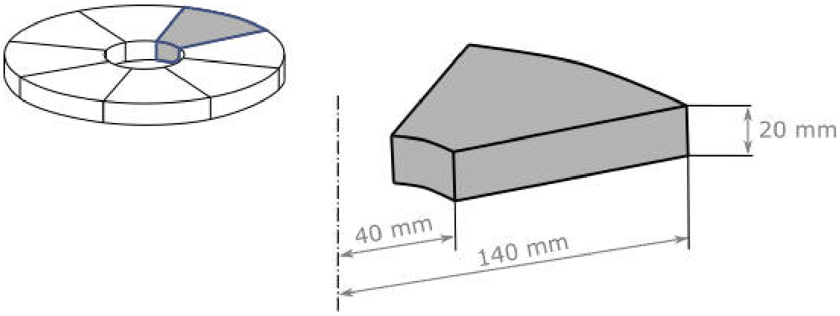

Figure 5.1. Geometry and dimensions of the domain

The mesh which meets the requirements for all intended turbulence models even with low-Reynolds approach was generated as shows Figure 5.2. It consists of 1 728 000 hexa elements with spatial resolution fulfilling strict requirements on wall functions for LES [133].

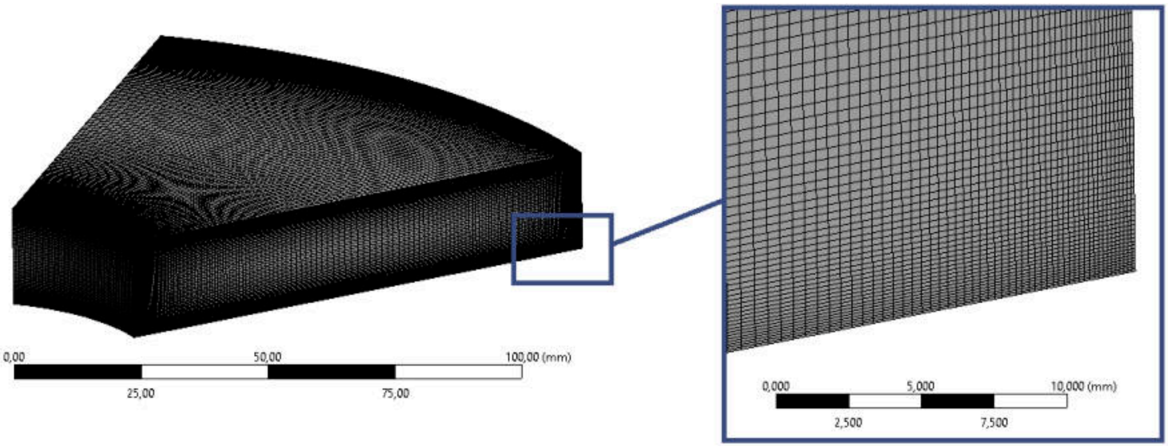

Figure 5.2. Computational mesh

5.1.2 Boundary conditions

All cavity walls were treated with no-slip boundary conditions. Constant angular velocity $\Omega = 20.4082$ rad.s^{-1} was prescribed to the inner cylinder and the bottom disk since it should result in unstable flow regime with vortical structures corresponding to rotational Reynolds number $Re = 4 \times 10^5$, as was experimentally captured in [131]. The outer cylinder with the upper disk was stationary walls. Periodic boundary condition was applied to the sidewalls of the domain.

5.1.3 Solver settings

ANSYS Fluent version 19.1 was used to perform all calculations. First, a steady-state simulation was run, after achieving convergence, it was used for initialization of transient calculations with specific settings appropriate for each approach.

The water inside the rotating cavity was considered incompressible using material data for water-liquid from the ANSYS Fluent library. For the first step steady-state simulation k-ϵ turbulence model with enhanced wall treatment was applied due to its good convergence. First orders of accuracy were used for advection terms in all transport equations and the SIMPLE scheme was set for pressure-velocity coupling. After obtaining the convergence, the pressure, the turbulence kinetic energy, and the turbulence dissipation rate were switched to the second order of accuracy and momentum to the QUICK scheme, which is the 3$^{\text{rd}}$ order of accuracy.

As mentioned before, different approaches to modeling turbulence were tested, namely: LES, SAS, DES, SBES, RSM, and SST k-ω. The simulations were switched to transient with the PISO pressure-velocity coupling algorithm recommended for unsteady flows. An appropriate time step for the known nature of instabilities and a particular model of turbulence was set. In previous studies [131,132] time step of order $\times 10^{-5}$ s was reported as sufficient to capture the nature of rotating instabilities, therefore, $\Delta t = 1 \times 10^{-5}$ s was used for LES. The less demanding computational models allow for coarser time resolution.

Length of the time step Δt was determined with respect to the Courant-Friedrichs-Lewy (CFL) condition according to which Courant number should not exceed 1:

$$C = U \cdot \Delta t / \Delta x, \tag{5.1}$$

where C is Courant number, U is the magnitude of velocity, Δt is time step and Δx is the minimum cell size. Then, for the testing cases, the maximum time step is $\Delta t = 4\times10^{-4}$ s. Nevertheless, the time step was initially set to $\Delta t = 1\times10^{-5}$ s for all approaches to ensure better convergence and afterwards was changed to $\Delta t = 4\times10^{-4}$ s.

5.1.4 Results

According to the map of regimes [20], the existence of Type II instability is expected for given operating conditions. It is observable in the form of spirals in 15° angle in the tangential direction, rotating in opposite direction than the disk. This regime of flow was proved by experiments documented in [131] and is shown in Figure 5.3.

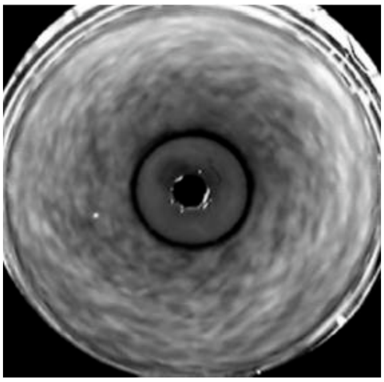

Figure 5.3. Experimental visualisation of the instabilities [132]

Q-criterion was used for visualization of potentially unstable flow structures, an overview of particular turbulent models summarizes Figure 5.4. The ability of the LES approach to capture the instabilities reliably was confirmed. The spiral vortices in the middle part of the cavity, as well as stronger unstructured turbulence near the hub described in experiment [132] were detected, see Figure 5.5. Unfortunately, other less computationally demanding models failed in the detection of the coherent structures. Some indications of vortices in the hub region with the strongest intensity of turbulence are noticeable also for SAS, however, trials with DES, SBES, RSM, and SST k-ω were entirely unsuccessful.

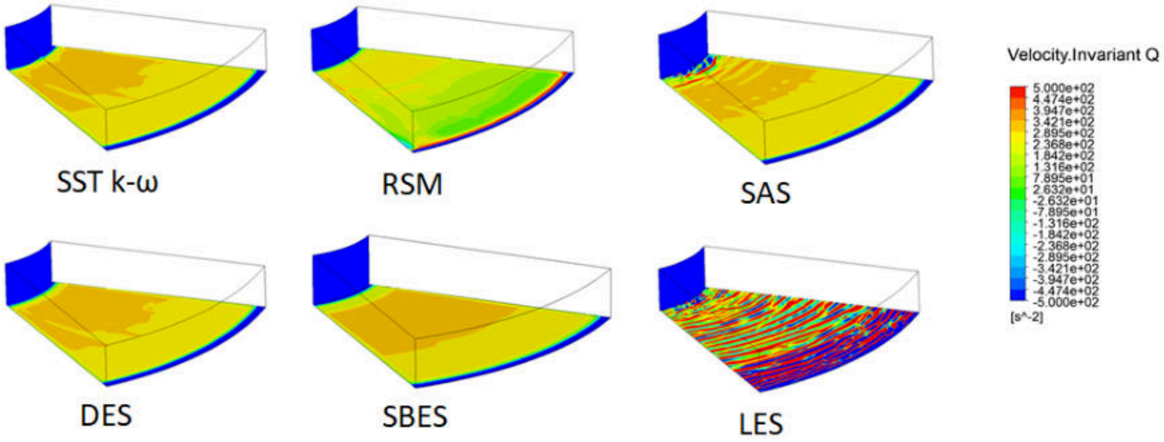

Figure 5.4. Q-criterion - comparison of different modelling approaches

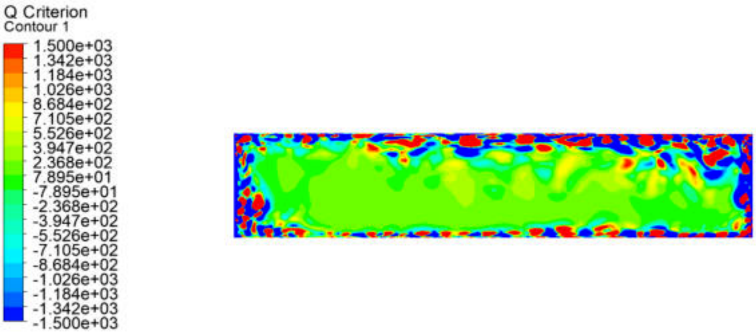

Figure 5.5. Q-criterion - LES (radial section)

For comparison of velocity profiles across the gap, a dimensionless axial and radial location is defined as follows:

$$z^* = z/h, \tag{5.2}$$

$$r^* = (r-a)/(b-a), \tag{5.3}$$

therefore, $z^* = 1$ gives the position of the stator and $z^* = 0$ is the location of the rotor. Dimensional radial location $r^* = 0$ describes the hub and $r^* = 1$ the shroud. Velocities were made dimensionless as well according to:

$$v_r{}^* = v_r/\Omega r, \tag{5.4}$$

$$v_t{}^* = v_t/\Omega r. \tag{5.5}$$

The axial velocity is not plotted since it approaches zero. Figure 5.6 shows the instantaneous radial (left) and tangential (right) velocity components obtained by different turbulence models and comparison with experimentally obtained data [132]. The profiles are plotted for the mean radius of the disk cavity (in the middle of the computational domain). The flow field consists of a core region and two boundary layers - the Bödewadt boundary layer on the stator and Ekman boundary layer on the rotor. The fluid flows centrifugally outwards along the rotor, declines in the axial direction, and as a consequence of the conservation of mass, is forced radially inwards along the stator.

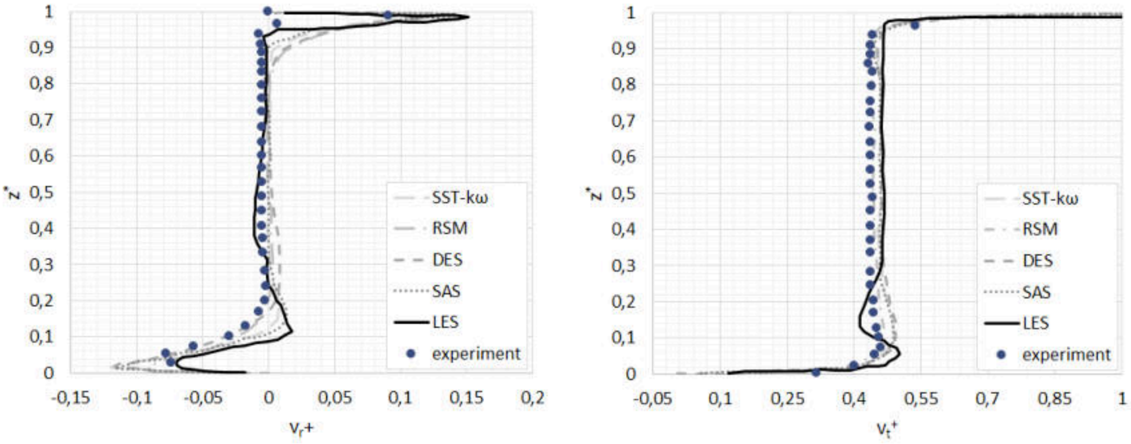

Figure 5.6. Radial and tangential velocity profile

All numerical simulations predict the experimentally obtained data with reasonable accuracy, especially in the core region. Larger discrepancies can be seen in the regions of boundary layers. Unfortunately, only a few measured points are available in those regions. Moreover, the measurement was averaged over time, thus unsteady phenomena were suppressed. On the other hand, it enables a comparison with numerical simulations. LES was the only model capable of capturing instabilities. It is visible in the velocity profile, especially near the rotor side ($z^* = 0$). This is why there is an obvious difference in the velocity profile between the experimental data and the LES model near the rotor boundary layer. The thickness of the Ekman boundary layer on the rotor is lower compared to the Bödewadt boundary layer on the stator, which corresponds to the theory and results published in [132]. However, in comparison with measured data, numerical models slightly underestimate the thickness of the Ekman boundary layer and overestimate the thickness of the Bödewadt layer. Velocity profiles in the near-wall regions can be seen in detail in Figure 5.7 and Figure 5.8.

A correctly determined velocity profile in the inner boundary layer is crucial for the calculation of the shear stress and therefore, friction losses. Only numerical results are compared in Figure 5.7 and Figure 5.8 due to the lack of experimental data in the viscous sublayer. In general, the velocity profiles computed by SAS, DES, RSM, and SST k-ω do not differ significantly. It is capable of the description of the tangential velocity profile with good accuracy, even though the instabilities were not captured by them. The slope of the tangential velocity in the viscous sublayer (y^+ <5) is very similar to the LES model, which includes the unstable nature of the boundary layer. The difference is most pronounced in the buffer layer region (5< y^+ <60), with increasing y^+ the

Figure 5.7. Radial and tangential velocity profile near stator wall

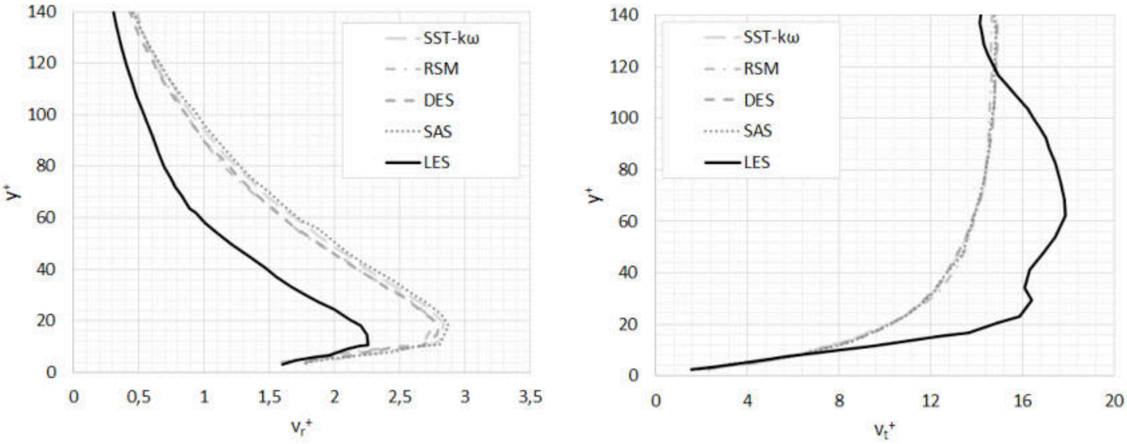

Figure 5.8. Radial and tangential velocity profile near rotor wall

velocity profiles obtained by different models approach each other. Larger discrepancies are observable in the radial velocity profile. The calculated slopes of the curves are different among particular models in the viscous sublayer as well as in the buffer layer. SST k-ω DES and SAS lead to similar results. The difference in the case of RSM is more pronounced in the less stable stator boundary layer. There is an apparent shift of the velocity profiles from LES, predicting a steeper gradient of the radial velocity in the viscous sublayer, while a lower gradient of the radial velocity is computed on the rotor side. The radial velocity magnitude determined by SAS, DES, RSM, and SST k-ω is smaller in the viscous sublayer as well as in the buffer layer of the stator compared to LES. On the other hand, the predicted radial velocity on the rotor side is larger for SAS, DES, RSM, and SST k-ω than that modeled by LES.

5.1.5 Conclusions

- The radial and tangential velocity profiles computed by SAS, DES, RSM, and SST k-ω do not differ very much among each other.

- The results given by SAS, DES, RSM, and SST k-ω agree with LES in the core flow, however, there is a discrepancy in the near-wall regions. Unfortunately, these regions are important for the determination of friction losses. Moreover, the boundary layers are important for the onset and further spreading of the instability.

- The less computationally demanding models (SAS, DES, SBES, RSM, and SST k-ω), are not able to capture the instabilities.

- The coherent unstable structures modeled by the LES approach match the experimental visualization, it is capable of capturing the spiral vortices on the rotor and the stator as well as stronger turbulence with unstructured swirling near the hub.

- The velocity profile computed by LES agrees also well with the measured data.

- LES in an inevitable level of modeling for the flow in rotating cavities. An effort to reduce the computational demands using less complex turbulence models leads to a significant reduction of accuracy and to the loss of important information about instabilities.

5.2 Application of the proposed approach to a real pump cavity

The outcomes from the initial study were applied to the simulation of the flow in a real pump cavity in order to validate the proposed methodology and show the potential of such an approach.

CFD simulations in turbomachinery often completely neglect the sidewall gaps, in other words, the regions of the front and back-sidewall disk gaps are not involved in the simulation at all. However, it has been shown that the flow in those tiny regions can have a great impact on the whole flow pattern inside the machine and thus significantly influence the calculated disk friction losses and efficiency. In the studies where it is included, no special attention is paid to the proper solution of the flow in those regions.

This part of the thesis demonstrates the CFD analysis of a centrifugal pump with emphasis on the flow inside impeller sidewall gaps. It builds on the knowledge, that the LES approach is necessary to resolve the boundary layers in those regions correctly.

5.2.1 Geometry and mesh

A low specific speed pump was chosen for the demonstration since the disk friction plays a very important role there. Moreover, numerically obtained results can be compared with data from experimental measurements carried out as a part of previous research at Viktor Kaplan Department of Fluid Engineering. The whole pump geometry consists of 5 separate domains connected by non-conformal interfaces, as shows Figure 5.9.

Figure 5.9. Fluid domains combined together

Full hexa mesh with wall refinements suitable for RANS turbulent model was generated on the inlet domain using ANSYS Meshing. TurboGrid meshing tool was used to create hexa mesh also in the impeller. Special attention was paid to generating mesh in the sidewall gaps domains. In order to use LES, hexa mesh with $y^+ \simeq 1$ was generated using ANSYS Meshing. The volute consisted of tetra elements with prismatic refinement in the boundary layer. Individual domains were coupled by 5 non-conformal interfaces. The whole mesh was composed of approximately 14 500 000 cells, details can be seen in Figure 5.10.

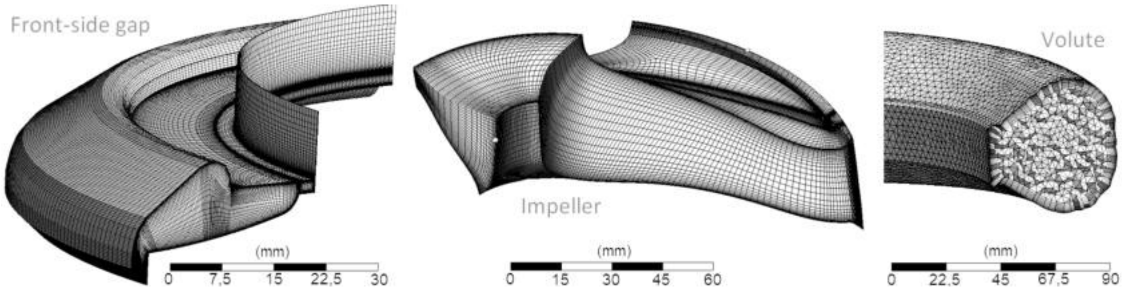

Figure 5.10. Details of computational mesh

5.2.2 Boundary conditions

The fluid enters the inlet domain as shows Figure 5.11 through mass flow inlet boundary condition. The simulation is set to BEP (best efficiency point) corresponding to mass flow rate 31 $\mathrm{kg} \cdot \mathrm{s}^{-1}$. Then it enters the impeller domain rotating with $n = 2\ 900$ rpm.

All of the other domains are stationary and only the impeller walls are treated with rotational wall boundary condition. Walls are treated with no-slip boundary condition. There are two pressure outlets as can be seen in Figure 5.11. One of them belongs to the volute fluid domain with pressure p = 434 793 Pa obtained by measurement. The second pressure outlet is located in the shaft region in the back-side gap domain and atmospheric pressure is set on it.

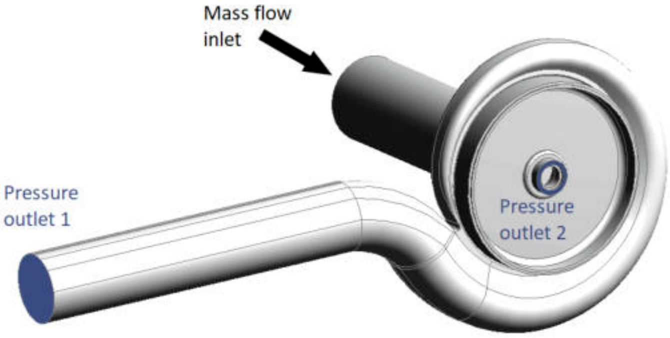

Figure 5.11. Boundary conditions

5.2.3 Solver settings

The default model for liquid water-liquid from the ANSYS library was used considering the fluid incompressible. Using LES in the whole domain of the pump would require extreme computational resources. In order to obtain accurate results in a reasonable time, an embedded LES approach combining Large Eddy simulation in the sidewall gaps and the RANS model in the rest of the fluid was used. Particular domains are combined by interfaces as shows Figure 5.12. For RANS domains, k-ϵ Realizable turbulence model was used, later on, SST k-ω was also tried. The convergence was slightly faster for it but it did not make a significant difference in the resulting flow field. The domains of front- and back-sidewall gaps were of special interest, therefore simulation by LES was performed in those regions. WALE subgrid-scale model which is recommended for the embedded LES approach was used. On LES-RANS interfaces, the need to resolve turbulent transportation between modeled (RANS) and directly computed (LES) zones arises.

There are a few methods for introducing the turbulent fluctuations into the interface between LES and RANS zones, a comprehensive review was done by Tabor and Baba-Ahmadi [134] or Wu [135]. In general, they are based either on the generation of synthetic turbulence or on the precursor simulation. The first approach is built on the injection of artificial fluctuations upon a prescribed mean flow, while the second requires performing a precursor simulation using the RANS model inside later intended LES domain in order to generate a library of turbulent content that can later be mapped onto the region [136]. The methods using synthetic turbulence are more efficient and generally

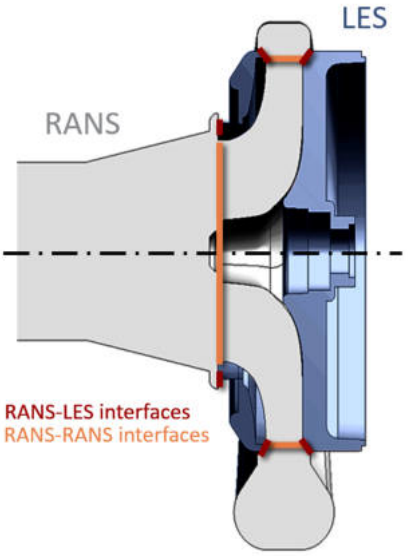

Figure 5.12. Boundary conditions

better applicable for various types of simulations [135], therefore they are implemented in commercial CFD codes.

In ANSYS Fluent solver, 3 possible treatments of RANS-LES interfaces are available: No Perturbations, Spectral Synthesizer and Vortex Method. According to the Best Practices in ANSYS CFD [137] and [138], the Vortex Method is preferred over the Spectral Synthesizer on RANS-LES interface, while on LES-RANS, No Perturbations are usually the best option. For the Vortex Method, the number of generated vortices is compulsory input. The number of the vortices should be set as the number of cells faces at the inlet $N/4$ [138]. For more details of the algorithm of the Vortex Method see [139]. The simulation of the pump followed the recommended procedure.

The time step was set to $\Delta t = 1 \times 10^{-6}\ s$ in order to fulfill the CFL condition and follow the common practice for CFD in turbomachinery to set such a time step, which ensures rotation of max 2 ° per Δt. Steady-state results were used for the initialization of the transient analysis. For pressure-velocity coupling, the SIMPLE scheme was used with the first orders of accuracy for advection terms in all transport equations. After achieving convergence it was switched to the second order. With the described settings, 5 revolutions of the impeller were computed.

5.2.4 Results

The flow inside the pump is very complex and its evolution is greatly affected by the rotation of the impeller. Pressure and velocity are dependent on the current position of blades with respect to the volute cutwater. Some insight into the time evolution of velocity field in meridional section gives Figure 5.13.

Taking a closer look at the flow in the sidewall gaps, it can be noted that in some

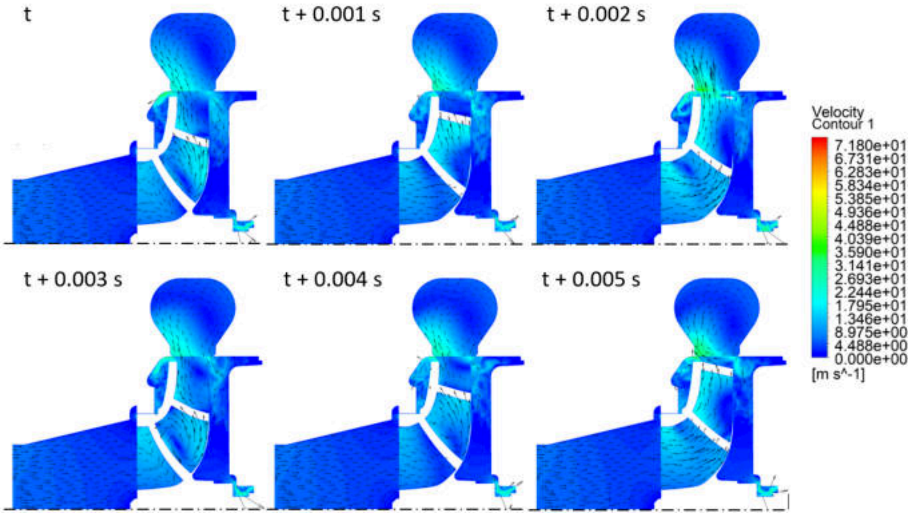

Figure 5.13. Vectors of velocity in meridional section

circumferential locations the fluid enters the sidewall gaps while in other regions it flows out of the gaps. The position periodically changes as the impeller rotates. Another periodical effects caused by the rotation of the impeller and by the shape of the pump spiral casing are pressure pulsation observable on pressure contours of the sidewall gaps. Those effects during 8 timesteps corresponding to 1/6 of impeller revolution (1 blade passes the volute cutwater) are illustrated in Figures 5.14 and 5.15.

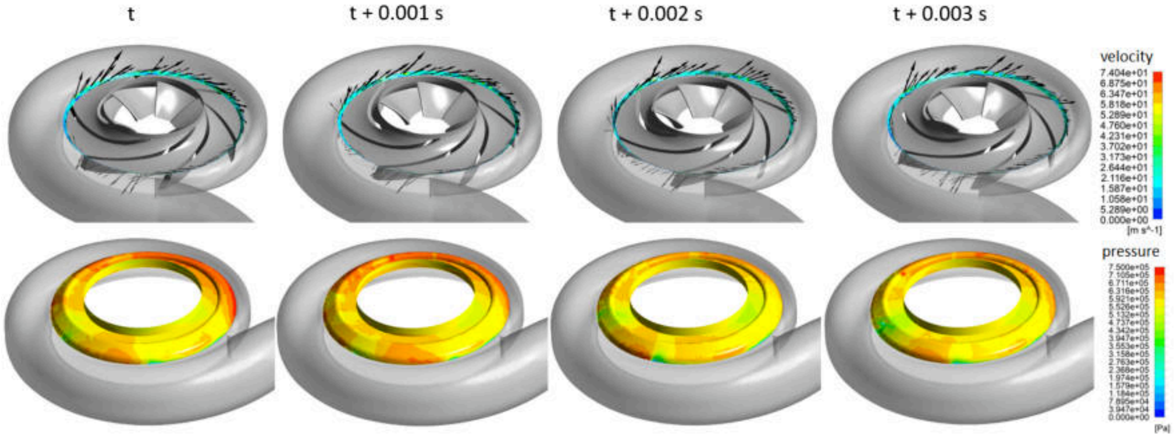

Figure 5.14. Evolution of velocity and pressure during 1 blade passage in front-sidewall gap

The uneven velocity at the interfaces of the sidewall gaps causes a very complex flow field with unstable vortical structures in those regions as shows the visualization of Q-criterion in the front-sidewall gap in Figure 5.16 and the velocity profiles across the gap Figure 5.17. The radial and the tangential components of velocity were evaluated in the middle of the cross-section of the front-sidewall gap. As can be seen, the typical S-shaped radial and tangential velocity profiles known from simplified disks in cylindrical cases are highly distorted as a result of the complicated shape of the spiral casing. Moreover,

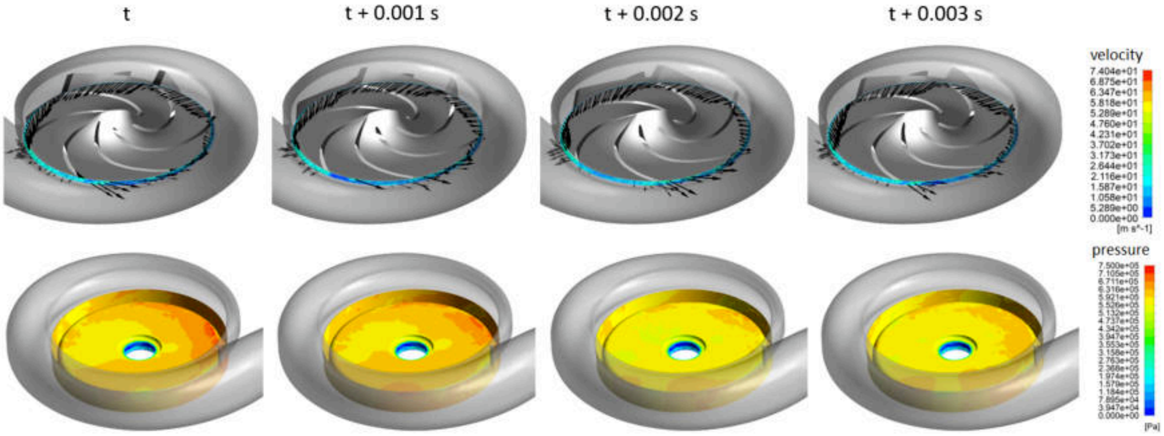

Figure 5.15. Evolution of velocity and pressure during 1 blade passage in back-sidewall gap

it changes rapidly in time with the rotation of the impeller. The same result with the strong vortices applies also to the back-sidewall gap.

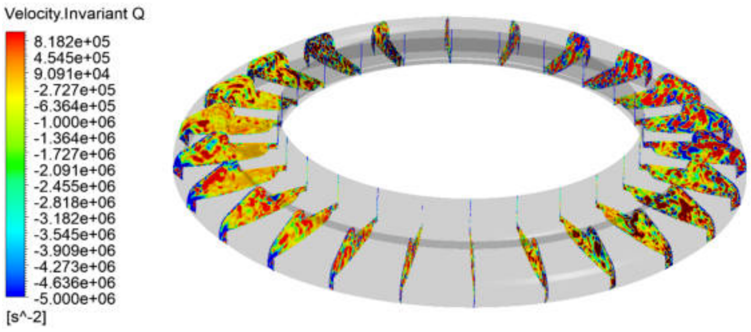

Figure 5.16. Q-criterion in front-sidewall gap

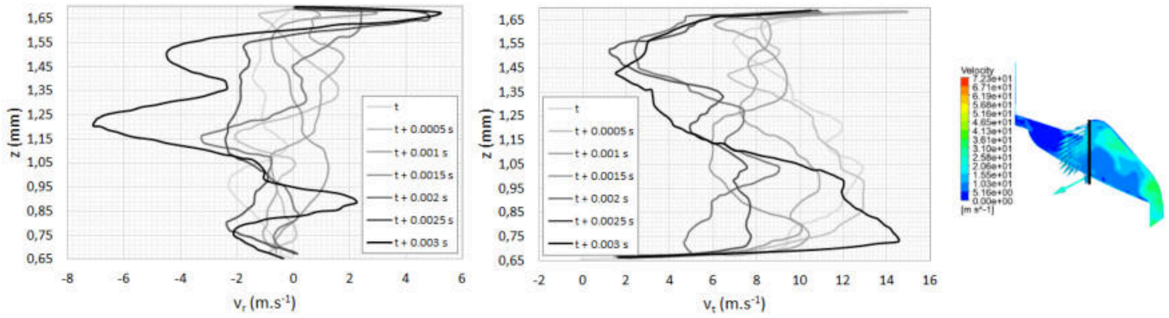

Figure 5.17. Evolution of radial and tangential velocity in time during 1 blade passage

Considering only the outer diameter, gap widths, and rotational speed, according to the stability diagram derived for simple disk [20] the flow regime IV with turbulent separated boundary layers should occur in both sidewall gaps. No transitions and vortical structures should be observable. Nevertheless, the result shows, that such an assumption is an oversimplification and can not be applied to the complex geometry of a real pump.

5.2.5 Conclusions

- The flow inside the sidewall gaps of the pump is much more complex in comparison with the flow in plain cylindrical cavities.
- It is given by its more complicated shape as well as by the evolution with rotation of the impeller.
- Swirling structures in sidewall gaps were captured.
- Embedded LES approach is suitable for simulation of a complex flow in sidewall gaps of the real pump.

CHAPTER 6

Experimental apparatus

6.1 Requirements

In order to study flow regimes in the back-sidewall gap, an experimental apparatus will be built. It should enable:

- To study experimentally the flow in the back-sidewall gap of a real hydraulic machine with appropriate, not over-simplified, geometry of the gap
- To use a real impeller
- Visualisation of the flow in the back-sidewall gap using an optical method, such as particle image velocimetry (PIV) or laser doppler anemometry (LDA)
- Achieving various flow regimes and possible transitions in the gap
- Measurement of disk friction and axial thrust
- Comparison with CFD results
- Modifications of the impeller, e.g. back vanes, in order to study the influence on axial thrust (for future studies)

6.2 Design of experimental apparatus

The experimental apparatus is of the author's original design and was devised from scratch to best meet the requirements for the dissertation research. Some ideas from previously published experimental studies on rotating disks inside simple cavities were considered as well as rigs used for testing in turbomachinery. The final concept consolidates the theoretical knowledge and experience of our laboratory with various hydraulic measurements. The main features are described in the following paragraphs. 3D CAD models of the apparatus assembly were created using Autodesk Inventor and technical drawings for manufacturing (see Attachment) were prepared. Most of the components were machined by OMOS, s.r.o. company, the whole rig was afterward set up and equipped with sensors in our laboratory.

6.2.1 Impeller

The experimental apparatus was designed in a way, that it can use the impeller, which was available in our laboratory from previous research. It was originally taken from low specific speed pump Beta 14, for more details see [140]. The design parameters of the original pump are summarized in Table 6.1. Using an impeller from a low specific speed pump enables us to emphasize the effect of disk friction, which plays a very important role in this type of pump. Moreover, the flat hub allows modifications, such as experiments with back vanes and research of the features for mitigation of axial thrust. Visualization of the impeller from 3D digitization shows Figure 6.1. The impeller was modified by covering the hub with a 1.5 mm thin plate in order to achieve a design, which is more common and which allows to equip back vanes for axial thrust reduction.

z - number of blades	5
D_2 - impeller diameter	320 mm
β - average value of outlet blade angle	32 °
Q - flow rate	6.94 $\mathrm{l.s^{-1}}$
Y - specific energy	314 $\mathrm{J.kg^{-1}}$
ω - rotational speed	24.167 $\mathrm{s^{-1}}$
n_s - specific speed	33

Table 6.1. Design parameters of original pump

Figure 6.1. Scanned geometry of the used impeller

6.2.2 Back-sidewall gap

The main purpose of the apparatus is an experimental investigation of the flow in the back-sidewall gap, behind the impeller. In order to achieve various flow regimes, the apparatus should enable the regulation of rotational speed and the height of the back-sidewall gap. The design assumes the existence of different regimes and transitions in a similar range of Re and G to previously obtained map [20]. A possible shift towards lower Re is presumed, so relatively wide range was chosen to cover it, as shows Figure 6.2. Since the impeller diameter $D = 320$ mm is given by the existing component, the maximum gap width $h = 19.2$ mm and rotational speed $\Omega = 320$ rpm for experimental visualisation was determined, as summarizes Figure 6.2.

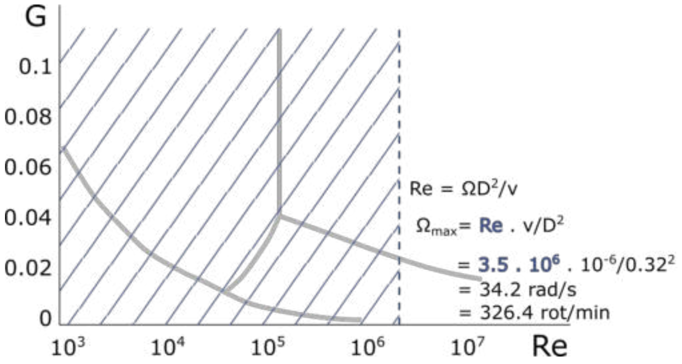

Figure 6.2. Determination of design parameters for the apparatus

The principle of the change of the back-sidewall gap width h illustrates Figure 6.3 left. The desired position of the back cover, which defines the gap, is achieved by inserting a spacing ring of particular width g.

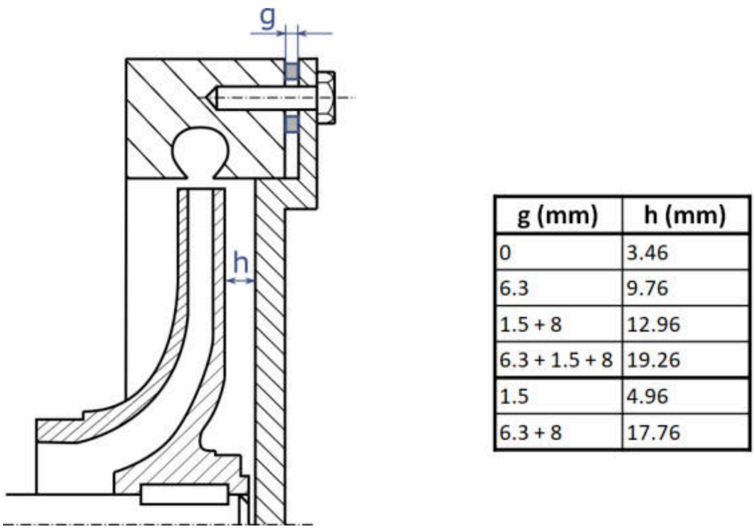

g (mm)	h (mm)
0	3.46
6.3	9.76
1.5 + 8	12.96
6.3 + 1.5 + 8	19.26
1.5	4.96
6.3 + 8	17.76

Figure 6.3. Principle of the change of the gap width h by inserting spacing ring (left), different spacer widths and achieved back-sidewall clearances (right)

To set wider h, various spacers can be combined together. With a reasonable choice of spacers dimensions, there is no need to manufacture a special spacing ring for each measured gap width h, but reach it by placing 2 spacers on top of each other. The first spacer was machined, which allowed any option of the width g. A clever choice of the dimension enables to use a cheaper manufacturing method for the rest of the spacers, which were cut by water jet from sheet metal semi-finished products. The final choice of the spacer widths g with relevant achieved back-sidewall gap dimensions h is summarized in Figure 6.3 right.

The apparatus itself without any spacer contains a clearance $h_1 = 3.46$ mm. By inserting the machined spacer of width $g = 6.3$ mm, back-sidewall gap $h_2 = 9.76$ mm is achieved. The border value, which corresponds to $h_4 = 19.26$ mm achieved by combination of machined ($g = 6.3$ mm) and 2 cut ($g = 8$ mm + 1.5 mm) spacers. Another combination that can be useful for purposes of the study is $h_3 = 12.96$ mm created by the 2 cut spacers. Those 4 gap widths will be taken into account in the experimental and numerical part of the study to cover more or less evenly the selected range. Such a choice covers all of the possible four regimes in the original diagram. There are theoretically another 2 meaningful combinations charted in the last two rows of the table for further research. Besides that, by adding another spacer with adequate width, any clearance can be easily achieved if required.

The use of the existing impeller poses some of the design challenges. One of them is outlined in Figure 6.4. In order to achieve all desired flow regimes according to Figure 6.2, it is necessary to be able to set very narrow height h, which leads to a less straightforward design than that suggested in Figure 6.3. The flat design of the back part (highlighted in yellow) would be better considering the visualization point of view as well as thanks to the less complicated manufacturing. However, to achieve the desired narrow h and fit the rest of the assembly at the same time, the use of the variant with cut (Figure 6.4 right) is inevitable.

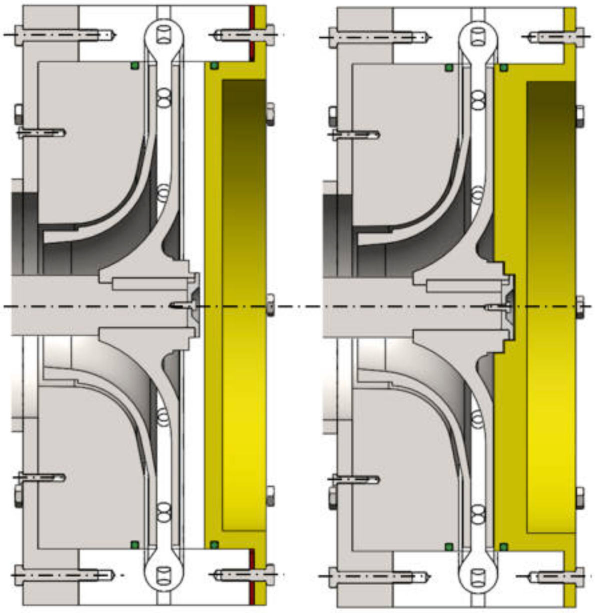

Figure 6.4. The design of the back part

Another challenge posses the manufacturing point of view. The transparent parts are made of plexiglass, which puts special requirements on the equipment and skill of the manufacturer. Only a few companies where the machining was demanded were able to work with such a material. Moreover, the geometry of the volute part is quite complex, it is not possible to machine it from a single part, so experience with gluing was necessary.

Finally, to meet the requirements for LDA/PIV, the surface of the transparent parts has to be polished.

6.2.3 Front-sidewall gap

The main purpose of this research is to extend the knowledge in the field of flow in rotating cavities towards turbomachinery application. Since the current state of the art is based on the measurements performed on the apparatus consisting of a plain disk rotating in a simple cylindrical cavity, either closed or with included throughflow, such as is described e.g. in [20], or [22] it would be beneficial to be able to verify the functionality of newly built apparatus on the same type of the flow and gradually add to the complexity of the geometry. The original idea was to create a modular system of interchangeable parts, which allows combinations of experiments with plain disk as well as with real impeller and also cylindrical casing or volute-like shape. Moreover, both variants with and without throughflow could be considered. It would be achieved by a change of 3 parts as is outlined in Figure 6.5. However, due to limited financial resources, only the combination of the impeller with volute casing was realized.

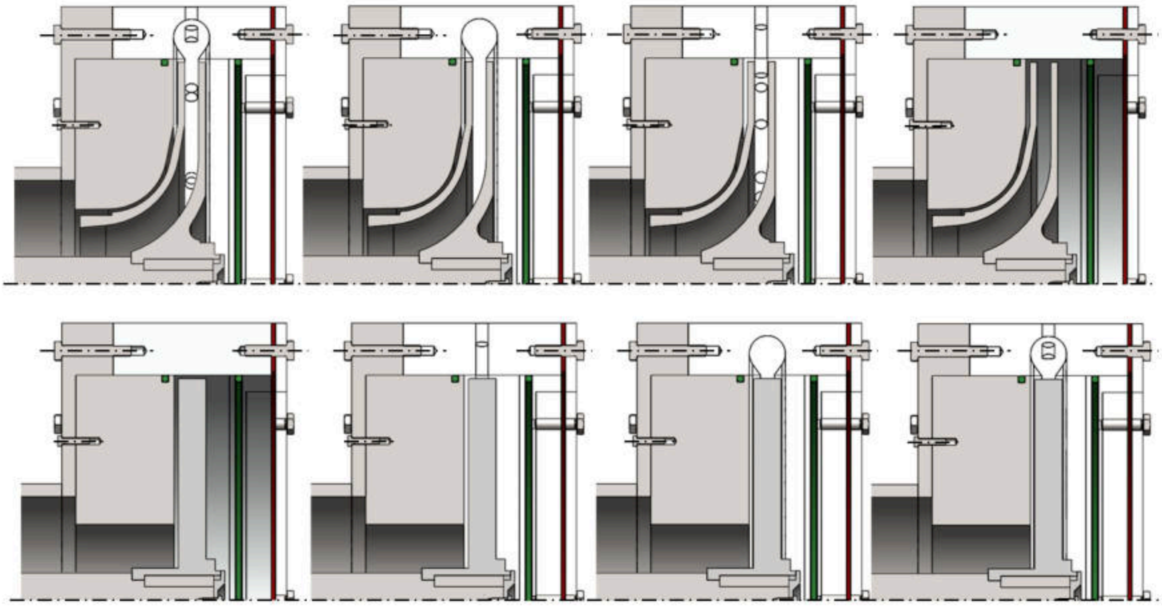

Figure 6.5. Various combinations of experiments with simple disk or impeller

6.2.4 Flow visualisation

In order to obtain an insight into the flow field in the back-sidewall gap, optical access to the fluid domain of the back-sidewall gap is required, therefore the boundary structures must be constructed from a transparent material (typically glass or Perspex/Plexiglass). 2D PIV for visualization of the single planar section is intended to be employed, which raises a need of a possibility to place the camera outside of the testing rig, perpendicularly to the intended plane of the laser light sheet as is shown in Figure 6.6 left. The access of laser beam for LDA is designed to be from the front of the cylindrical transparent back part, as shows Figure 6.6 right. In addition to the exact measurement of the velocity field, the transparent part can be used to visualize the flow by various experimental methods, e.g. using colored particles. An example of such an experiment with MICA powder is shown in Figure 6.7.

Figure 6.6. Layout of the apparatus for PIV (left) and LDA (right)

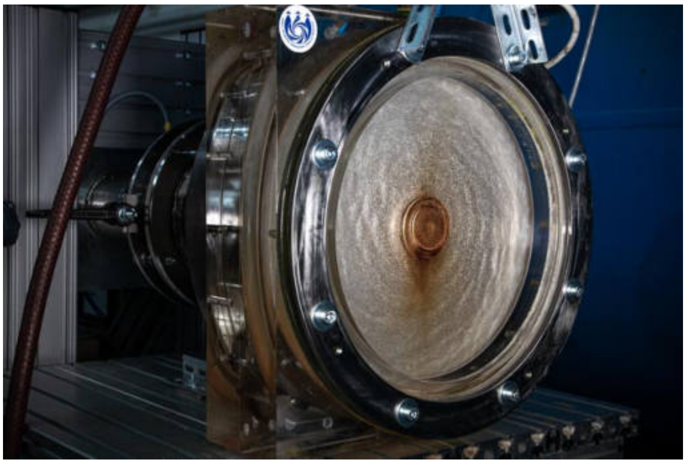

Figure 6.7. Experimental visualisation of the flow by shiny particles

6.2.5 LDA

Laser Doppler Anemometry (LDA) was used for the experimental measurement of radial and tangential components of velocity across the back-sidewall gap. LDA equipment was borrowed from the Institute of Water Structures, Faculty of Civil Engineering. FlowExplorer DPSS 300 2D kit for measurement of two velocity vector components was used.

It consists of two solid-state lasers with power up to 300 mW, emitting at wavelengths 532 nm and 561 nm, and of a front converging lens with a focal length of 109 mm. The obtained signal was processed by a two-channel BSA F600 2D processor and BSA Flow Software v.6.60. (Dantec). The overall view of the apparatus shows Figure 6.8.

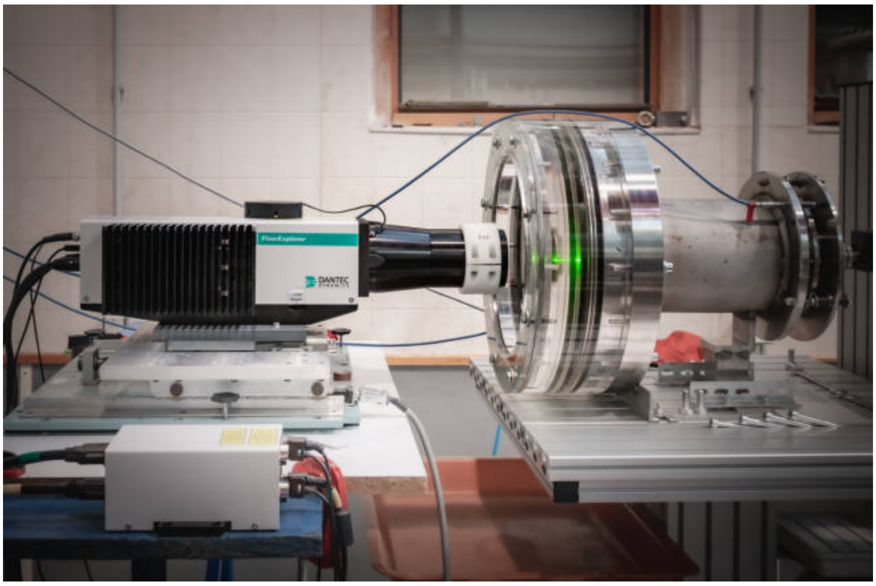

Figure 6.8. LDA setup

The backplate of the impeller was painted in black color to minimize the laser beam reflection and enable the measurement in close proximity of the wall in order to capture the velocity gradient in the boundary layer. It was possible to achieve 14 points across the clearance width starting from the plexiglass cover, aiming perpendicularly to the impeller surface. The radial and tangential velocity components were measured simultaneously. Each measured sequence contains between 5000 and 20 000 samples gathered in 30-second intervals.

6.2.6 Measurement of axial thrust

One of the intended features of the experimental apparatus is a possibility to determine the axial thrust. Its principle is outlined in Figure 6.10. The testing rig consists of parts that are stationary (mainly the outer cover, indicated in grey) and the parts with allowed axial displacement under the loading (the impeller, the shaft, and tied-up components, indicated in red). The movement is axially guided using ball bushing allowing the translation and rotation provided with minimal friction. It has to be pointed out, that the friction will inevitably take place in such type of connection, however, compared to other methods, such as sliding bearings, it is significantly lower. The used ball bushing for securing the axial displacement with schematics of its assembly is shown in Figure 6.9.

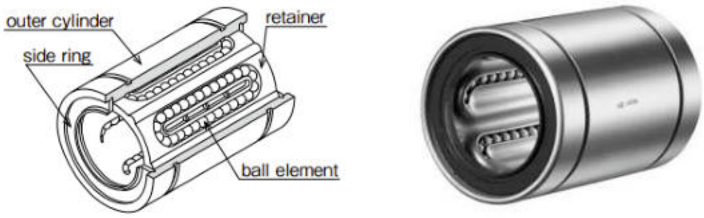

Figure 6.9. Ball bushing [141]

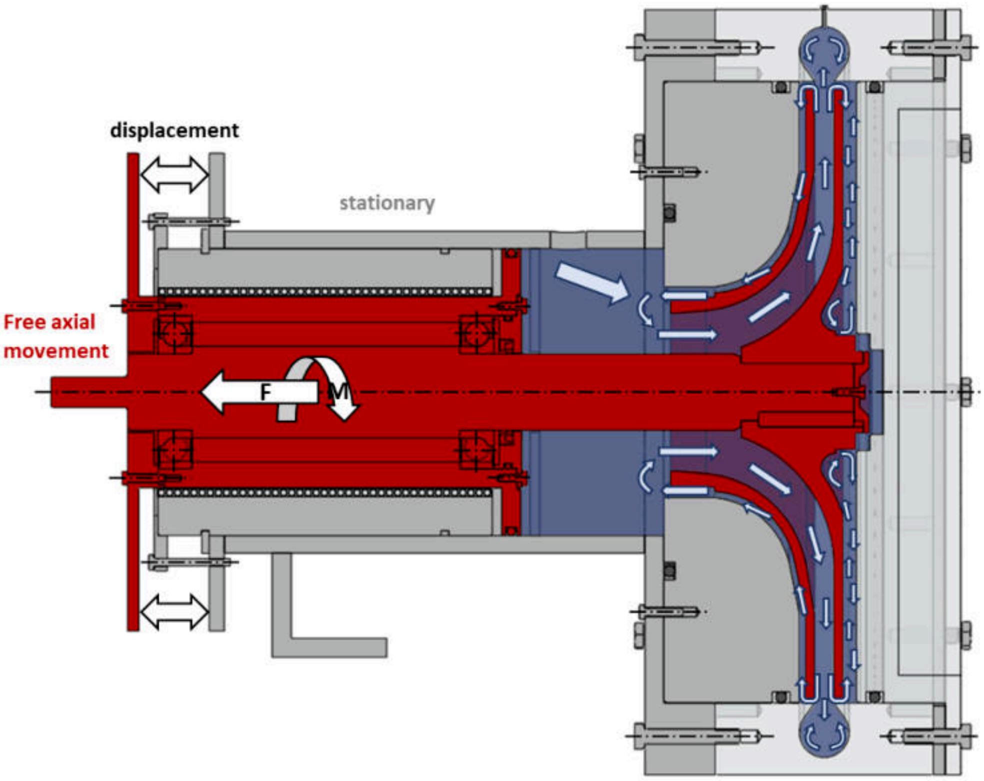

Figure 6.10. Principle of axial thrust measurement

As the fluid flows and creates pressure acting on the impeller, the axially free part of the assembly moves guided by the ball bushing. As a consequence, the distance between marked flanges can be measured. Our laboratory is equipped with sensors of vibrations SCHENCK IN - 085 for the purposes of very precise displacements measurement based on the eddy-current principle. The output voltage of the sensor is proportional to the distance between the probe tip and the measuring surface, within the displacement measuring range of 1.5 mm.

Regarding that, it was decided to adapt the flanges in a way that those sensors can be utilized. The sensors are designed for the measurement of vibrations which are in orders of micrometers, whereas the displacement caused by axial thrust is expected to be orders of magnitude larger. Therefore, the assembly needed to be equipped with added stiffness, which ensures smaller amplitudes of the axial movement. This was provided by 3 sets of pre-loaded springs placed around the flange on threaded rods, as documents Figure 6.11 left. The constant stiffness of the springs in desired measuring range ensures linear response of the displacement on the loading. The springs were chosen so that their stiffness is several times higher than the stiffness of the torque transmission coupling and thus forms the main element determining the range of axial displacement. Since this parameter was in the design phase to some extent an estimate, four sets of springs with even connection dimensions and different stiffness were bought from Vanel company, summarized in Table 6.2. By changing them and observing the response of the whole system, the best trade-off between the total stiffness and the range of the displacements under loading corresponding to 43.6009 N/mm was chosen.

designation	stifness (N/mm)
C.110.160.0228.I	12.553
C.120.200.0230.I	24.5614
C.122.210.0190.A	43.6009
C.123.230.0220.A	54.02299

Table 6.2. Springs and their stiffness

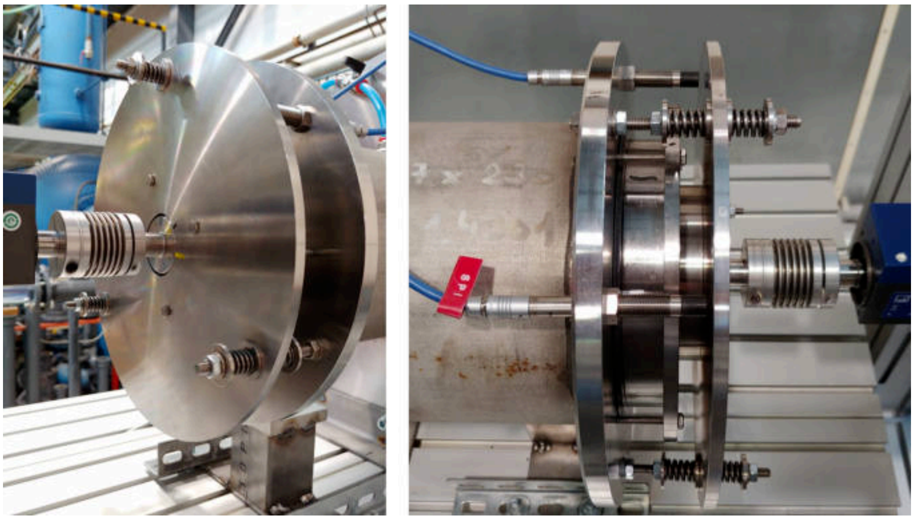

Figure 6.11. Sets of pre-loaded springs to ensure required range of displacement (left), sensors for displacement measurement (right)

Calibration of sensors

In order to obtain the response of the electric signal to the loading, a calibration had to be performed. Its principle is outlined in Figure 6.12 left. The movable part of the apparatus was loaded by calibrated weights, while it was connected to the dynamometer by bellows coupling to ensure that its stiffness is also accounted for. The loading was carried out using a pulley to provide axial direction. The weight corresponding to desired measuring axial thrust range led to the loading up to 7 kg. The data of the voltage obtained by increasing the weight are charted in Table 6.3.

$\boldsymbol{m}$ (kg)	$\boldsymbol{F}$ (N)	$\boldsymbol{U_1}$ (V)	$\boldsymbol{U_2}$ (V)	$\boldsymbol{dU_1}$ (mV)	$\boldsymbol{dU_2}$ (mV)
0	0	-4.4107	-4.5523	0	0
1	9.81	-4.4349	-4.5757	24.24	23.39
2	19.62	-4.6838	-4.8149	273.06	262.61
3	29.43	-4.7991	-4.9264	388.43	374.06
4	39.24	-4.8337	-4.9598	422.95	407.43
5	49.05	-4.9334	-5.0563	522.74	504.01
7	68.67	-5.1319	-5.2467	721.21	694.39

Table 6.3. Data from calibration of the sensors

The first column m gives the weight of the calibrated weight hung on the pulley, the second is the corresponding force, the third and the fourth U_1, U_2 list the output voltage from the two sensors. In the columns designated dU_1, dU_2 the change in voltage compared to the unloaded state is calculated. A linear interpolation of obtained data was done as shows Figure 6.12 right and the equation describing the dependency of the weight and the corresponding change of the output voltage was derived.

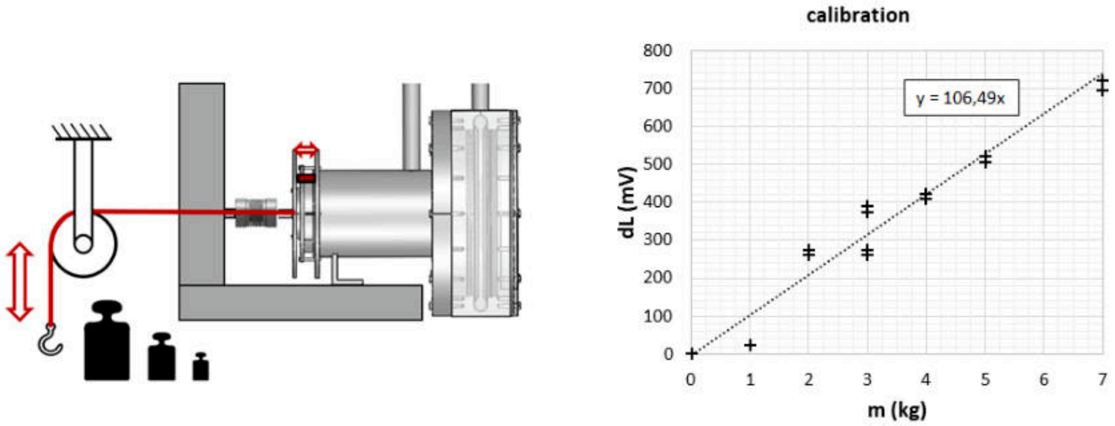

Figure 6.12. Principle of the calibration (left), obtained calibration constant (right)

The first calibration was done before the actual experiments without water inside the apparatus. However, during the measurements, it turned out, that the resulting force is two orders of magnitude higher than it should be. The causes were investigated and new calibration has been performed when the apparatus was filled with water. The obtained constant differs dramatically. It can be explained by the difference between the value of the coefficient of friction in dry conditions and in the presence of water which acts as a lubricant. The displacements are higher than in the dry state leading to the differences in the derived calibration constants. It shows the importance of performing calibration under conditions as similar to measurements as possible.

6.2.7 Measurement of disk friction

The experimental apparatus is connected to dynamometer Amtek AMDYN 20, which allows measuring and control of rotational speed. It consists of a driving machine whose output shaft is connected to a strain gauge shaft equipped with coupling for the measurement of torque. The output shaft with a free cylindrical end serves for the connection of a measured machine. Its 10 kW asynchronous servomotor AMK DW 10-20-4-IOW-5000-B5 is driven by a frequency converter allowing to adjust the speed of rotation (0–6000) rpm. The measuring shaft HBM T21W enables measurements in the range of (0–20) Nm with 0.2% accuracy.

The torque is transmitted from the dynamometer output shaft to the driven shaft of the apparatus by flexible bellows coupling STS WK 3-100-48, as can be seen in Figure 6.13. Its purpose is beside the torque transmission to allow axial displacement of the axially free parts of the testing assembly and therefore the measurement of the axial thrust as was described in the previous section. The stiffness in the axial direction is an order of magnitude smaller than the stiffness of the spring and therefore does not significantly influence the measured displacement and so axial thrust.

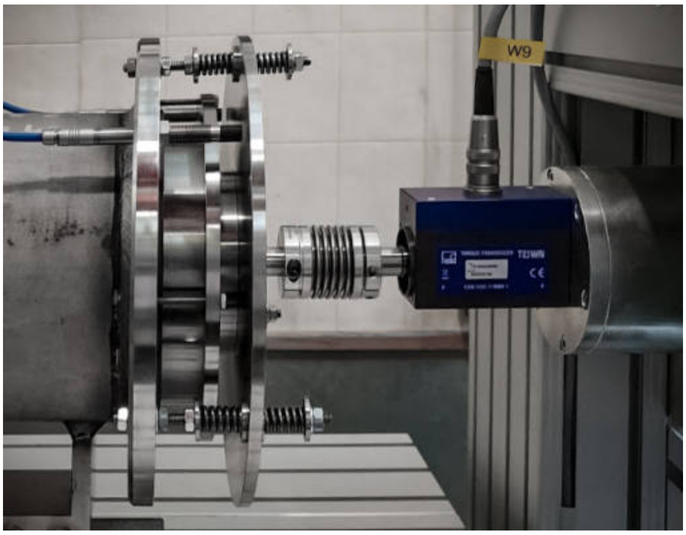

Figure 6.13. Flexible bellows coupling

In this study, the scope of interest is given by Figure 6.2 as described before, which implies the range of rotation speed (0–320) rpm. The measurement of the torque is integrated within the machine. For precise determination of the torque, the frictional torque of the shaft is subtracted. Therefore, the first step is to measure the torque when the impeller is rotating at different rotational speeds in the air. Measured values in the water are subsequently lowered by corresponding torque obtained in the air.

The output signals from the sensors of vibrations for measurement of axial displacement are via the measuring system transmitted to PC, see Table 6.4 for the details. Also, the data logged by the dynamometer are available there, and a simple graphical user interface for visualization and saving particular datasets was created in LabView software as shows Figure 6.14. It stores measured voltage signals for the last 120 s in a buffer, its time record, and mean values are displayed directly on the screen. The user is able to choose the file on a hard drive for saving, reset the buffer and save the currently displayed sequence. The sampling frequency is 2 kHz.

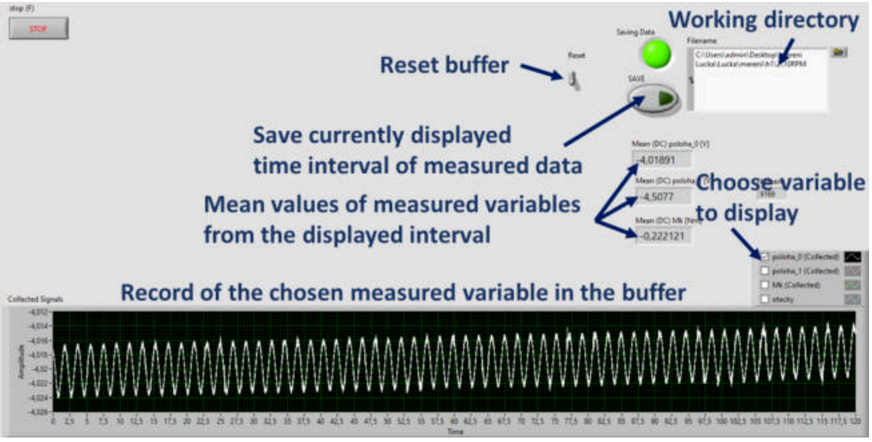

Figure 6.14. LabView graphical user interface

Power supply BK 123	(0–20) V/1 A	
Measuring station NI 9184	4 ethernet ports, 1Gb	
Voltage measuring card NI 9222	16-bit converter, 500 kS/s	Q
Voltage measuring card NI 9239	24-bit converter, 50 kS/s	M_k, U_1, U_2
Current measuring card NI 9203	16-bit converter, 200 kS/s	p_1, p_2
Digital module NI 9411		

Table 6.4. Data from calibration of the sensors

6.2.8 Experiments with throughflow

To study the effect of the presence of the throughflow in the back-sidewall gap, the apparatus is slightly modified and connected to the tank, as documents Figure 6.15 left. The inlet to the apparatus was manufactured with pipe thread to enable easy connection of a pipe. In order to save resources, the experiments with the closed cavity were performed first, then a hole was drilled into the part of the plexiglass volute. The cross-sectional area of the inlet is the same as the outlet and therefore the same pipe size can be used for the entire test circuit. The tank is not pressurized, there is a free surface and it is opened to the atmosphere. The pipe leading out of the tank is equipped with a valve for the control of the flow rate. It is followed by a magnetic-induction flowmeter IMQI99-SN, DN10/PN40 for its monitoring. There is one absolute pressure probe at the inlet to the apparatus and the second is located at the outlet. The fluid is then led back to the tank. There is also a connection to a water supply, which besides water filling serves also for deaeration of the system. The layout of the test circuit with the locations of the sensors is shown in Figure 6.15 right. The signals from both pressure sensors as well as from the flowmeter are collected by measuring cards and processed using LabVieW software interface.

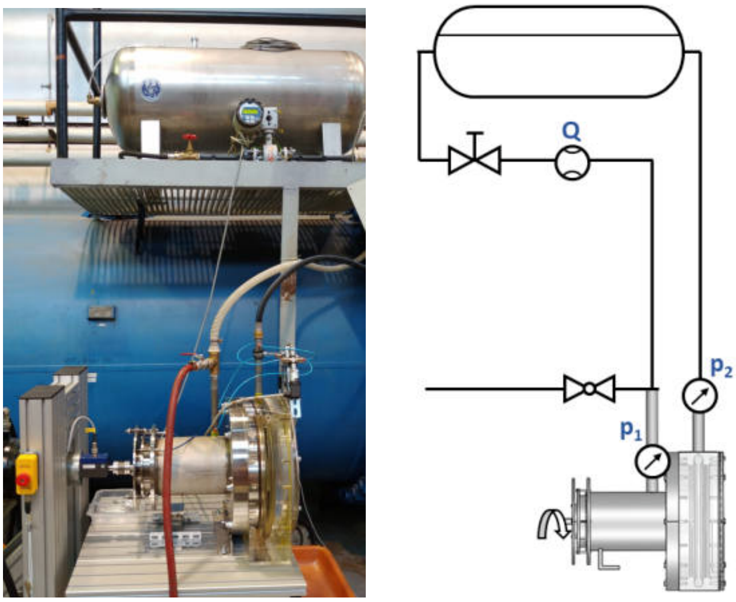

Figure 6.15. Experimental circuit for measurement with throughflow and its scheme

6.3 Measurements Uncertainty

The type A-uncertainty U_A is compared to the B-uncertainty U_B very low and has an only insignificant effect on the overall uncertainty, therefore the A-uncertainty is neglected and is not reported.

Uncertainty U_B will be evaluated using characteristics of particular sensors. The following tables summarize the types and details used for the calculations.

Expanded uncertainty considering 95% confidence level and normal distribution will be obtained by multiplying the standard uncertainty by the appropriate quantile ($k = 1.96$).

Measuring shaft			
Manufacturer:	HBM	Range:	(0–20) Nm
Type:	T21W	Accuracy:	0.2%
$U = 0.08$ Nm			

Table 6.5. Sensors - torque

Flowmeter			
Manufacturer:	ELA-BRNO	Range:	(0–0.8) l/s
Type:	IMQI99-SN	Accuracy:	0.3%
$\boldsymbol{U} = \mathbf{0.005}$ **l/s**			

Table 6.6. Sensors - flow rate

Pressure probes			
Manufacturer:	BD SENZORS	Range:	(0–250) kPa (A)
Type:	DMP 331	Accuracy:	0.5%
$\boldsymbol{U} = \mathbf{2.45}$ **kPa**			

Table 6.7. Sensors - pressure

Displacement sensors			
Manufacturer:	Brüel Kjaer Vibro	Range:	(0–1.5) mm
Type:	IN-085	Accuracy:	5%

Table 6.8. Sensors - displacement

Table 6.8 is mentioned only for informative purposes, the uncertainty of the determination of the axial thrust was done from the calibration by evaluation of deviations, which is outlined in Figure 6.16. The standard uncertainty U_B was calculated using the following equation:

$$U_B = \sqrt{\frac{\sum_{i=1}^{n}(F_i - F_{pi})^2}{n+1}}. \tag{6.1}$$

Considering 95% confidence level, the expanded uncertainty for the measurement of the axial thrust was determined $\boldsymbol{U} = \mathbf{9}$ **N**.

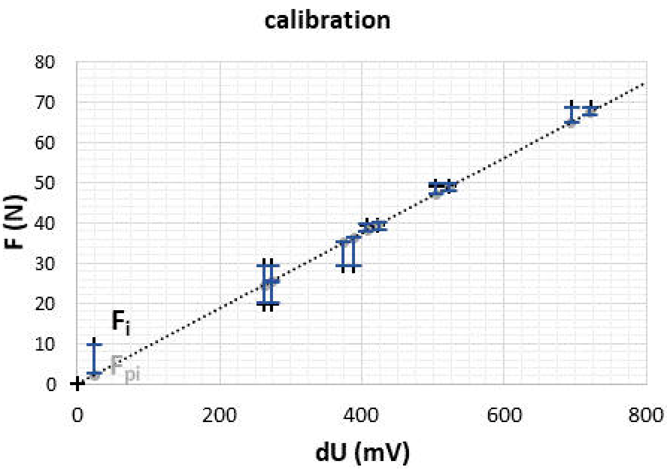

Figure 6.16. Determination of uncertainty from calibration

Rotational speed			
Manufacturer:	HBM	Range:	20 000 min^{-1}
Type:	T21WN	Accuracy:	360 marks/rev
$\boldsymbol{U} = \mathbf{1.7\ min^{-1}}$			

Table 6.9. Sensors - rotational speed

The uncertainty of the velocity obtained by LDA is evaluated directly within the measuring system and the calculated value is a part of the exported result file. It is plotted for each point as its error line.

6.4 Suggestions for future improvements

The experimental apparatus was designed and built from scratch without any previous experience with such measurements. Although it meets the requirements for the research well and enables a quite wide variety of experiments, there is still space for improvement. Based on the experience with the manufacturing, assembling, and conducting the experimental measurement itself, a few points that would be worth reconsidering were found.

The first point to improve is the use of larger clearance on the outer diameter of the plexiglass cover, as illustrates Figure 6.17 left. The recommendation for guidance diameter clearance of metal parts is applicable, however, for the plexiglass with different mechanical properties and surface roughness, a looser fit would work better. The manipulation is quite tough and since the plexiglass is relatively brittle, it requires skill.

Another feature that would simplify handling and speed up the preparation of experiments is to equip the apparatus with another discharge plug or screw. The one shown in Figure 6.17 left was designed for the deaeration of the system and draining the water requires opening the back plexiglass cover, which is not very convenient. Supplying the system with another similar discharge screw in the lower part of the spiral casing would improve operator comfort.

An element for reconsideration is a sealing O-ring on the interface between the stationary and movable part shown in Figure 6.17 middle. Its purpose is to prevent water leakage from the pump section and insulation of the ball bearing. Its disadvantage is the unknown friction generated while the displacement necessary for the axial thrust measurement occurs. Its influence is covered by the calibration, however, it brings a source of uncertainty to the measurement and different solution is worth thinking of.

There is also an idea for widening the range of axial thrust measurement. The springs could be replaced by other elements whose behavior would be more appropriate, meaning with a not necessarily linear (but known) displacement-force response. If the material would become tougher with increasing force, it would increase the range of possibly measured axial thrust to the higher values with maintaining the capability of measurement of low forces at the same time. It may also lead to higher accuracy.

Additional features if considering a redesign of the device in the future, would include a better solution of the connection to the measuring circuit for experiments with throughflow (upgrade of what shows Figure 6.17 right) and placing extra pressure probes to the sidewall gaps to get even better insight into the flow field.

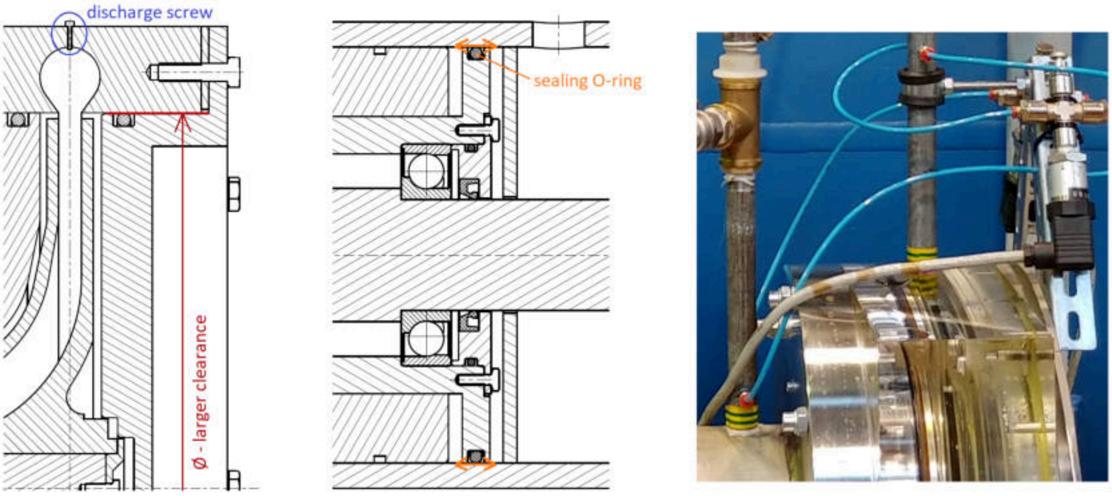

Figure 6.17. Points measured by LDA

6.5 Design of experiment

For the purposes of this thesis, the scope of the research needs to be narrowed, and limited but meaningful number of geometrical configurations to study has to be chosen.

In order to bring the current knowledge in the area of the flow inside rotating cavities closer to real applications such as turbomachinery, the configurations of the experiment including rotating disk and simplified cylindrical casing as explained in Figure 6.5 will be omitted. Only the combination of the real impeller rotating in simplified symmetrical volute will be the target of the thesis. In order to save resources, the closed cavity will be manufactured, the whole set of experiments will be performed and afterward, it will be modified in order to use it for the study with the presence of throughflow.

Also the number of the back-sidewall gaps needs to be picked. In order to achieve different flow regimes, four heights of the clearance were chosen according to Table 6.10.

h_1	3.46 mm
h_2	9.76 mm
h_3	12.96 mm
h_4	19.26 mm

Table 6.10. Heights of the back-sidewall gap

6.5.1 LDA

For financial situation, it was not possible to realize PIV, nor more than one set of measurements using laser methods. Considering this, the set of measurements will be used for verification of the CFD model and subsequent parts of the study will be based on the numerical computations.

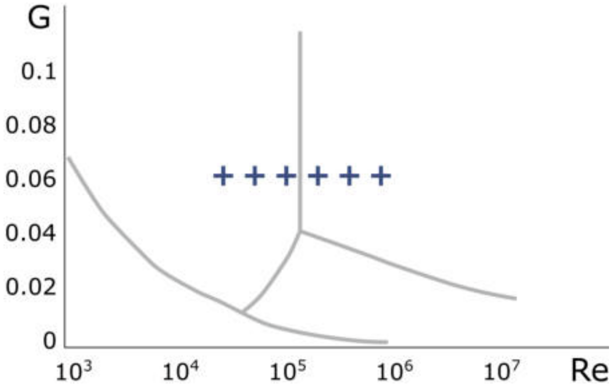

Figure 6.18. Points measured by LDA

For the mentioned measurement, the medium width of the back-sidewall gap clearance $h_2 = 9.76$ mm was chosen. The measurement with the narrower gap would be problematic because of extreme demands on laser and positioning system precision, while the width h_2 provides better practicability and the transition between regimes should be observable as well, see Figure 6.18. Moreover, it corresponds to the commonly used range of G in turbomachinery according to [29, 46]. The measurements were carried out on a closed configuration (without throughflow). The covered range of rotational speeds was $\Omega = (10, 20, 40, 80, 160, 320)$ rpm.

As the next step, it is necessary to choose positions for which LDA measurement of velocity components will be performed. Limits are given by the laser light refraction on the plexiglass edges close to the outer impeller diameter and the shaft. The available LDA equipment restricts the endpoints locations to maximal radius $R = 134$ mm and minimal radius $R = 40$ mm. Three locations evenly distributed over the back-sidewall gap were added to cover the flow field in most of the back-sidewall gap domain, as documents Figure 6.19. Radial and tangential components of velocity were captured at 30-second intervals in 14 locations across the gap.

Since there was a suspicion of possible asymmetry of the flow field, although there was no obvious reason for that, it was decided to do the measurement on both, left and right, sides of the back-sidewall gap in order to confirm or disprove it. As those measurements were relatively time-consuming, the number of measured rotational speeds on the right-hand side was slightly reduced. The complete overview of accomplished LDA measurement is given by Figure 6.19 right.

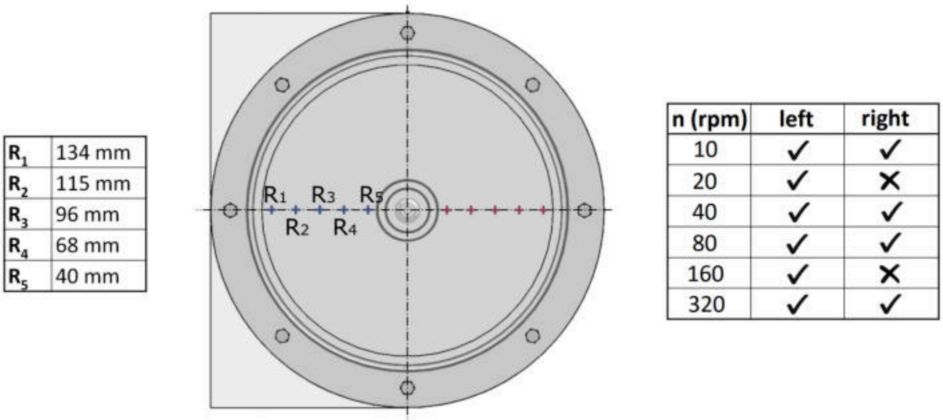

R_1	134 mm
R_2	115 mm
R_3	96 mm
R_4	68 mm
R_5	40 mm

n (rpm)	left	right
10	✓	✓
20	✓	✗
40	✓	✓
80	✓	✓
160	✓	✗
320	✓	✓

Figure 6.19. Radial locations for LDA and overview of measured rotational speeds

6.5.2 Disk friction

Torque was measured for all four gap heights ($h_1 - h_4$) in such a way, that rotational speed was increasing from 0 to 320 rpm by 20 rpm. Afterward, the values obtained for corresponding speed in the air were subtracted.

6.5.3 Axial thrust

Axial thrust was measured at the same time as the torque, therefore for all gap heights, the rotational speed was increasing from 0 to 320 rpm by 20 rpm.

6.5.4 Influence of throughflow

In order to study the influence of the presence of the throughflow in the system and not to over-complicate it by other parameters, the back-sidewall gap of the height h_2 was chosen. From the nature of the machine (centrifugal pump), the flow rate is changing with the rotational speed. Therefore, it is not possible to maintain a constant flow rate for different rotational speeds without using an external pump, as was performed in previous studies of the throughflow with simple cylindrical cavities. The aim of the research is to study the flow in the back-sidewall gaps of real hydraulic machines, therefore it was decided to keep the experiments as close to the real operating conditions as possible. Hence, the flow rate varies over the measured range. The experiments with the throughflow are performed the following way: The maximum considered rotational speed (320 rpm) is set. The desired flow rate is established by opening/closing the control valve. Its value can be viewed on the flowmeter next to the valve. This value is referred to as the flow rate Q for a given set of measurements. To asses the effect of the flow rate on the axial thrust and disk friction, five sets of measurements with different flow rates were performed. Its designation and the exact flow rates for different rotational speeds illustrates Figure 6.20

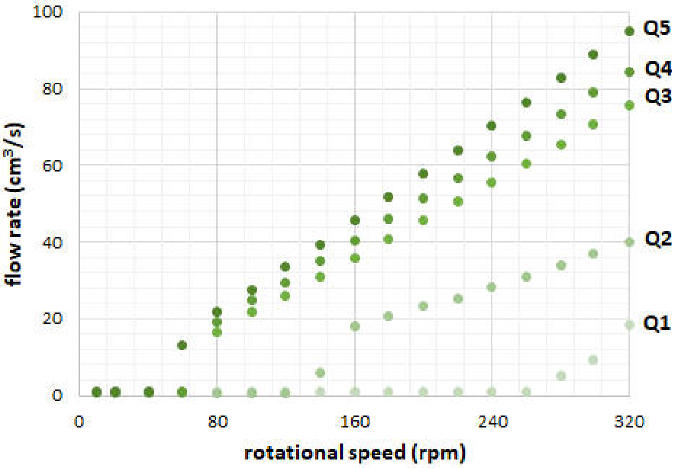

Figure 6.20. Flow rates for the investigation of the effect of the throughflow

6.5.5 Flow visualisation experiments

The experiments inspired by the visualization of the instabilities of the flow in simple disk cavities were considered. Since no advanced equipment such as stroboscopic light or fluorescent particles is available in our laboratory, a combination of shiny particles and ordinary LED light was utilized. In order not to contaminate the apparatus with unwanted particles for other exact measurements, this was carried out at the very end of the research. The solution of silver mica powder and water was prepared (5 g of the powder mixed with 100 ml of water) and inject by a syringe into the region of the impeller. By the rotation of the impeller, it was mixed into the whole volume. Videos and photos capturing the state of the flow in the back-sidewall gap for different rotational speeds were taken.

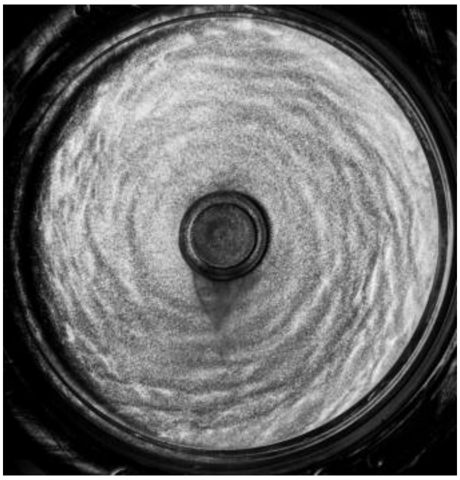

Figure 6.21. Flow visualisation experiments with mica particles

CHAPTER 7

Numerical simulation

The flow in the experimental apparatus was also simulated by CFD in order to analyze more regimes and conditions, which are not easily achievable in reality. It also gives us better insight into the flow field by the ability to plot various variables, which is impossible to measure experimentally.

7.1 Geometry and mesh

The fluid domain was divided into 5 subdomains (entrance part, impeller, volute, back-sidewall gap, front-sidewall gap). They were connected together by non-conformal interfaces (I–V), as is outlined in Figure 7.1 left. The fluid flows from the entrance part (1) through the interface I to the impeller (2). Interface I separates the stationary fluid zone (1) and rotating fluid zone of the impeller (2). The fluid leaves the impeller zone through one of three interfaces (II, III, or IV) and enters either the volute (3) or one of the side-wall gaps (4,5). The portion of the fluid flowing through the front-sidewall gap returns through interface V to the entrance subdomain and recirculates. The back-sidewall gap

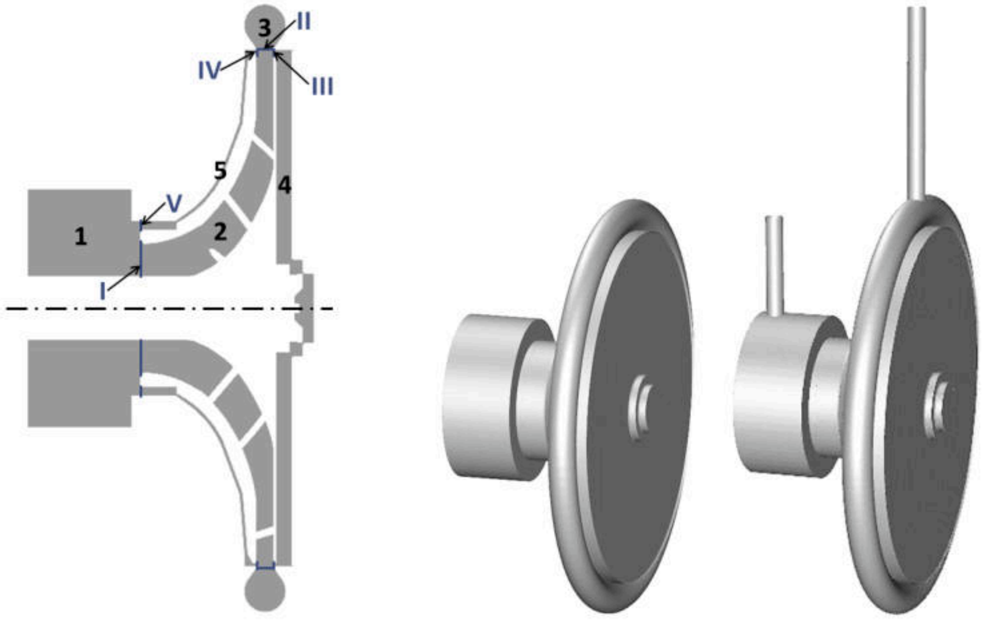

Figure 7.1. Fluid domain overview and its division into 5 parts

subdomain varied with changing of the gap width. The detail of its cross-section for $h_1 - h_3$ shows Figure 7.2. Due to the very long time required for the simulations, only 3 gap widths were considered, the primary h_2, for which LDA measurements exist and then narrower h_1 and wider h_3. For the calculation with throughflow, the subdomains of entrance and volute slightly differ, since they contain parts for boundary conditions inlet and outlet, whereas, for a closed cavity, there is no need to include it which reduces the demands on the mesh size. The different subdomains for a cavity with throughflow are shown in Figure 7.1 right.

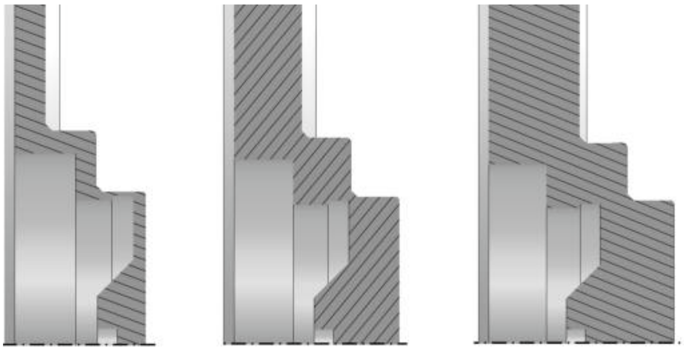

Figure 7.2. Back-sidewall gap domain for gap widths $h_1 - h_3$

The mesh consists of approximately 20 million elements, the precise number differs depending on the configuration (presence of throughflow, back-sidewall gap width), for more details, see Table 7.1 and Table 7.2. The mesh is fully hexahedral. It was created using ANSYS ICEM 19.2 except for the impeller, which was meshed in ANSYS TurboGrid 19.2. Wall refinements with $y^+ \simeq 1$ suitable for low-Reynolds RANS turbulent model were generated, where special attention was paid to the back-sidewall gap subdomain, for which the LES model is intended. The details of mesh in particular domains show Figure 7.3, Figure 7.4 and Figure 7.5.

gap	entrance	impeller	volute	back. gap	front. gap	total
h_1	1 565 148	2 508 975	1 647 756	9 136 611	4 935 644	19 794 134
h_2	1 565 148	2 508 975	1 647 756	10 480 932	4 935 644	21 138 455
h_3	1 565 148	2 508 975	1 647 756	11 888 219	4 935 644	22 545 742

Table 7.1. Number of elements for different CFD simulations - without throughflow

gap	entrance	impeller	volute	back. gap	front. gap	total
h_1	1 645 070	2 508 975	2 553 914	9 136 611	4 935 644	20 780 214
h_2	1 645 070	2 508 975	2 553 914	10 480 932	4 935 644	22 124 535
h_3	1 645 070	2 508 975	2 553 914	11 888 219	4 935 644	23 531 822

Table 7.2. Number of elements for different CFD simulations - with throughflow

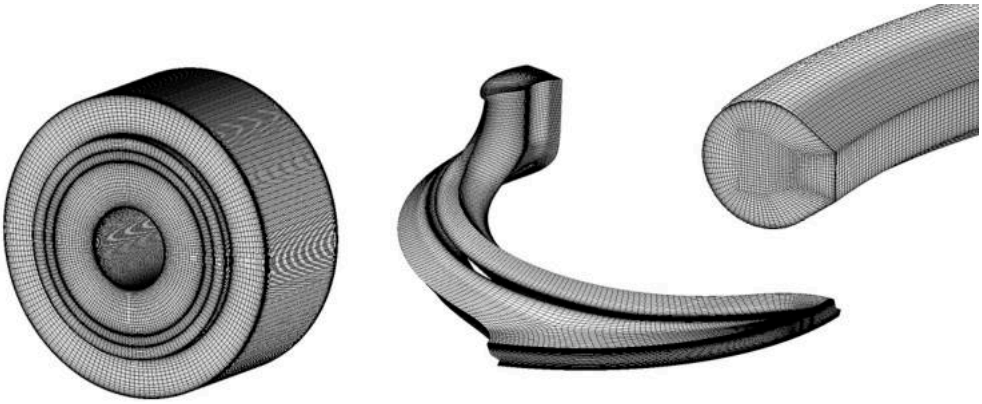

Figure 7.3. Mesh of the entrance, one impeller channel and volute

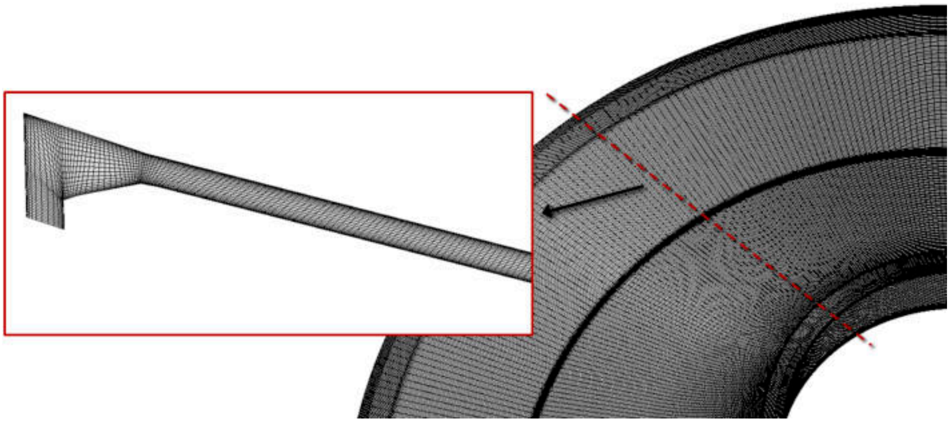

Figure 7.4. Mesh of the front-sidewall gap domain

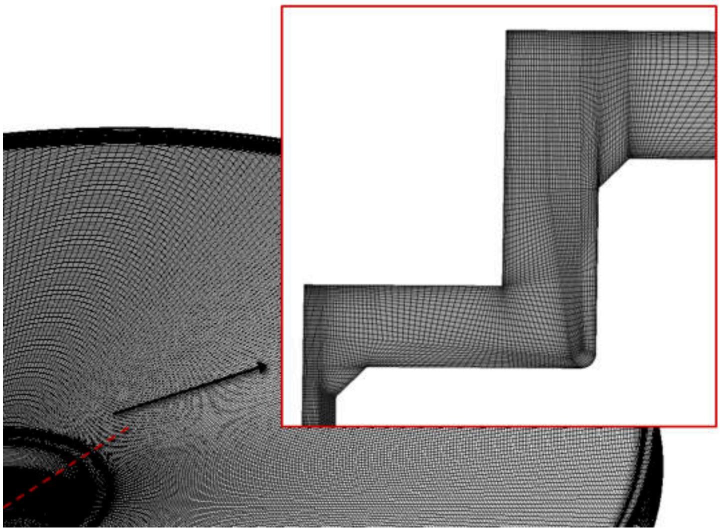

Figure 7.5. Mesh of the back-sidewall gap domain

7.2 Boundary conditions

Boundary conditions are schematically shown in Figure 7.6 left for simulations with enclosed rotating impeller and in Figure 7.6 right for cases with imposed throughflow. No-slip boundary condition is applied on walls. Rotating walls and domains belonging to the impeller are marked by red color, whilst stationary are black. Rotating and stationary zones are coupled by interfaces, whereby the interface between impeller and back-side wall gap treats the transition from RANS to LES turbulence model. According to the FLUENT recommendation and based on previous experience, fluctuating velocity algorithm was set to Vortex Method with a number of generated vortices corresponding to N/4, where N is a number of cells on the interface. For the cases with throughflow, mass flow inlet and pressure outlet is added to the original domain. The lengths of added parts are $5D$ fore the inlet and dimension corresponding to the pressure probe placement for experimental measurement fore the outlet. The values of rotational speed, mass flow rate, and pressure at the outlet for particular cases correspond to experimental measurements. A Water-liquid model from the ANSYS library considering incompressible fluid was used.

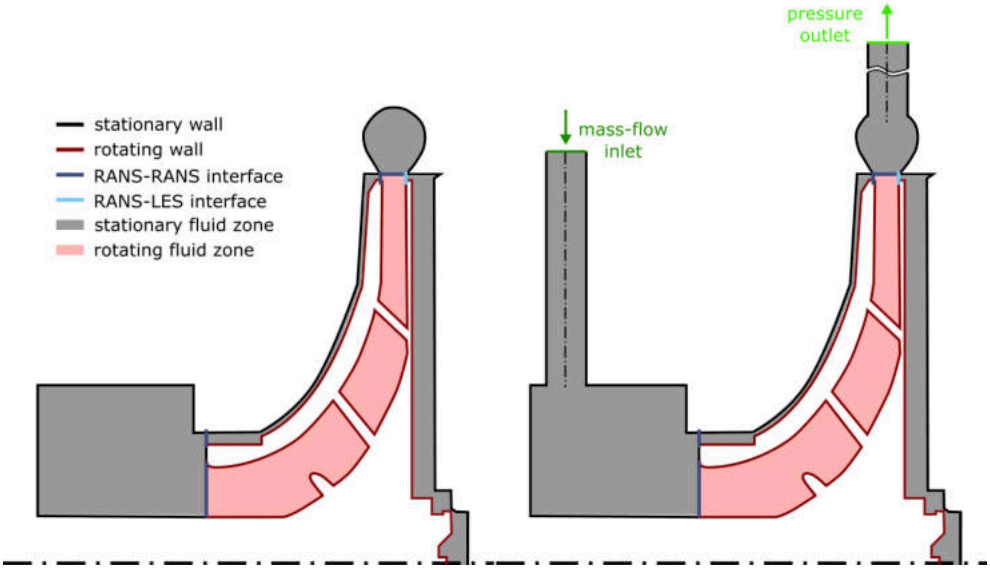

Figure 7.6. Mesh of the back-sidewall gap domain

7.3 Solver settings

The Embedded LES approach described before was applied. The main focus was on the flow in the back-sidewall gap, which was treated with LES, whereas the SST k-ω turbulence model was applied to the rest of the domain. WALE subgrid-scale model with Bounded Central Differencing momentum spatial discretization scheme, which is recommended for embedded LES approach, was used. For pressure-velocity coupling, the SIMPLE scheme was used with the first orders of accuracy for advection terms in all transport equations. After achieving convergence on first orders it was switched to the second orders. The time step settings for RANS modeling followed the common practice for CFD in turbomachinery, where for given rotational speed, 2° rotation corresponds to Δt. After achieving convergence and turning on LES in the back-sidewall gap domain, Δt was lowered in an order to fulfill the CFL condition and obtain convergence for embedded LES. The complete workflow from initialization through achieving convergence to statistic extraction is described in Table 7.3. By testing, it was found out, that the hybrid initialization works better than the standard one and leads to quicker convergence of subsequent steady-state cases. After 1000 iterations in a steady regime the analysis can be switched to transient with a moving reference frame (MRF). It does not take more than 500 timesteps with 5 inner iterations to converge. Afterward, it is possible to switch to second orders of accuracy. Again, the convergence is achieved relatively quickly, less than 250 timesteps were always sufficient. Next, mesh motion was applied with the number of timesteps corresponding to 2 impeller revolutions for each rotational speed. It turned out to be enough to stabilize the simulation before switching the LES zone on. Enabling LES in the backside-wall domain requires lowering the time step. A few revolutions are computed while observing velocity components in a monitor point until a periodic pattern governed by the passage of blades is developed. Finally, the collection of transient statistics for evaluation and comparison with the experiment is set. The whole sequence is automated by the FLUENT journal file.

analysis type	**accuracy**	**Δt**	**duration**
hybrid initialization	-	-	-
steady	1st orders	-	1000 iterations
transient, frame motion	1st orders	Δt	500 timesteps
transient, frame motion	2nd orders	Δt	250 timesteps
transient, mesh motion	2nd orders	Δt	2 impeller revs
embedded LES	2nd orders	$\Delta t/10$	3 impeller revs
embedded LES - collecting results	2nd orders	$\Delta t/10$	1 impeller rev

Table 7.3. CFD procedure

Part IV

Results

CHAPTER 8

Experimental measurements

8.1 LDA

Data collected during LDA measurement were analyzed by visualization of particular velocity components (radial and tangential) across the back-sidewall gap, in time and frequency domains by means of Fourier transform.

8.1.1 Velocity profiles

An illustration of typical radial and tangential velocity profile for particular radius and rotational speed is shown in Figure 8.1. The complete set for all measured points is attached in appendix. The endpoints on the rotor and stator were added, since the LDA apparatus due to its technical limitations was not capable of measurement in the immediate vicinity of walls. Tangential velocity on the stator ($h = 0$ mm) is equal to zero and the rotor ($h = 10$ mm) corresponds to the peripheral speed of the impeller on a given radius. In turbomachinery applications, a simplified formula for estimation of the tangential velocity across the gap is used, as was described in the theoretical section. According to it the velocity in the core of the fluid is half of the rotational speed of

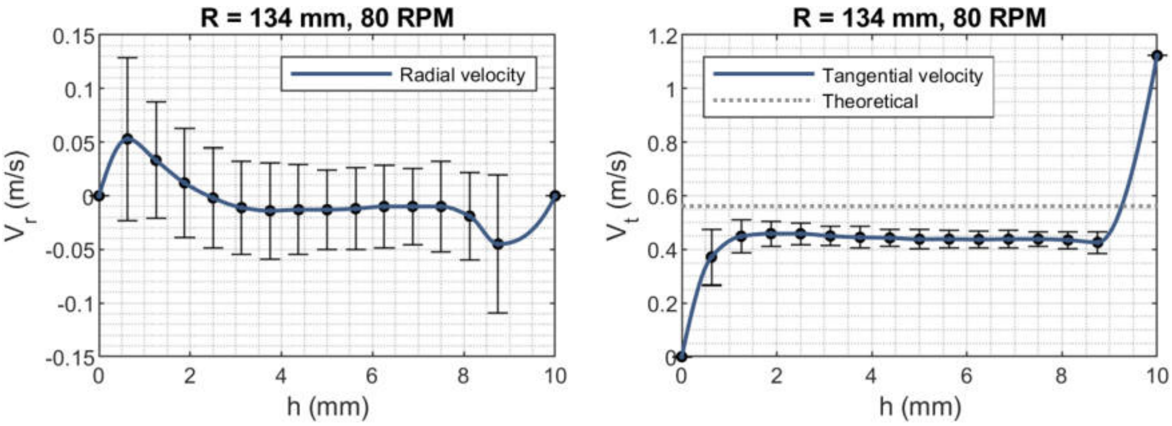

Figure 8.1. Radial and tangential component of velocity vector

the rotor. This is displayed in charts of tangential velocity as dashed line denoted as ”Theoretical”.

Velocity profiles for the left and the right side of the domain fit on each other well, as documents Figure 8.2. Therefore, the suspicion of asymmetry of the flow field was disproven.

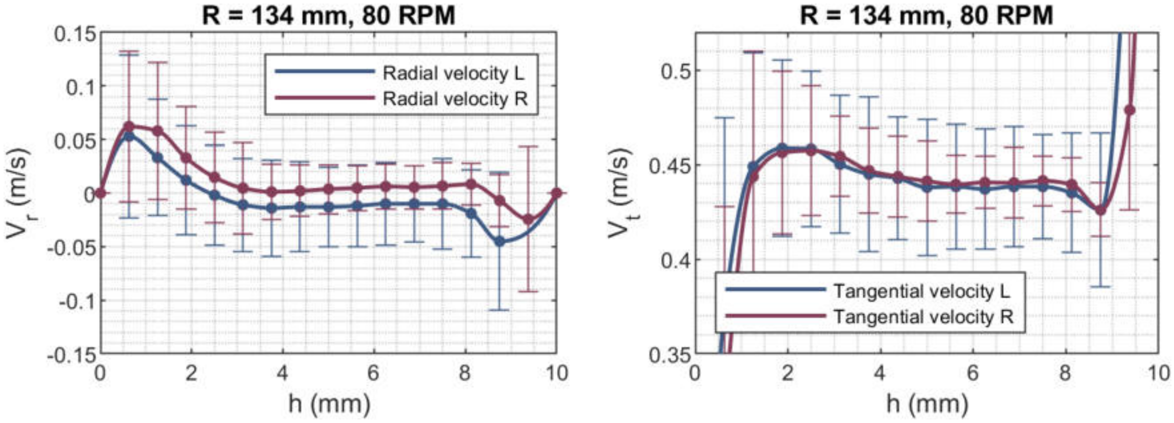

Figure 8.2. Radial and tangential component of velocity vector

The evolution of velocity profiles with an increase of the rotational speed was observed for different radii. Especially the radial velocity profile is a good indication of the flow regime in the gap. Typical shape for regime III with merged boundary layers is shown in Figure 8.3 left for $R = 68$ mm and $\Omega = 10$ rpm. With an increase of the rotational speed in the central region, flow with constant radial velocity evolves. As can be seen in Figure 8.3 right, for mentioned radius, it occurs between 10 and 20 rpm. With further increase in the rotational speed, the core flow occupies larger volume and thus the boundary layers become thinner as is demonstrated Figure 8.4 for 80 rpm (left) and maximum rotational speed 320 rpm (right).

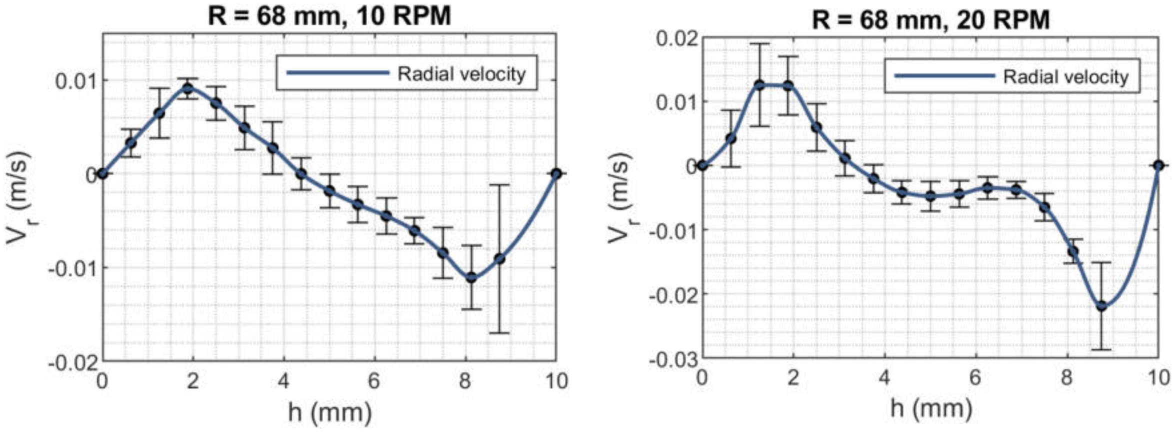

Figure 8.3. Evolution of radial component of velocity vector

By detecting the rotational speed of transition, it was intended to create a similar map of regimes as was published by Daily and Nece [20] for a simplified rotating cavity.

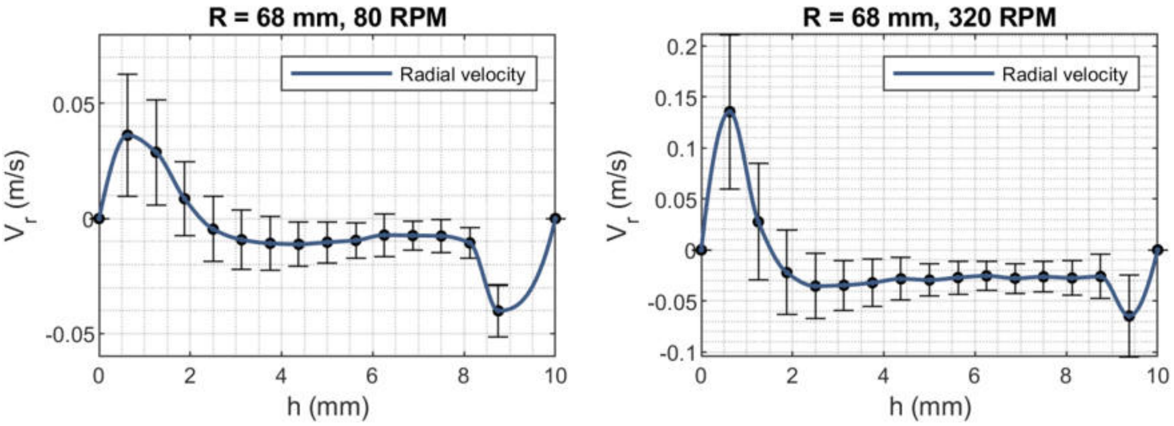

Figure 8.4. Evolution of radial component of velocity vector

However, LDA measurement for various gap heights was not due to financial reasons possible. Therefore, a slightly modified approach was adopted by redefining the way of determining rotational Reynolds number. Originally, it is calculated from the definition introduced in Section 1.1:

$$Re = \frac{\Omega b^2}{\nu}, \tag{8.1}$$

where b is the outer radius of the impeller, Ω is rotational speed, and ν is the kinematic viscosity of the fluid. Authors of previous studies were tracking when the transition from one regime to another occurs in the whole domain and such a state is considered to be the transition point. The modified approach is based on replacing the impeller radius, which is constant, by actual radius, where the velocity profile is taken from. Therefore, the formula for rotational Reynolds number can be rewritten to the form:

$$Re = \frac{\Omega R^2}{\nu}. \tag{8.2}$$

Analogically, the aspect ratio of the cavity G was also calculated using R instead of b:

$$G = \frac{h}{R}. \tag{8.3}$$

Using the described approach, Re and G were calculated for each measured radius, its flow regime was identified and plotted in dimensionless Re - G coordinates, as can be seen in Figure 8.5. For the given combination of gap width, dimensions of the impeller, and rotational speeds, only turbulent regimes appeared. Turbulent flow with merged boundary layers (III) is marked by a yellow color, turbulent flow with separated boundary layers (IV) is labeled by red, and the transition is indicated by the orange dashed line.

In Figure 8.6 the new map of regimes for impeller back-sidewall gap is plotted against the original for simple cavity by Daily and Nece [20]. It is obvious that the assumption of similarity between the maps is not valid. The whole map for the impeller is shifted

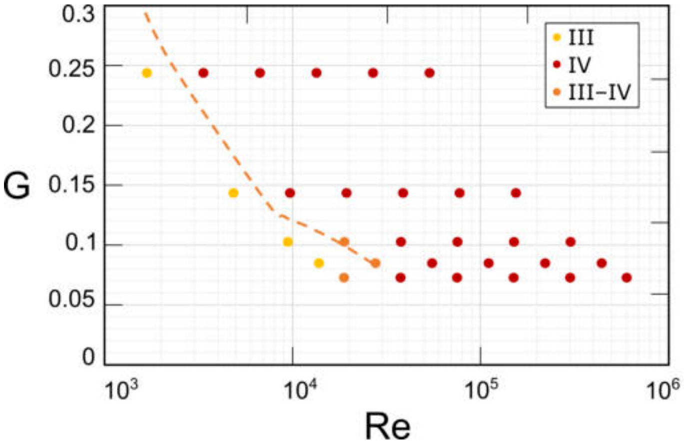

Figure 8.5. Map of regimes in impeller back-sidewall gap

towards higher aspect ratios and lower Reynolds numbers, which could be to some extent expected. Any irregularity or disturbance, such as the presence of the blades or a more complex shape, leads to the earlier emergence of instabilities and transition to turbulent flow. In the region of original laminar regime II, turbulent regime III was detected, moreover, for higher G even turbulent regime IV occurs.

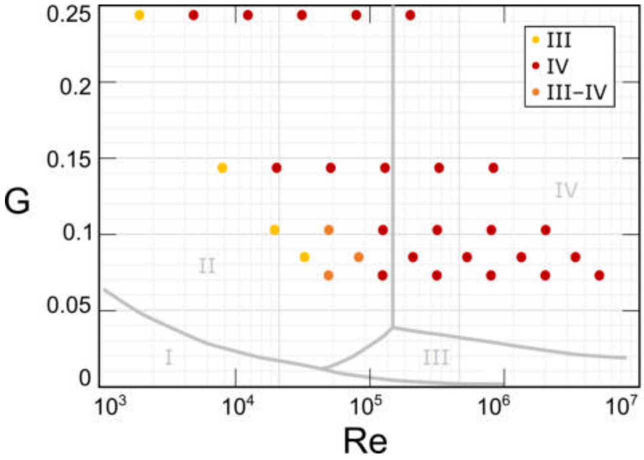

Figure 8.6. Original and new map of regimes

8.1.2 Spectral analysis

The signals from the LDA measurement contain information on how many particles were detected at a particular moment. Such a characteristic is not very meaningful for further analysis in the time domain, however, in the frequency domain, it can possibly reveal some dominant frequencies to help detect phenomena of a periodic nature in the flow.

For the investigation in the frequency domain, the Fourier transform of the time signal has to be performed. To do that using the FFT algorithm implemented in MATLAB, the time series has to have a constant sampling frequency, which is not true for the LDA data. Therefore, the first inevitable step is the resampling of measured signals. It was done using MATLAB script with a function *resample* with linear interpolation setting, which is based on the previous experience with LDA data processing. A demonstration of the process on one sample is shown in Figure 8.7. The left figure shows the original captured signal, the resampled data are shown in the middle and for a better idea of the accuracy of the process, its comparison is shown on the right.

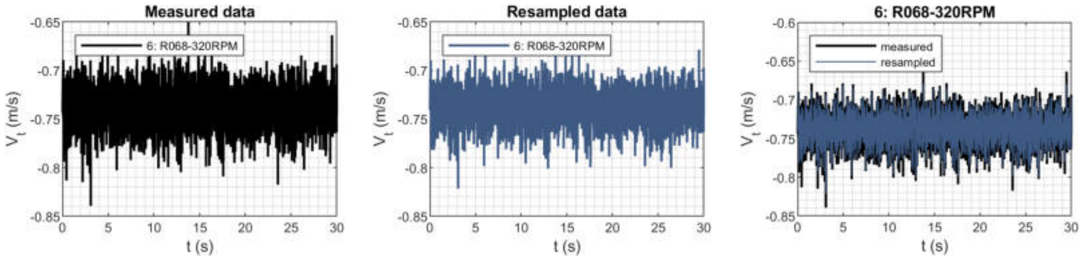

Figure 8.7. Original and resampled LDA signal

Fast Fourier Transform (FFT) algorithm implemented in MATLAB was applied to the resampled datasets in order to obtain the frequency spectra. For each point across the gap on each measured radius (see previous description in Figure 6.19 and Figure 8.9) the frequency spectra was acquired. The LDA data for rotational speeds 320 rpm and 160 rpm were analyzed since for the rest of the lower rotational speeds the LDA signal does not contain enough particle passages to meet the Nyquist criterion and FFT would not yield in meaningful output. The resulting spectra from previous sample shows Figure 8.8 left. Two dominant frequencies can be clearly seen. The first one corresponds to the rotational frequency of the impeller for a given rotational speed and then higher harmonic frequencies (its multiples) are distinguishable. In some locations closer to the impeller, also the frequency equivalent to passages of the blades is distinguishable. For easier orientation, without the need for having knowledge of the impeller frequency, normalization with respect to the frequency of the impeller was done, as is demonstrated in Figure 8.8 right. The peaks corresponding to the whole number multiples of the rotational frequency are obvious.

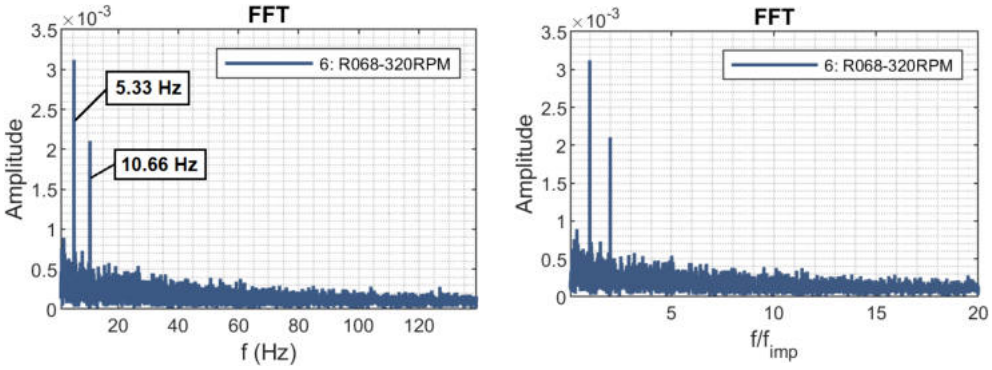

Figure 8.8. Frequency spectra of LDA signal

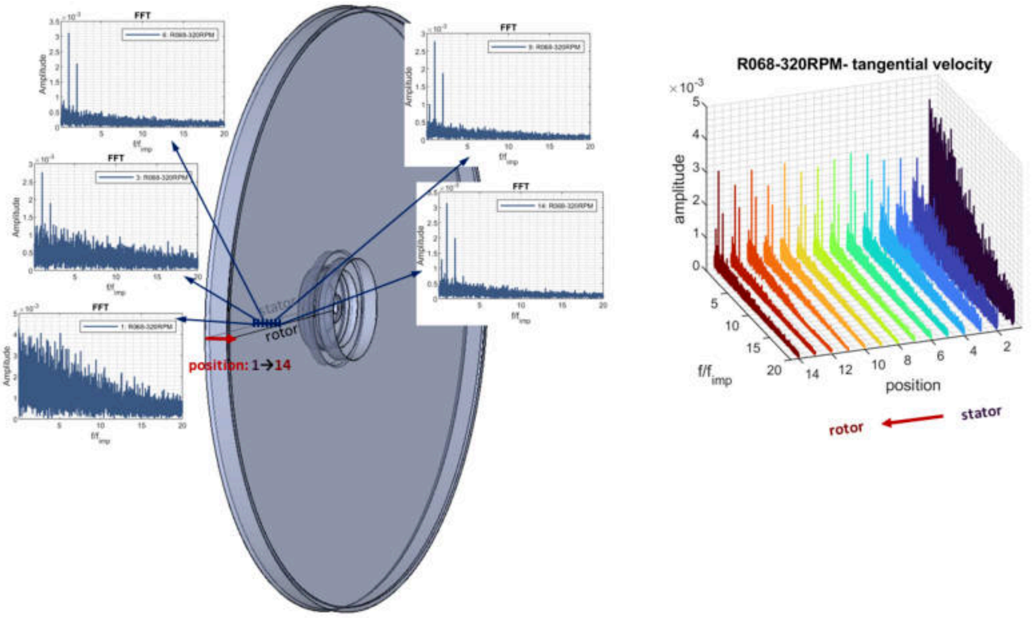

Figure 8.9. Measured axial thrust depending on rotational speed and gap width

To obtain an overview of all spectra for particular operating points, visualizations of signals obtained through the whole back-sidewall gap were plotted as is shown in Figure 8.9. LDA signal was captured for each radius and rotational speed in 14 separate points across the width starting from the position (1) near the stator up to (14) adjacent to the rotor. Both the radial and the tangential components of the velocity were processed. The complete set of 3D spectra is included in the appendix.

Looking at the whole dataset in general, it can be seen that the signal coming from the points located near the stator has more random character, which can be possibly caused by the propagation of turbulent vortical structures from the stator boundary layer, which is based on previously published results always less stable and disturbances occur earlier on it.

For the largest radius $R = 134$ mm and rotational speed 320 rpm, the spectra are almost identical for the left and right sides. Dominant frequencies corresponding to the frequency of the impeller and its double can be clearly distinguished. Also the blade frequency ($f/f_{imp} = 5$) is obvious. In the gap center, its multiplies can be observed as well. This is true for radial as well as for tangential components of velocity. The frequency of blades is not quite apparent for 160 rpm. It can be seen only in a few captured points, more in the tangential component. The frequency of the impeller strongly dominates here.

The radius $R = 115$ mm also does not show any signs of difference between left and right side of the domain as document Figures 8.10 and 8.11. For 320 rpm the blade frequency is the most pronounced in the radial component in the whole width except for the stator region, where it is accompanied also by peaks given by impeller frequency and its double $f/f_{imp} = 1, 2$. In signal from tangential component, blade frequency emerges near stator, while near rotor $f/f_{imp} = 1, 2$ prevail. For rotational speed 160 rpm near-wall regions, both rotor, and stator, are dominated by impeller frequency. In the case of the radial component, blade frequency can also be seen in the middle of the width whilst in the tangential LDA signal, it is not pronounced.

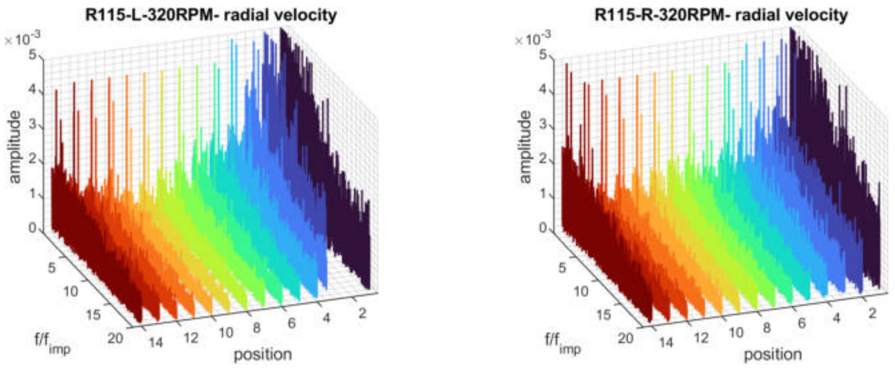

Figure 8.10. Comparison of frequency spectra - left and right side of the domain

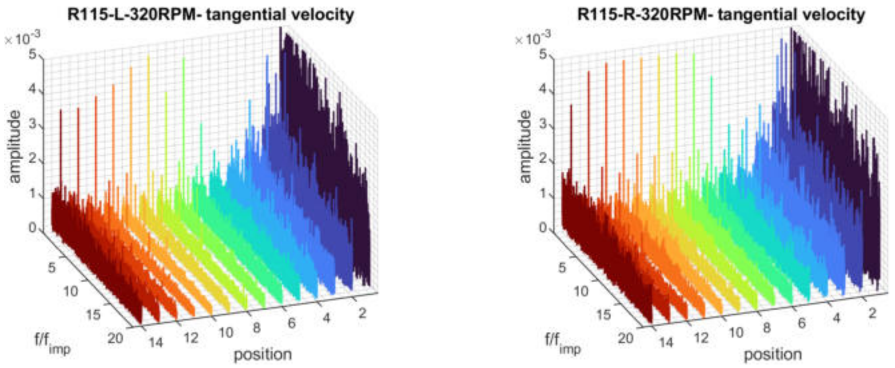

Figure 8.11. Comparison of frequency spectra - left and right side of the domain

No discrepancies between the left and the right side can be found also for $R = 95$ mm. The rotational frequency of the impeller $f/f_{imp} = 1, 2$ is distinctive in the whole domain, which is a characteristic sign in both radial and tangential components. Blade frequency $f/f_{imp} = 5$ is noticeable in radial velocity, however its amplitude is lower. In the tangential signal, the blade frequency is almost insignificant. The same description is applicable also for rotational speed 160 rpm.

The closer the center of the domain, the lesser is the impact of the blade frequency. For $R = 68$ mm it can not be distinguished at all neither in radial nor tangential component. Only rotational frequency and its multiplies can be seen for 320 rpm as well as for 160 rpm. The results are identical for the left and the right side.

A slight discrepancy between the left and the right side is observable for inner radius $R = 40$ mm. It is probably due to the fact that for the right side, fewer data were captured which causes the noise-like character of resulting spectra. The dominant frequencies corresponding to the rotation of the impeller are the same for the left and right sides, nevertheless, the right side comprises more peaks close to each other, as can be seen in Figure 8.12.

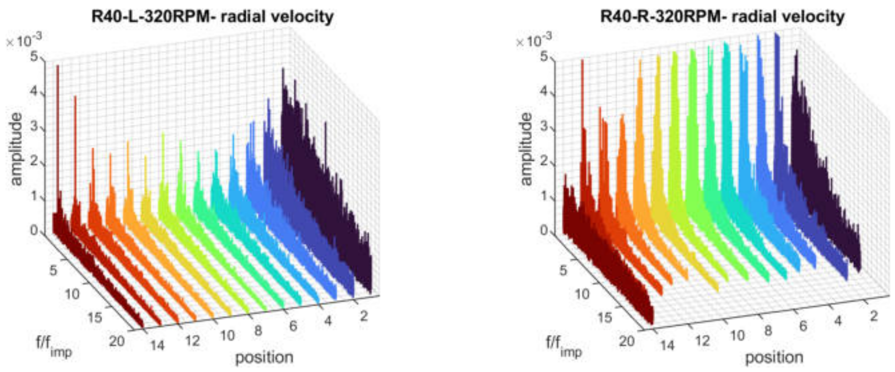

Figure 8.12. Comparison of frequency spectra - left and right side of the domain

8.2 Disk friction

In order to determine torque without influences of friction on the shaft, measurements without water were performed as a first step. Two sets of measurements for various rotational speeds were done and an average value was further used for the subtraction. Obtained data and its average values shows Figure 8.13 left. Raw data (including frictional torque) from subsequent measurements for various back-sidewall gap widths and rotational speeds can be seen in Figure 8.13 right. Unfortunately, data from measurement of h_3 were corrupted and thus are not displayed. Processed data without mechanical friction are then shown in Figure 8.14.

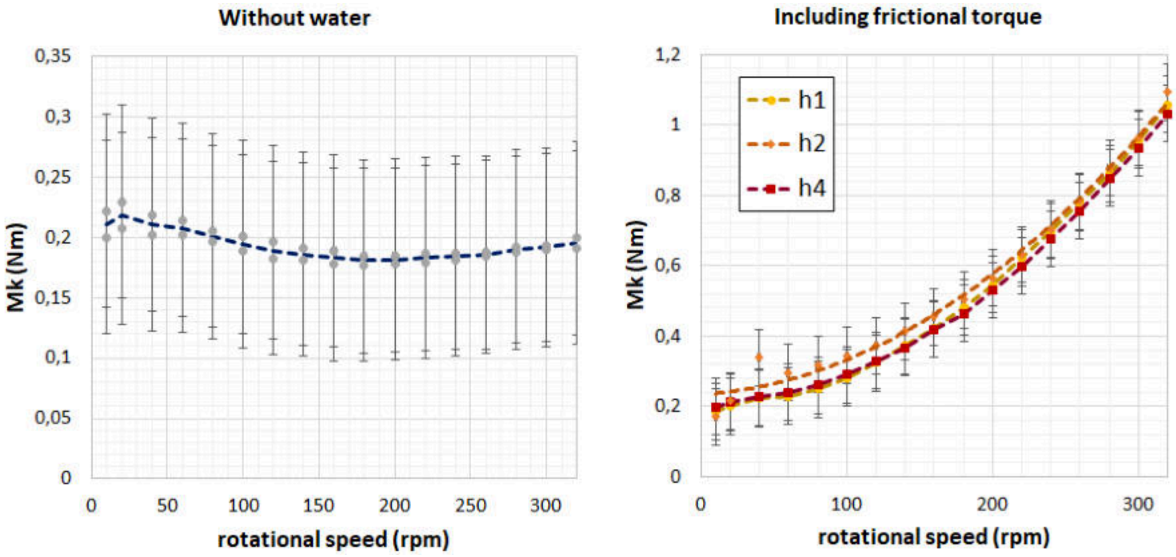

Figure 8.13. Measured torque depending on rotational speed without fluid (left), measured torque data for various gap widths before subtraction of friction

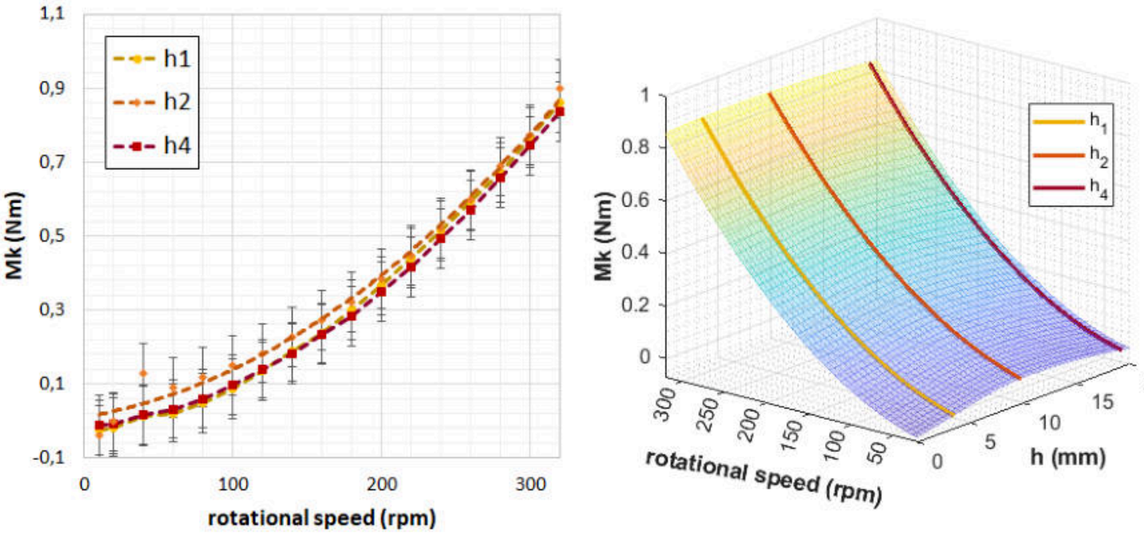

Figure 8.14. Torque depending on rotational speed and gap width

The resulting torque increases with increasing rotational speed. There is no sign of changing regimes from III to IV, such as an abrupt change of the trend, which corresponds to the findings presented in [22, 104]. If the dependence on the gap width is considered, it can be seen, that no significant differences were found between the configurations. The friction first decreases with increasing h and later the trend changes and with further increase of h, the torque rises, however, the difference is insignificant and barely recognizable. The finer resolution would be helpful for a better description, especially considering the missing data for h_3.

8.3 Axial thrust

Axial thrust increases with increasing rotational speed approximately quadratically as shows Figure 8.15 left. Its increase is steeper in comparison with the trend for the torque. There is no noticeable change of regime either. No changes of direction were observed, the values which go under 0 for low rotational speeds are within a range of measurement uncertainty. No physical reason for it was found and neither CFD does not show any negative axial thrust.

The dependence of axial thrust on the back-sidewall gap width is opposite to the torque trend. As illustrates Figure 8.15 right, with increasing h the measured axial thrust tends to increase up to a certain value. Further increase of h results in the decrease of axial thrust on the whole range of rotational speeds. For a more precise description of this phenomenon, measurements with finer resolution (more measured h) would be also here necessary.

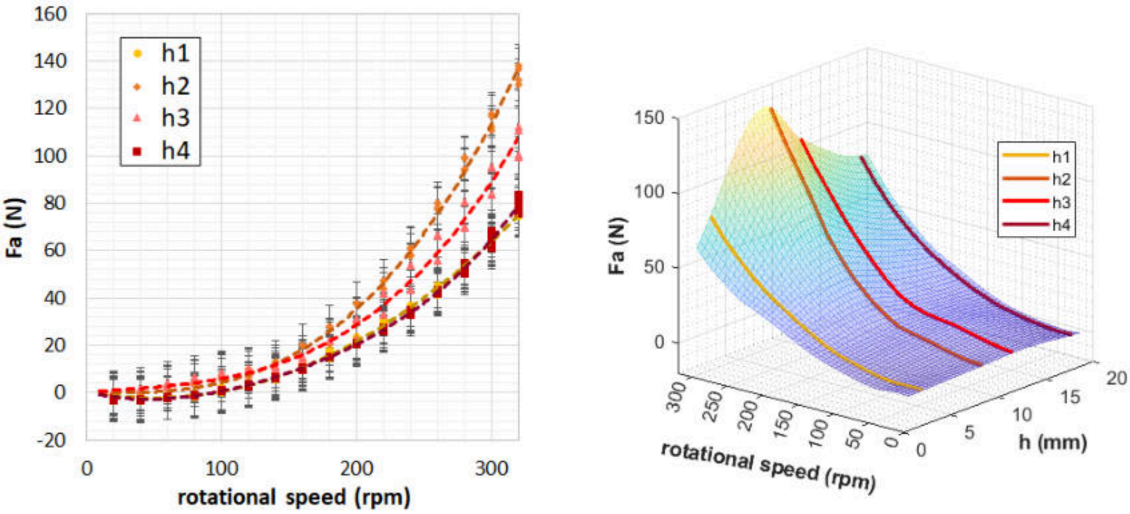

Figure 8.15. Measured axial thrust depending on rotational speed and gap width

8.4 Effect of throughflow

The effect of the presence of the throughflow on the measured torque is negligible. As can be seen in Figure 8.16 the torque does not change with the change of the flow rate, moreover, it stays the same even when the valve is closed (without the throughflow).

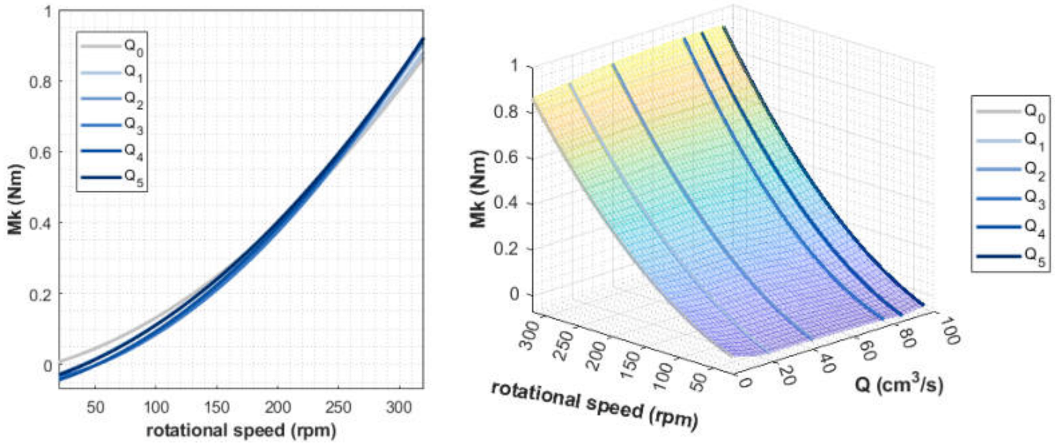

Figure 8.16. Effect of throughflow on torque

On the other hand, the throughflow plays important role in the resulting axial thrust. Its presence and rate change the trend of emerging axial force dramatically as shows Figure 8.17. It can be seen that for higher imposed flow rates the axial thrust gradually grows with rotational speed first, after achieving its maximum (around 260 rpm) it in the studied range decreases. For lower flow rates the increase is more rapid and the first local maximum is shifted towards lower rotational speeds. The force is almost constant in the range (150 – 250) rpm and afterward, quadratic increase with increasing rotational speed can be observed. The lower the flow rate, the closer is the curve to the one with parabolic shape for zero throughflow (the grey curve in Figure 8.17).

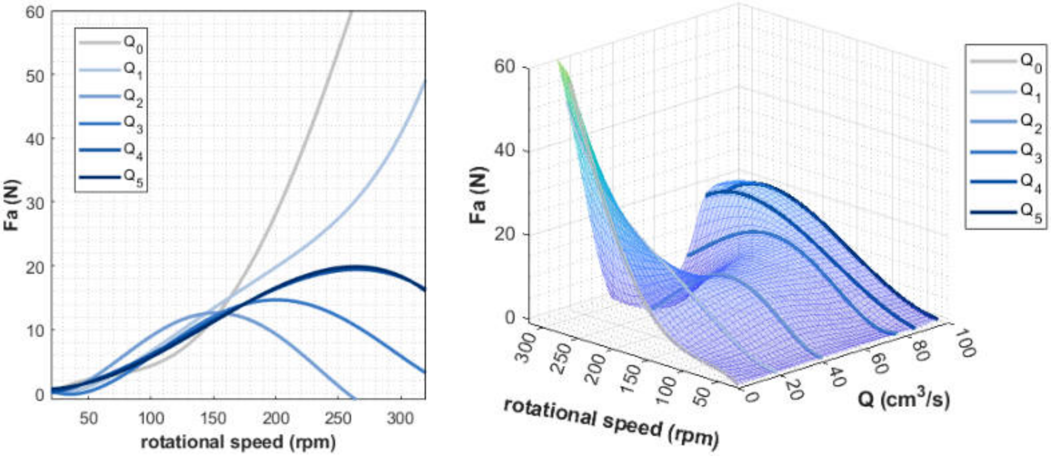

Figure 8.17. Effect of throughflow on axial thrust

CHAPTER 9

Numerical simulations

9.1 Validation of numerical model

9.1.1 Velocity profiles

Numerical simulations done using described methodology were done for the same operating conditions and geometrical configuration for which velocity profiles from LDA are available. The complete comparison of radial and tangential velocity profiles can be found in Appendix, in the following paragraphs, a few samples are chosen to demonstrate trends.

The CFD model in general fits very well with measured data. Good agreement is obtained in the central part of the domain in both, the radial and the tangential velocity profiles almost for all radial locations except for $R = 40$ mm. It is shown on an example of radial velocity profiles for two different rotational speeds and chosen radial positions in Figure 9.1. For better clarity of the charts, only 3 of 5 radial positions are shown, but the appendix contains also the rest of the profiles.

The discrepancy is very likely due to the fact that in the central region, the magnitude of velocity is lower, therefore, fewer particles passing laser beam are detected by the LDA

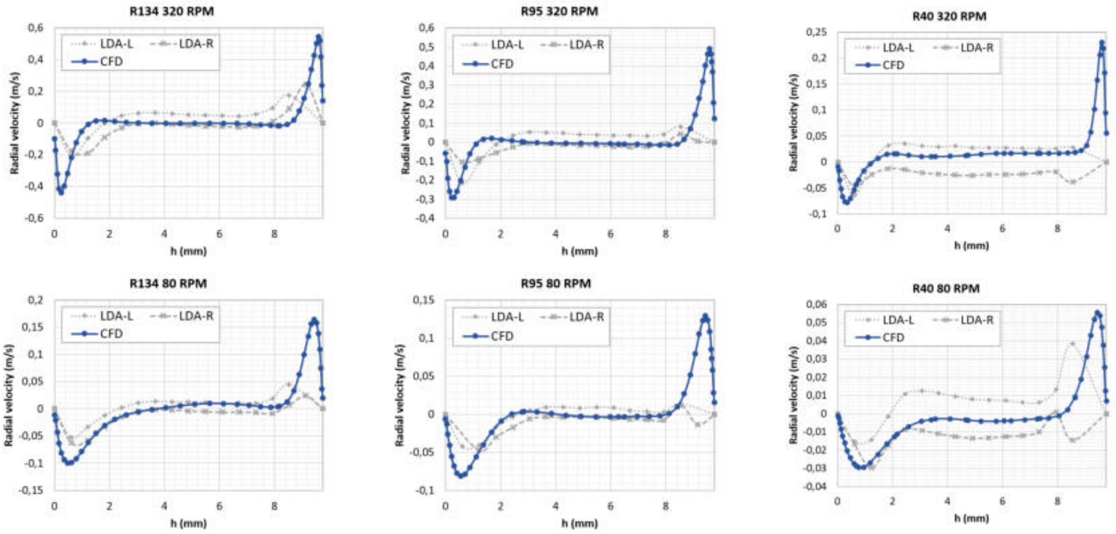

Figure 9.1. Radial velocity profiles comparison

system, which leads to lower accuracy expressed also by the greater discrepancy between left and right side measured velocity profiles (see gray curves in Figure 9.1).

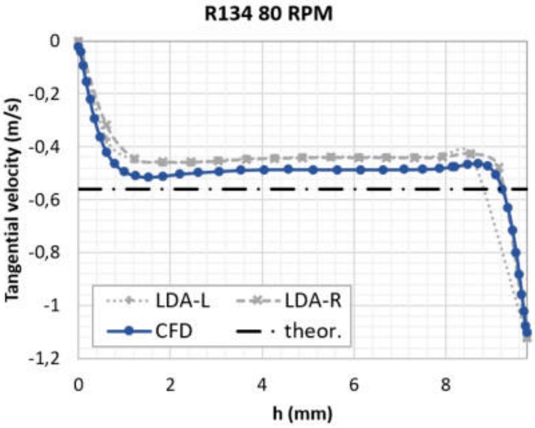

Figure 9.2. Tangential velocity profiles comparison

Another, even more pronounced discrepancy between numerical and experimental data can be observed in near-wall regions. The reason is the limited positioning accuracy of the LDA system, which was not capable of approaching the disks to reach boundary layers reliably. The stator side was easier to reach, since it is steady, made of fully transparent flat plexiglass and it was closer to the positioning system. It can be clearly demonstrated on an example of tangential velocity profile shown in Figure 9.2. The boundary layer belonging to the stator ($h = 0$) is better described, the agreement between both measurements as well as with CFD is good. On the other hand, the rotor boundary layer does not contain any data for LDA measurement made on the left side (denoted as LDA-L), hence the curve is not fitted properly in the near-wall region. For the right side measurement (LDA-R), the last point was closer to the wall (h = 9.5 mm) and it agrees with CFD well.

Earlier mentioned facts on accuracy are applicable similarly on the tangential component of velocity. The discrepancy for R = 40 mm is pronounced as shows Figure 9.3.

Nevertheless, despite the mentioned discrepancies, the CFD model proved itself to provide quite good results in general, even for the lower rotational Reynolds numbers (lower rotational speed of impeller) as can be seen in Figure 9.4.

The comparison with the simplified empirical formula for core tangential velocity was also done, represented by the dot-and-dash black line. As can be seen, the empirical formula overestimates the tangential velocity of the central region for all rotational speeds and radial positions. For the outer radius (R = 134 mm), the simplified formula provides a good approximation of the core tangential velocity. However, the closer to the center, the bigger discrepancy between the theoretical value and measurement/CFD. A similar trend can be observed when focusing on the same radial position but different rotational speeds. With decreasing rotational speed the discrepancy increases. It

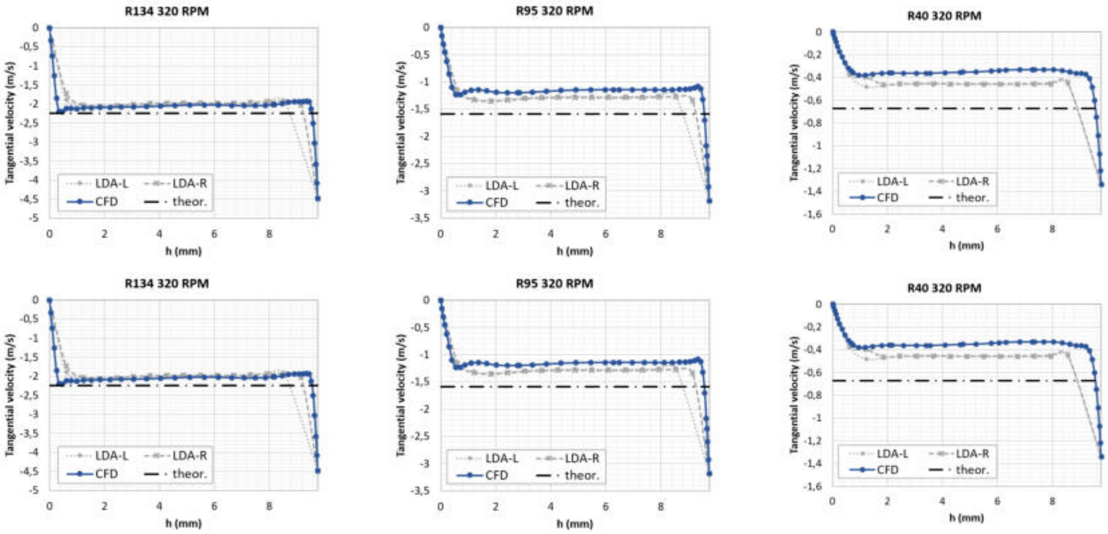

Figure 9.3. Tangential velocity profiles comparison

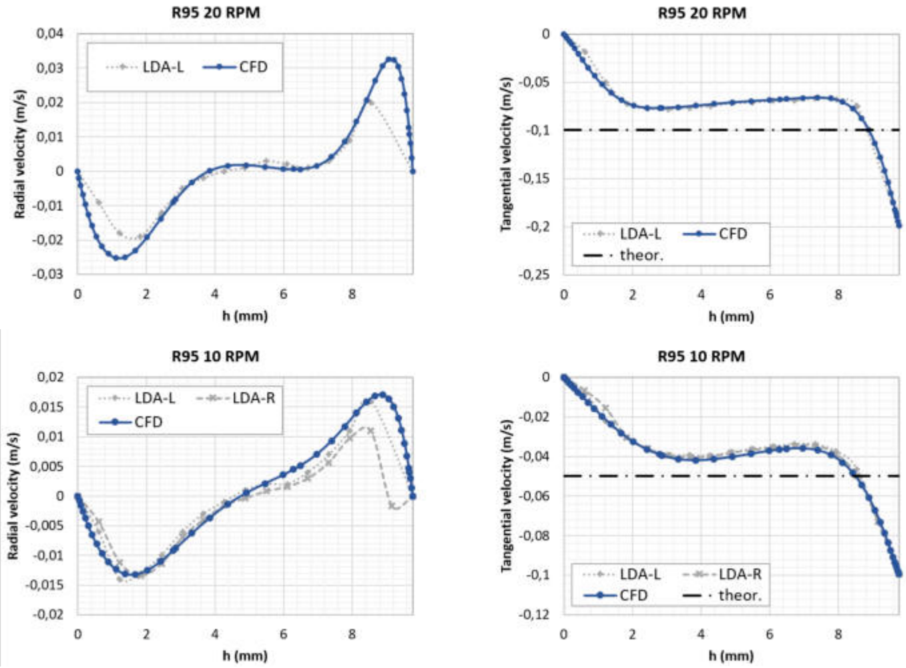

Figure 9.4. Radial and tangential velocity profiles comparison - low rotational speeds

suggests that the formula has been obtained for a fully developed turbulent regime with separated boundary layers (IV). Considering constant gap width, regime IV occurs for higher rotational Reynolds numbers (implicated by either higher rotational speed or by larger rotating disk diameter). Therefore, the empirical formula does not provide such a precise estimation for the transition or the other regimes.

9.1.2 Disk friction

Another sign of a good CFD solution of the velocity gradients in near-wall regions is values of frictional torque. As can be seen from comparison with experimental data in Figure 9.5 the numerical simulation matches the experimental measurement reasonably. The captured trend is similar, the differences are for the narrow gap h_1 within the measurement uncertainty in the whole studied range, for the higher width the discrepancy increases with increasing rotational speed.

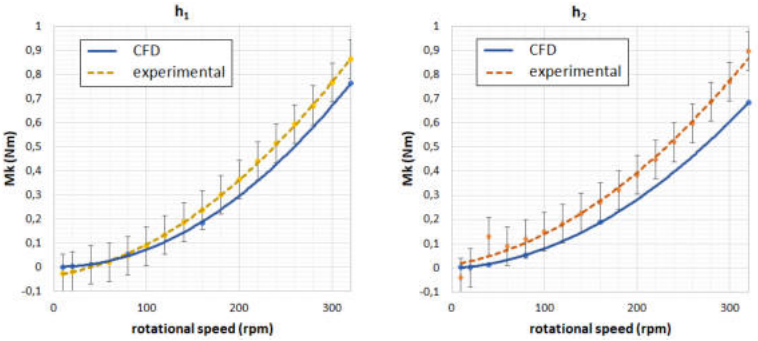

Figure 9.5. Frictional torque

9.1.3 Axial thrust

Experimental and numerical data agree well for the lower rotational speeds (up to 200 rpm). The agreement for higher rotational speeds is not good. This is likely a result of the choice of the springs, which were primarily designed for the measurement of low forces. For higher forces, and thus, higher displacements, their characteristic may become nonlinear leading to the discrepancy. The chosen springs were the trade-off to do not have to change them during the measurements. It would mean another calibration and considerably complicate the whole process. Nevertheless, measurement with stiffer springs in the range of higher rotational speeds is a good point for future investigation.

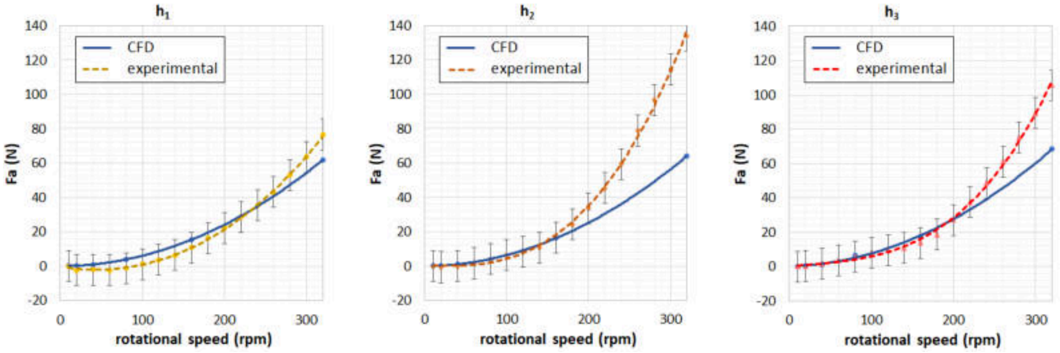

Figure 9.6. Axial thrust

9.1.4 Visualization of the flow field

The good capability of the CFD model to capture the unstable vortices supports also the result of the visualization experiment. The comparison of photographs for particular rotational speeds and volume renders of vorticity magnitude shows Figure 9.7. Especially for lower rotational speed, the agreement with experimental visualization is very good. With increasing *Re* the decay of vortex structures is apparent and the CFD simulations lose detail, likely as a consequence of relatively coarser mesh resolution for those Reynolds numbers.

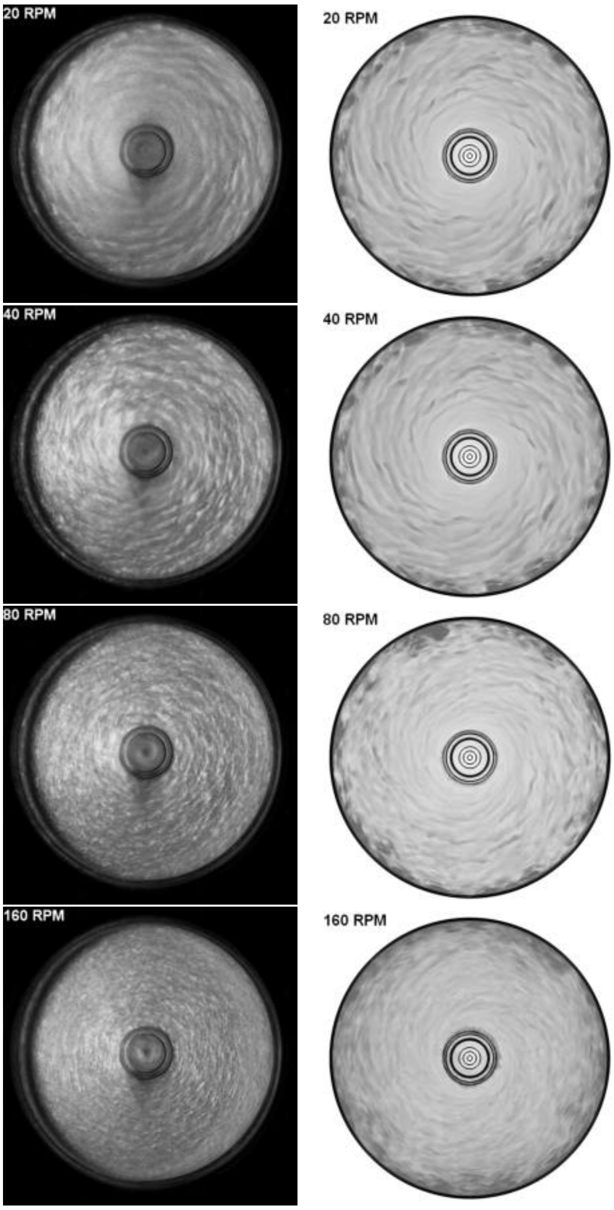

Figure 9.7. Experimental visualization of the flow (left), volume renders of vorticity magnitude obteined by CFD (right)

9.2 Flow field in back-sidewall gap without throughflow

The flow field of the back-sidewall gap domain is quite complex and differs from the flow in a simple rotating cavity, which has been described in previous studies. Even for the higher rotational Reynolds number, where fully developed regime IV was expected, volume rendering of velocity magnitude with suitable scale reveals the presence of vortical structures in the whole domain, as can be seen in Figure 9.8. It shows the 3D rendering of velocity magnitude across the domain, which has no featureless, monotonous distribution at all. The visualized structures were not recognizable in velocity profiles, since both the experimental and the CFD results were obtained by averaging over time to be able to compare them, therefore those effects were suppressed.

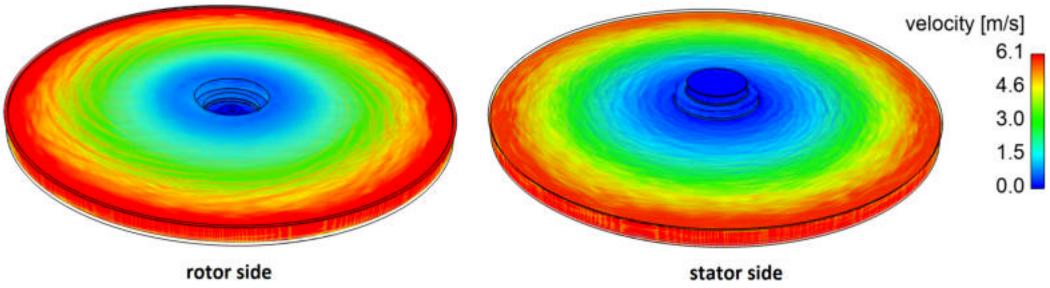

Figure 9.8. Structures in the back-sidewall gap flow field

Since those effects are worth further investigation, more variables on which they could be studied were plotted. As can be seen from vorticity in Figure 9.9, its overall value is higher on the rotor side, however, it is more uniform whereas on the stator side which tends to be less stable, spotted, disturbed character with many localized vortices can be observed.

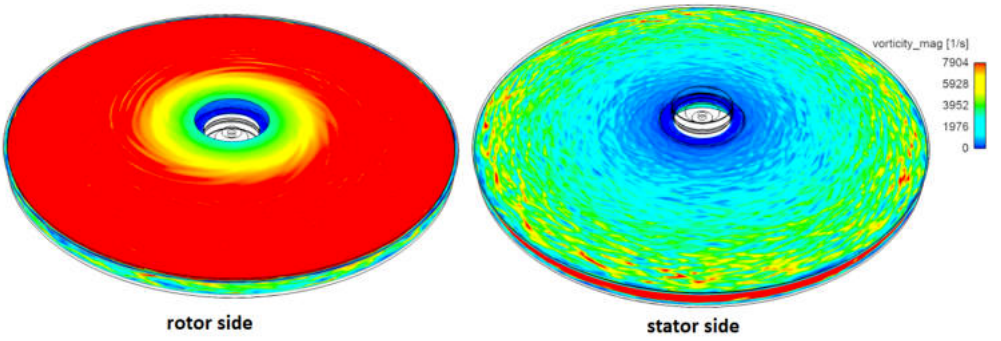

Figure 9.9. Vorticity near the rotor and the stator sides

Nevertheless, the structures are not localized only in near-wall regions, as demonstrates cross-sectional visualization of vorticity in Figure 9.10 and Q-criterion in in Figure 9.11.

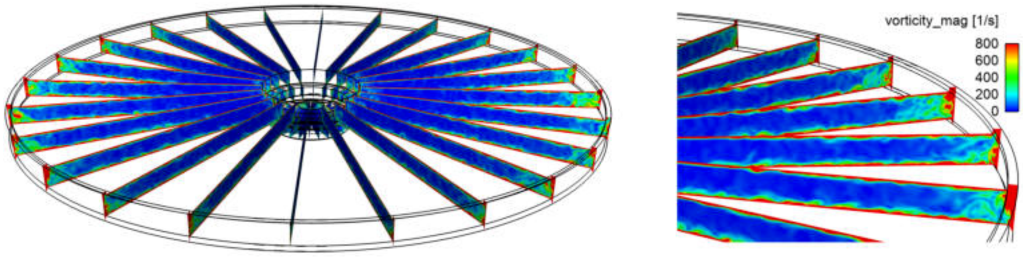

Figure 9.10. Vorticity in gap cross-section

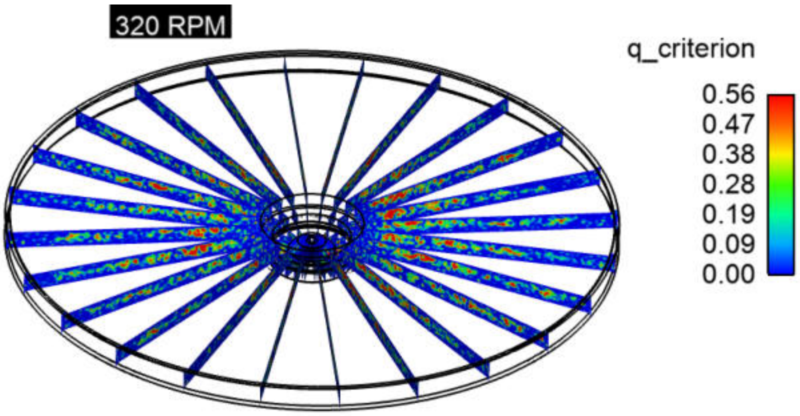

Figure 9.11. Q-criterion in gap cross-section

Since the nature of the structures is periodical, it is very likely linked to the rotation of the impeller and the passing of the blades through a particular location. The evolution of the flow in the cross-section of the cavity is documented in Figure 9.12. The figures show the same location as one blade passes.

Focusing on the starting position, where the blade trailing edge is aligned with investigated cross-section marked by the blue arrow, the wavy character of the flow can be observed. The flow enters the domain on the outer radius of the gap, collides with the stator, which changes its direction towards the rotor side. It continues in the same manner quite regularly to the center of the cavity, as shows the figure denoted as blade pass 0.

The blade passing the location accelerates the flow in the outer region of the sidewall gap, strongly developed direction from the stator to the rotor prevails, while in the rest of the domain, wavy character persists, as documents figure blade pass 1.

With the blade moving away, the direction of the vortex formed in the outer cavity radius changes, and flow from the rotor towards the stator and outwards become dominant. It initiates backflow from the back-sidewall cavity domain to the volute. Moreover, such vortex forces a part of the flow in the middle region of the cavity to change its direction as well, as shows blade pass 2.

Interference of the outwards directed flow with the outer wall of the cavity again drives the change of the sense of vortices. As can be seen from the cross-section in Fig. Figure 9.12 blade pass 3, the flow is directed from the rotor to the stator, which propagates into the middle region by change of the flow direction here as well. The inwards prevailing character develops again.

It persists during the next blade approaches, the wavy profile between the rotor and the stator side is formed again.

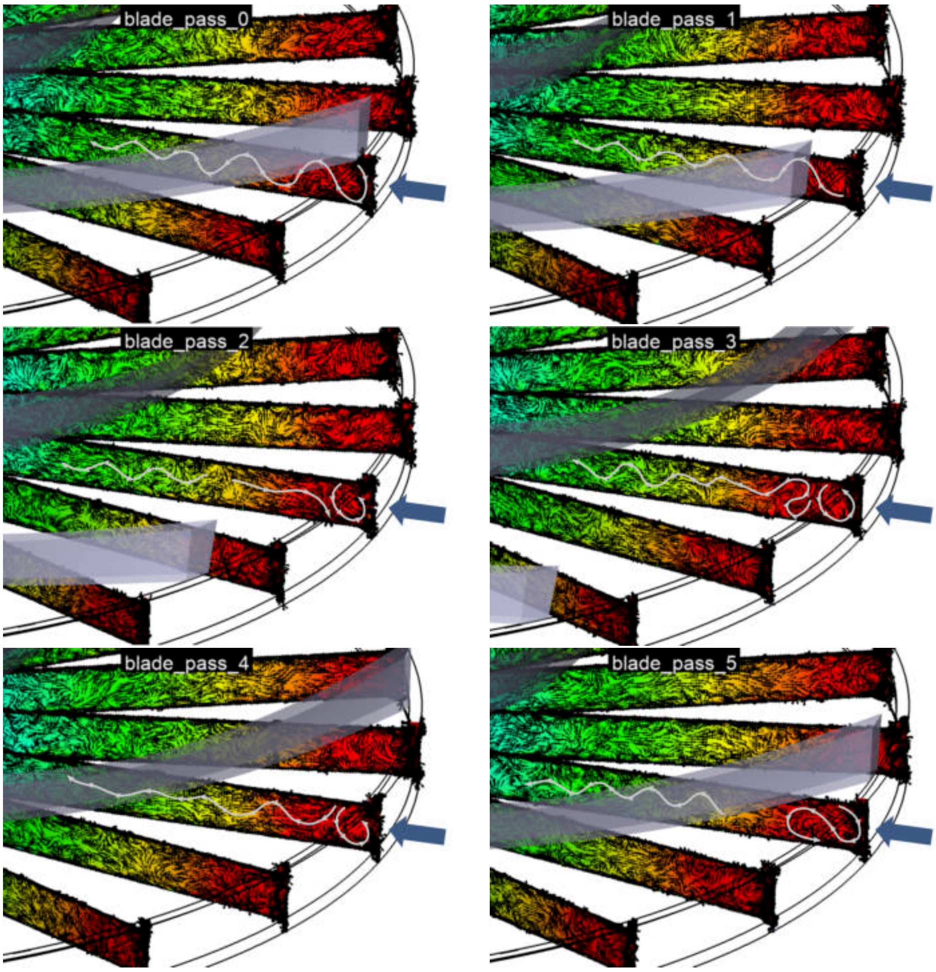

Figure 9.12. Vectors of velocity in cross-section - evolution in time

The described character evolving with the motion of the blades results in the existence of the angular positions, where the flow enters the domain of the back-sidewall cavity and oppositely, where the fluid returns to the volute part. As was already described and as is shown in Figure 9.13, in the position of the blades (in the immediate vicinity, either in front or behind), the velocity vectors point to the back-sidewall gap and the magnitude has its maximum. On the other hand, in the angular position corresponding to the middle of the blade channel, the flow directs out of the back-sidewall gap and enters the volute. Since there is no feature, which brings an asymmetry (e.g. volute cutwater), the flow has the same nature in the whole domain.

The changes of fluid direction from and out of the back-sidewall cavity are the link between the spiral structures observable on the rotor side whether in the velocity field, vorticity, or wall shear stress, as shows Figure 9.14. The number of the spiral arms is independent of the rotational speed, if it occurs, 15 separate vortices are always formed. The hypothesis that those structures are induced by the rotation of the blades supports also the fact, that the spirals rotate with the impeller, and 3 of them can be traced in each of the blade channels.

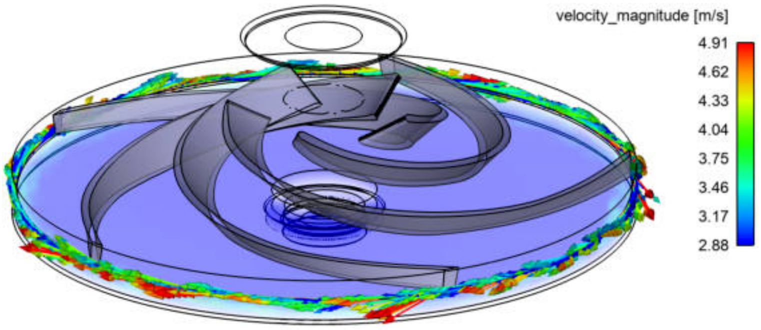

Figure 9.13. Flow entering and leaving the back-sidewall gap domain

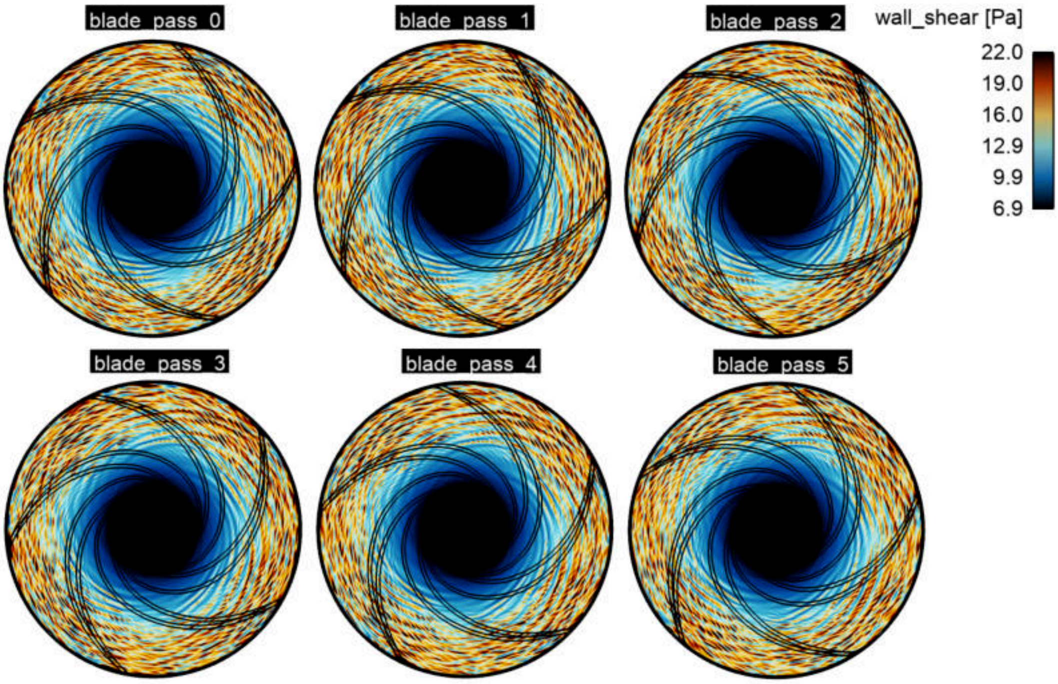

Figure 9.14. Wall shear stress on the rotor side

The evolution of the flow inside the back-sidewall gap with the change of rotational speed of the impeller in the overall picture show Figures 9.15 and 9.16. On the rotor (left side), it is obvious that with increasing speed, the smooth flow becomes disturbed by the onset of the spiral structures. On the other hand, the stator side is covered with disordered vortices for almost the whole studied range. They disappear for very low rotational speeds (under 10 rpm), but it can be observed as well, that they get gradually weaker when the rotational speed increases over 160 rpm.

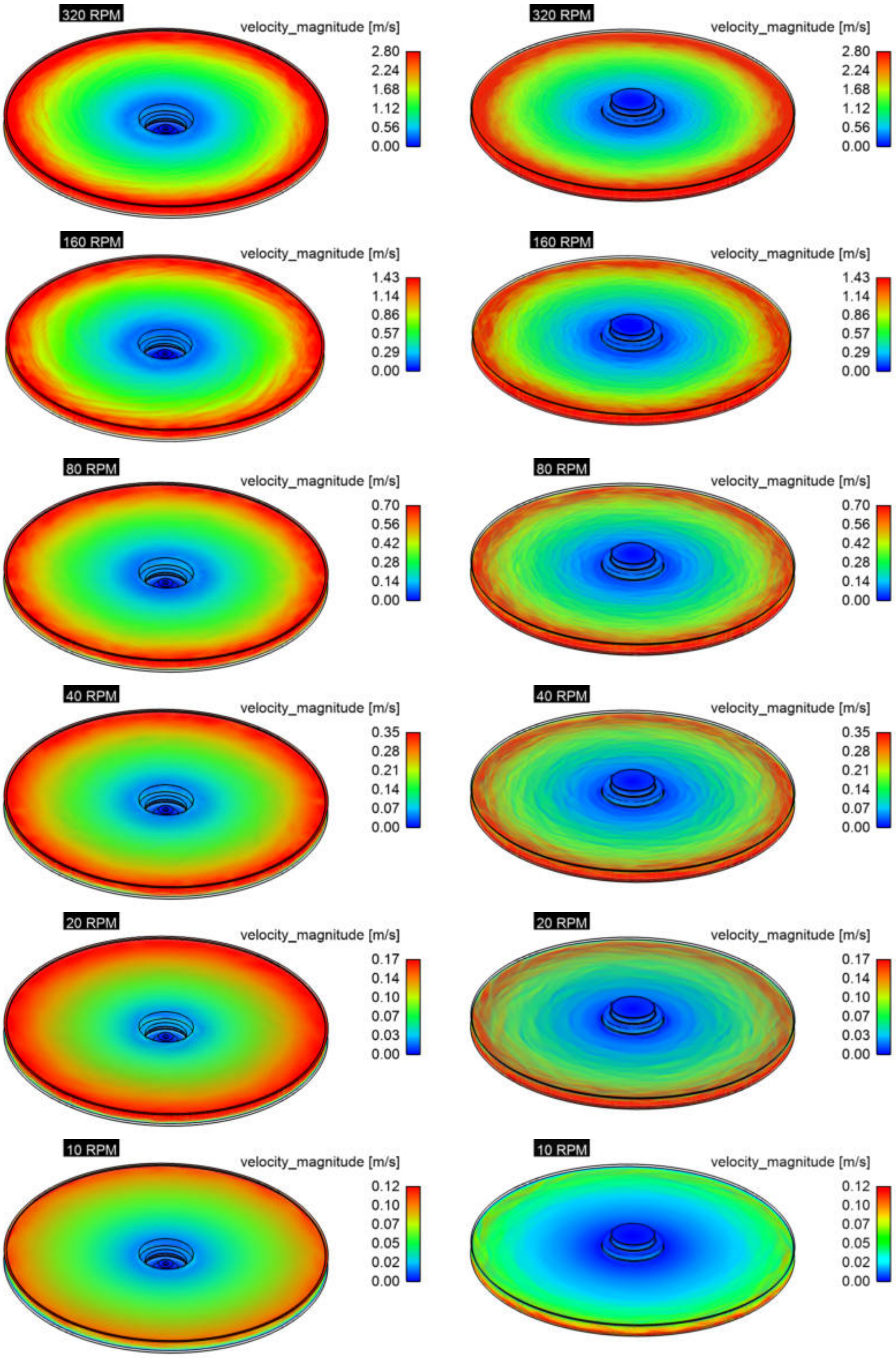

Figure 9.15. Structures near rotor (left) and stator (right) for different rotational speeds

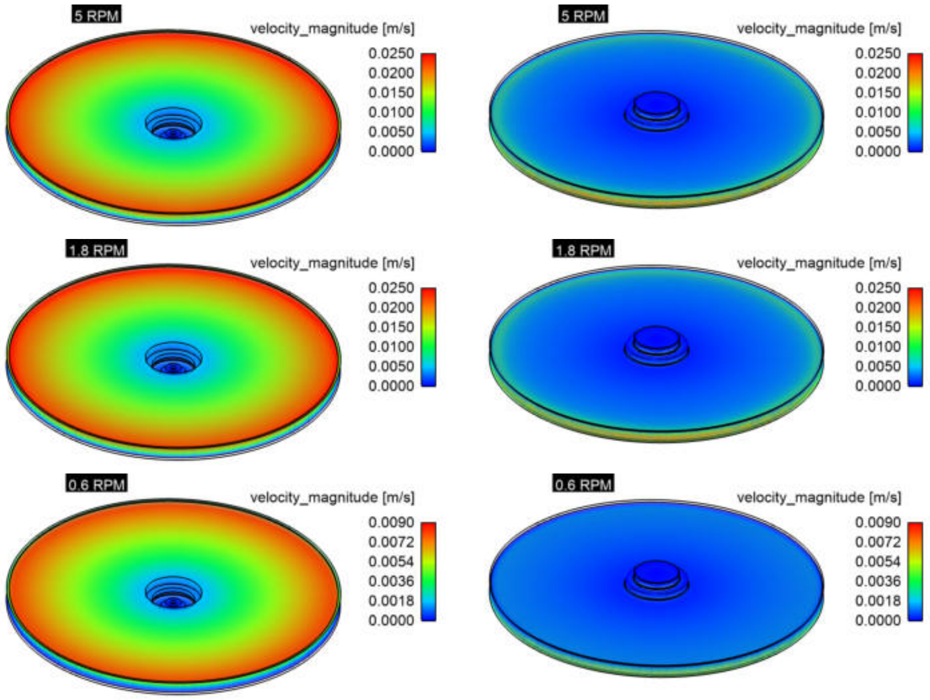

Figure 9.16. Structures near rotor (left) and stator (right) for different rotational speeds

From the visualization of the vorticity (Figure 9.17) and the Q-criterion (Figure 9.18), it can be seen that the swirling structures are present in the whole domain, however, their intensity drops down with the decrease of the rotational speed. When the rotational speed decreases under 20 rpm, they are localized only in the inflow and the central part. Only some visualizations capturing the trend are shown here, the complete overview of CFD results for all solved rotational speeds can be found in the appendix.

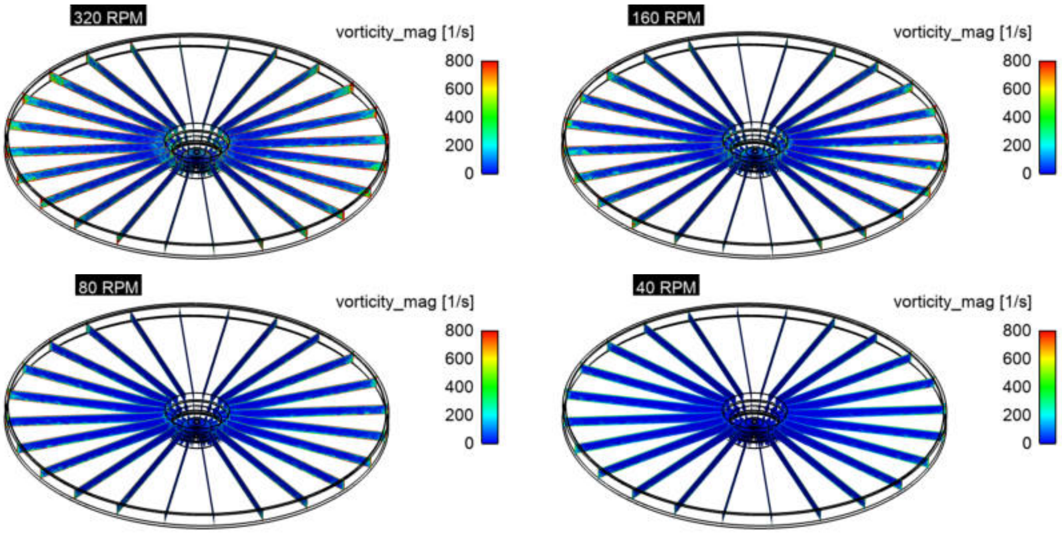

Figure 9.17. Vorticity for different rotational speeds

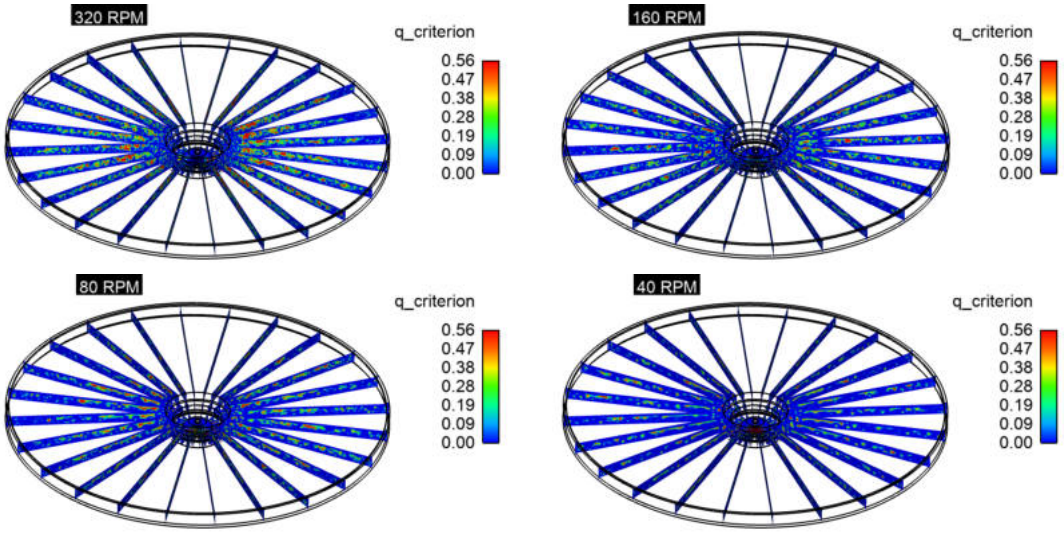

Figure 9.18. Q-criterion for different rotational speeds

The periodical character given by the blades is obvious for all the rotational speeds. The typical changeovers between inflow to the domain and outflow back to the volute demonstrates Figure 9.19. It does not disappear even for the lowest rotational speeds. Nevertheless, the lower the rotational speed, the lower the magnitude of the velocity either in the positions of the inflow or the outflow.

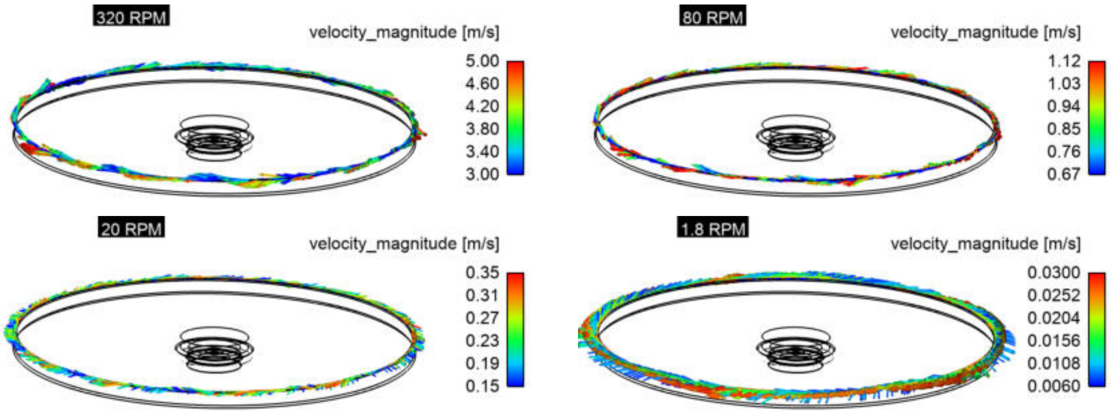

Figure 9.19. Inflow to the back-sidewall gap for different rotational speeds

Another expression of this periodicity can be seen in contours of wall shear on the rotor side, see Figure 9.20. For higher rotational speeds, a set of spiral structures rotating in the opposite direction than the impeller emerges. As was already said, the number of spirals is always the same, independent of the rotational speed. What changes with the change of the rotational speed is its extent and width. The higher the speed, the narrower the arms, however, it occupies almost half of the radial position. With decreasing speed it becomes wider and it shrinks to the outer diameter of the cavity. The central region turns smooth, and this character gradually fills the whole domain, as rotational speed decreases. On the contrary, for the stator side, no significant character change can be seen with the change of the rotational speed. As show Figure 9.21 the instability pattern on the stator side stays the same, the change of the rotational speed causes only the difference in the values of the shear stress.

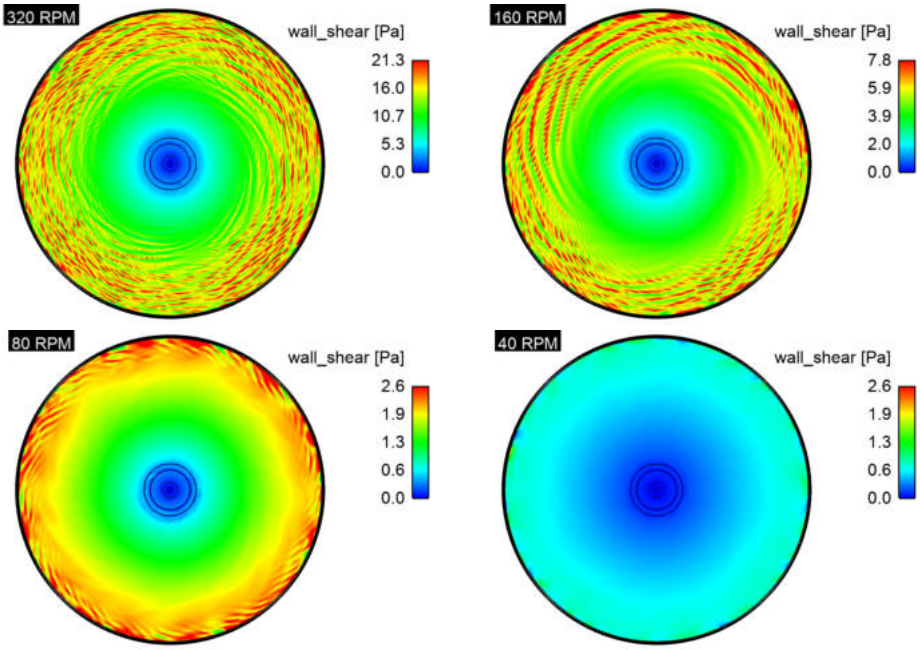

Figure 9.20. Wall shear on the rotor side for different rotational speeds

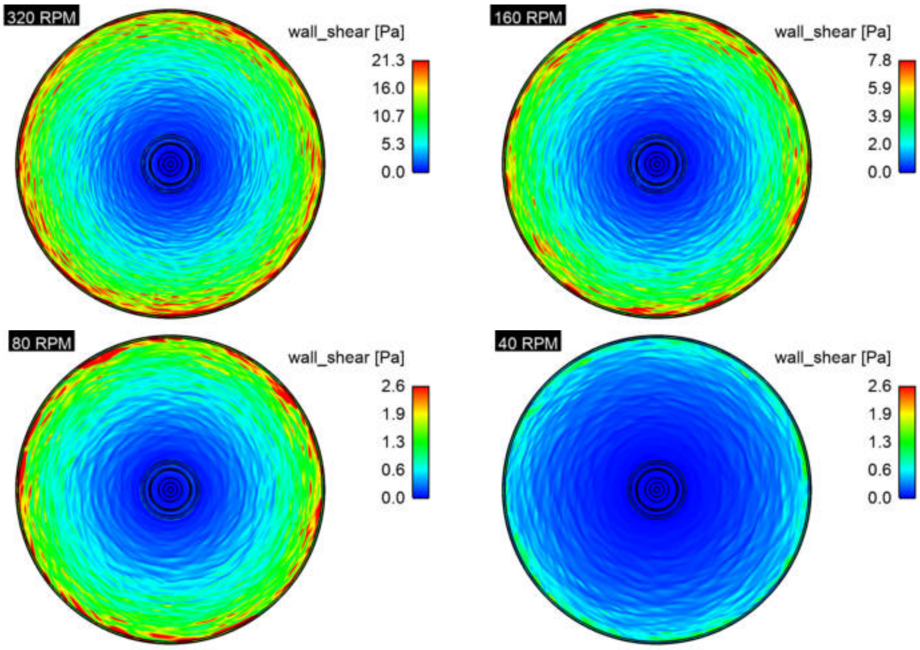

Figure 9.21. Wall shear on the stator side for different rotational speeds

The evolution of the velocity magnitude in the whole domain for decreasing rotational speed is shown in Figure 9.22. It illustrates how and for which speed the character of the flow in the back-sidewall gap changes. It can be seen, that between 20 rpm and 10 rpm the strong vortex at the inlet to the back-sidewall gap disappears and therefore does not influence the flow formation in the whole gap anymore. With the further decrease of the rotational speed to 5 rpm the flow field with uniform character, where the velocity magnitude grows in the axial direction from the stator to the impeller, is developed.

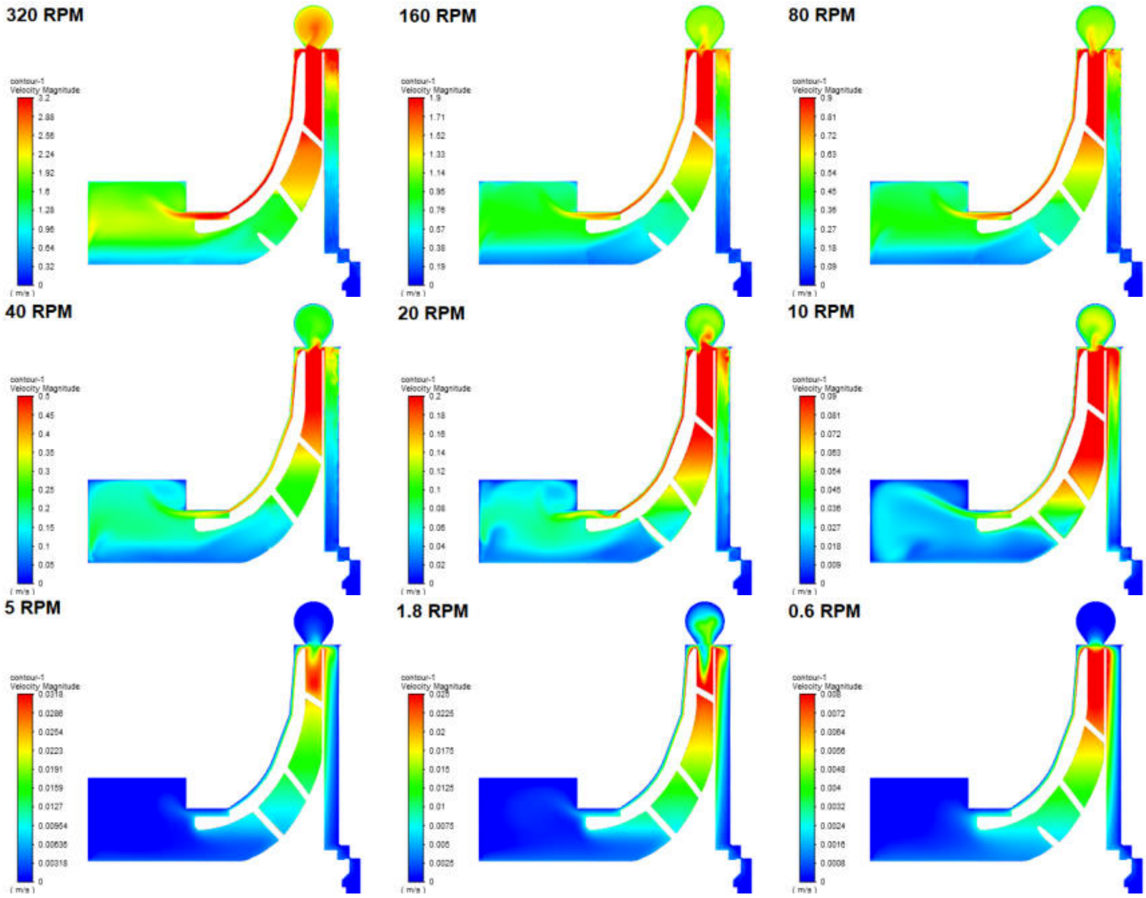

Figure 9.22. Velocity field in the whole domain for different rotational speeds

The rotating vortex on the outer radius which changes orientation as the blade passes is formed at any rotational speed higher than 10 rpm. (see Figure 9.23), however, its ability to influence the direction of the flow in the rest of the back-sidewall gap is for such a low rotational speed relatively week. Nevertheless, it gets stronger with increasing rotational speeds fast. As can be seen for 20 rpm, the significant portion of the domain is already distorted by its presence.

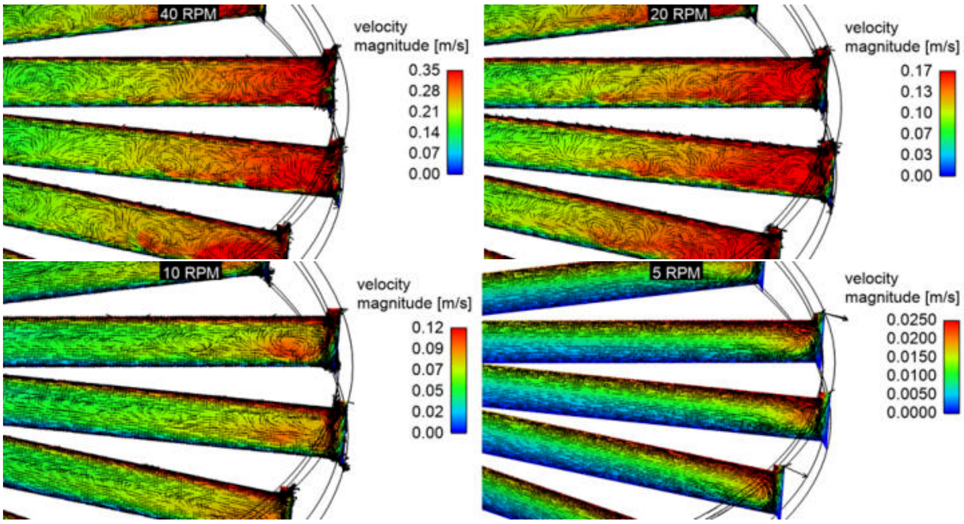

Figure 9.23. Velocity in cross sections for different rotational speed

The evolution of the flow was studied in detail by means of velocity profiles, similarly to the experimental data processing. For 5 radial positions and each rotational speed the radial and the tangential velocity profiles were plotted, as suggests Figure 9.24. This is a powerful tool for the easier identification of particular flow regimes.

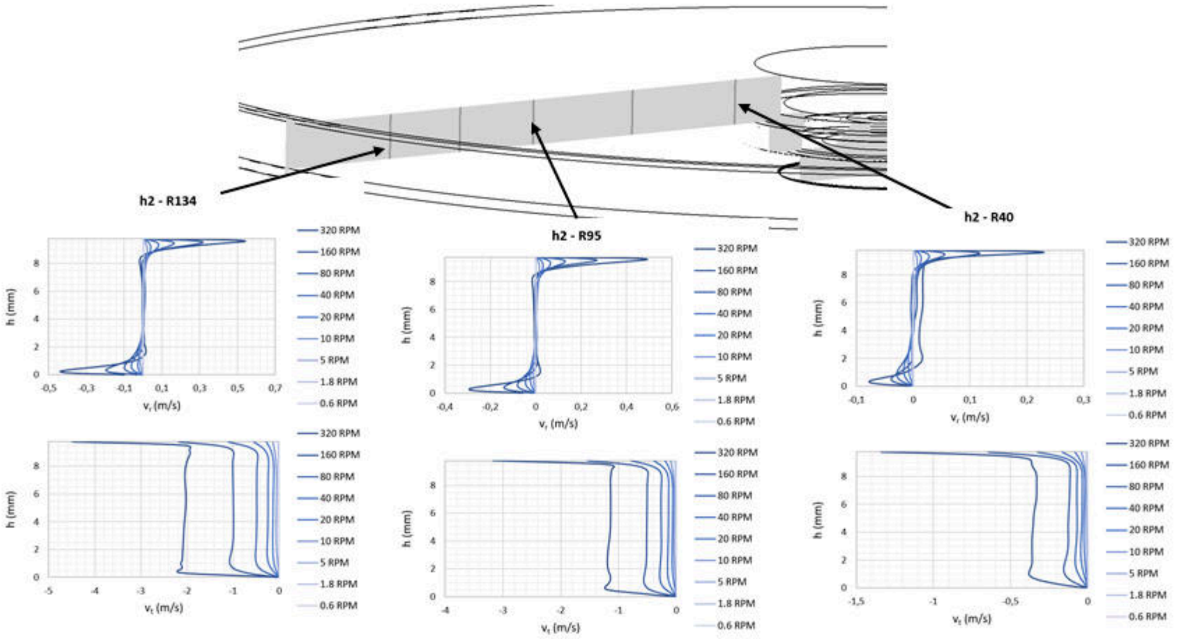

Figure 9.24. Velocity profiles across the back-sidewall gap for different rotational speed

As is obvious from the overview the velocity profiles in Figure 9.24 the most of the profiles indicates turbulent flow with separated boundary layers (regime IV) for this gap width (h_2). In fact, any of the radial positions is occupied by this regime when the rotational speed exceed 40 rpm.

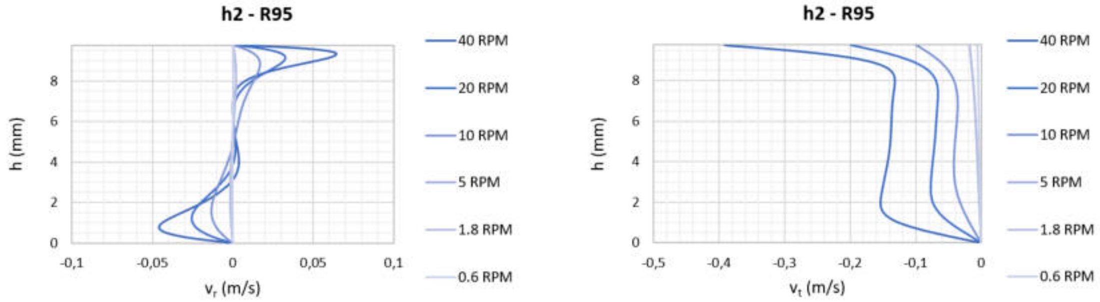

Figure 9.25. Radial and tangential velocity profiles for low rotational speeds

A typical transition can be observed on an example of the radial and the tangential velocity profile for $R = 95$ mm and rotational speed under 20 rpm in Figure 9.25. In the radial velocity profile for 40 and 20 rpm is a clearly distinguishable central vertical region with zero velocity between the gradients belonging to the boundary layers. The analogical shape distinguishing regime IV can be observed in the tangential velocity profile as well. For 10 rpm the core radial velocity inclines and intervenes both boundary layers, which is the typical evidence of regime III. Below 5 rpm the radial velocity profile becomes S-shaped, which is characteristic of laminar flow with merged boundary layers (regime I). It can be identified also from the change of the tangential velocity profile from curved to straight.

Not every of the possible four flow regimes can develop for a particular combination of gap width, rotational speed, and radial position. As an example of it can be mentioned regime II, which was not detected for any point of the map.

The map of regimes obtained experimentally was extended using the CFD data including more rotational speeds and gap widths. More regimes and transitions were identified for such operating conditions which were not reachable experimentally.

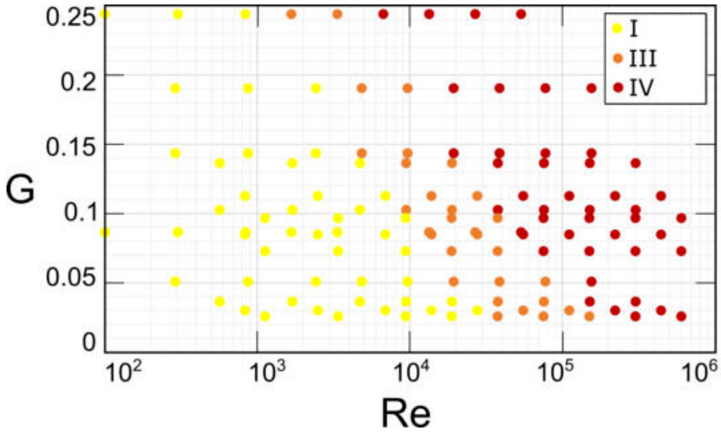

Figure 9.26. Map of regimes obtained from CFD results

9.2.1 Effect of back-sidewall gap width

The effect of the back-sidewall gap width on the flow was studied by CFD simulations as well as by means of the experiments. The results presented so far were obtained for the middle gap width (h_2) for which LDA measurements exist. As expected, with increasing rotational speed, the flow field of the narrower (h_1) and wider (h_3) geometries evolves differently.

For the narrower gap h_1, the vortices occur earlier on the rotor side earlier than for the gap h_2, and for h_3 its presence is detected even later. Upon closer inspection can be seen, that the difference is not only in the speed of the onset of the instability but also in its character. As shows Figure 9.27, a huge amount of fine spirals is emerging in the narrow gap, stronger spirals can be observed in the middle width and only a few ring-shaped waves propagate in the wide gap. As the rotational speed increases, all of them tend to converge towards the spiral shape of the instabilities described in the case h_2 in the previous section.

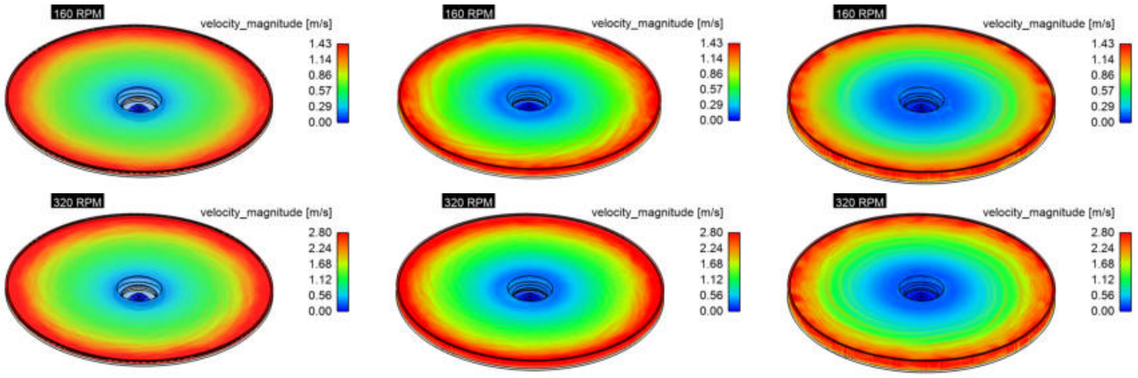

Figure 9.27. Structures on the rotor side for h_1 (left), h_2 (middle) and h_3 (right)

Regardless of the back-sidewall gap width, the first signs of instabilities are visible on the stator side already around rotational speed 10 rpm. Nevertheless, relatively significant differences in character are evident on the stator as well as on the rotor. For the narrow gap h_1, the vortices are localized only in the outer region until 80 rpm, when they spread to the whole domain, as illustrates Figure 9.28 left. In the middle gap h_2, the unstable structures fill the whole extent without significant change within the analyzed range of rotational speed, see Figure 9.28 middle. For the wide gap h_3, and 20 rpm the instabilities occupy only a very limited region around the outer radius, when rotational speed increases to 40 rpm they rapidly spread across the gap, with further increase of the speed they slightly vanish to emerge once again around 160 rpm in a different form.

As is illustrated in Figure 9.29, there are circular rolls in the central region of the stator, while the outer radius is occupied by a mix of spirals and chaotic turbulent structures. The rotor side is covered by spirals which are more pronounced with increasing rotational speed.

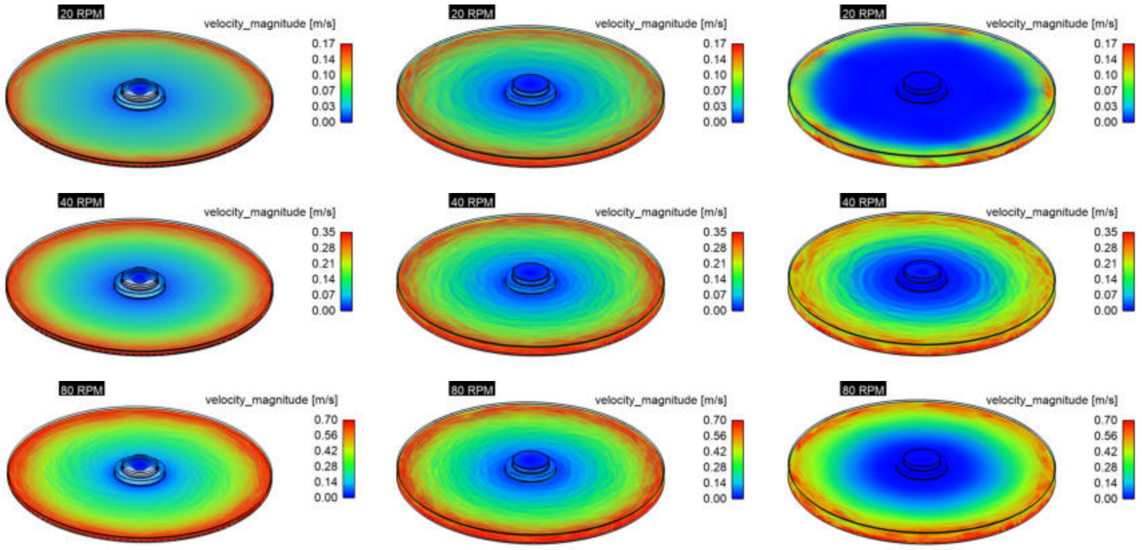

Figure 9.28. Structures on the stator side for h_1 (left), h_2 (middle) and h_3 (right)

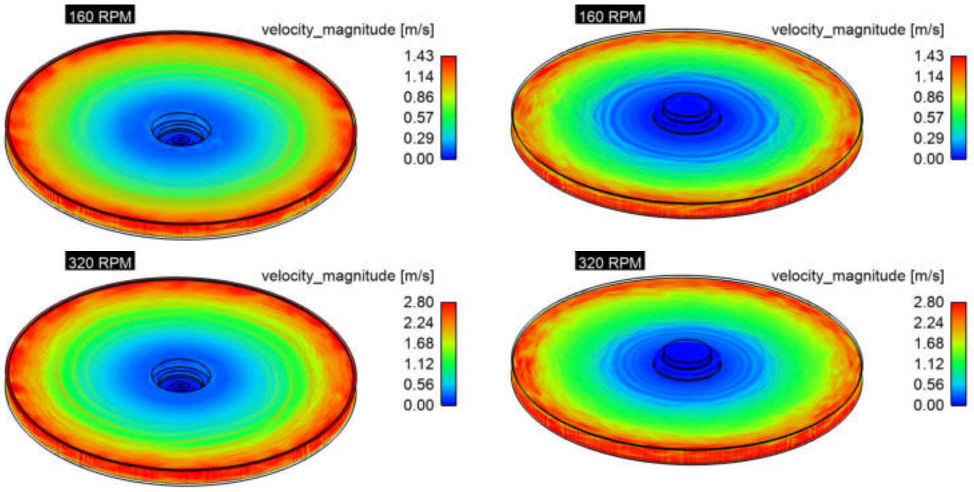

Figure 9.29. Structures on the rotor and stator side for h_3 (right)

Another insight into the flow field evolution provides vorticity. For low rotational speeds below 10 rpm its overall value in the gap is lower for h_1 and it is evenly distributed in the whole domain, whereas for wider gaps h_2 and h_3 the maximum is concentrated at the inlet to the sidewall gap, as can be seen on example in Figure 9.30 top. When the rotational speed increases to 10 rpm, the vorticity becomes concentrated in the boundary layers for gaps h_2 and h_3, while for the narrow h_1 it is still spread across the gap, see Figure 9.30 bottom. The localization into the boundary layer for the narrow gap occurs when rotational speed reaches 20 rpm.

For the rotational speeds in the middle of the analyzed range, the vorticity character differs among h_2 and h_3. For the wider gap, a region with a significant maximum exists on the outer radius, the rest of the domain does not contain such high values. On the

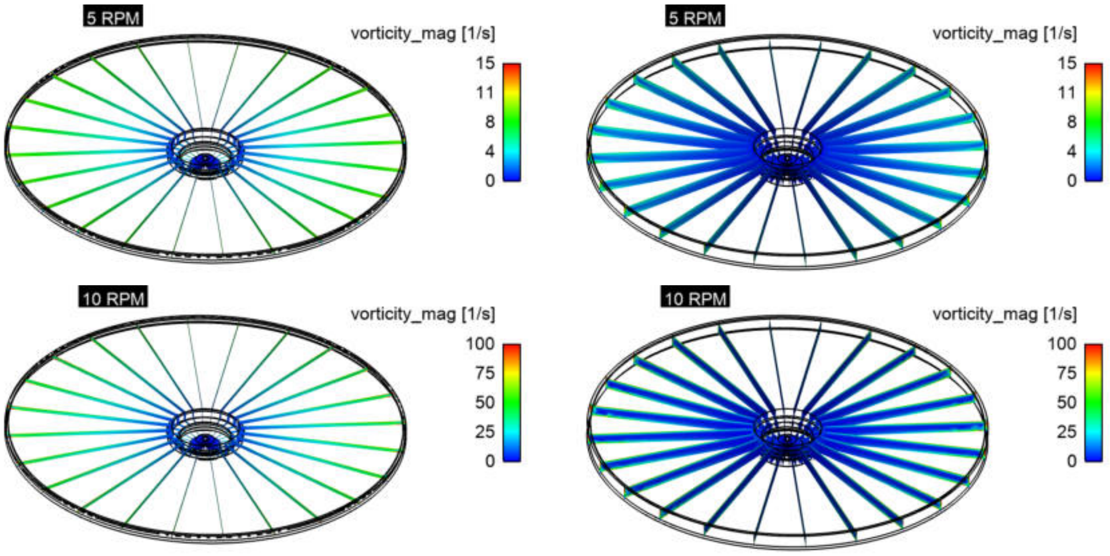

Figure 9.30. Vorticity for h_1 (left), h_2 (right)

other hand, vortices protruded through the whole cross-section can be clearly seen for h_2, as shows Figure 9.31. With increasing rotational speed the regions with higher vorticity propagate further also for the gap width h_3.

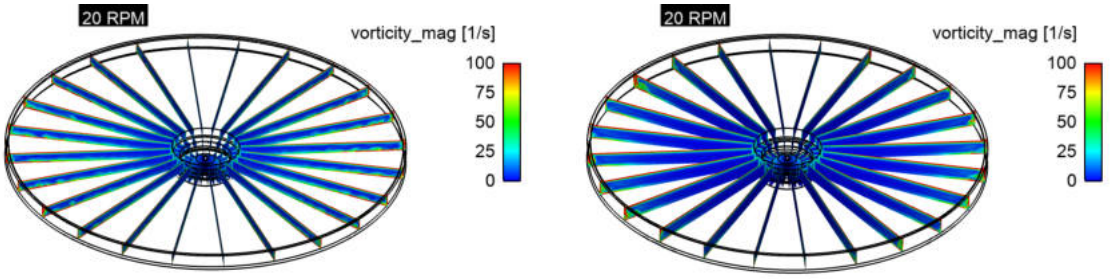

Figure 9.31. Vorticity for h_2 (left), h_3 (right)

The changes of spreading of the vortices through the domain and therefore completely different mechanisms of the transition can be nicely illustrated on the plot of Q-criterion for gap widths h_2 and h_3. As shows Figure 9.32, there is gradual progress in the number and strength of the vortices with rotational speed across the gap h_2. On the contrary, for the gap h_3 almost no vortices are detected at 20 rpm corresponding to the vorticity plot with the only significant region at the inlet to the domain. Then, sudden change can be observed at 40 rpm followed by the disappearance of the vortices at 80 rpm and their redevelopment and intensification in the central region over 160 rpm.

The narrower the gap, the less space for the development of variability of the vortical structures. The Q-criterion was not able to detect nearly any vortices in the back-sidewall gap h_1 even for 320 rpm. The narrow gap does not give much space at the inlet to develop the rotating flow and spread the instability, rather mitigates its propagation, as can be illustrated on the overall picture of the flow field for the whole range of the rotational speed in Figure 9.33. The evenly distributed velocity magnitude across the gap radius can be seen up to 40 rpm, whereas for wider gaps h_2 and h_3 the inlet turbulence corrupts the laminar profile already at 10 rpm, as was shown before (Figure 9.22).

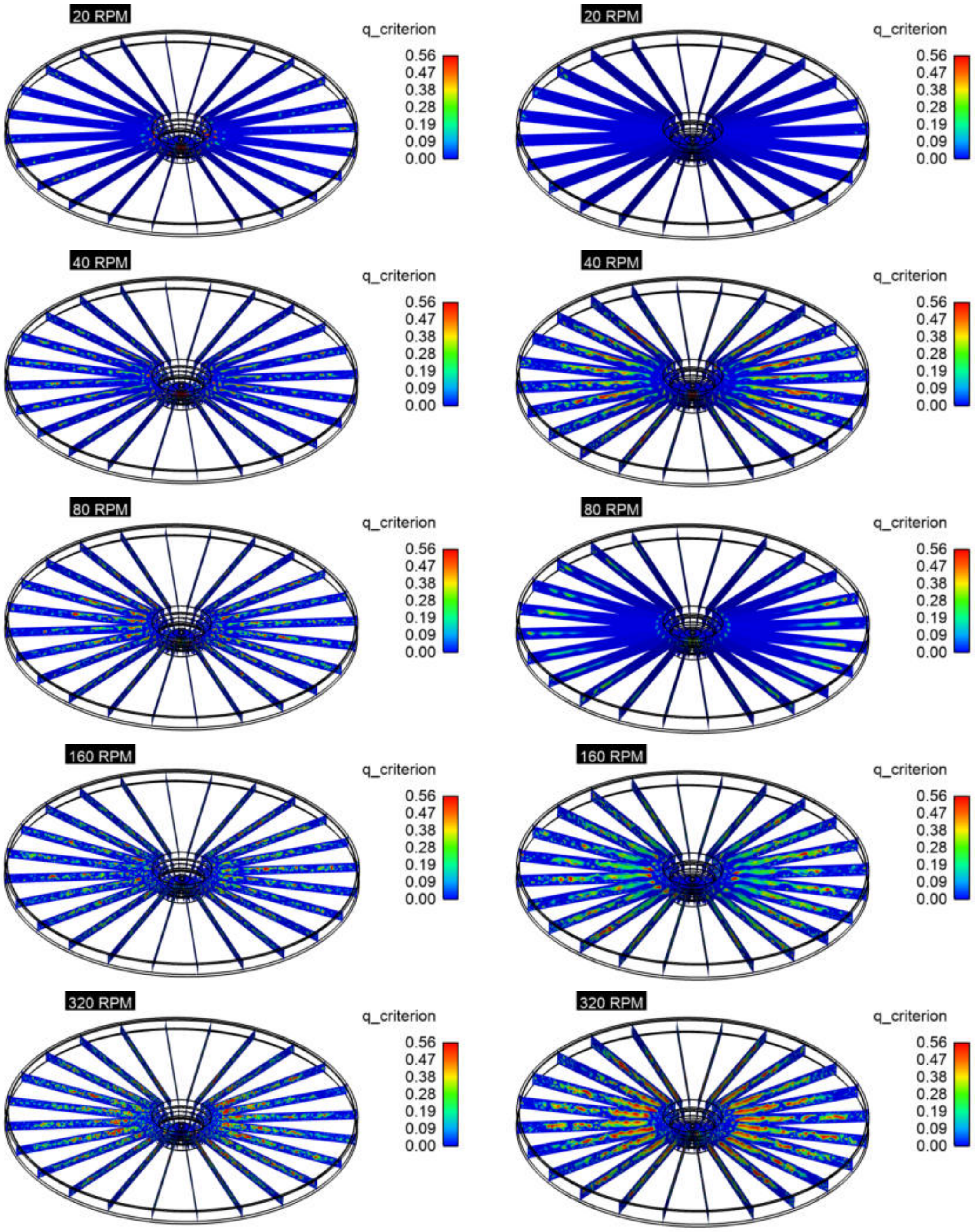

Figure 9.32. Q-criterion for h_2 (left), h_3 (right)

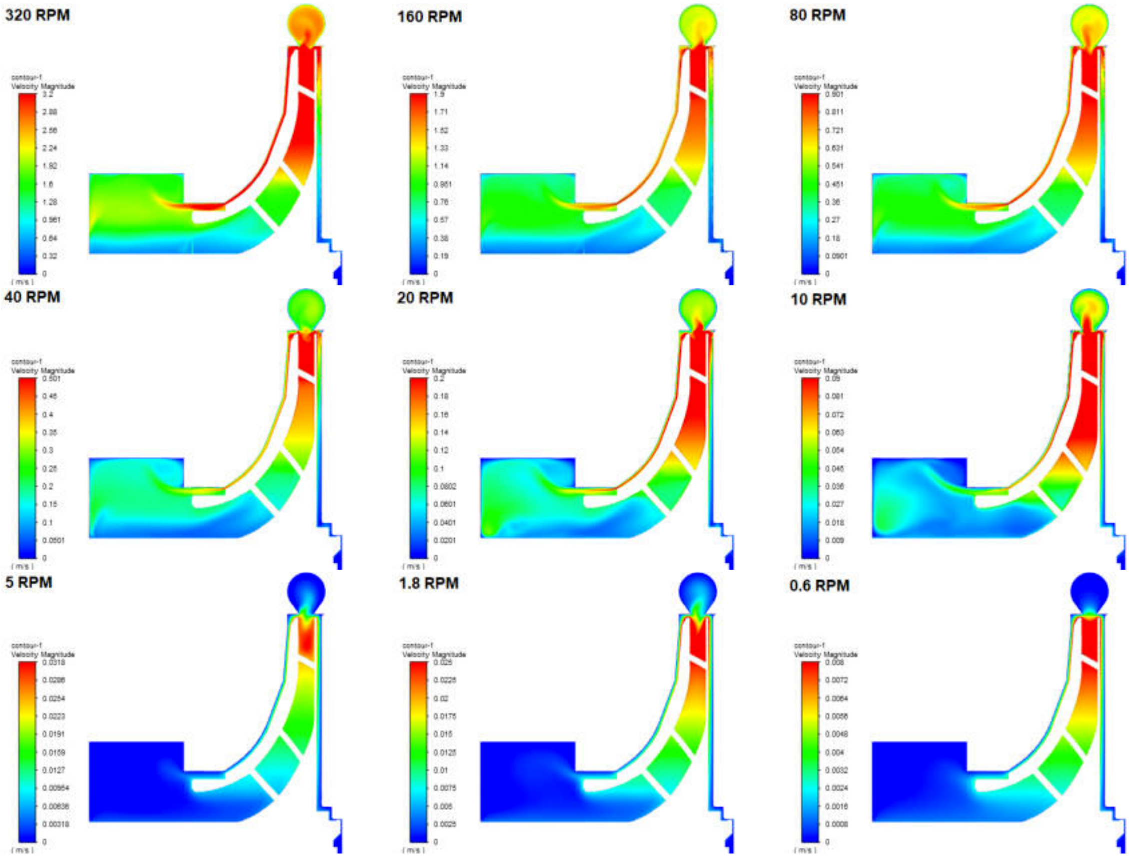

Figure 9.33. Velocity field in the whole domain for different rotational speeds

The wider the back-sidewall gap, the more space provided for the development of diverse patterns of the vortices. Figure 9.34 compares vectors of velocity in cross-section of the gaps h_2 and h_3 for a few rotational speeds. It can be noticed, that for h_2 is the whole gap width filled with vortical structures extending from rotor to stator and those sides interact and influence each other through the flow. On the other hand, in the wider gap h_3 there are structures near the stator, which evolves nearly separately from what is happening on the rotor side. See for example 80 rpm, for which almost horizontal flow direction appears along the rotor and wavy curved trajectories prevail on the stator without much intervention into each other. For higher rotational speeds the influence of each side propagates towards the other, however, the separate character is still apparent. Also, the diffusion in the radial direction (to the center of the cavity) is limited in the case of the wider gap h_3, which can be indicated by lower overall velocity magnitude in the central region compared to the gap h_2.

Considering the impact of the gap width on disk friction, no significant differences can be identified. The wall shear stress rises with increasing rotational speed, however, the character of its increase, regions of its maximums are the same for both, the rotor and the stator side, regardless of the gap width. It is in agreement with experimental data, that do not show any difference in the measured torque for different gap configurations.

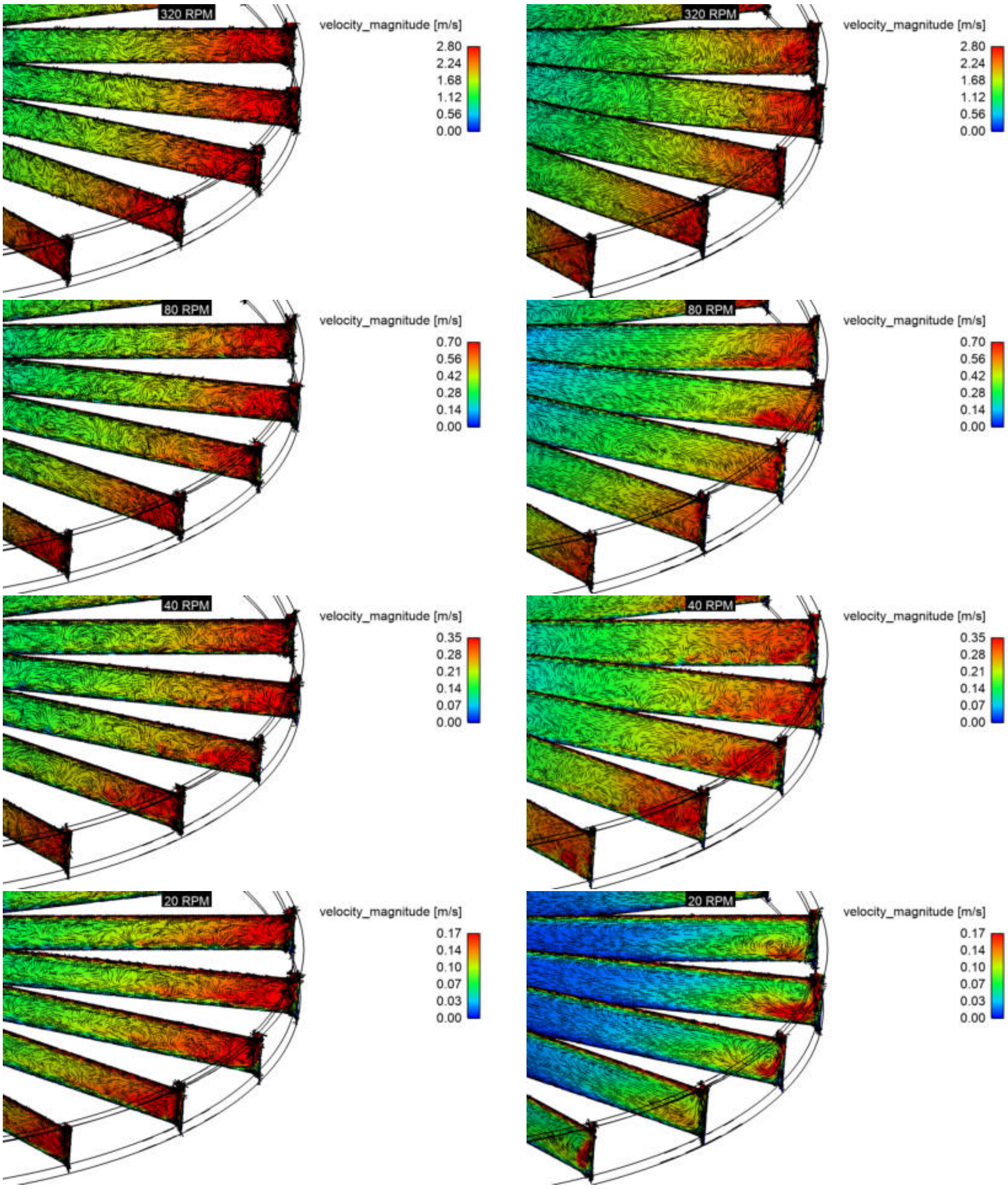

Figure 9.34. Velocity field in the cross section for different rotational speeds and gaps h_2 (left), h_3 (right)

9.3 Flow field in back-sidewall gap with throughflow

Since the intention of the research was to study the flow related to real operating conditions of the pump, it implies low flow rates for the low rotational speed, as was described in detail in see subsection 6.4.4. Although for the CFD simulations the case with a fully opened control valve was chosen, therefore the highest achievable values without using an external pump, it was not sufficient to influence the flow field in the whole pump significantly. The changes in the flow in the back-sidewall gap compared to the same gap configuration without the throughflow were almost indistinguishable up to 80 rpm. It can be demonstrated on an example on Figure 9.35. The flow field looks the same on the rotor side as well as on the stator side.

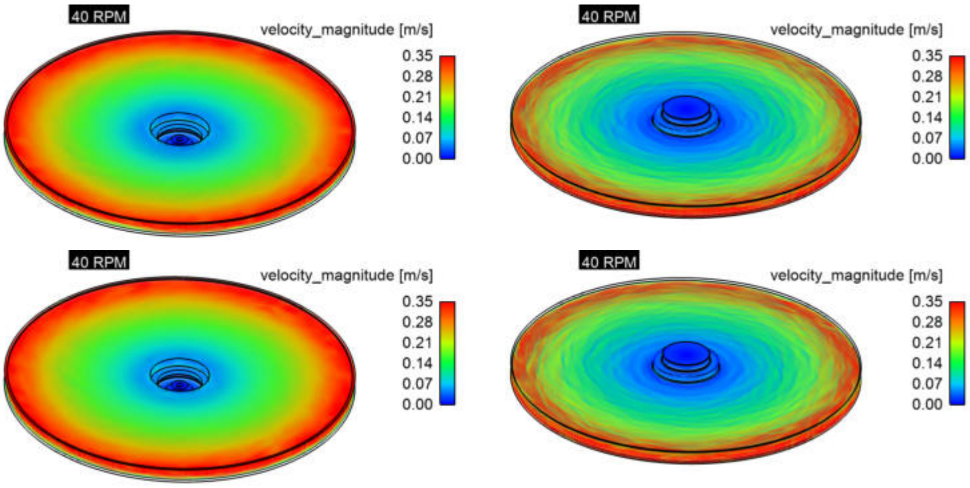

Figure 9.35. Structures near rotor and stator for closed cavity (top) and with presence of throughflow (bottom)

When exploring the cross-section of the cavity, no significant differences can be seen neither on vorticity nor on the q-criterion, see Figure 9.36. It can be also noted, that no asymmetry caused by the presence of the outflow is visible. The axisymmetric pattern of the flow field is not corrupted on the location of the outflow, only the regular distortion caused by the blades of the impeller can be distinguished on the wall shear on the rotor side. The stator side is equally covered by turbulent vortices for both cases, regardless of the throughflow as shows Figure 9.37.

The first notable influence of the flow field in the back-sidewall gap can be seen as the rotational speed increases from 40 rpm to 80 rpm. The stator region is occupied by the instabilities equally, however, spiral vortices on the rotor appear earlier, when the throughflow is present. For the closed cavity, no indications of instability can be seen for 80 rpm, while for the case with throughflow the spiral structures are clear, see Figure 9.38. Its earlier onset is possible to identify by the contours of shear stress as displays Figure 9.39. Nevertheless, the area of the higher shear is almost the same for both cases and thus the different characters do not manifest themselves as a change in the torque.

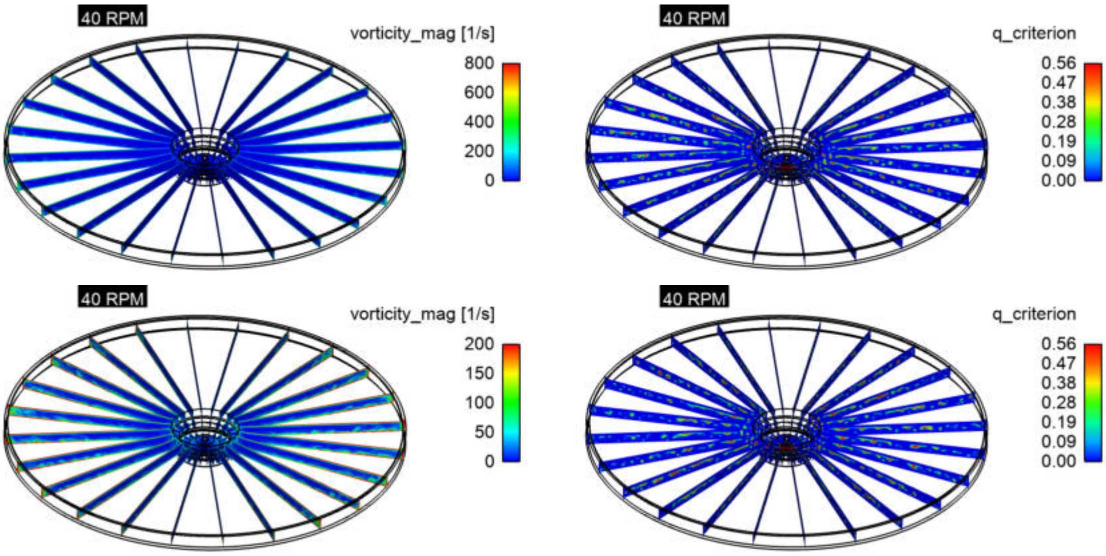

Figure 9.36. Vorticity magnitude and q-criterion for closed cavity (top) and with presence of throughflow (bottom)

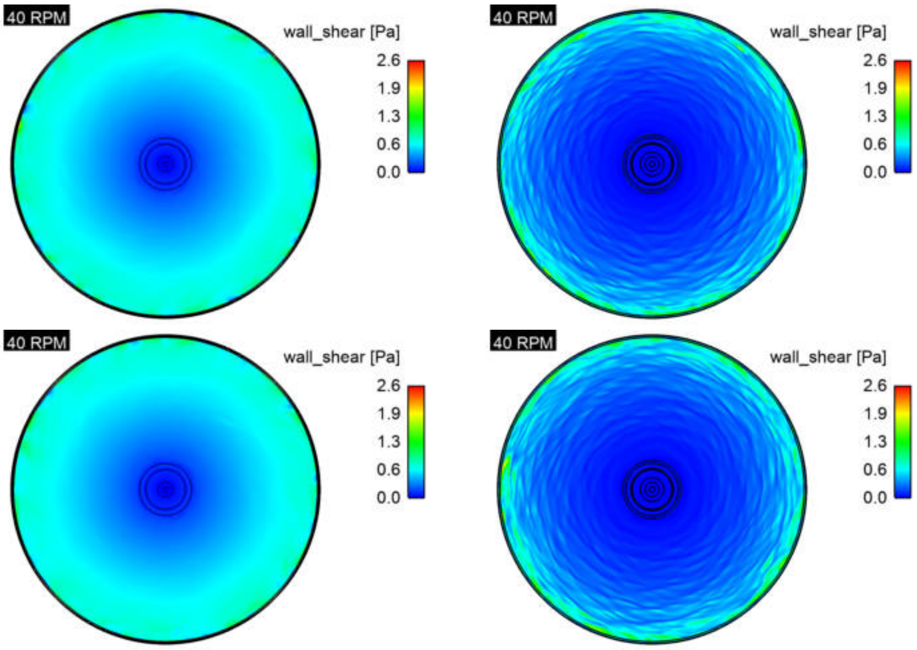

Figure 9.37. Wall shear on the rotor and stator side for closed cavity (top) and with presence of throughflow (bottom)

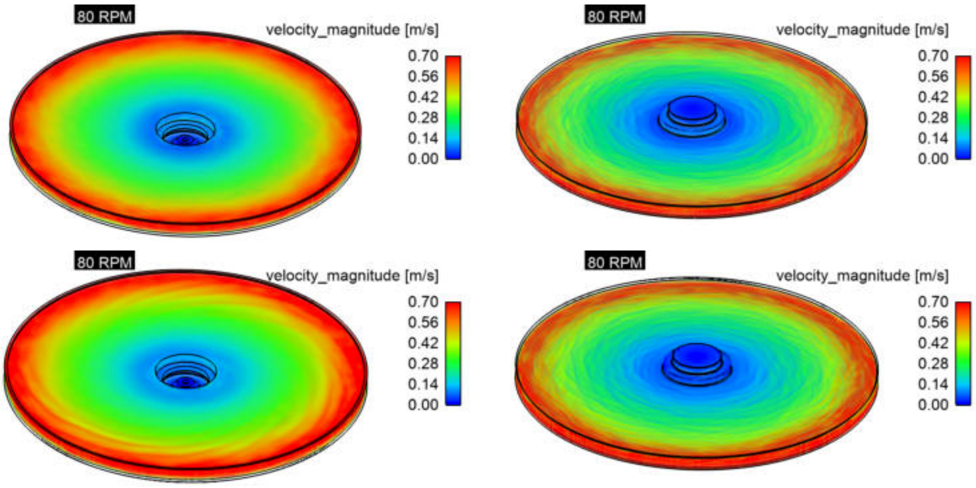

Figure 9.38. Structures near rotor and stator for closed cavity (top) and with presence of throughflow (bottom)

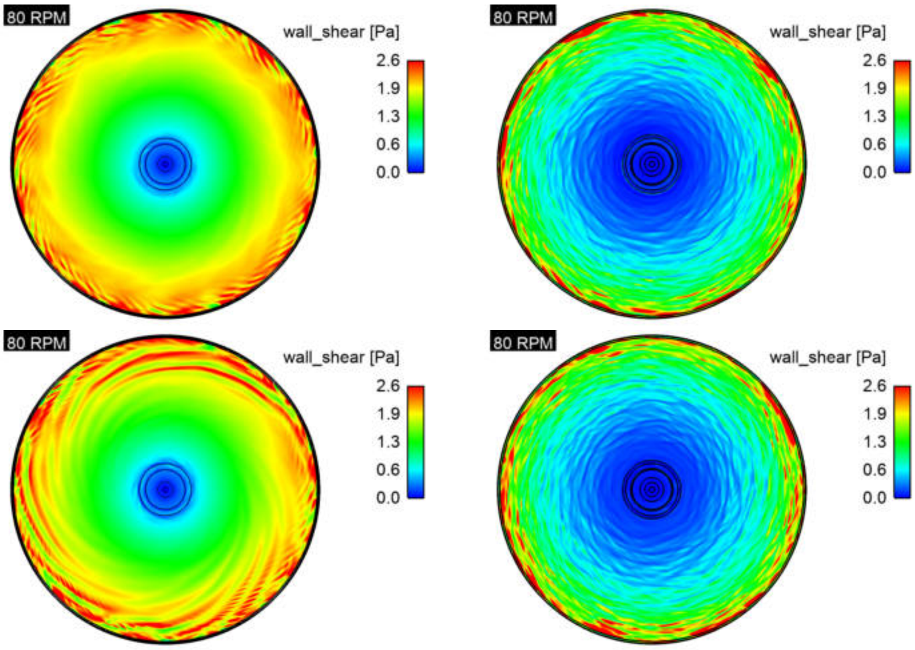

Figure 9.39. Wall shear on the rotor and stator side for closed cavity (top) and with presence of throughflow (bottom)

The increasing effect of the throughflow on the overall flow field can be also seen in Figure 9.40. For 40 rpm, barely any change compared to the closed case can be seen. For 80 rpm the outlet velocity is apparently higher and the flow conditions from volute propagate more to the outflow. This trend is more pronounced with increasing rotational speed. For low rotational speeds, the circumferential (tangential) component of velocity which drives the fluid in the direction of the volute strongly dominates. Its magnitude is orders of magnitude higher than the radial component which has the outflow direction (see an example of 10 rpm in Figure 9.41). The difference gradually decreases with the increase of the rotational speed and flow rate, as illustrates plots for 80 and 320 rpm in Figure 9.41. Nevertheless, even for 320 rpm it is still not strong enough to create flow conditions which would be a source of asymmetry in the back-sidewall gap. Such behavior is expected, however, it does not appear in the analyzed range of rotational speeds.

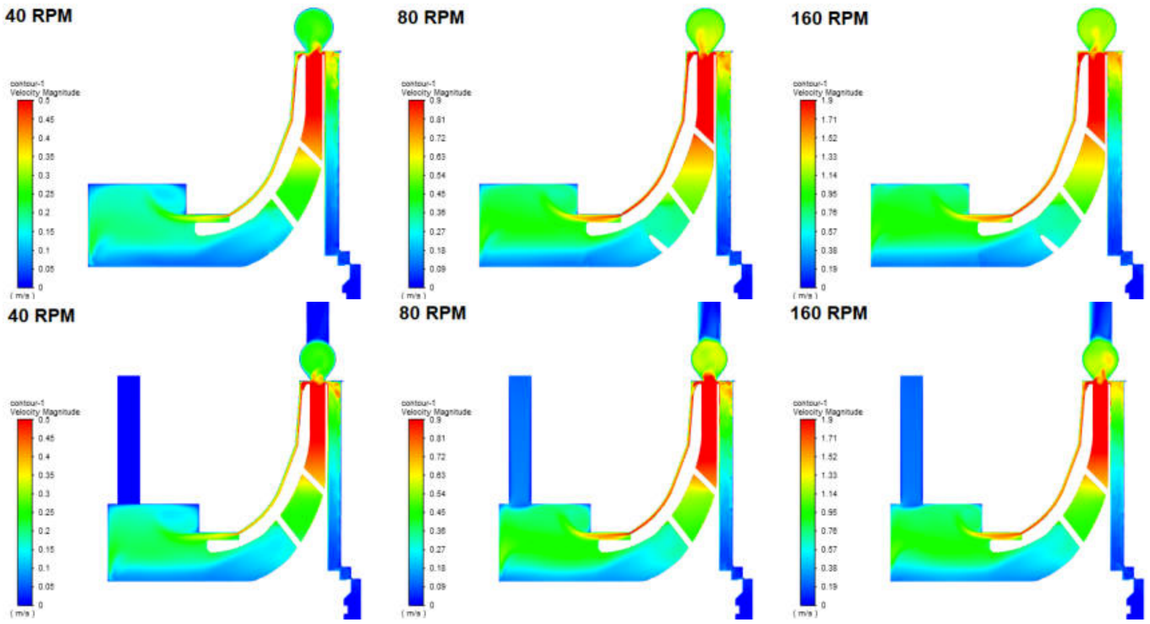

Figure 9.40. Overall flow field for closed cavity (top) and with presence of throughflow (bottom)

Any significant differences in the evolution of the flow field except for the earlier appearance of the instability on the rotor side were not found. The vorticity, as well as the q-criterion shows the same patterns, and also the contours of wall shear, do not display distinctions between cases with and without throughflow. For more details, see plots in Appendix.

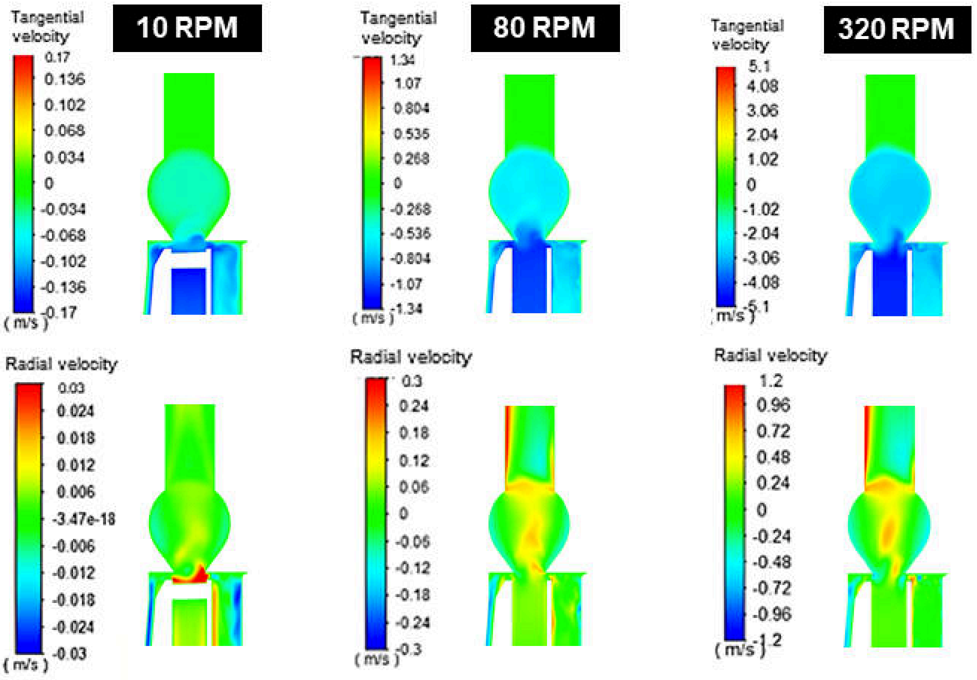

Figure 9.41. Components of velocity at the outlet part for different rotational speeds

The comparison of velocity profiles for the case with and without throughflow confirmed the earlier transition to the turbulent regime. For low rotational speeds, the profiles are almost identical, as can be seen on Figure 9.42 left. Whereas Figure 9.42 right shows that for the case without throughflow (blue curves), the profile for 20 rpm still has obviously merged boundary layers on the contrary to the case with throughflow (red curves), where the constant core velocity and separated boundary layers can be distinguished.

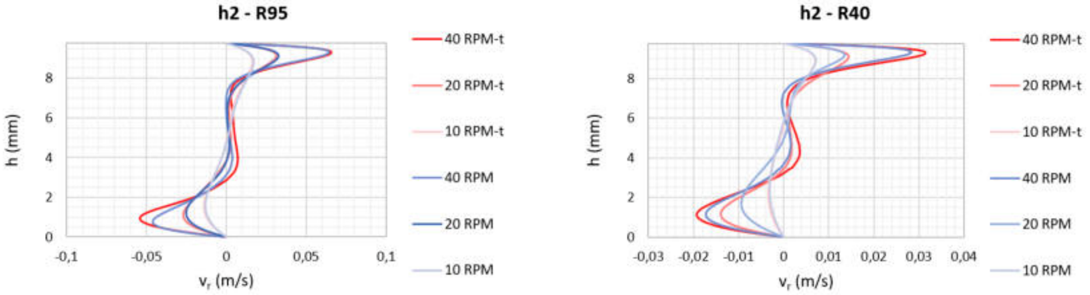

Figure 9.42. Comparison of radial velocity profiles for low rotational speeds for closed cavity (blue) and with presence of throughflow (red)

For higher rotational speeds the discrepancies in the shapes of radial velocity profiles increases, the curves for the case with throughflow do not have such a smooth shapes, which is a result of destabilizing effect of the imposed throughflow. It can be demonstrated in Figure 9.43 left.

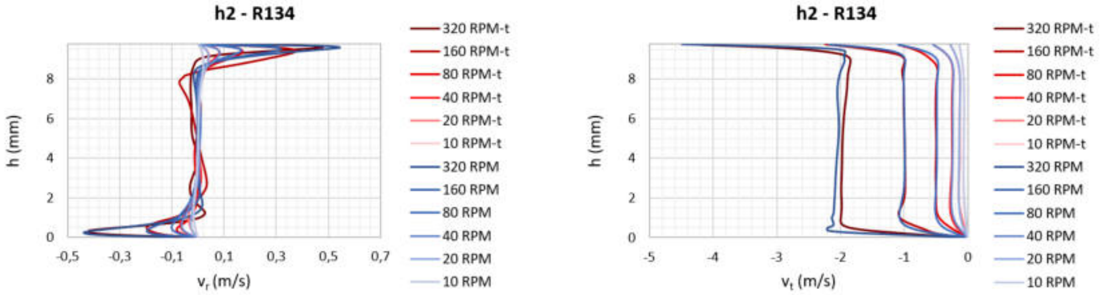

Figure 9.43. Comparison of tangential velocity profiles for all rotational speeds for closed cavity (blue) and with presence of throughflow (red)

The tangential velocity profiles revealed that the tangential component is slightly higher for the cases with throughflow and lower rotational speeds. It applies to all locations and speeds up to 40 rpm. The differences tend to fade away with a radial location closer to the outer boundary, i.e. the biggest discrepancy can be seen for $R = 40$ mm, and with increasing R the profiles almost merge, as shows Figure 9.44. The trend is exactly the opposite for higher rotational speeds, where the tangential rotational speed is a little higher for closed cavities, see Figure 9.43 right.

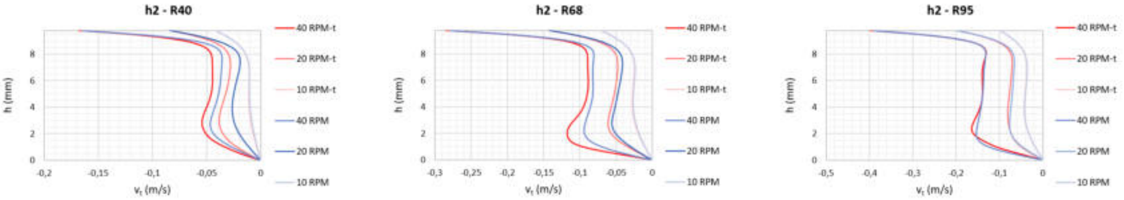

Figure 9.44. Comparison of tangential velocity profiles for low rotational speeds for closed cavity (blue) and with presence of throughflow (red)

The only parameter among the observed, that is significantly affected by the presence of throughflow, is the axial thrust. It is given by completely different pressure ratios inside the whole system after connecting it to the test circuit. The pressure acting on the hub and the shroud of the impeller is very different compared to the case of the closed cavity. The pressure distribution on the shroud (front-sidewall gap) is qualitatively similar for both cases and all analyzed rotational speeds, as shows Figure 9.45. However, its value is an order of magnitude higher with throughflow.

Though, the resulting axial thrust is given by the pressure in both front- and back-sidewall gaps. The evolution of the pressure distribution on the hub (i.e. in the back-sidewall gap) is not so straightforward. It evolves with the rotational speed, there is an observable qualitative difference between the closed cavity and the case with the throughflow, moreover, the disparity varies over rotational speed. It results in lower, but more complicated character of resulting axial thrust as was discovered by the measurements.

For the complete overview of CFD results for all considered back-sidewall gap widths and flow rates, see Appendix.

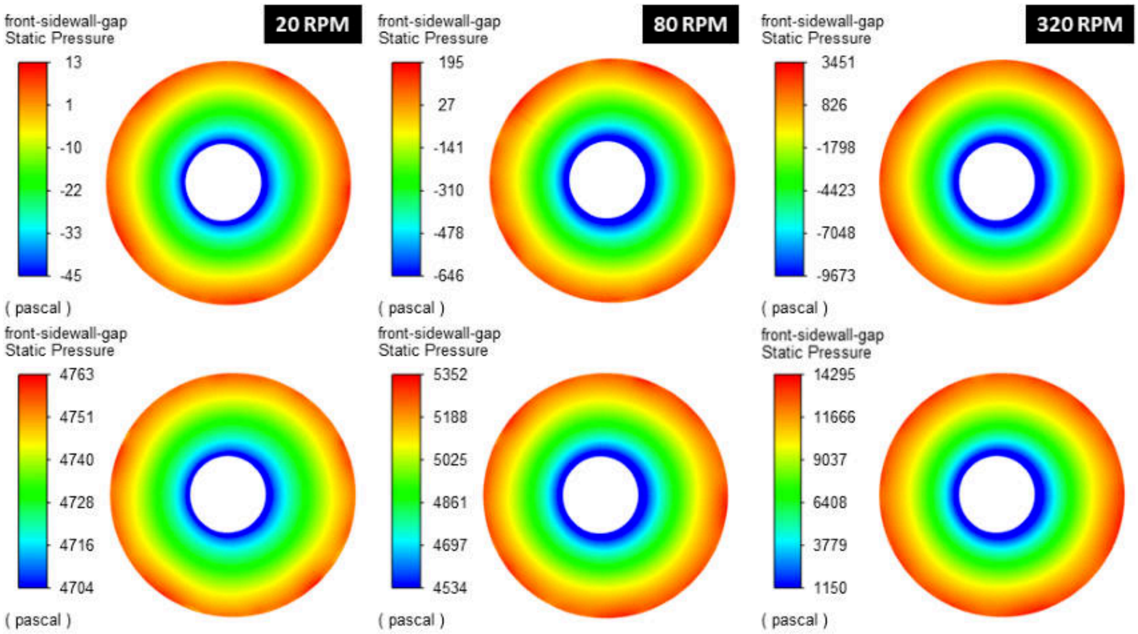

Figure 9.45. Pressure distribution on the shroud for closed cavity (top) and with presence of throughflow (bottom)

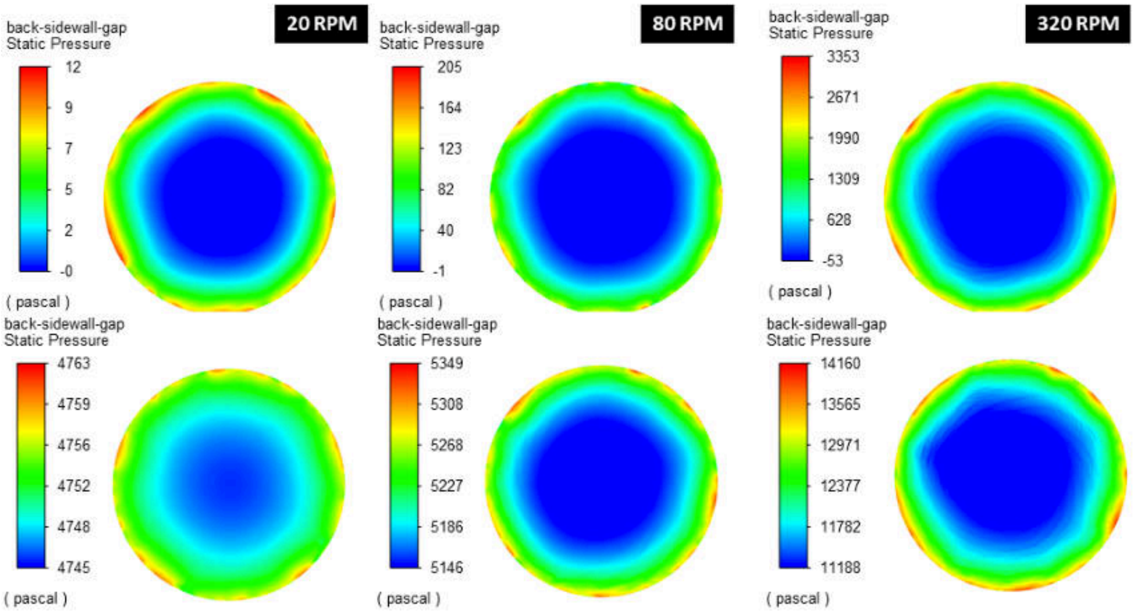

Figure 9.46. Pressure distribution on the hub for closed cavity (top) and with presence of throughflow (bottom)

Conclusion

The main objective of the thesis was to investigate the flow inside back-sidewall gaps of the hydraulic machines under various flow conditions and study its impact on associated phenomena (disk friction and axial thrust). The topic has been covered both, experimentally and by CFD.

For the purpose of the research, an experimental apparatus including not oversimplified inner geometry of the gap and a real impeller has been designed and built. It allows observing the flow in the back-sidewall gap by means of optical methods, such as Laser Doppler Anemometry or Particle Image Velocimetry. Moreover, torque and axial thrust can be recorded.

Since there was a need to establish a reliable numerical methodology for the investigation of the flow in those rotating cavities, a CFD study on the abilities of various turbulence models to describe the flow in a narrow gap between rotating and stationary disks has been performed. The aim was to explore and compare their capabilities to describe the velocity profile precisely and to capture the instabilities emerging in rotor-stator cavities. The results were published in [142].

It was found out, that simpler and less computationally demanding RANS models can provide a reasonable solution for base flow, however, they are not able to capture instabilities in boundary layers. Even the low-Reynolds approach and hybrid models (DES, SAS) were not able to resolve the boundary layers correctly. It led to the conclusion, that LES is an inevitable level of modeling for such type of flow. Reduction of computational demands by using different (less demanding) turbulence models resulted in a significant reduction of accuracy and the loss of important information about instabilities.

CFD simulation of the real radial pump with special emphasis on the flow inside impeller sidewall gaps was performed to verify the approach in practice. LES approach could not be applied to the whole pump domain due to its extreme demands on computational resources. In order to obtain accurate results in a reasonable time, an embedded LES approach combining Large Eddy Simulation in the sidewall gaps and the RANS model in the rest of the fluid was used. It was compared with measurements that were done on the modeled pump and the results were published in [143].

Those preliminary studies aroused a suspicion that the flow in side-wall gaps of hydraulic machines is much more complex than the often presented model obtained for a simplified case of a plain disk rotating in a cylindrical cavity and is worth further research.

The CFD part of the thesis revealed that the simplified theory derived for the rotating disk in a cylindrical cavity and the map of its flow regimes obtained before is not applicable. The flow field is strongly influenced by the presence of an impeller with a certain number of blades, which governs the flow in the back-sidewall gap. Periodical phenomena directly linked to the positions of the blades were detected and the rotation of the impeller is a crucial factor for the development of the flow in the back-sidewall cavity. The number of spiral structures emerging at higher rotational speeds is a whole number multiple of the number of the blades. It is created as a result of variation in direction of the flow into and outside of the back-sidewall gap along with the circumferential position. The numerical simulations unveiled also quite a more complex evolution with increasing rotational speed in comparison to the simplified case of the plain disk in a cylindrical cavity.

Another factor that significantly influences the character of the flow is the width of the back-sidewall gap. It was found out, that the wider the gap, the more space for the evolution of various vortices and the greater variability of emerging structures. For the middle gap width, the whole cross-section is filled with vortical structures (extending from the rotor to the stator). When the gap is wider, the flow is to some extent separate in the rotor and the stator regions. Also, the propagation of vortices in the radial direction (towards the center of the cavity) is limited in the wider gap. On the other hand, in the narrower gap, the formation of vortices is suppressed at the inlet, and therefore the flow is more stable up to higher rotational speeds.

Such a complexity of the flow in the back-sidewall gap results also in the shift of the map of the regimes. Three regimes were observed (I - laminar with merged boundary layers, III - turbulent with merged boundary layers, and VI - turbulent with separate boundary layers). The transitions between them were described and an alternative map for turbomachinery applications has been created. For the studied range of rotational speeds and gap widths, the laminar regime with separate boundary layers was not achieved. For its detection, another even wider gap would need to be analyzed.

The study of the influence of the throughflow revealed that it does not change the state of the flow in the back-sidewall gap significantly when considering given rotational speeds and resulting flow rates. The throughflow is not strong enough to create neither the asymmetry of the flow field nor transform the existing flow structures. The destabilizing effect of the throughflow was observed only as a slightly earlier transition from regime III to IV.

Although the transitions between regimes I - III, III - IV and countless changes of flow character were achieved experimentally and in CFD cases, no manifestation of those phenomena are distinguishable on the torque or axial thrust. The recorded data are smooth curves without abrupt changes. A potentially dangerous operating condition in which the direction of the axial thrust changes does not occur in this range and therefore is not associated with the transition between flow regimes.

In the studied range, the torque increases with increasing rotational speed, independently of the gap width. The measurements are supported by the CFD results, where is no significant difference in the contours of wall shear stress among the geometrical configurations. The character of its increase with rotational speed as well as the regions of its maximums is the same for both, the rotor and the stator side for all studied gap widths. Moreover, the presence of the throughflow (in the studied range) also does not make any difference in the torque.

Axial thrust also increases with increasing rotational speed, steeper compared to the torque, approximately quadratically. Its relation to the gap width is not so clear and more investigation would be necessary. The experimental data obtained for h_1–h_4 suggest that with increasing gap width the measured axial thrust tends to increase up to a certain value. Further increase of the gap width results in the decrease of axial thrust. This was not in agreement with CFD, which shows a simple increasing trend of axial thrust with increasing gap width. Nevertheless, due to time constraints, only h_1–h_3 were considered in numerical simulations. It is possible, that for a wider gap the trend would change, however, the uncertainty of the measurement could be the explanation as well. No conclusion can be drawn definitely, more measurements and simulations for more geometries should be performed. On the other hand, what can be observed without any doubt, is, that the existence of the throughflow influences the axial thrust significantly. In the observed range of rotational speed, even the presence of a low flow rate results in a decrease in axial thrust. The reason is the complete change of the pressure conditions after connecting the testing rig to the circuit. The resulting axial thrust is governed by the difference of the pressure acting on the hub and the shroud. Since the pressure distribution on the shroud (front-sidewall gap) is qualitatively similar for the case of the closed cavity for all analyzed rotational speeds, the cause of the behavior is the pressure distribution on the hub (back-sidewall gap). There is an observable qualitative difference between the closed cavity and the case with the throughflow, moreover, the variation changes with the rotational speed. It results in lower, but more complicated character of resulting axial thrust for different combinations of rotational speeds and flow rates as was discovered by the measurements. No clear assumption can be made for the trend outside the investigated range.

Although some of the questions on the flow inside the sidewall gaps of hydraulic machines were answered, some new ones emerged. The outcomes from the thesis provide a better idea of how the flow field in the back-sidewall gaps is formed, however it reveals also many related topics for future studies. Any of those directions could be a good topic for further research:

- Clarification of the dependency of the axial thrust on the back-sidewall gap width (covering a wider range of widths).
- Extension of the studied range of rotational speeds towards the higher values, which comes along with higher flow rates.
- Including real shape of volute (with cutwater) which probably brings into the flow field some asymmetrical behavior and possible source of more unstable structures.
- Investigation of the flow in the back-sidewall gap when some features for balancing of the axial thrust (such as back vanes or balancing holes in the hub) are present.

Bibliography

[1] V. Ekman, *On the Influence of the Earth's Rotation on Ocean-currents.* Arkiv for Matematik, Astronomi och Fysik, 1905.

[2] T. V. Kármán, "Über laminare und turbulente reibung," *ZAMM - Journal of Applied Mathematics and Mechanics / Zeitschrift für Angewandte Mathematik und Mechanik*, vol. 1, no. 4, pp. 233–252, 1921.

[3] U. T. Bödewadt, "Die drehströmung über festem grunde," *ZAMM - Journal of Applied Mathematics and Mechanics / Zeitschrift für Angewandte Mathematik und Mechanik*, vol. 20, no. 5, pp. 241–253, 1940.

[4] G. K. Batchelor, "Note on a class of solutions of the navier-stokes equations representing steady rotationally-symmetric flow," *The quarterly journal of mechanics and applied mathematics*, vol. 4, no. 1, pp. 29–41, 1951.

[5] K. Stewartson, "On the flow between two rotating coaxial disks," *Mathematical Proceedings of the Cambridge Philosophical Society*, vol. 49, no. 2, p. 333–341, 1953.

[6] W. G. Cochran, "The flow due to a rotating disc," *Mathematical Proceedings of the Cambridge Philosophical Society*, vol. 30, no. 3, p. 365–375, 1934.

[7] E. M. Sparrow and J. Gregg, "Mass transfer, flow, and heat transfer about a rotating disk," *Journal of Heat Transfer*, vol. 82, no. 4, p. 294–302, 1960.

[8] E. C. del Arco, E. Serre, P. Bontoux, and B. Launder, "Stability, transition and turbulence in rotating cavities," in *Instability of Flows*, pp. 141–195, WIT Press, jan 2005.

[9] H. Schlichting and K. Gersten, *Boundary-Layer Theory.* Springer Berlin Heidelberg, 2017.

[10] A. J. Faller, "Instability and transition of disturbed flow over a rotating disk," *Journal of Fluid Mechanics*, vol. 230, p. 245, sep 1991.

[11] N. H. Smith, "Exploratory investigation of laminar-boundary-layer oscillations on a rotating disk," tech. rep., National Advisory Commitee for Aeronautics, 1947.

[12] Y. Kohama, "Study on boundary layer transition of a rotating disk," *Acta Mechanica*, vol. 50, pp. 193–199, sep 1984.

[13] A. J. Faller and R. E. Kaylor, “Investigations of Stability and Transition in Rotating Boundary Layers,” in *Dynamics of Fluids and Plasmas* (S. I. Pai, A. J. Faller, T. L. Lincoln, D. A. Tidman, G. N. Trytton, and T. D. Wilkerson, eds.), p. 309, 1966.

[14] O. Savaş, “Circular waves on a stationary disk in rotating flow,” *Physics of Fluids*, vol. 26, no. 12, p. 3445, 1983.

[15] J. P. Vanyo, *Rotating Fluids in Engineering and Science.* Butterworth-Heinemann, 2015.

[16] D. K. Lilly, “On the instability of ekman boundary flow,” *Journal of the Atmospheric Sciences*, vol. 23, no. 5, pp. 481–494, 1966.

[17] P. R. Tatro and E. L. Mollo-Christensen, “Experiments on ekman layer instability,” *Journal of Fluid Mechanics*, vol. 28, p. 531, may 1967.

[18] W. M. Stuart and S. Biringen, “On the spatial instability modes of the laminar ekman boundary layer,” *Journal of the Atmospheric Sciences*, vol. 51, pp. 3539–3542, dec 1994.

[19] J. F. Brady and L. Durlofsky, “On rotating disk flow,” *Journal of Fluid Mechanics*, vol. 175, p. 363, feb 1987.

[20] J. W. Daily and R. E. Nece, “Chamber dimension effects on induced flow and frictional resistance of enclosed rotating disks,” *Journal of Basic Engineering*, vol. 82, no. 1, p. 217, 1960.

[21] B. Sultanian, *Internal Flow around Rotors and Stators*, p. 182–236. Cambridge Aerospace Series, Cambridge University Press, 2018.

[22] B. Hu, D. Brillert, H. Dohmen, and F.-K. Benra, “Investigation on the flow in a rotor-stator cavity with centripetal through-flow,” *International Journal of Turbomachinery, Propulsion and Power*, vol. 2, p. 18, oct 2017.

[23] B.-C. Will, *Theoretical, Numerical and Experimental Investigation of theFlow in Rotor-Stator Cavities with Application to a Centrifugal Pump.* PhD thesis, Universität Duisburg-Essen, 2011.

[24] M. M. de Beer, *Hydrodynamics and Heat Transfer of Single and Multiphase Flows in Rotor-Stator Spinning Disc Reactors.* PhD thesis, Department of Chemical Engineering and Chemistry, 2016.

[25] B. Launder, S. Poncet, and E. Serre, “Laminar, transitional, and turbulent flows in rotor-stator cavities,” *Annual Review of Fluid Mechanics*, vol. 42, pp. 229–248, jan 2010.

[26] S. C. Cheah, H. Iacovides, D. C. Jackson, H. Ji, and B. E. Launder, "Experimental investigation of enclosed rotor-stator disk flows," *Experimental Thermal and Fluid Science*, vol. 9, pp. 445–455, nov 1994.

[27] G. Gauthier, P. Gondret, and M. Rabaud, "Axisymmetric propagating vortices in the flow between a stationary and a rotating disk enclosed by a cylinder," *Journal of Fluid Mechanics*, vol. 386, pp. 105–126, may 1999.

[28] B.-C. Will, F.-K. Benra, and H.-J. Dohmen, "Investigation of the flow in the impeller side clearances of a centrifugal pump with volute casing," *Journal of Thermal Science*, vol. 21, 06 2012.

[29] W. Li, "Model of flow in the side chambers of an industrial centrifugal pump for delivering viscous oil," *Journal of Fluids Engineering*, vol. 135, p. 051201, 05 2013.

[30] P. San'kov and E. M. Smirnov, "Bifurcation and transition to turbulence in the gap between rotating and stationary parallel disks," *Fluid Dynamics*, vol. 19, no. 5, pp. 695–703, 1984.

[31] L. Schouveiler, P. L. Gal, and M. P. Chauve, "Instabilities of the flow between a rotating and a stationary disk," *Journal of Fluid Mechanics*, vol. 443, sep 2001.

[32] A. Cros and P. L. Gal, "Spatiotemporal intermittency in the torsional couette flow between a rotating and a stationary disk," *Physics of Fluids*, vol. 14, pp. 3755–3765, nov 2002.

[33] A. Cros, R. Ali, P. L. Gal, P. J. Thomas, L. Schouveiler, P. W. Carpenter, and M.-P. Chauve, "Effects of wall compliance on the laminar–turbulent transition of torsional couette flow," *Journal of Fluid Mechanics*, vol. 481, pp. 177–186, apr 2003.

[34] L. Schouveiler, P. L. Gal, M.-P. Chauve, and Y. Takeda, "Spiral and circular waves in the flow between a rotating and a stationary disk," *Experiments in Fluids*, vol. 26, pp. 179–187, feb 1999.

[35] R. Hide, "On source-sink flows in a rotating fluid," *Journal of Fluid Mechanics*, vol. 32, pp. 737 – 764, 06 1968.

[36] J. Owen and J. Pincombe, "Velocity measurements inside a rotating cavity with a radial outflow of fluid," *Journal of Fluid Mechanics*, vol. 99, pp. 111 – 127, 07 1980.

[37] E. Crespo del Arco, P. Maubert , A. Randriamampianina , and P. Bontoux, "Spatio—temporal behaviour in a rotating annulus with a source—sink flow," *Journal of Fluid Mechanics*, vol. 328, pp. 271 – 296, 12 1996.

[38] E. Serre, S. Hugues, E. Crespo del Arco, A. Randriamampianina, and P. Bontoux, "Axisymmetric and three-dimensional instabilities in an ekman boundary layer flow," *International Journal of Heat and Fluid Flow*, vol. 22, pp. 82–93, 02 2001.

[39] A. Cros, E. Floriani, P. L. Gal, and R. Lima, "Transition to turbulence of the batchelor flow in a rotor/stator device," *European Journal of Mechanics - B/Fluids*, vol. 24, pp. 409–424, jul 2005.

[40] P. L. Gal, Y. Tasaka, J. Nagao, A. Cros, and K. Yamaguchi, "A statistical study of spots in torsional couette flow," *Journal of Engineering Mathematics*, vol. 57, pp. 289–302, oct 2006.

[41] M. Munekata, N. Jobi, K. Kubo, and H. Yoshikawa, "Characteristics of transient vortices in the boundary layer on a rotating disk under orbital motion," *Journal of Thermal Science*, vol. 22, pp. 600–605, nov 2013.

[42] S. Chyi-Yeou, W. Chang-Chie, L. Tung-Ping, and L. Tao-Ping, "Flow structure between two co-axial disks rotating independently," *Experimental Thermal and Fluid Science*, vol. 27, pp. 295–311, mar 2003.

[43] S. Poncet and M.-P. Chauve, "Crossflow instability in rotor-stator flows with axial inward throughflow," *Journal of Fluid Mechanics*, vol. 545, p. 281, dec 2005.

[44] G. Gauthier, P. Gondret, F. Moisy, and M. Rabaud, "Instabilities in the flow between co- and counter-rotating disks," *Journal of Fluid Mechanics*, vol. 473, dec 2002.

[45] F. Moisy, T. Pasutto, and M. Rabaud, "Instability patterns between counter-rotating disks," *Nonlinear processes in Geophysics*, vol. 10, no. 3, pp. 281–288, 2003.

[46] J. Gülich, *Centrifugal Pumps.* Springer Berlin Heidelberg, 2014.

[47] C. Trivedi and O. Dahlhaug, "Interaction between trailing edge wake and vortex rings in a francis turbine at runaway condition: Compressible large eddy simulation," *Physics of Fluids*, vol. 30, p. 075101, 07 2018.

[48] M. Nechleba, A. G. Evans, and C. Mayer, *Hydraulic Turbines. Their Design and Equipment.* Prague, 1957.

[49] A. Abou El-Azm Aly, A. Hassan, and H. Abdalla, "Study of the effect of impeller side clearance on the centrifugal pump performance using cfd," in *Proceedings of the 15th ASME International Mechanical Engineering Congress & Exposition*, 12 2015.

[50] A. Abou El-Azm Aly, A. Hassan, and H. Abdallah, "Effect of semi-open impeller side clearance on the centrifugal pump performance using cfd," *Aerospace Science and Technology*, vol. 47, pp. 247–255, 12 2015.

[51] J. Yan, Z. Zuo, W. Guo, H. Hou, Z. Xin, and H. Chen, "Influences of wear-ring clearance leakage on performance of a small-scale pump-turbine," *Proceedings of the Institution of Mechanical Engineers, Part A: Journal of Power and Energy*, 07 2019.

[52] C. Trivedi, “A review on fluid structure interaction in hydraulic turbines: A focus on hydrodynamic damping,” *Engineering Failure Analysis*, vol. 77, pp. 1–22, 03 2017.

[53] Z. Sun, C. Tan, and D. Zhang, “Flow field structures of the impeller backside cavity and its influences on the centrifugal compressor,” vol. Volume 7: Turbomachinery, Parts A and B of *Turbo Expo: Power for Land, Sea, and Air*, pp. 1349–1360, 06 2009.

[54] J. Schiffer, H. Benigni, H. Jaberg, T. Schneidhofer, and M. Ehrengruber, “Numerical simulation of the flow in a francis turbine including the runner seals on crown and band side,” in *HYDRO 2015*, 10 2015.

[55] Y. Wu, X. Chen, H.-S. Dou, L. Zheng, Z. Zhu, B. Cui, and B. Khoo, “Numerical simulation and analysis of flow characteristics in the front chamber of a centrifugal pump,” *Journal of Mechanical Science and Technology*, vol. 31, pp. 5131–5140, 11 2017.

[56] D. Zhou, H. Chen, J. Zhang, S. Jiang, J. Gui, C. Yang, and A. YU, “Numerical study on flow characteristics in a francis turbine during load rejection,” *Energies*, vol. 12, p. 716, 02 2019.

[57] D. Čelič and H. Ondráčka, “The influence of disc friction losses and labyrinth losses on efficiency of high head francis turbine,” *Journal of Physics: Conference Series*, vol. 579, 01 2015.

[58] D. Jošt, A. Škerlavaj, M. Morgut, P. Mežnar, and E. Nobile, “Numerical simulation of flow in a high head francis turbine with prediction of efficiency, rotor stator interaction and vortex structures in the draft tube,” *Journal of Physics Conference Series*, vol. 579, p. 012006, 01 2015.

[59] A. J. Peter Mössinger, Jester-Zurker Roland, “Investigation of different simulation approaches on a high-head francis turbine and comparison with model test data: Francis-99,” *Journal of Physics: Conference Series*, vol. 579, 01 2015.

[60] J. Feng, X. Luo, G. Zhu, and G. Wu, “Investigation on disk friction loss and leakage effect on performance in a francis model turbine,” *Advances in Mechanical Engineering*, vol. 9, 08 2017.

[61] E. Casartelli, D. Cimmino, and T. Staubli, “Interaction of leakage flow with the main runner-outflow in a francis turbine,” *Proceedings of the HYDRO 2005, Villach, Austria*, 2005.

[62] E. Casartelli, T. Staubli, M. Sallaberger, and D. Cimmino, “Impact of rotor side space flow on draft tube performance,” *HydroVision 2006*, 05 2006.

[63] X. Su, S. Huang, X. Zhang, and S. Yang, “Numerical research on unsteady flow rate characteristics of pump as turbine,” *Renewable Energy*, vol. 94, pp. 488 – 495, 2016.

[64] S. Gautam, H. Neopane, N. Acharya, S. Chitrakar, B. Thapa, and B. Zhu, “Sediment erosion in low specific speed francis turbines: A case study on effects and causes,” *Wear*, p. 203152, 12 2019.

[65] D. L. Rhode, J. A. Demko, U. K. Traegner, G. L. Morrison, and S. R. Sobolik, “Prediction of Incompressible Flow in Labyrinth Seals,” *Journal of Fluids Engineering*, vol. 108, pp. 19–25, 03 1986.

[66] D. L. Rhode, J. W. Johnson, and D. H. Broussard, “Flow Visualization and Leakage Measurements of Stepped Labyrinth Seals: Part 1—Annular Groove,” *Journal of Turbomachinery*, vol. 119, pp. 839–843, 10 1997.

[67] W. Wang, Y. Liu, P.-N. Jiang, and H. Chen, “Numerical analysis of leakage flow through two labyrinth seal,” *Journal of Hydrodynamics - J HYDRODYN*, vol. 19, pp. 107–112, 02 2007.

[68] J. Younger, “Flow visualization and leakage measurements of stepped labyrinth seals: Part 2—sloping surfaces,” *Journal of Turbomachinery*, vol. 119, p. 844, 10 2008.

[69] R. Bouderlique, F. Guibault, A. Garon, and T. Vu, “A computational model for hydraulic labyrinth seals,” in *Proceedings of the ASME 2010 3rd Joint US-European Fluids Engineering Summer Meeting collocated with 8th International Conference on Nanochannels, Microchannels, and Minichannels.*, 01 2010.

[70] W. Wang, S. Su, and Y. Yan, “Study on comb labyrinth seals of francis turbine at different reynolds number,” *Applied Mechanics and Materials*, vol. 0, pp. 423–426, 10 2013.

[71] X. Li, J. Yang, and W. Xu, “Research and comparison on the leakage and fluid force between the axial and the radial labyrinth seal,” *Journal of Mechanical Science and Technology*, vol. 29, no. 11, pp. 4611–4620, 2015.

[72] J. M. Lopez, “Characteristics of endwall and sidewall boundary layers in a rotating cylinder with a differentially rotating endwall,” *Journal of Fluid Mechanics*, vol. 359, pp. 49–79, mar 1998.

[73] E. Serre, E. Tuliszka-Sznitko, and P. Bontoux, “Coupled numerical and theoretical study of the flow transition between a rotating and a stationary disk,” *Physics of Fluids*, vol. 16, pp. 688–706, mar 2004.

[74] Y. Zhiyin, “Large-eddy simulation: Past, present and the future,” *Chinese Journal of Aeronautics*, vol. 28, pp. 11–24, feb 2015.

[75] K. Abe, “A hybrid LES/RANS approach using an anisotropy-resolving algebraic turbulence model,” *International Journal of Heat and Fluid Flow*, vol. 26, pp. 204–222, apr 2005.

[76] C. G. Speziale, “Analytical methods for the development of reynolds-stress closures in turbulence,” *Annual Review of Fluid Mechanics*, vol. 23, pp. 107–157, jan 1991.

[77] R. Avva, C. Smith, and A. Singhal, “Comparative study of high and low reynolds number versions of k-epsilon models,” in *28th Aerospace Sciences Meeting*, American Institute of Aeronautics and Astronautics, jan 1990.

[78] D. Wilcox, “A half century historical review of the k-omega model,” in *29th Aerospace Sciences Meeting*, American Institute of Aeronautics and Astronautics, jan 1991.

[79] F. R. Menter, “Two-equation eddy-viscosity turbulence models for engineering applications,” *AIAA Journal*, vol. 32, pp. 1598–1605, aug 1994.

[80] P. R. Spalart, “Detached-eddy simulation,” *Annual Review of Fluid Mechanics*, vol. 41, pp. 181–202, jan 2009.

[81] P. R. Spalart, *Young-Person’s Guide to Detached-eddy Simulation Grids.* NASA contractor report, National Aeronautics and Space Administration, 2001.

[82] F. R. Menter and Y. Egorov, “The scale-adaptive simulation method for unsteady turbulent flow predictions. part 1: Theory and model description,” *Flow, Turbulence and Combustion*, vol. 85, pp. 113–138, Jul 2010.

[83] J. W. Chew, “Prediction of flow in rotating DISC systems using the k-ϵ turbulence model,” in *Volume 4: Heat Transfer; Electric Power*, ASME, jun 1984.

[84] J. W. Chew and C. M. Vaughan, “Numerical predictions for the flow induced by an enclosed rotating disc,” in *Volume 1: Turbomachinery*, ASME, jun 1988.

[85] L. Elena and R. Schiestel, “Turbulence modeling of rotating confined flows,” *International Journal of Heat and Fluid Flow*, vol. 17, pp. 283–289, jun 1996.

[86] S. Poncet, M.-P. Chauve, and R.Schiestel, “Batchelor versus stewartson flow structures in a rotor-stator cavity with throughflow,” *Physics of Fluids*, vol. 17, p. 075110, jul 2005.

[87] S. Haddadi and S. Poncet, “Turbulence modeling of torsional couette flows,” *International Journal of Rotating Machinery*, vol. 2008, pp. 1–27, 2008.

[88] S. Poncet, R. D. Soghe, and B. Facchini, “Rans modeling of flow in rotating cavity system,” in *V European Conference on Computational Fluid Dynamics (ECCOMAS CFD 2010)*, (Lisbonne, Portugal), June 2010.

[89] D. C. Wilcox, “Formulation of the k-w turbulence model revisited,” *AIAA Journal*, vol. 46, pp. 2823–2838, nov 2008.

[90] R. D. Soghe, L. Innocenti, A. Andreini, and S. Poncet, “Numerical benchmark of turbulence modeling in gas turbine rotor-stator system,” in *Volume 7: Turbomachinery, Parts A, B, and C*, ASME, 2010.

[91] R. Jacques, P. L. Quéré, and O. Daube, “Axisymmetric numerical simulations of turbulent flow in rotor stator enclosures,” *International Journal of Heat and Fluid Flow*, vol. 23, no. 4, pp. 381 – 397, 2002.

[92] E. Serre, E. C. D. Arco, and P. Bontoux, “Annular and spiral patterns in flows between rotating and stationary discs,” *Journal of Fluid Mechanics*, vol. 434, may 2001.

[93] E. Tuliska-Sznitko, E. Serre, and P. Bontoux, “On the nature of the boundary layers instabilities in a flow between a rotating and a stationary disc,” *Comptes Rendus Mécanique*, vol. 330, pp. 91–99, jan 2002.

[94] W. Lo, C. W. Chen, and C.-A. Lin, “Large eddy simulation of enclosed rotor-stator flow,” in *TSFP DIGITAL LIBRARY ONLINE*, Begel House Inc., 2003.

[95] R. Pasquetti, E. Séverac, E. Serre, P. Bontoux, and M. Schäfer, “From stratified wakes to rotor–stator flows by an SVV–LES method,” *Theoretical and Computational Fluid Dynamics*, vol. 22, pp. 261–273, nov 2007.

[96] E. Severac and E. Serre, “A spectral vanishing viscosity for the LES of turbulent flows within rotating cavities,” *Journal of Computational Physics*, vol. 226, pp. 1234–1255, oct 2007.

[97] J. Guelich, “Disk friction losses of closed turbomachine impellers,” *Forschung im Ingenieurwesen*, vol. 68, 12 2003.

[98] C. Trivedi, M. Cervantes, and O. Dahlhaug, “Experimental and numerical studies of a high-head francis turbine: A review of the francis-99 test case,” *Energies*, vol. 9, p. 74, 01 2016.

[99] B. Thapa, B. Thapa, and O. Dahlhaug, “Empirical modelling of sediment erosion in francis turbines,” *Energy*, vol. 41, p. 386–391, 05 2012.

[100] R. E. Nece and J. W. Daily, “Roughness Effects on Frictional Resistance of Enclosed Rotating Disks,” *Journal of Basic Engineering*, vol. 82, pp. 553–560, 09 1960.

[101] A. Poullikkas, “Surface roughness effects on induced flow and frictional resistance of enclosed rotating disks,” *Journal of Fluids Engineering*, vol. 117, 09 1995.

[102] J. Daily, V. Asbedian, and W. Ernst, *Enclosed Rotating Disks with Superposed Throughflow: Mean Steady and Periodic Unsteady Characteristics of the Induced Flow*. Hydrodynamics Laboratory, Department of Civil Engineering, Massachusetts Institute of Technology, 1964.

[103] J. M. Owen, "An Approximate Solution for the Flow Between a Rotating and a Stationary Disk," *Journal of Turbomachinery*, vol. 111, pp. 323–332, 07 1989.

[104] B. Hu, D. Brillert, H. Dohmen, and F.-K. Benra, "Investigation on thrust and moment coefficients of a centrifugal turbomachine," *International Journal of Turbomachinery, Propulsion and Power*, vol. 3, p. 9, 04 2018.

[105] M. Daqiqshirazi, R. Torabi, A. Riasi, and A. Nourbakhsh, "Impeller gap width effect on losses in a water pump; numerical study," in *The 23rd Annual International Conference on Mechanical Engineering-ISME2015*, 05 2015.

[106] S. Mikhail, M. G. Khalafallah, and M. El-Nady, "Disk friction loss in centrifugal and mixed flow pumps," in *Proceedings of ICFDP7: Seventh International Congress on Fluid Dynamics and Propulsion*, 2001.

[107] L. Cho, S. Lee, and J. Cho, "Use of cfd analyses to predict disk friction loss of centrifugal compressor impellers," *Japan Society of Aeronautical Space Sciences Transactions*, vol. 55, pp. 150–156, 05 2012.

[108] A. Nemdili, "Development of an empirical equation to predict the disc friction losses of a centrifugal pump," in *The 6th International Conference on Hydraulic Machinery and Hydrodynamics*, (Timisoara, Romania,), 04 2004.

[109] A. Tamm and B. Stoffel, "The influences of gap clearance and surface roughness on leakage loss and disc friction of centrifugal pumps," in *American Society of Mechanical Engineers, Fluids Engineering Division (Publication) FED*, vol. 257, 2002.

[110] H. Fukuda, "The effects of runner surface roughness on the performance of a francis turbine," *Transactions of the Japan Society of Mechanical Engineers*, vol. 29, no. 204, pp. 1284–1293, 1963.

[111] J. F. Gülich, "Effect of Reynolds Number and Surface Roughness on the Efficiency of Centrifugal Pumps ," *Journal of Fluids Engineering*, vol. 125, pp. 670–679, 08 2003.

[112] S. Brodersen, "Reduzierung der scheibenreibung bei strömungsmaschinen," *Forschung im Ingenieurwesen*, vol. 59, no. 9, pp. 184–186, 1993.

[113] J. Kurokawa and T. Toyokura, "Axial thrust, disk friction torque and leakage loss of radial flow turbomachinery," *International Conference on Design and Operation of Pumps and Turbines*, 1976.

[114] P. Maruzewski, V. Hasmatuchi, H. Mombelli, D. Burggraeve, J. Iosfin, P. Finnegan, and F. Avellan, “Surface roughness impact on francis turbine performances and prediction of efficiency step up,” *International Journal of Fluid Machinery and Systems*, vol. 2, 12 2009.

[115] M. Daqiqshirazi, A. Riasi, and A. Nourbakhsh, “Numerical study of flow in side chambers of a centrifugal pump and its effect on disk friction loss,” in *Proceedings of IRF International Conference*, 02 2014.

[116] M. Gančo, “Axiálna sila hydrodynamických čerpadiel s radiálnym obežným kolesom.” Slovenská technická unoverzita v Bratislavě - Strojnická fakulta, 1999. Habilitační práce.

[117] T. T. J. Kurokawa, “Study on axial thrust of radial flow turbomachinery,” in *The Second International JSME Symposium-Fluid Machinery and Fluidics*, 1972.

[118] S. S. Evgen’ev, G. G. Petrosyan, and V. A. Futin, “Calculation of axial gasodynamic forces, disk friction losses and overflow in semiopen impellers of centrifugal compressors,” *Russian Aeronautics (Iz VUZ)*, vol. 52, pp. 319–326, sep 2009.

[119] T. Iino, H. Sato, and H. Miyashiro, “Hydraulic Axial Thrust in Multistage Centrifugal Pumps,” *Journal of Fluids Engineering*, vol. 102, pp. 64–69, 03 1980.

[120] T. Yamashita, S. Watanabe, Y. Hara, H. Watanabe, and K. Miyagawa, “Measurements of axial and radial thrust forces working on a three-stages centrifugal pump rotor,” in *Proceedings of the ASME/JSME/KSME 2015 Joint Fluids Engineering Conference*, vol. Volume 1A: Symposia, Part 2, (Seoul, South Korea), 07 2015. V01AT33A013.

[121] H. Pehlivan and Z. Parlak, “Investigation of parameters affecting axial load in an end suction centrifugal pump by numerical analysis,” *Journal of Applied Fluid Mechanics*, vol. 12, pp. 1615–1627, 09 2019.

[122] M. Gantar, D. Florjancic, and B. Sirok, “Hydraulic axial thrust in multistage pumps—origins and solutions,” *Journal of Fluids Engineering-transactions of The Asme - J FLUID ENG*, vol. 124, 06 2002.

[123] J. Kurokawa, M. Inagaki, H. Imamura, T. Taguchi, and K. Niikura, “Transient axial thrust of high-head pump-turbine at load rejection,” *The proceedings of the JSME annual meeting*, vol. 2002.3, 09 2002.

[124] X.-Y. Ji, X.-B. Li, W.-T. Su, X. Lai, and T.-X. Zhao, “On the hydraulic axial thrust of francis hydro-turbine,” *Journal of Mechanical Science and Technology*, vol. 30, no. 5, pp. 2029–2035, 2016.

[125] X. Ji, L. Xu, and X. Liu, “Calculation of axial hydraulic thrust of francis turbine,” in *ASME 2012 Fluids Engineering Division Summer Meeting collocated with the*

ASME 2012 Heat Transfer Summer Conference and the ASME 2012 10th International Conference on Nanochannels, Microchannels, and Minichannels, 07 2012.

[126] J. Li, Y. Zhang, K.-h. Liu, H.-z. Xian, and J.-x. Yu, “Numerical simulation of hydraulic force on the impeller of reversible pump turbines in generating mode,” *Journal of Hydrodynamics, Ser. B*, vol. 29, pp. 603–609, 08 2017.

[127] W.-D. Shi, H.-L. Wang, Z. Ling, and W. Chuan, “The estimation and experiment of axial force in deep well pump basing on numerical simulation,” *International Journal of Modern Education and Computer Science*, vol. 2, 12 2010.

[128] I. Harada, K. Kobayasi, and S. Ono, “Prediction of axial thrust for mixed-flow pumps with vaned diffuser by using cfd,” *International Journal of Fluid Machinery and Systems*, vol. 3, no. 2, pp. 160–168, 2010.

[129] S. Wei-dong, W. Hong-liang, L. Zhou, Z. Ping-ping, and C. Wang, “The estimation and experiment of axial force in deep well pump basing on numerical simulation,” *International Journal of Modern Education and Computer Science*, vol. 2, no. 2, p. 53, 2010.

[130] L. Zemanová and P. Rudolf, “Flow inside the sidewall gaps of hydraulic machines: A review,” *Energies*, vol. 13, no. 24, 2020.

[131] E. Severac, S. Poncet, E. Serre, and M.-P. Chauve, “Large eddy simulation and measurements of turbulent enclosed rotor-stator flows,” *Physics of Fluids*, vol. 19, no. 8, p. 085113, 2007.

[132] S. Viazzo, S. Poncet, E. Serre, A. Randriamampianina, and P. Bontoux, “High-order large eddy simulations of confined rotor-stator flows,” *Flow, Turbulence and Combustion*, vol. 88, no. 1, pp. 63–75, 2012.

[133] L. Davidson, “Large eddy simulations: How to evaluate resolution,” *International Journal of Heat and Fluid Flow*, vol. 30, no. 5, pp. 1016–1025, 2009. The 3rd International Conference on Heat Transfer and Fluid Flow in Microscale.

[134] G. Tabor and M. Baba-Ahmadi, “Inlet conditions for large eddy simulation: A review,” *Computers & Fluids*, vol. 39, no. 4, pp. 553–567, 2010.

[135] X. Wu, “Inflow turbulence generation methods,” *Annual Review of Fluid Mechanics*, vol. 49, no. 1, pp. 23–49, 2017.

[136] J. Holgate, A. Skillen, T. Craft, and A. Revell, “A review of embedded large eddy simulation for internal flows,” *Archives of Computational Methods in Engineering*, vol. 26, no. 4, pp. 865–882, 2019.

[137] F. R. Menter, “Best practice: scale-resolving simulations in ansys cfd,” *ANSYS Germany GmbH*, vol. 1, 2012.

[138] A. Gerasimov, *Quick Guide to Setting Up LES-type Simulations.* European Technology GroupANSYS Sweden AB, 5 2016. Version 1.4.

[139] F. Mathey, D. Cokljat, J.-P. Bertoglio, and E. Sergent, “Specification of les inlet boundary condition using vortex method,” 01 2006.

[140] R. Klas, *Hydraulický návrh hydrodynamického stroje s vloženými lopatkami.* PhD thesis, Brno University of Technology, 2009.

[141] NIPPON BEARINGS, *Slide bush catalogue*, 2020.

[142] L. Zemanová and P. Rudolf, “Turbulence models for simulation of the flow in a rotor-stator cavity,” *EPJ Web Conf.*, vol. 213, 2019.

[143] L. Zemanová, P. Rudolf, A. V. Naumov, and V. V. Volkov, “Simulation of the flow in rotor-stator gaps and disk friction of radial centrifugal pump,” *Hydraulic Machines, Hydraulic Drives and Hydropneumatic Automation*, 2019.

Nomenclature

List of symbols

α	Angle of unstable vortical structures	$^\circ$
δm	Weight difference	kg
Δp_{La}	Static pressure above the impeller inlet	Pa
Δt	Time step	s
δU	Voltage difference	V
Δx	Minimum cell size	m
δ	Depth of rotating boundary layer	mm
ϵ	Equivalent sand roughness	μm
η	Efficiency	$-$
γ	Angle of hub	$^\circ$
λ	Throughflow parameter	$-$
μ	Dynamic viscosity	$\mathrm{Pa \cdot s}$
ν	Kinematic viscosity	$\mathrm{m^2 \cdot s^{-1}}$
Ω	Rotational speed of the disk	$\mathrm{rad \cdot s^{-1}}$
ω	Rotational speed	$\mathrm{rad \cdot s^{-1}}$
ω	Specific dissipation rate	$\mathrm{s^{-1}}$
Ω_d	Disk angular velocity	$\mathrm{rad \cdot s^{-1}}$
Ω_f	Fluid angular velocity	$\mathrm{rad \cdot s^{-1}}$
Ω_{ij}	Vorticity tensor	$\mathrm{s^{-1}}$
ρ	Density	$\mathrm{kg \cdot m^3}$
τ	Shear stress	Pa
θ	Circumferential coordinate	$^\circ$
ε	Turbulent dissipation rate	$\mathrm{m^2 \cdot s^{-3}}$
φ_{sp}	Leakage coefficient	$-$
$\vec{v}$	Velocity vector	$\mathrm{m \cdot s^{-1}}$
a	Inner radius of cavity	mm

b	Outer radius of cavity	mm
b/k	Relative surface roughness	–
C	Courant number	–
c_{2u}	Average circumferential velocity at the impeller outlet	$\mathrm{m \cdot s^{-1}}$
c_A	Axial thrust reduction coefficient	–
c_f	Friction coefficient	–
c_{m1}	Meridional velocity at inlet	$\mathrm{m \cdot s^{-1}}$
c_{m2}	Meridional velocity at outlet	$\mathrm{m \cdot s^{-1}}$
c_m	Torque coefficient	–
c_q	Non-dimensional characteristic of the leakage flow	–
c_u	Circumferential absolute velocity of fluid	$\mathrm{m \cdot s^{-1}}$
C_w, c_w	Flow rate coefficient (throughflow Reynolds number)	–
d	Diameter	mm
d_D	Diameter at shaft seal	m
d_{sp}	Diameter of leakage gap	m
F	Force	N
F_A, F_a	Axial thrust	N
f_b	Thrust on blade	N
F_{DS}	Axial force acting on hub	N
f_{fh}	Thrust on hub	N
F_I	Axial force resulting from change of flow direction	N
f_l	Factor accounting for net through flow	–
f_R	Factor accounting for effect of roughness on disk friction	–
f_{sh}	Thrust on front shroud	N
F_{TS}	Axial force acting on shroud	N
F_w	Unbalanced axial forces	N
G	Aspect ratio of cavity	–
g	Width of spacer	mm
H	Head	m
K	Entrainment coefficient	–
k	Turbulent kinetic energy	$\mathrm{m^2 \cdot s^{-2}}$
k_E	Rotation factor at the side-room inlet	–
k_o	Rotation factor of the flow with zero leakage	–

k_{RR}	Friction coefficient for impeller	–
L	Length scale	m
l	Exponent related to leakage	–
M	Friction torque	$\mathrm{N \cdot m}$
m	Weight	kg
N_q, n_q	Specific speed	–
p_1	Pressure on inner radius of disk or impeller	Pa
p_2	Pressure on outer radius of disk or impeller	Pa
p_{atm}	Atmospheric pressure	Pa
P_{RP}	Friction power	W
P_{RR}	Friction power of the impeller	W
Q	Flow rate	$\mathrm{m^3 \cdot s^{-1}}$
Q	Q-criterion	$\mathrm{s^{-2}}$
Q_{sp}	Leakage flow rate through impeller neck ring	$\mathrm{m^3 \cdot s^{-1}}$
R	Radial location	mm
r	Radius	mm
r^*	Dimensionless radial coordinate	–
r_1	Inner radius of disk or impeller	mm
r_2	Outer radius of disk or impeller	mm
R_m	Curvature parameter of cavity	–
r_{sp}	Radius of leakage gap	mm
Re	Reynolds number	–
Re_δ	Reynolds number of rotating boundary layer	–
Ro	Rosby number	–
Ro_δ	Rosby number of rotating boundary layer	–
s	Width of cavity	mm
s_{ax}	Axial gap of impeller	mm
s_{ax}^*	Ratio of axial gap to impeller outer radius	–
S_{ij}	Rate of strain tensor	$\mathrm{s^{-1}}$
T_p	Total thrust	N
U	Expanded uncertainty	
U	Velocity of fluid	$\mathrm{m \cdot s^{-1}}$
U	Voltage	V

u	Circumferential impeller velocity	$\mathrm{m \cdot s^{-1}}$
U_A	A-uncertainty	
U_B	B-uncertainty	
$v_\theta, v_t, V_\theta, V_t$	Tangential velocity	$\mathrm{m \cdot s^{-1}}$
V_r, v_r	Radial velocity	$\mathrm{m \cdot s^{-1}}$
v_r^*	Dimensionless radial velocity	–
v_r^*	Dimensionless tangential velocity	–
x_{ov}	Overlap between impeller side disks and casing	mm
Y	Spacific energy	$\mathrm{J \cdot kg^{-1}}$
y^+	Wall function	–
z	Axial coordinate	mm
z^*	Dimensionless axial coordinate	–

Abbreviations

3D	Three-dimensional
ASM	Algebraic stress model
BF	Basic flow
CFD	Computational fluid dynamics
CR	Circural rolls
DES	Detached eddy simulation
DNS	Direct numerical simulation
LED	Light-emitting diode
LES	Large eddy simulation
RANS	Reynolds-averaged Navier Stokes equations
RNG	Re-normalisation group
RSM	Reynolds stress model
SAS	Scale-adaptive simulation
SP	Spots
SR	Spiral rolls
SST	Shear stress transport

List of Appendixes

Experimental data

- LDA velocity profiles
- Amplitude-frequency spectra

CFD data

- Comparison of LDA and CFD
- Back-sidewall gap h_2
- Back-sidewall gap h_1
- Back-sidewall gap h_3
- Back-sidewall gap h_2 - with throughflow

Appendices

LDA data

Velocity profiles

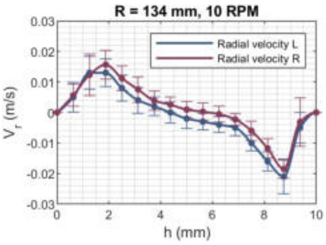

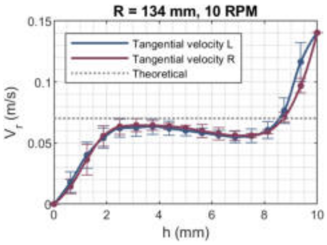

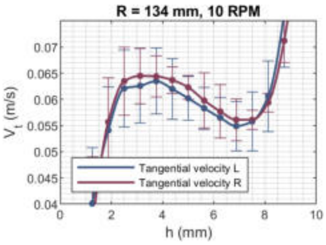

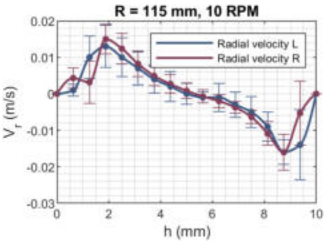

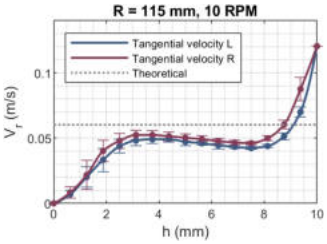

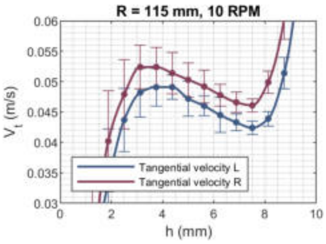

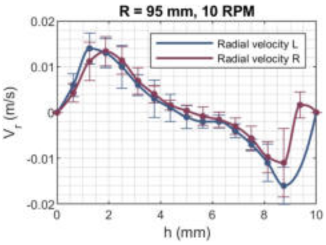

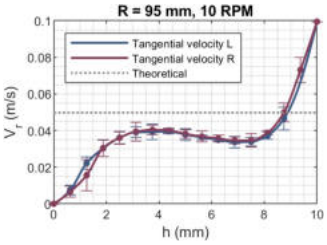

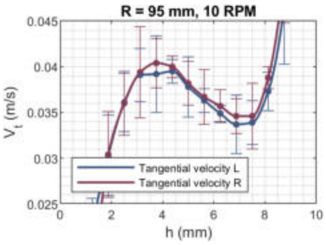

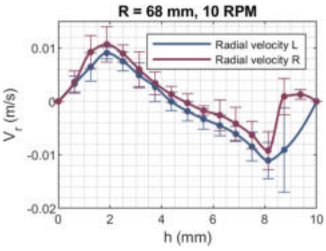

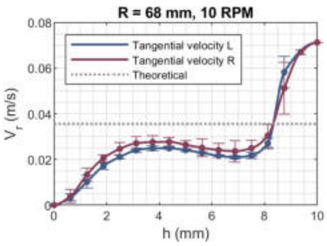

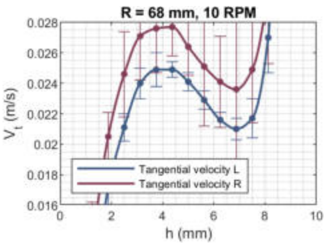

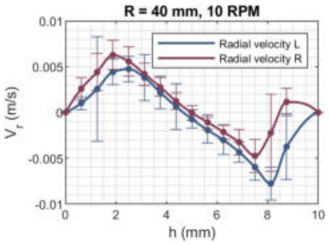
R = 40 mm, 10 RPM
Radial velocity L
Radial velocity R
V_r (m/s)
0.01
0.005
0
-0.005
-0.01
0
2
4
6
8
10
h (mm)

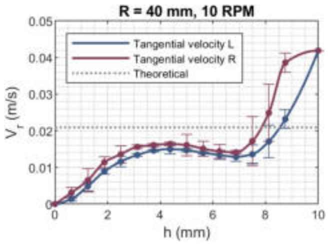
R = 40 mm, 10 RPM
Tangential velocity L
Tangential velocity R
Theoretical
V_t (m/s)
0.05
0.04
0.03
0.02
0.01
0
0
2
4
6
8
10
h (mm)

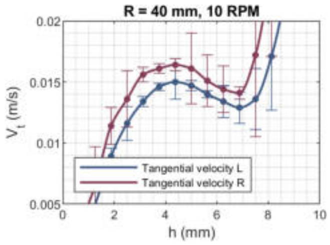
R = 40 mm, 10 RPM
Tangential velocity L
Tangential velocity R
V_t (m/s)
0.02
0.015
0.01
0.005
0
2
4
6
8
10
h (mm)

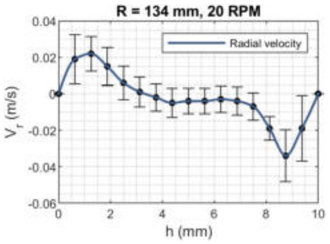
R = 134 mm, 20 RPM
Radial velocity
V_r (m/s)
0.04
0.02
0
-0.02
-0.04
-0.06
0
2
4
6
8
10
h (mm)

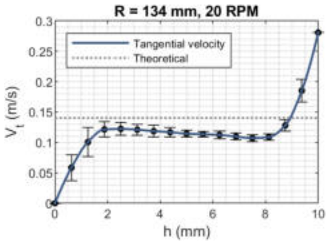
R = 134 mm, 20 RPM
Tangential velocity
Theoretical
V_t (m/s)
0.3
0.25
0.2
0.15
0.1
0.05
0
0
2
4
6
8
10
h (mm)

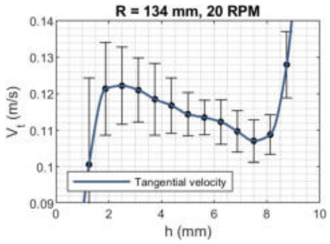
R = 134 mm, 20 RPM
Tangential velocity
V_t (m/s)
0.14
0.13
0.12
0.11
0.1
0.09
0
2
4
6
8
10
h (mm)

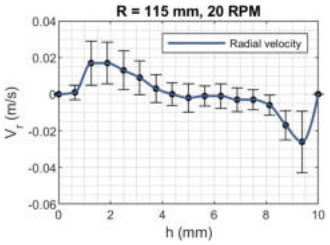
R = 115 mm, 20 RPM
Radial velocity
V_r (m/s)
0.04
0.02
0
-0.02
-0.04
-0.06
0
2
4
6
8
10
h (mm)

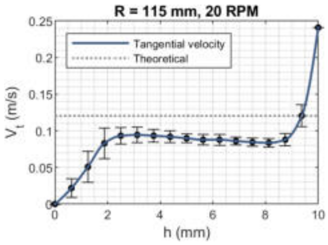
R = 115 mm, 20 RPM
Tangential velocity
Theoretical
V_t (m/s)
0.25
0.2
0.15
0.1
0.05
0
0
2
4
6
8
10
h (mm)

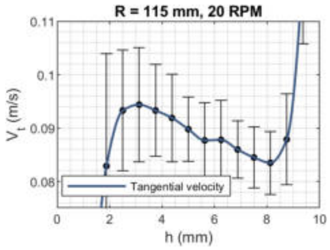
R = 115 mm, 20 RPM
Tangential velocity
V_t (m/s)
0.11
0.1
0.09
0.08
0
2
4
6
8
10
h (mm)

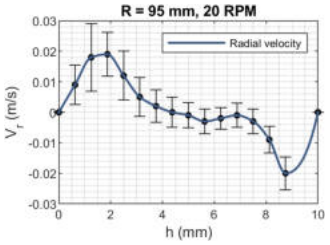
R = 95 mm, 20 RPM
Radial velocity
V_r (m/s)
0.03
0.02
0.01
0
-0.01
-0.02
-0.03
0
2
4
6
8
10
h (mm)

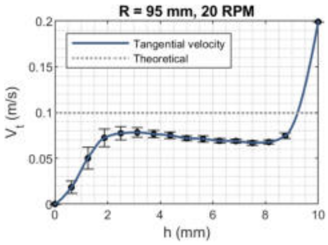
R = 95 mm, 20 RPM
Tangential velocity
Theoretical
V_t (m/s)
0.2
0.15
0.1
0.05
0
0
2
4
6
8
10
h (mm)

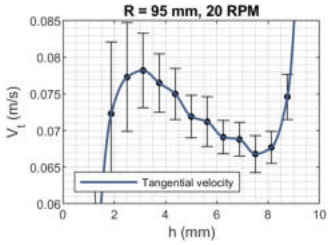
R = 95 mm, 20 RPM
Tangential velocity
V_t (m/s)
0.085
0.08
0.075
0.07
0.065
0.06
0
2
4
6
8
10
h (mm)

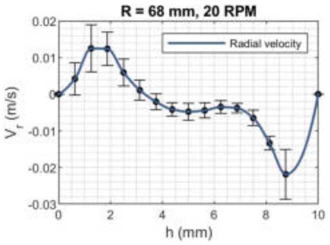
R = 68 mm, 20 RPM
Radial velocity
V_r (m/s)
0.02
0.01
0
-0.01
-0.02
-0.03
0
2
4
6
8
10
h (mm)

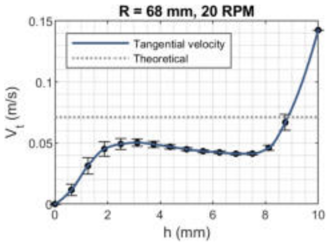
R = 68 mm, 20 RPM
Tangential velocity
Theoretical
V_t (m/s)
0.15
0.1
0.05
0
0
2
4
6
8
10
h (mm)

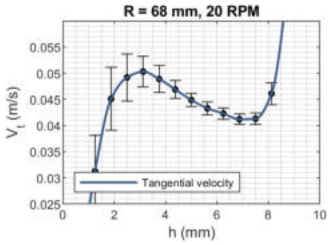
R = 68 mm, 20 RPM
Tangential velocity
V_t (m/s)
0.055
0.05
0.045
0.04
0.035
0.03
0.025
0
2
4
6
8
10
h (mm)

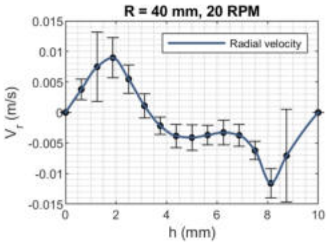
R = 40 mm, 20 RPM
Radial velocity
V_r (m/s)
0.015
0.01
0.005
0
-0.005
-0.01
-0.015
0
2
4
6
8
10
h (mm)

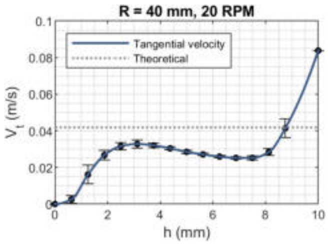
R = 40 mm, 20 RPM
Tangential velocity
Theoretical
V_t (m/s)
0.1
0.08
0.06
0.04
0.02
0
0
2
4
6
8
10
h (mm)

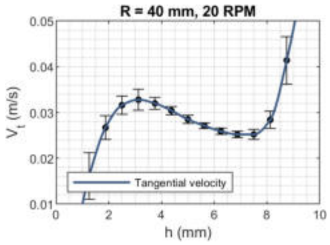
R = 40 mm, 20 RPM
Tangential velocity
V_t (m/s)
0.05
0.04
0.03
0.02
0.01
0
2
4
6
8
10
h (mm)

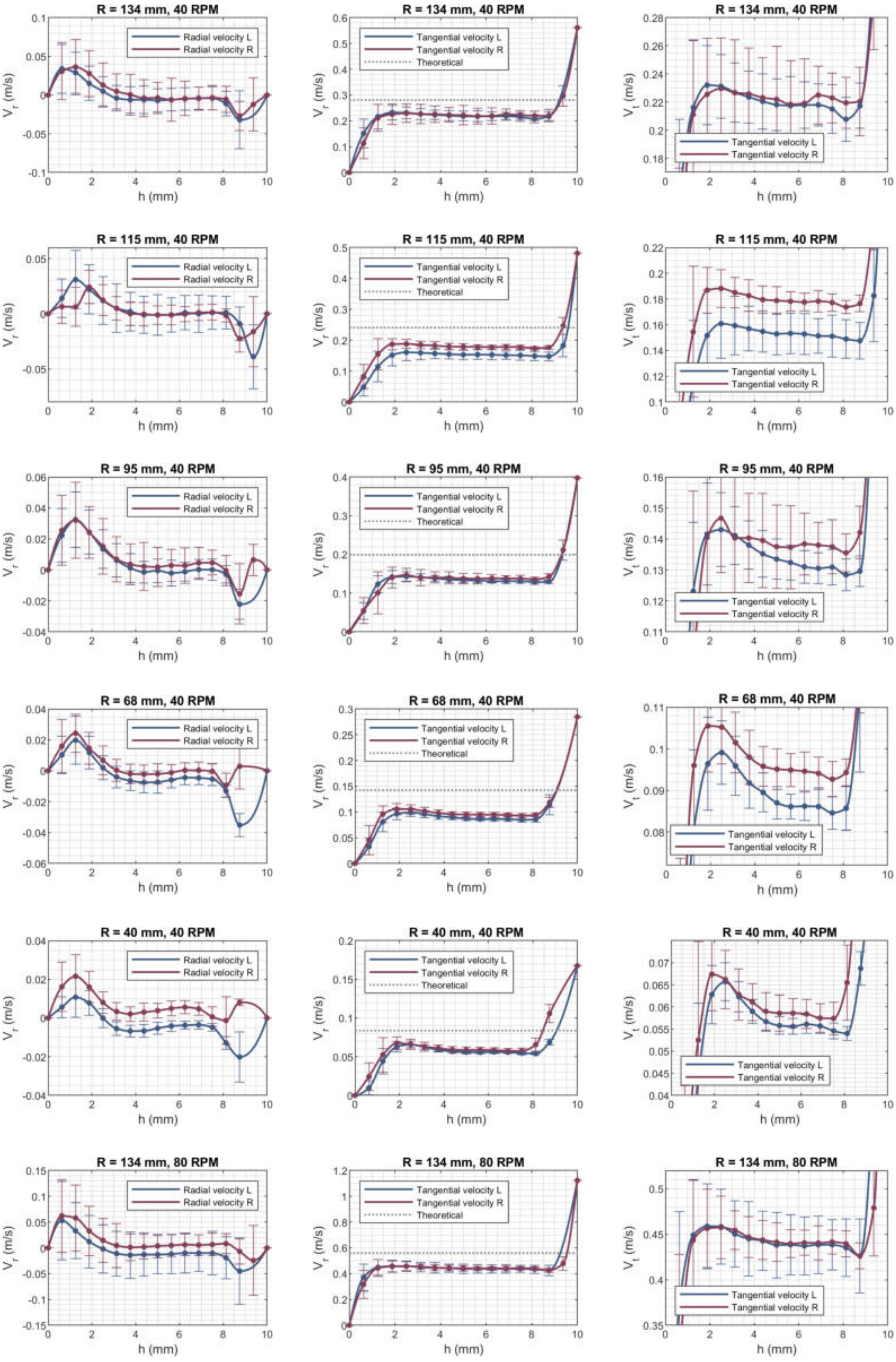
R = 134 mm, 40 RPM
Radial velocity L
Radial velocity R
Tangential velocity L
Tangential velocity R
Theoretical
R = 115 mm, 40 RPM
R = 95 mm, 40 RPM
R = 68 mm, 40 RPM
R = 40 mm, 40 RPM
R = 134 mm, 80 RPM
V_r (m/s)
V_t (m/s)
h (mm)

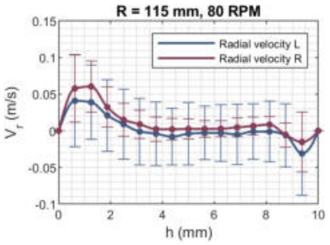
R = 115 mm, 80 RPM
Radial velocity L
Radial velocity R
V_r (m/s)
h (mm)
0.15
0.1
0.05
0
-0.05
-0.1
0
2
4
6
8
10

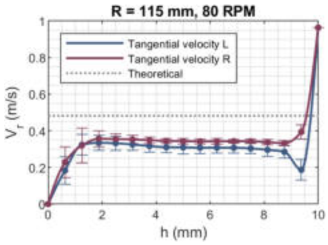
R = 115 mm, 80 RPM
Tangential velocity L
Tangential velocity R
Theoretical
V_r (m/s)
h (mm)
1
0.8
0.6
0.4
0.2
0
0
2
4
6
8
10

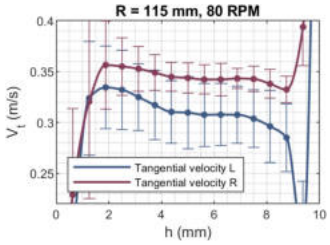
R = 115 mm, 80 RPM
Tangential velocity L
Tangential velocity R
V_t (m/s)
h (mm)
0.4
0.35
0.3
0.25
0
2
4
6
8
10

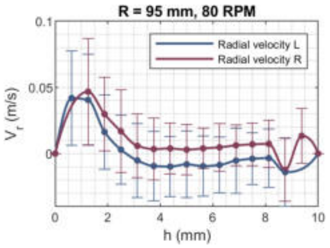
R = 95 mm, 80 RPM
Radial velocity L
Radial velocity R
V_r (m/s)
h (mm)
0.1
0.05
0
0
2
4
6
8
10

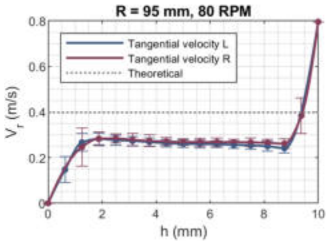
R = 95 mm, 80 RPM
Tangential velocity L
Tangential velocity R
Theoretical
V_r (m/s)
h (mm)
0.8
0.6
0.4
0.2
0
0
2
4
6
8
10

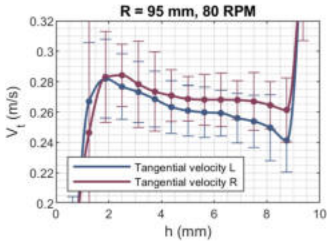
R = 95 mm, 80 RPM
Tangential velocity L
Tangential velocity R
V_t (m/s)
h (mm)
0.32
0.3
0.28
0.26
0.24
0.22
0.2
0
2
4
6
8
10

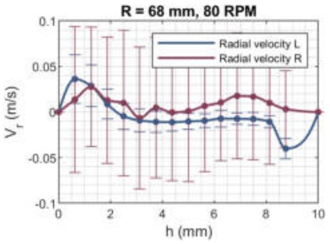
R = 68 mm, 80 RPM
Radial velocity L
Radial velocity R
V_r (m/s)
h (mm)
0.1
0.05
0
-0.05
-0.1
0
2
4
6
8
10

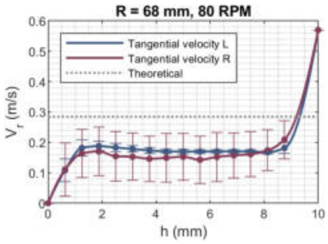
R = 68 mm, 80 RPM
Tangential velocity L
Tangential velocity R
Theoretical
V_r (m/s)
h (mm)
0.6
0.5
0.4
0.3
0.2
0.1
0
0
2
4
6
8
10

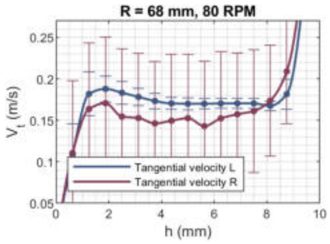
R = 68 mm, 80 RPM
Tangential velocity L
Tangential velocity R
V_t (m/s)
h (mm)
0.25
0.2
0.15
0.1
0.05
0
2
4
6
8
10

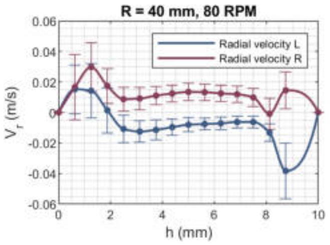
R = 40 mm, 80 RPM
Radial velocity L
Radial velocity R
V_r (m/s)
h (mm)
0.06
0.04
0.02
0
-0.02
-0.04
-0.06
0
2
4
6
8
10

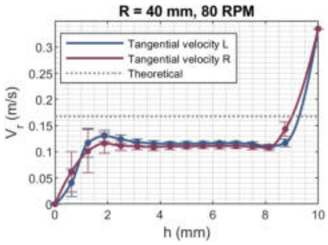
R = 40 mm, 80 RPM
Tangential velocity L
Tangential velocity R
Theoretical
V_r (m/s)
h (mm)
0.3
0.25
0.2
0.15
0.1
0.05
0
0
2
4
6
8
10

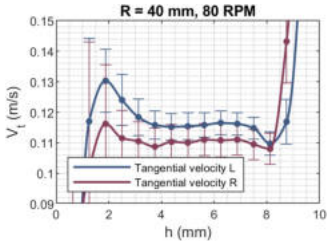
R = 40 mm, 80 RPM
Tangential velocity L
Tangential velocity R
V_t (m/s)
h (mm)
0.15
0.14
0.13
0.12
0.11
0.1
0.09
0
2
4
6
8
10

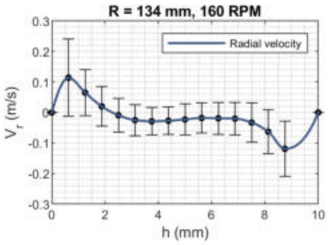
R = 134 mm, 160 RPM
Radial velocity
V_r (m/s)
h (mm)
0.3
0.2
0.1
0
-0.1
-0.2
-0.3
0
2
4
6
8
10

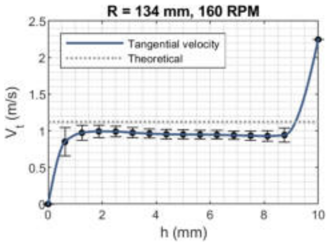
R = 134 mm, 160 RPM
Tangential velocity
Theoretical
V_t (m/s)
h (mm)
2.5
2
1.5
1
0.5
0
0
2
4
6
8
10

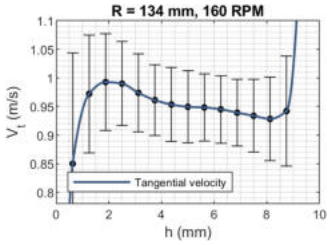
R = 134 mm, 160 RPM
Tangential velocity
V_t (m/s)
h (mm)
1.1
1.05
1
0.95
0.9
0.85
0.8
0
2
4
6
8
10

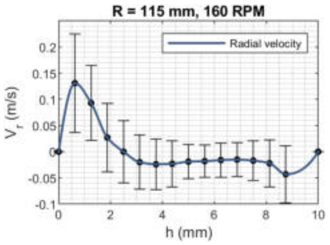
R = 115 mm, 160 RPM
Radial velocity
V_r (m/s)
h (mm)
0.2
0.15
0.1
0.05
0
-0.05
-0.1
0
2
4
6
8
10

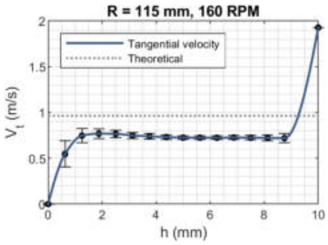
R = 115 mm, 160 RPM
Tangential velocity
Theoretical
V_t (m/s)
h (mm)
2
1.5
1
0.5
0
0
2
4
6
8
10

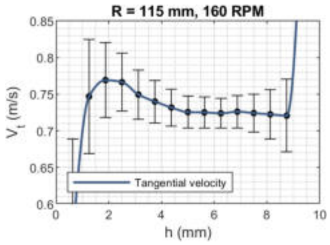
R = 115 mm, 160 RPM
Tangential velocity
V_t (m/s)
h (mm)
0.85
0.8
0.75
0.7
0.65
0.6
0
2
4
6
8
10

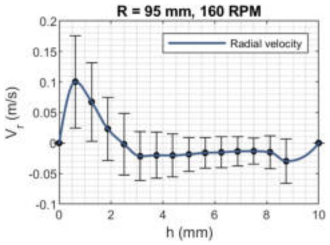
R = 95 mm, 160 RPM

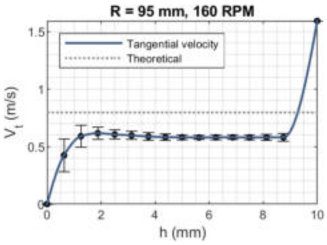
R = 95 mm, 160 RPM

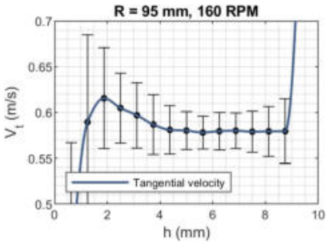
R = 95 mm, 160 RPM

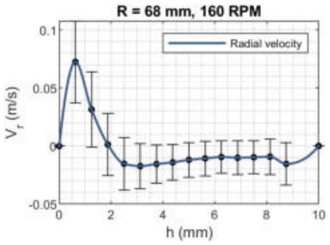
R = 68 mm, 160 RPM

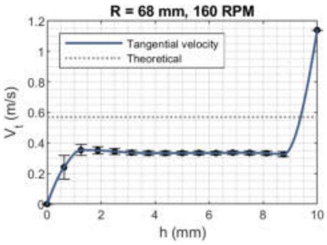
R = 68 mm, 160 RPM

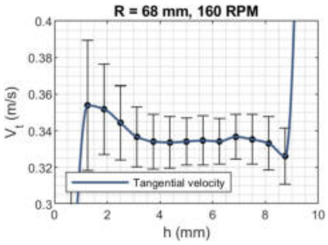
R = 68 mm, 160 RPM

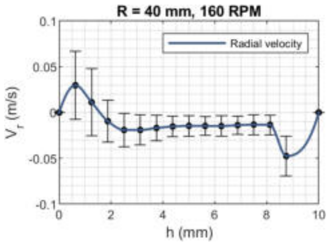
R = 40 mm, 160 RPM

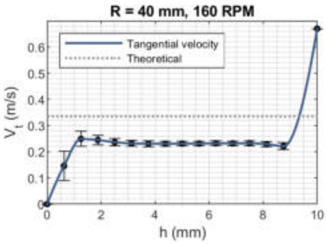
R = 40 mm, 160 RPM

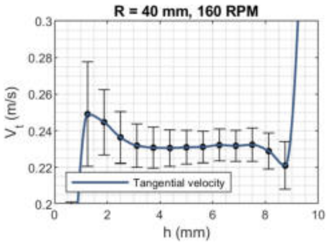
R = 40 mm, 160 RPM

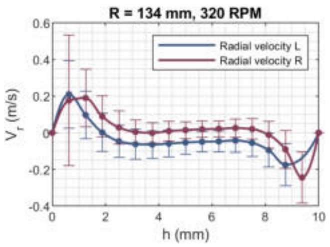
R = 134 mm, 320 RPM

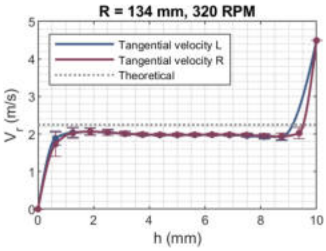
R = 134 mm, 320 RPM

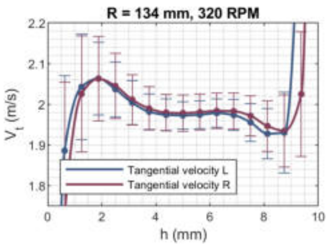
R = 134 mm, 320 RPM

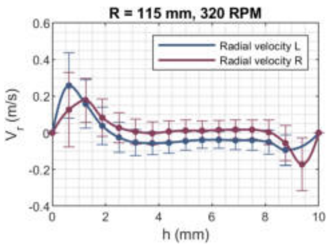
R = 115 mm, 320 RPM

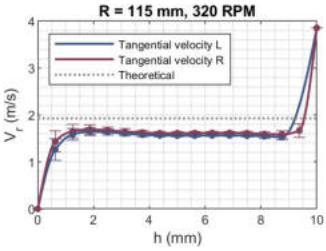
R = 115 mm, 320 RPM

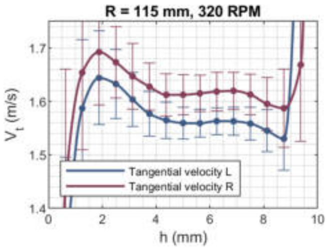
R = 115 mm, 320 RPM

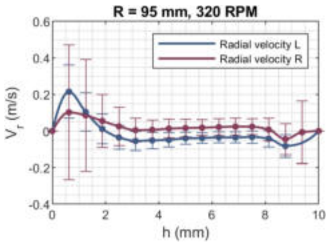
R = 95 mm, 320 RPM

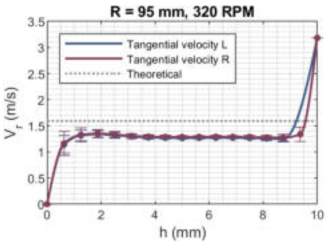
R = 95 mm, 320 RPM

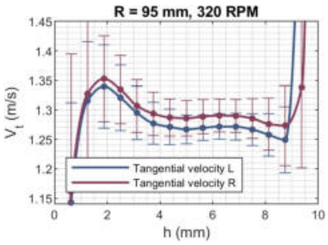
R = 95 mm, 320 RPM

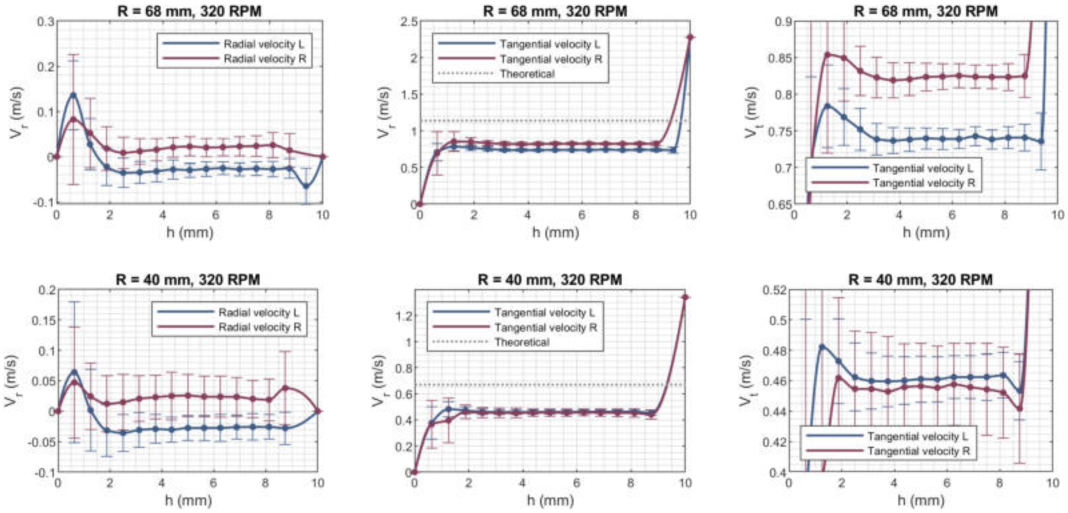

Amplitude-frequency spectra

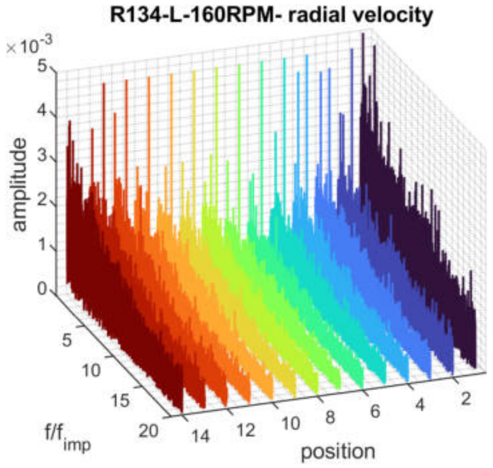

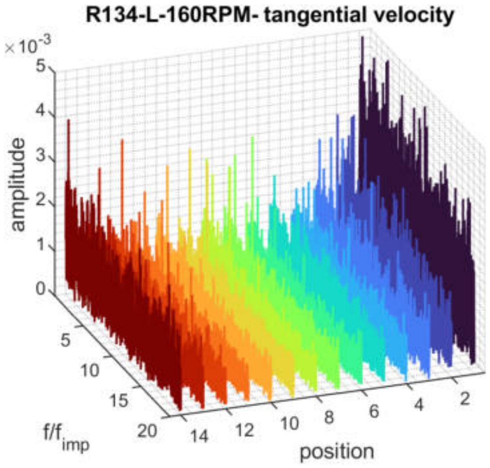

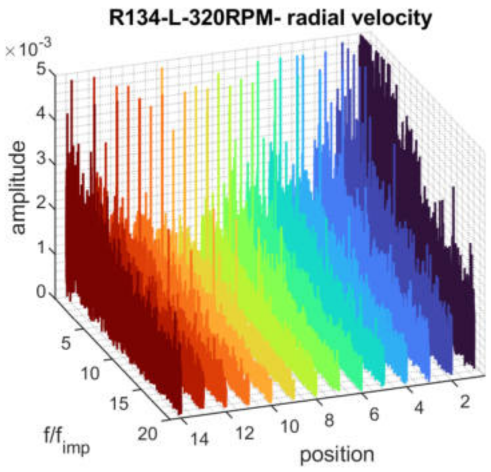
R134-L-320RPM- radial velocity

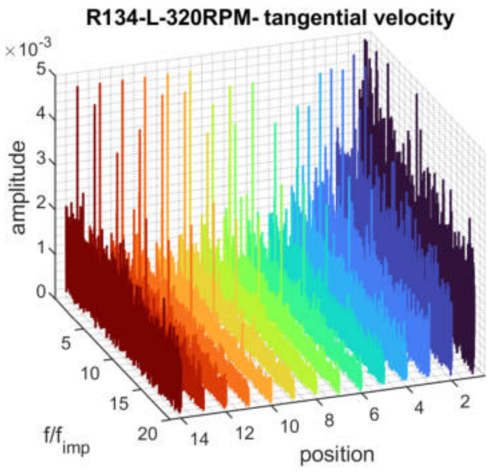
R134-L-320RPM- tangential velocity

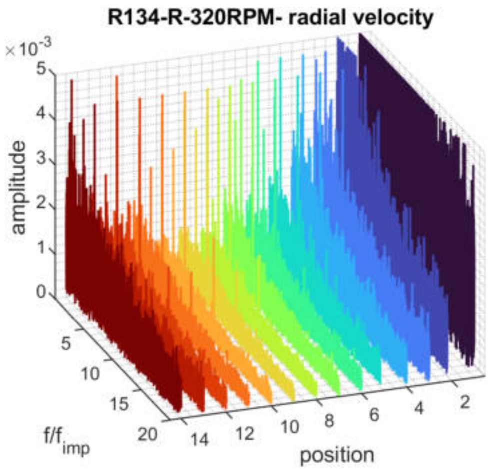
R134-R-320RPM- radial velocity

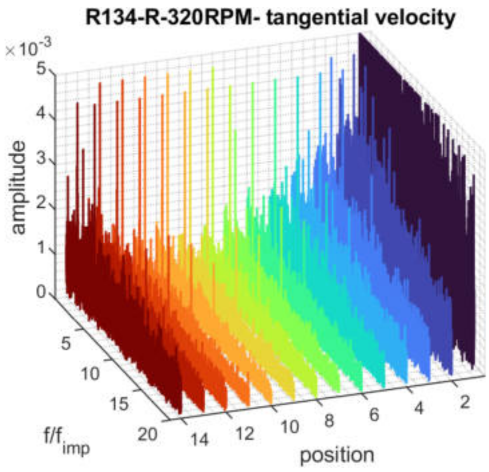
R134-R-320RPM- tangential velocity

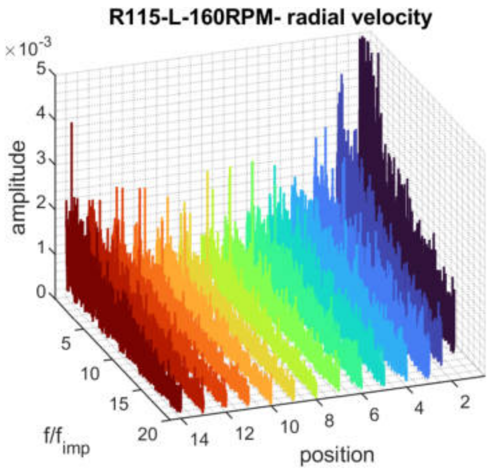
R115-L-160RPM- radial velocity

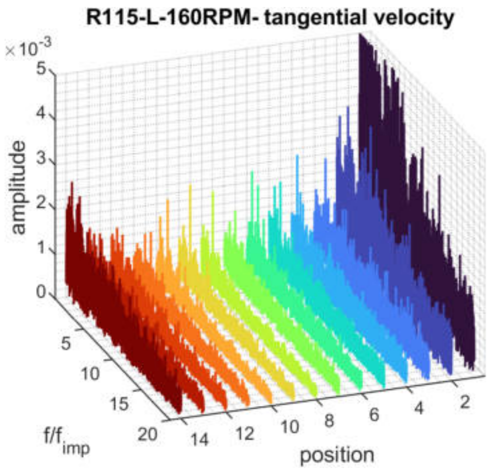
R115-L-160RPM- tangential velocity

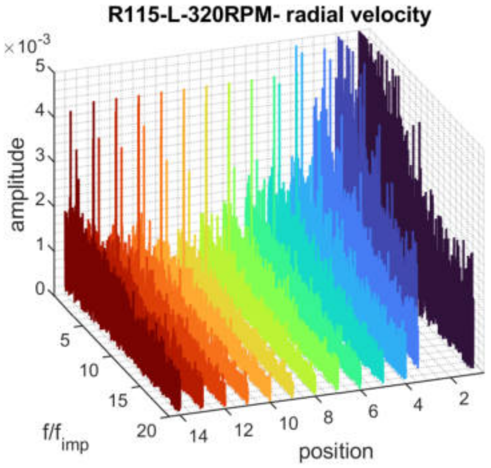
R115-L-320RPM- radial velocity
×10^-3
5
4
3
2
1
0
amplitude
5
10
15
20
f/f_imp
14
12
10
8
6
4
2
position

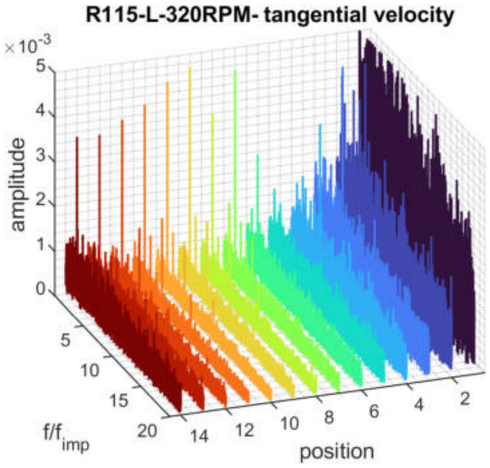
R115-L-320RPM- tangential velocity
×10^-3
5
4
3
2
1
0
amplitude
5
10
15
20
f/f_imp
14
12
10
8
6
4
2
position

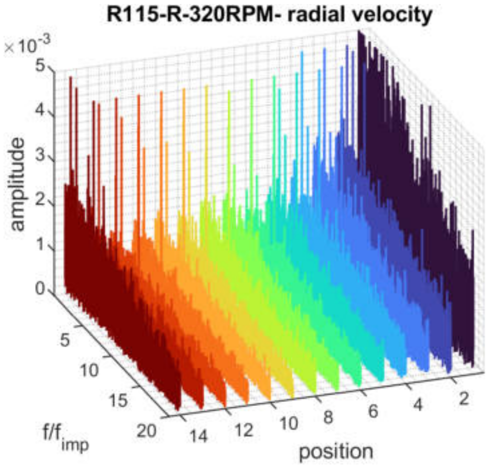
R115-R-320RPM- radial velocity
×10^-3
5
4
3
2
1
0
amplitude
5
10
15
20
f/f_imp
14
12
10
8
6
4
2
position

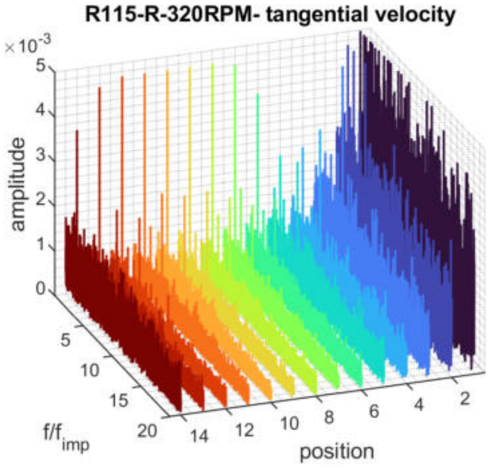
R115-R-320RPM- tangential velocity
×10^-3
5
4
3
2
1
0
amplitude
5
10
15
20
f/f_imp
14
12
10
8
6
4
2
position

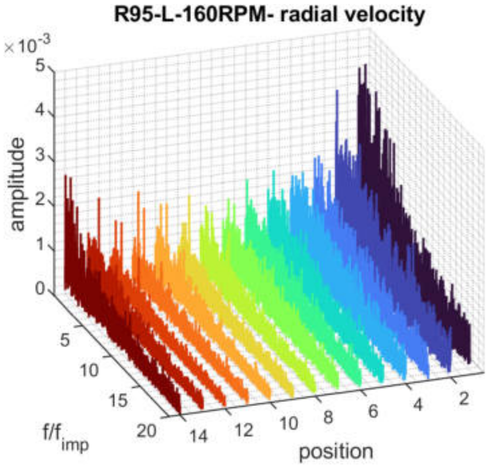
R95-L-160RPM- radial velocity
×10^-3
5
4
3
2
1
0
amplitude
5
10
15
20
f/f_imp
14
12
10
8
6
4
2
position

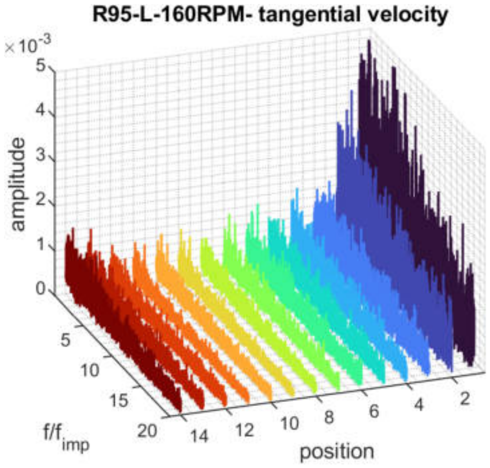
R95-L-160RPM- tangential velocity
×10^-3
5
4
3
2
1
0
amplitude
5
10
15
20
f/f_imp
14
12
10
8
6
4
2
position

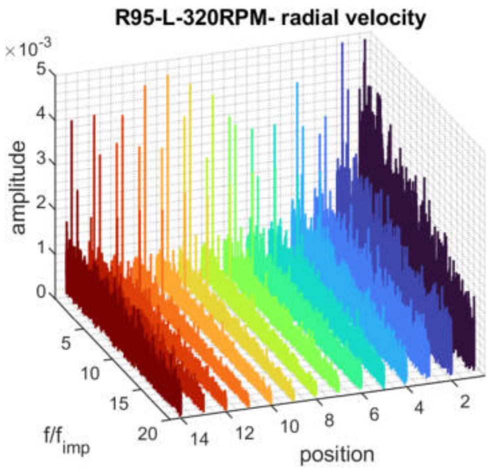
R95-L-320RPM- radial velocity

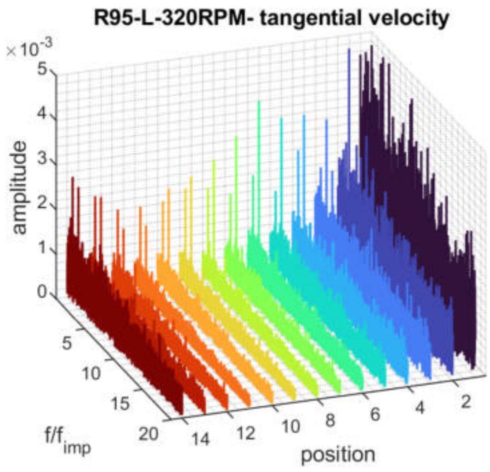
R95-L-320RPM- tangential velocity

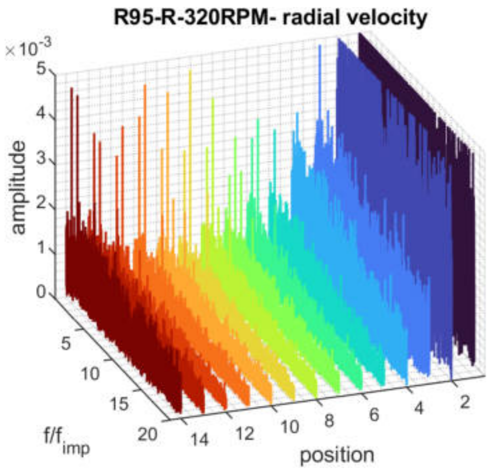
R95-R-320RPM- radial velocity

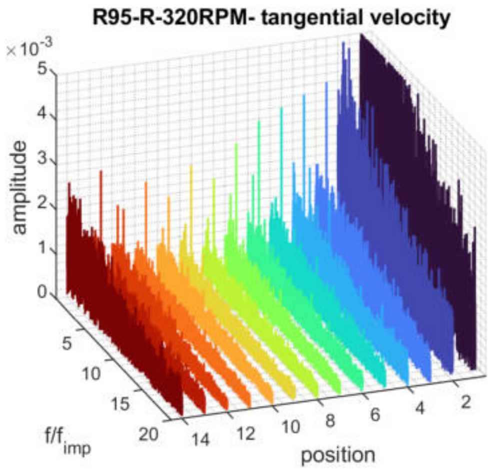
R95-R-320RPM- tangential velocity

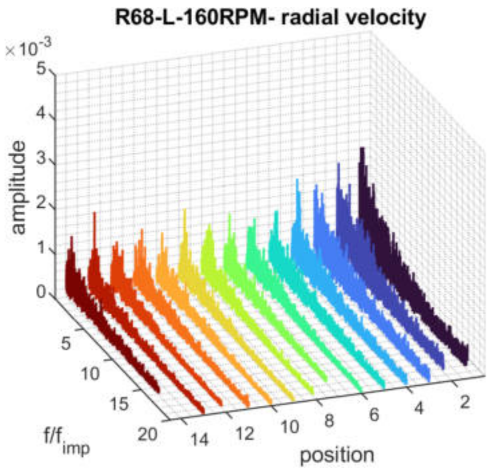
R68-L-160RPM- radial velocity

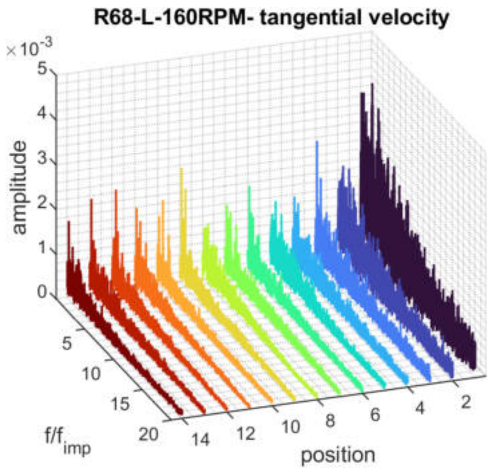
R68-L-160RPM- tangential velocity

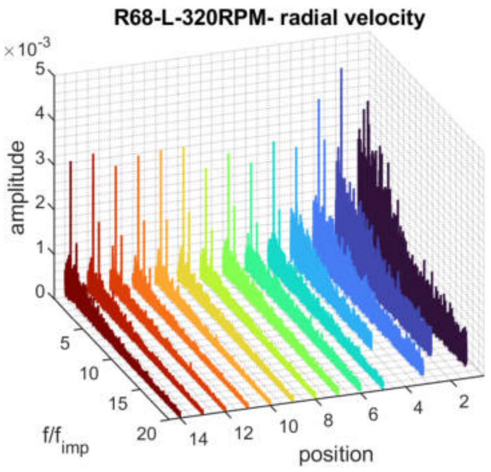
R68-L-320RPM- radial velocity

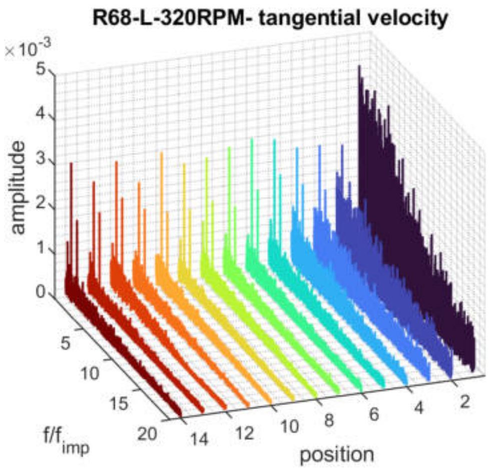
R68-L-320RPM- tangential velocity

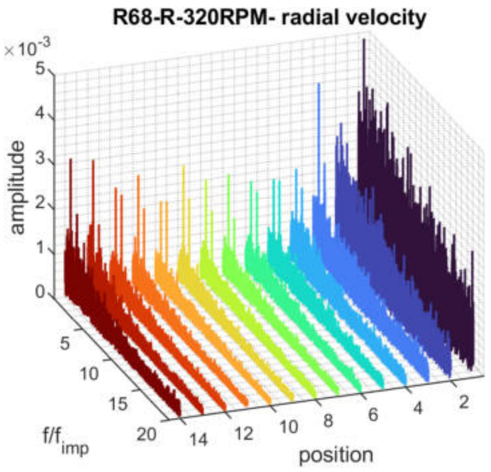
R68-R-320RPM- radial velocity

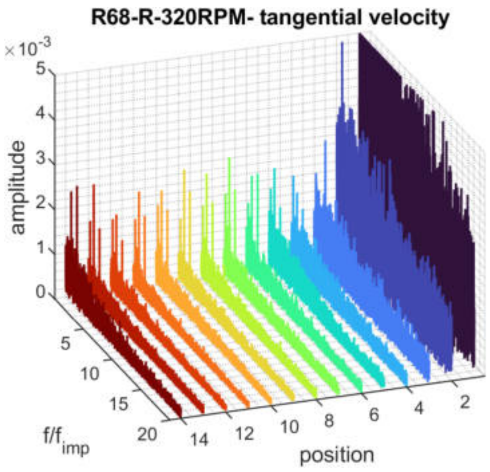
R68-R-320RPM- tangential velocity

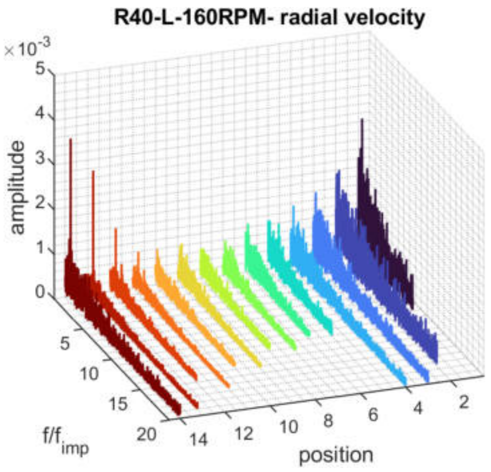
R40-L-160RPM- radial velocity

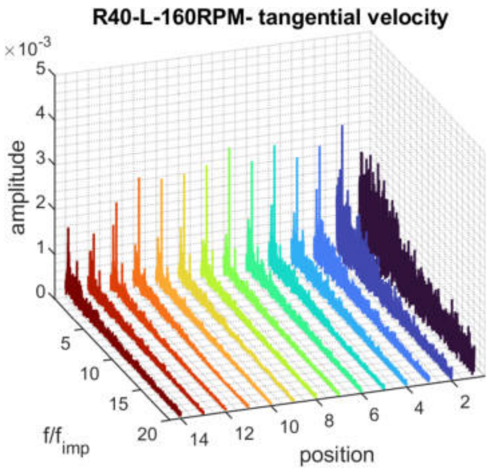
R40-L-160RPM- tangential velocity

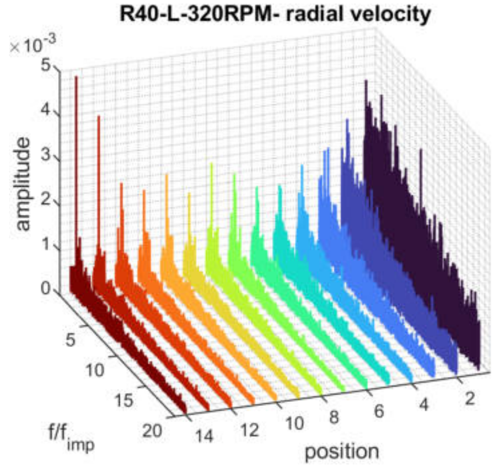
R40-L-320RPM- radial velocity

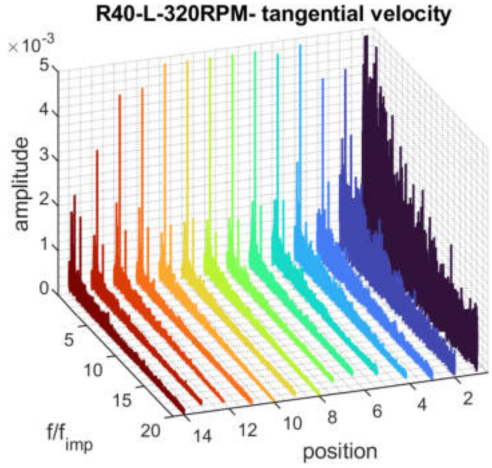
R40-L-320RPM- tangential velocity

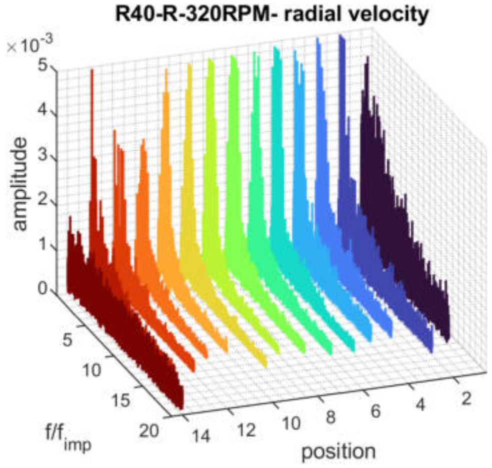
R40-R-320RPM- radial velocity

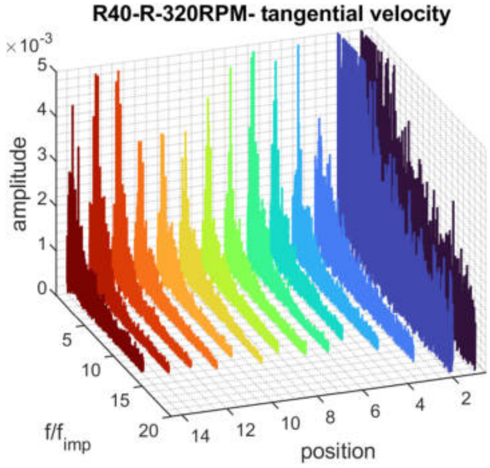
R40-R-320RPM- tangential velocity

CFD data

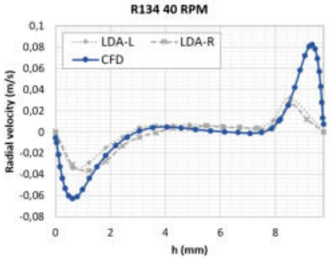
R134 40 RPM
Radial velocity (m/s)
0,1
0,08
0,06
0,04
0,02
0
-0,02
-0,04
-0,06
-0,08
0
2
4
6
8
h (mm)
LDA-L
LDA-R
CFD

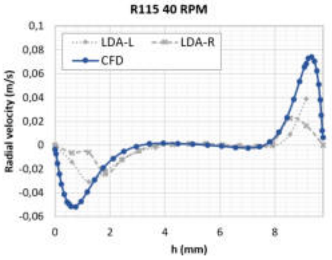
R115 40 RPM
Radial velocity (m/s)
0,1
0,08
0,06
0,04
0,02
0
-0,02
-0,04
-0,06
0
2
4
6
8
h (mm)
LDA-L
LDA-R
CFD

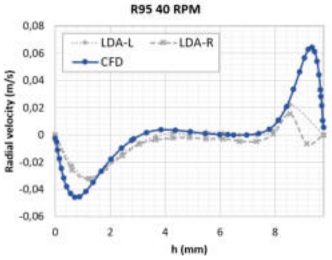
R95 40 RPM
Radial velocity (m/s)
0,08
0,06
0,04
0,02
0
-0,02
-0,04
-0,06
0
2
4
6
8
h (mm)
LDA-L
LDA-R
CFD

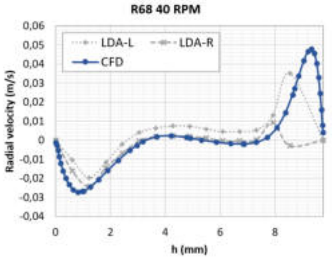
R68 40 RPM
Radial velocity (m/s)
0,06
0,05
0,04
0,03
0,02
0,01
0
-0,01
-0,02
-0,03
-0,04
0
2
4
6
8
h (mm)
LDA-L
LDA-R
CFD

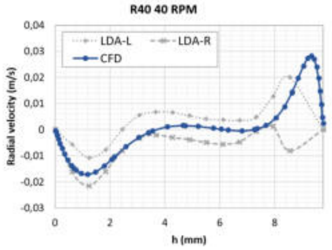
R40 40 RPM
Radial velocity (m/s)
0,04
0,03
0,02
0,01
0
-0,01
-0,02
-0,03
0
2
4
6
8
h (mm)
LDA-L
LDA-R
CFD

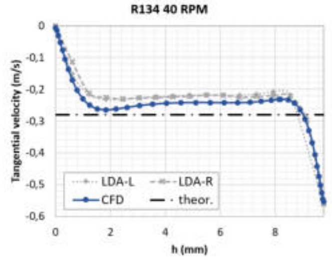
R134 40 RPM
Tangential velocity (m/s)
0
-0,1
-0,2
-0,3
-0,4
-0,5
-0,6
0
2
4
6
8
h (mm)
LDA-L
LDA-R
CFD
theor.

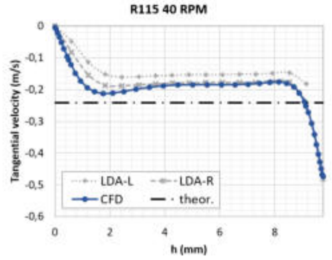
R115 40 RPM
Tangential velocity (m/s)
0
-0,1
-0,2
-0,3
-0,4
-0,5
-0,6
0
2
4
6
8
h (mm)
LDA-L
LDA-R
CFD
theor.

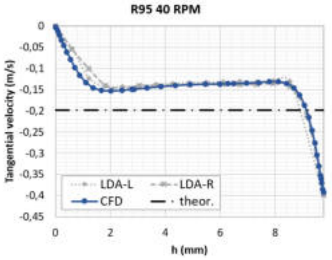
R95 40 RPM
Tangential velocity (m/s)
0
-0,05
-0,1
-0,15
-0,2
-0,25
-0,3
-0,35
-0,4
-0,45
0
2
4
6
8
h (mm)
LDA-L
LDA-R
CFD
theor.

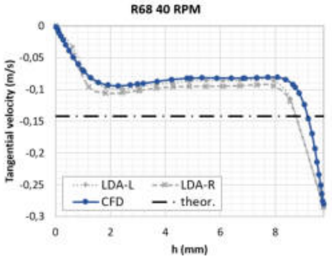
R68 40 RPM
Tangential velocity (m/s)
0
-0,05
-0,1
-0,15
-0,2
-0,25
-0,3
0
2
4
6
8
h (mm)
LDA-L
LDA-R
CFD
theor.

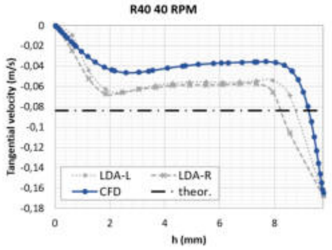
R40 40 RPM
Tangential velocity (m/s)
0
-0,02
-0,04
-0,06
-0,08
-0,1
-0,12
-0,14
-0,16
-0,18
0
2
4
6
8
h (mm)
LDA-L
LDA-R
CFD
theor.

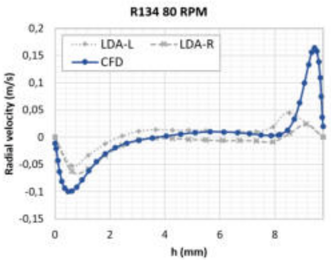
R134 80 RPM
LDA-L
LDA-R
CFD
Radial velocity (m/s)
0,2
0,15
0,1
0,05
0
-0,05
-0,1
-0,15
h (mm)
0
2
4
6
8

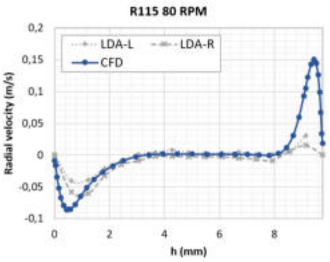
R115 80 RPM
LDA-L
LDA-R
CFD
Radial velocity (m/s)
0,2
0,15
0,1
0,05
0
-0,05
-0,1
h (mm)
0
2
4
6
8

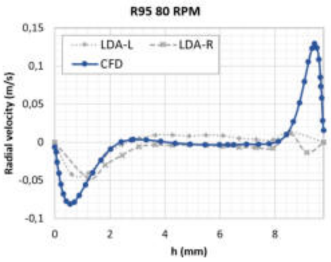
R95 80 RPM
LDA-L
LDA-R
CFD
Radial velocity (m/s)
0,15
0,1
0,05
0
-0,05
-0,1
h (mm)
0
2
4
6
8

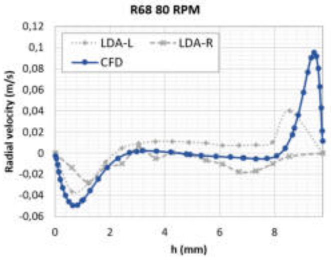
R68 80 RPM
LDA-L
LDA-R
CFD
Radial velocity (m/s)
0,12
0,1
0,08
0,06
0,04
0,02
0
-0,02
-0,04
-0,06
h (mm)
0
2
4
6
8

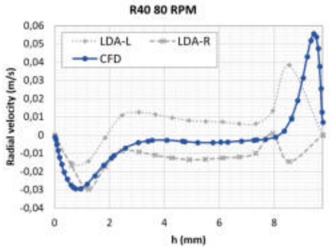
R40 80 RPM
LDA-L
LDA-R
CFD
Radial velocity (m/s)
0,06
0,05
0,04
0,03
0,02
0,01
0
-0,01
-0,02
-0,03
-0,04
h (mm)
0
2
4
6
8

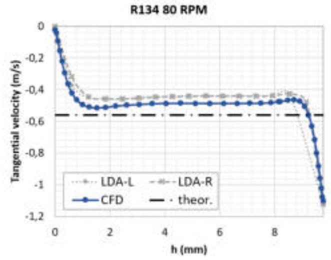
R134 80 RPM
LDA-L
LDA-R
CFD
theor.
Tangential velocity (m/s)
0
-0,2
-0,4
-0,6
-0,8
-1
-1,2
h (mm)
0
2
4
6
8

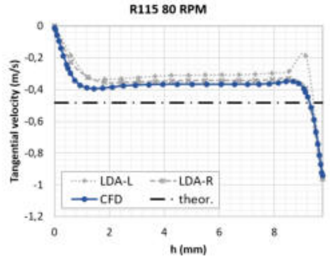
R115 80 RPM
LDA-L
LDA-R
CFD
theor.
Tangential velocity (m/s)
0
-0,2
-0,4
-0,6
-0,8
-1
-1,2
h (mm)
0
2
4
6
8

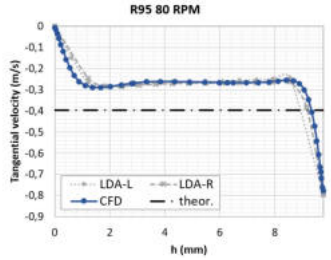
R95 80 RPM
LDA-L
LDA-R
CFD
theor.
Tangential velocity (m/s)
0
-0,1
-0,2
-0,3
-0,4
-0,5
-0,6
-0,7
-0,8
-0,9
h (mm)
0
2
4
6
8

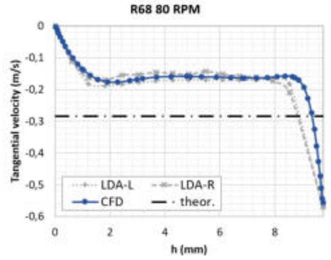
R68 80 RPM
LDA-L
LDA-R
CFD
theor.
Tangential velocity (m/s)
0
-0,1
-0,2
-0,3
-0,4
-0,5
-0,6
h (mm)
0
2
4
6
8

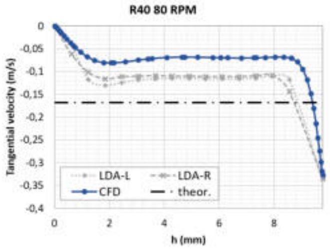
R40 80 RPM
LDA-L
LDA-R
CFD
theor.
Tangential velocity (m/s)
0
-0,05
-0,1
-0,15
-0,2
-0,25
-0,3
-0,35
-0,4
h (mm)
0
2
4
6
8

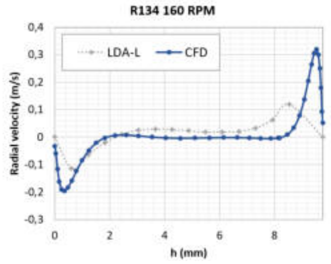
R134 160 RPM
LDA-L
CFD
Radial velocity (m/s)
0,4
0,3
0,2
0,1
0
-0,1
-0,2
-0,3
h (mm)
0
2
4
6
8

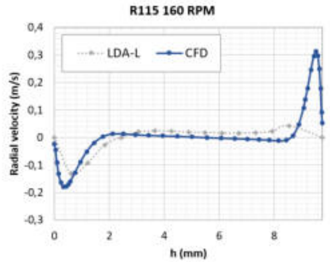
R115 160 RPM
LDA-L
CFD
Radial velocity (m/s)
0,4
0,3
0,2
0,1
0
-0,1
-0,2
-0,3
h (mm)
0
2
4
6
8

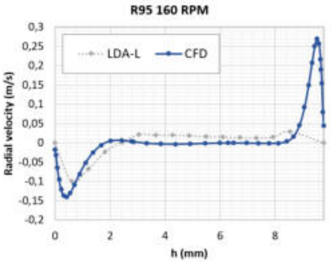
R95 160 RPM
LDA-L
CFD
Radial velocity (m/s)
0,3
0,25
0,2
0,15
0,1
0,05
0
-0,05
-0,1
-0,15
-0,2
h (mm)
0
2
4
6
8

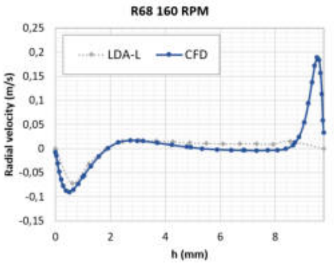
R68 160 RPM

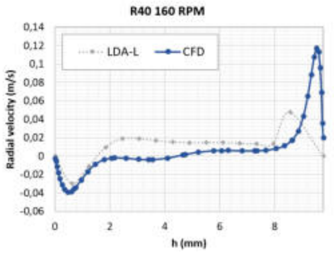
R40 160 RPM

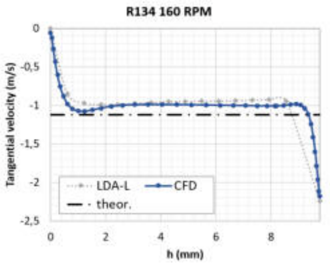
R134 160 RPM

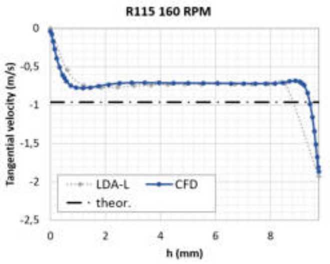
R115 160 RPM

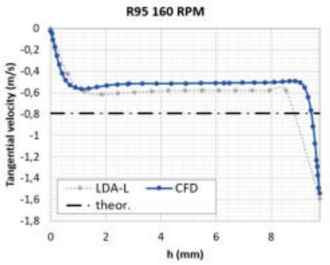
R95 160 RPM

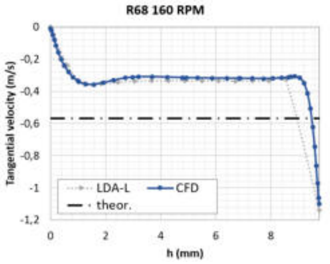
R68 160 RPM

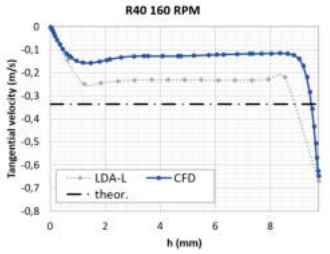
R40 160 RPM

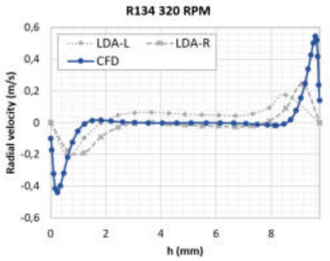
R134 320 RPM

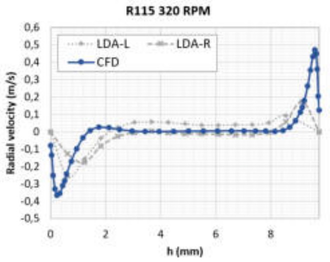
R115 320 RPM

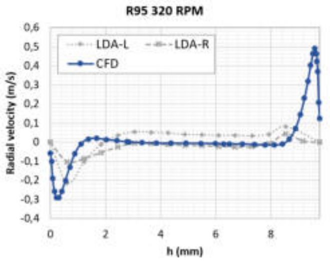
R95 320 RPM

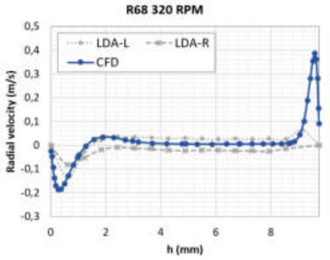
R68 320 RPM

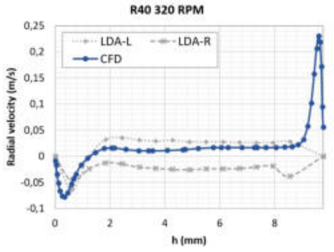
R40 320 RPM

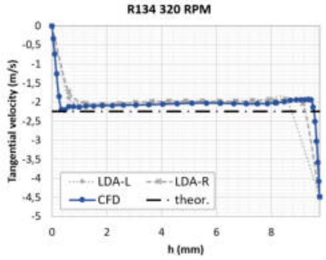
R134 320 RPM
Tangential velocity (m/s)
0
-0,5
-1
-1,5
-2
-2,5
-3
-3,5
-4
-4,5
-5
0
2
4
6
8
h (mm)
LDA-L
LDA-R
CFD
theor.

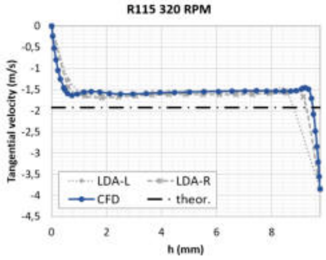
R115 320 RPM
Tangential velocity (m/s)
0
-0,5
-1
-1,5
-2
-2,5
-3
-3,5
-4
-4,5
0
2
4
6
8
h (mm)
LDA-L
LDA-R
CFD
theor.

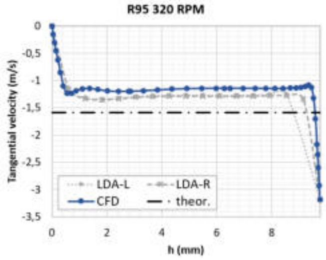
R95 320 RPM
Tangential velocity (m/s)
0
-0,5
-1
-1,5
-2
-2,5
-3
-3,5
0
2
4
6
8
h (mm)
LDA-L
LDA-R
CFD
theor.

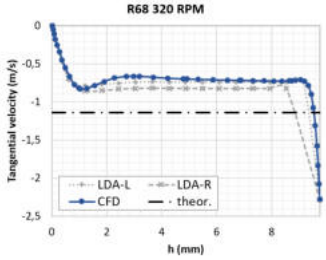
R68 320 RPM
Tangential velocity (m/s)
0
-0,5
-1
-1,5
-2
-2,5
0
2
4
6
8
h (mm)
LDA-L
LDA-R
CFD
theor.

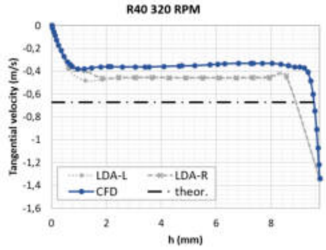
R40 320 RPM
Tangential velocity (m/s)
0
-0,2
-0,4
-0,6
-0,8
-1
-1,2
-1,4
-1,6
0
2
4
6
8
h (mm)
LDA-L
LDA-R
CFD
theor.

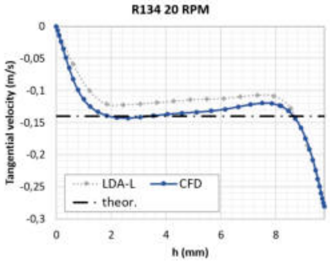
R134 20 RPM
Tangential velocity (m/s)
0
-0,05
-0,1
-0,15
-0,2
-0,25
-0,3
0
2
4
6
8
h (mm)
LDA-L
CFD
theor.

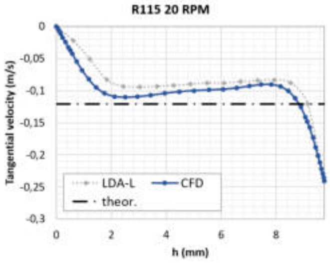
R115 20 RPM
Tangential velocity (m/s)
0
-0,05
-0,1
-0,15
-0,2
-0,25
-0,3
0
2
4
6
8
h (mm)
LDA-L
CFD
theor.

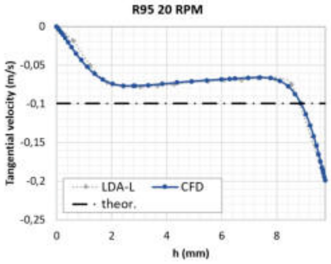
R95 20 RPM
Tangential velocity (m/s)
0
-0,05
-0,1
-0,15
-0,2
-0,25
0
2
4
6
8
h (mm)
LDA-L
CFD
theor.

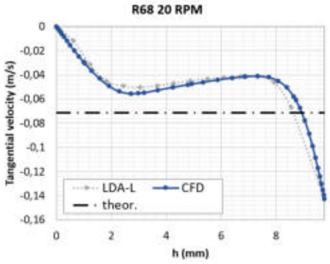
R68 20 RPM
Tangential velocity (m/s)
0
-0,02
-0,04
-0,06
-0,08
-0,1
-0,12
-0,14
-0,16
0
2
4
6
8
h (mm)
LDA-L
CFD
theor.

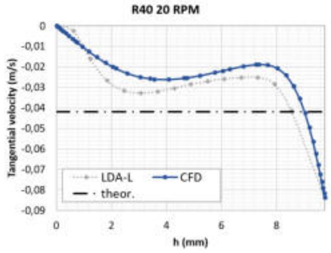
R40 20 RPM
Tangential velocity (m/s)
0
-0,01
-0,02
-0,03
-0,04
-0,05
-0,06
-0,07
-0,08
-0,09
0
2
4
6
8
h (mm)
LDA-L
CFD
theor.

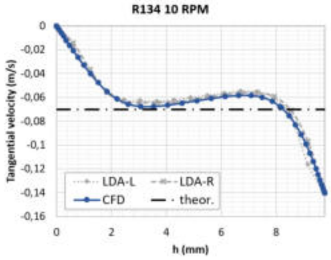
R134 10 RPM
Tangential velocity (m/s)
0
-0,02
-0,04
-0,06
-0,08
-0,1
-0,12
-0,14
-0,16
0
2
4
6
8
h (mm)
LDA-L
LDA-R
CFD
theor.

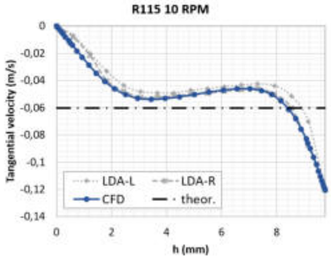
R115 10 RPM
Tangential velocity (m/s)
0
-0,02
-0,04
-0,06
-0,08
-0,1
-0,12
-0,14
0
2
4
6
8
h (mm)
LDA-L
LDA-R
CFD
theor.

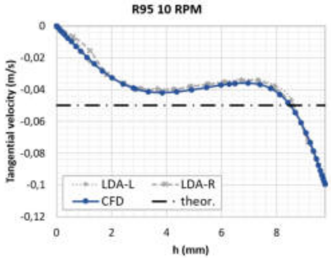
R95 10 RPM
Tangential velocity (m/s)
0
-0,02
-0,04
-0,06
-0,08
-0,1
-0,12
0
2
4
6
8
h (mm)
LDA-L
LDA-R
CFD
theor.

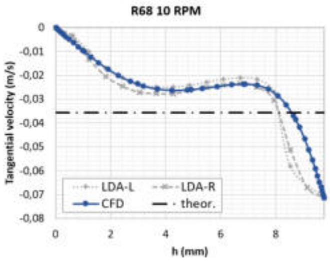

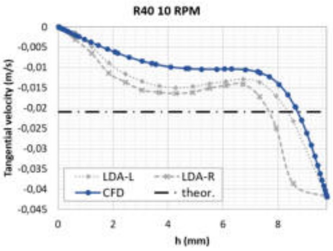

Gap width h_2

320 RPM

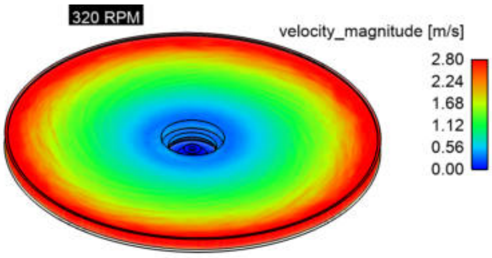

320 RPM

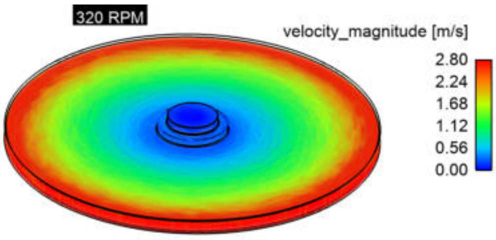

160 RPM

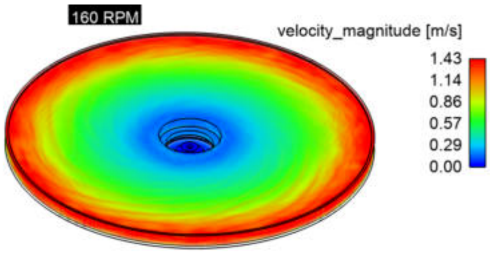

160 RPM

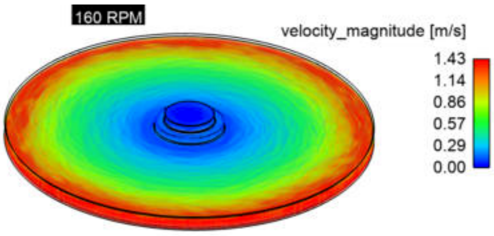

80 RPM

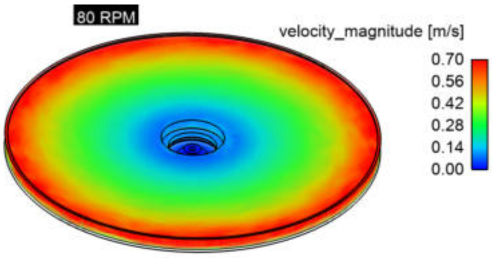

80 RPM

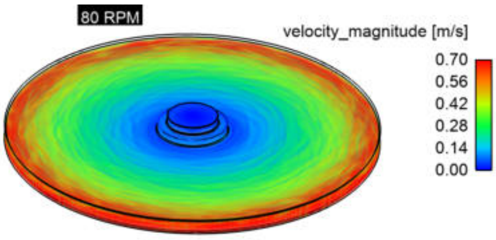

40 RPM

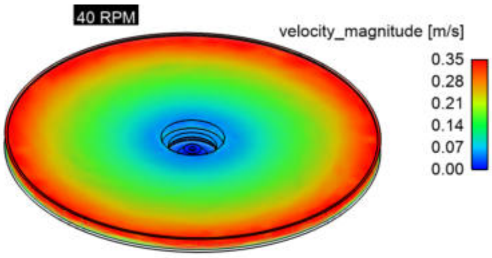

40 RPM

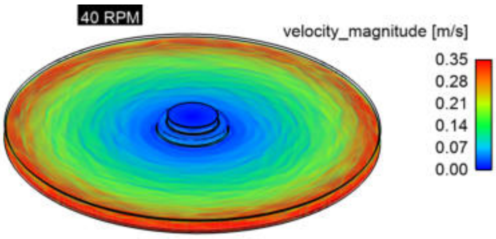

20 RPM

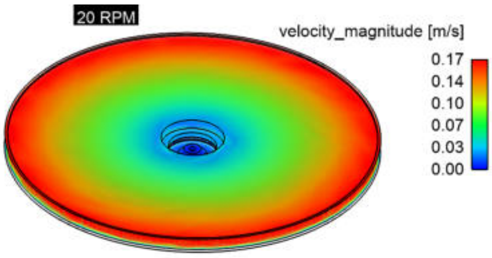

20 RPM

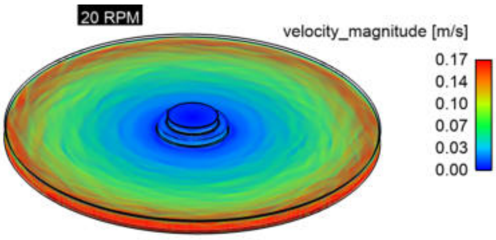

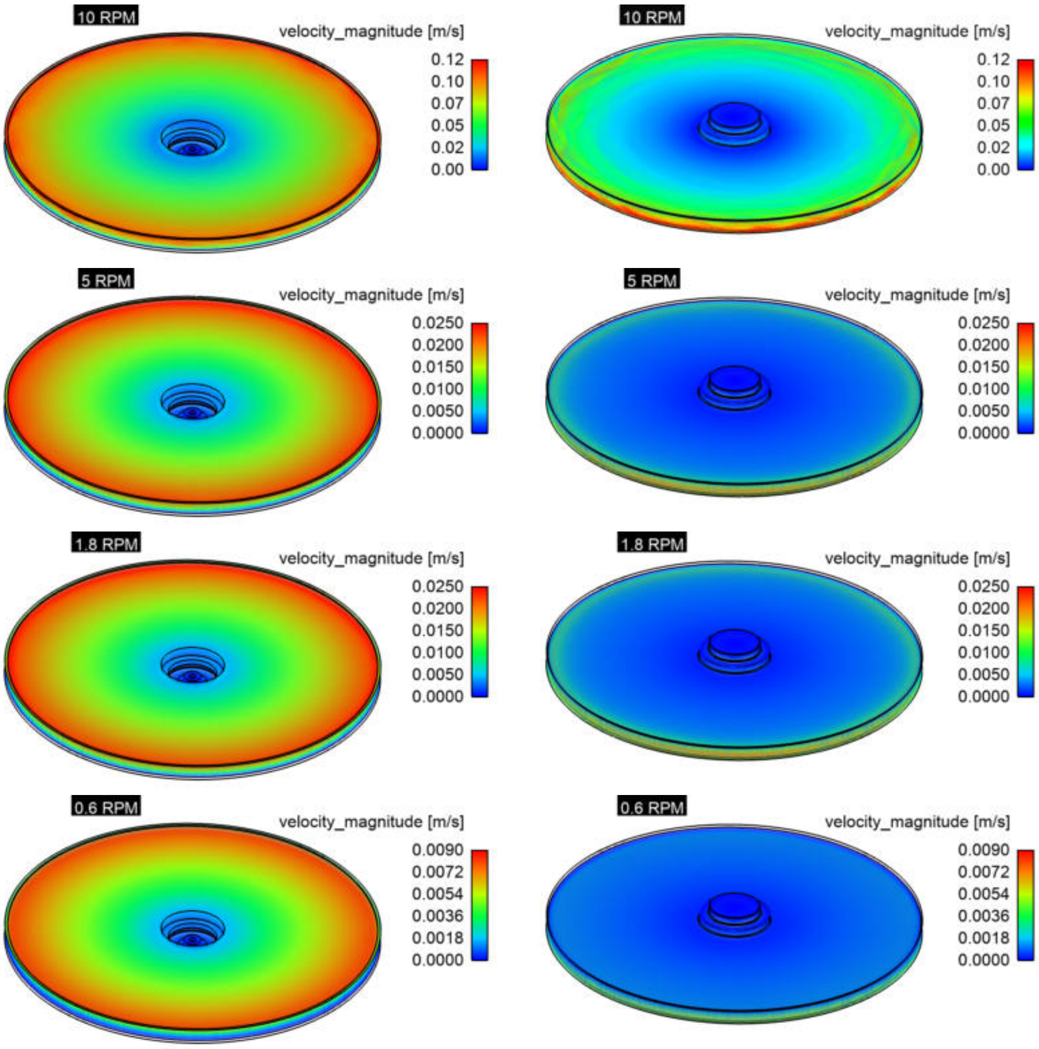
10 RPM
velocity_magnitude [m/s]
0.12
0.10
0.07
0.05
0.02
0.00
10 RPM
velocity_magnitude [m/s]
0.12
0.10
0.07
0.05
0.02
0.00
5 RPM
velocity_magnitude [m/s]
0.0250
0.0200
0.0150
0.0100
0.0050
0.0000
5 RPM
velocity_magnitude [m/s]
0.0250
0.0200
0.0150
0.0100
0.0050
0.0000
1.8 RPM
velocity_magnitude [m/s]
0.0250
0.0200
0.0150
0.0100
0.0050
0.0000
1.8 RPM
velocity_magnitude [m/s]
0.0250
0.0200
0.0150
0.0100
0.0050
0.0000
0.6 RPM
velocity_magnitude [m/s]
0.0090
0.0072
0.0054
0.0036
0.0018
0.0000
0.6 RPM
velocity_magnitude [m/s]
0.0090
0.0072
0.0054
0.0036
0.0018
0.0000

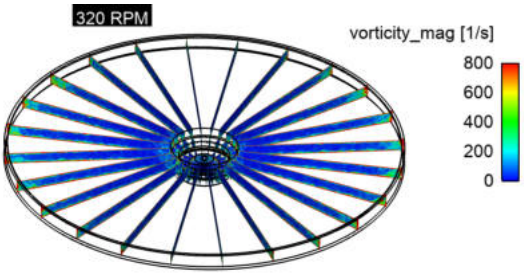
320 RPM

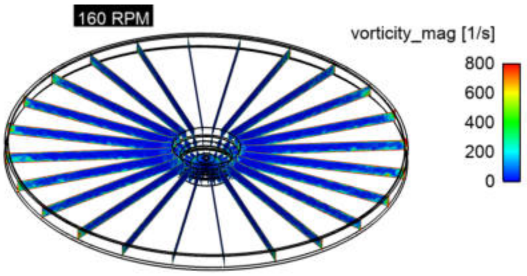
160 RPM

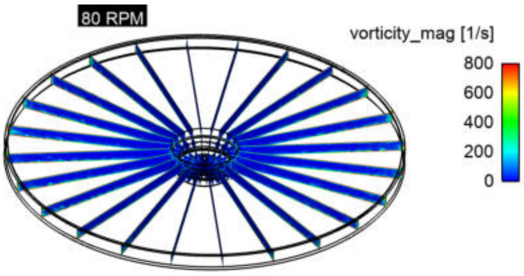
80 RPM

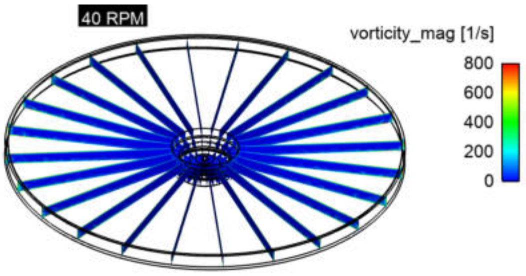
40 RPM

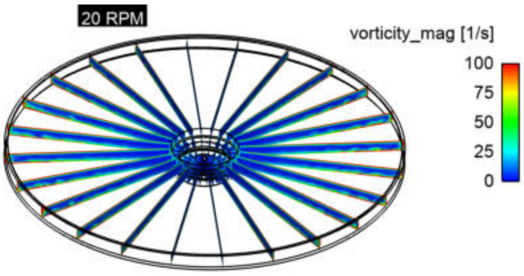
20 RPM

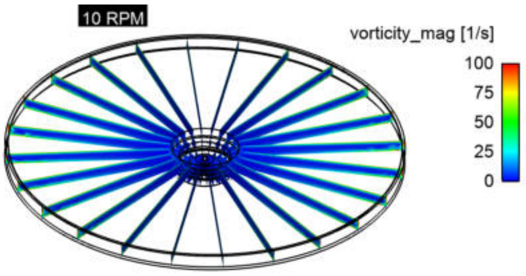
10 RPM

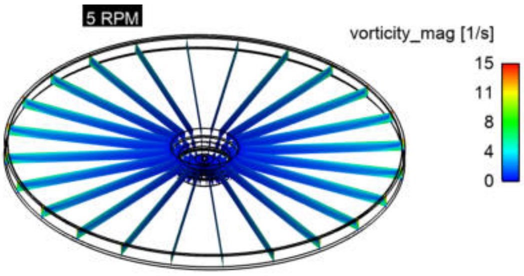
5 RPM

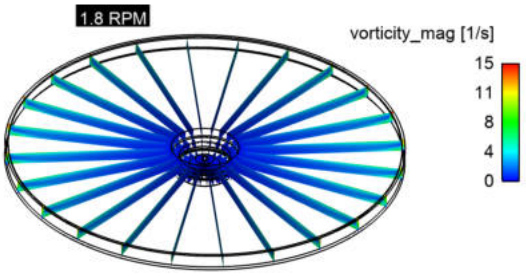
1.8 RPM

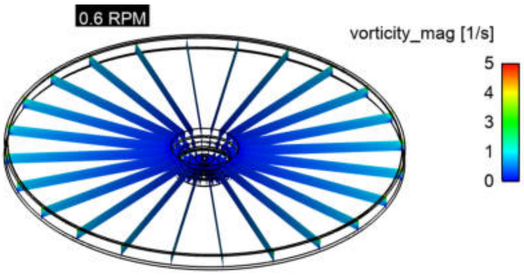
0.6 RPM

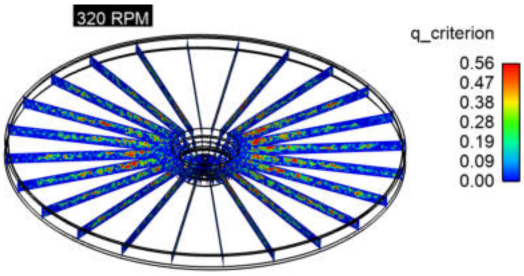
320 RPM
q_criterion
0.56
0.47
0.38
0.28
0.19
0.09
0.00

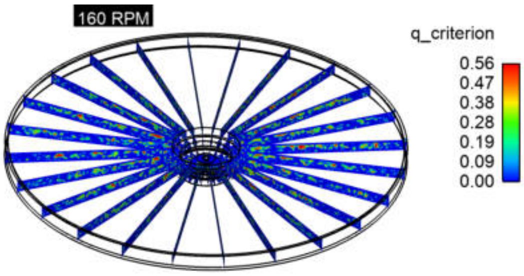
160 RPM
q_criterion
0.56
0.47
0.38
0.28
0.19
0.09
0.00

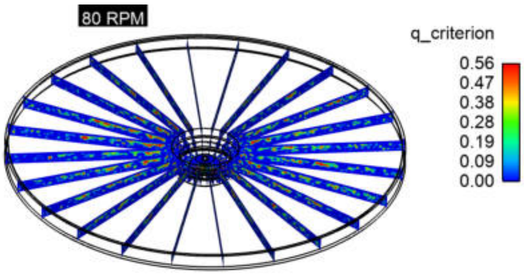
80 RPM
q_criterion
0.56
0.47
0.38
0.28
0.19
0.09
0.00

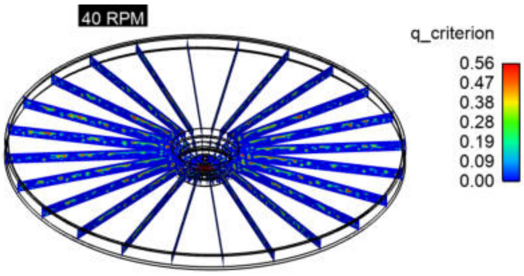
40 RPM
q_criterion
0.56
0.47
0.38
0.28
0.19
0.09
0.00

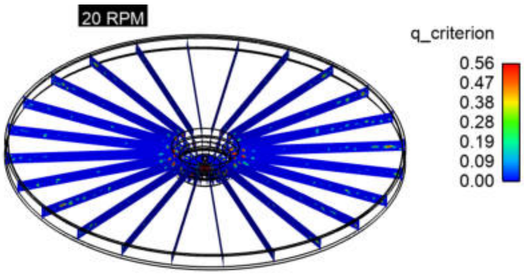
20 RPM
q_criterion
0.56
0.47
0.38
0.28
0.19
0.09
0.00

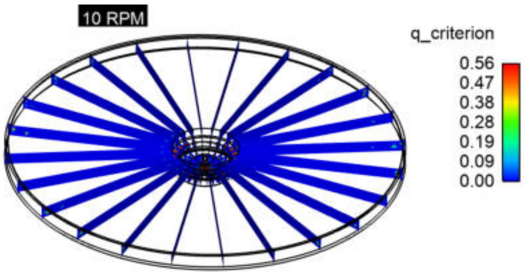
10 RPM
q_criterion
0.56
0.47
0.38
0.28
0.19
0.09
0.00

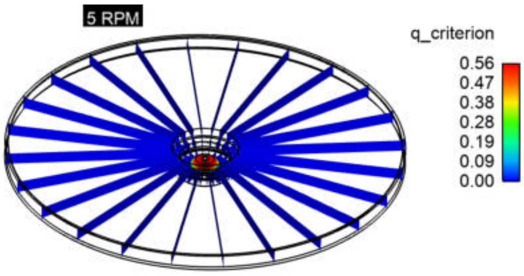
5 RPM
q_criterion
0.56
0.47
0.38
0.28
0.19
0.09
0.00


1.8 RPM
q_criterion
0.56
0.47
0.38
0.28
0.19
0.09
0.00


0.6 RPM
q_criterion
0.56
0.47
0.38
0.28
0.19
0.09
0.00

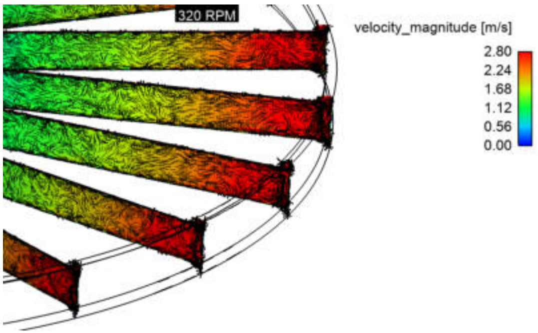
320 RPM
velocity_magnitude [m/s]
2.80
2.24
1.68
1.12
0.56
0.00

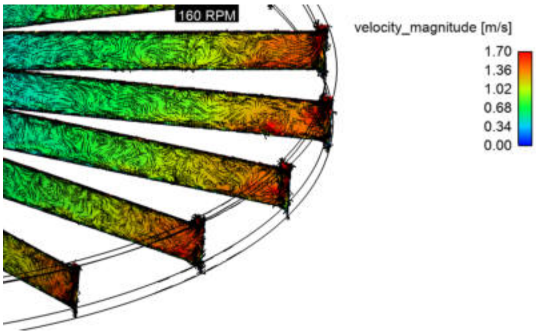
160 RPM
velocity_magnitude [m/s]
1.70
1.36
1.02
0.68
0.34
0.00

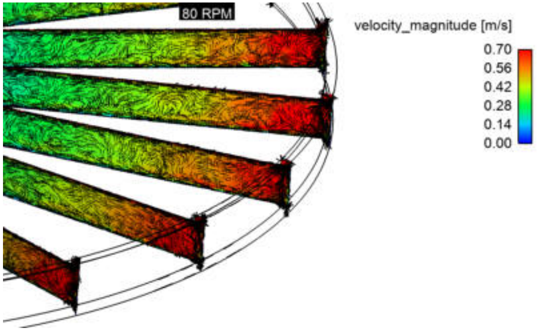
80 RPM
velocity_magnitude [m/s]
0.70
0.56
0.42
0.28
0.14
0.00

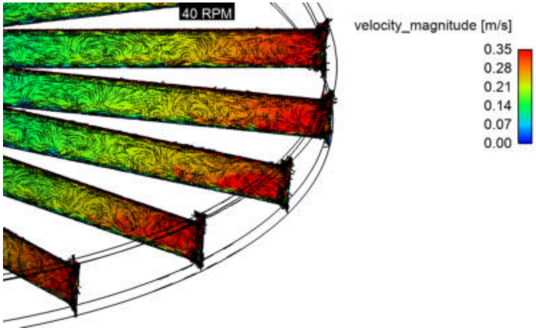
40 RPM
velocity_magnitude [m/s]
0.35
0.28
0.21
0.14
0.07
0.00

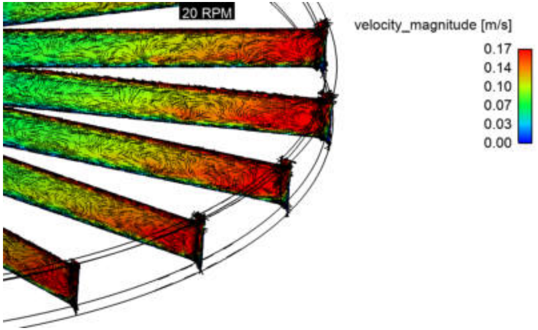
20 RPM
velocity_magnitude [m/s]
0.17
0.14
0.10
0.07
0.03
0.00

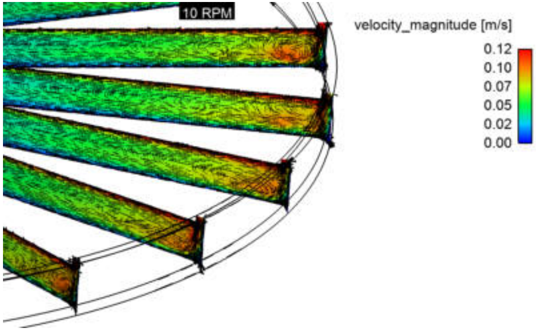
10 RPM
velocity_magnitude [m/s]
0.12
0.10
0.07
0.05
0.02
0.00

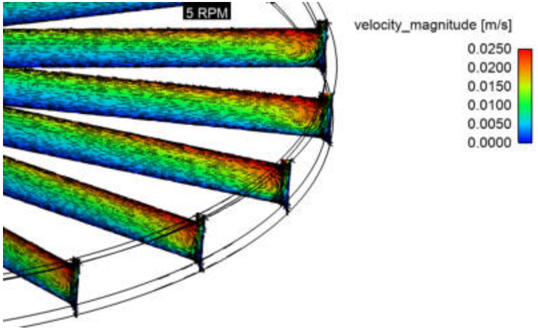
5 RPM
velocity_magnitude [m/s]
0.0250
0.0200
0.0150
0.0100
0.0050
0.0000

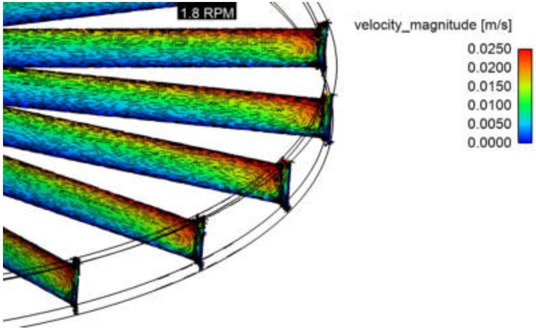
1.8 RPM
velocity_magnitude [m/s]
0.0250
0.0200
0.0150
0.0100
0.0050
0.0000

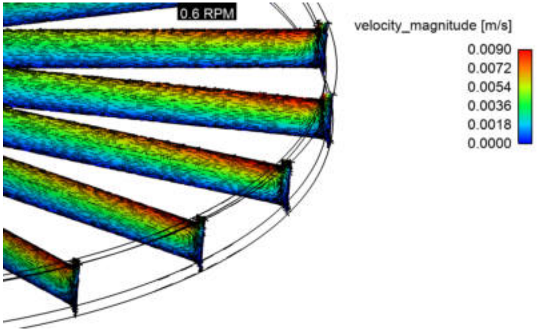
0.6 RPM
velocity_magnitude [m/s]
0.0090
0.0072
0.0054
0.0036
0.0018
0.0000

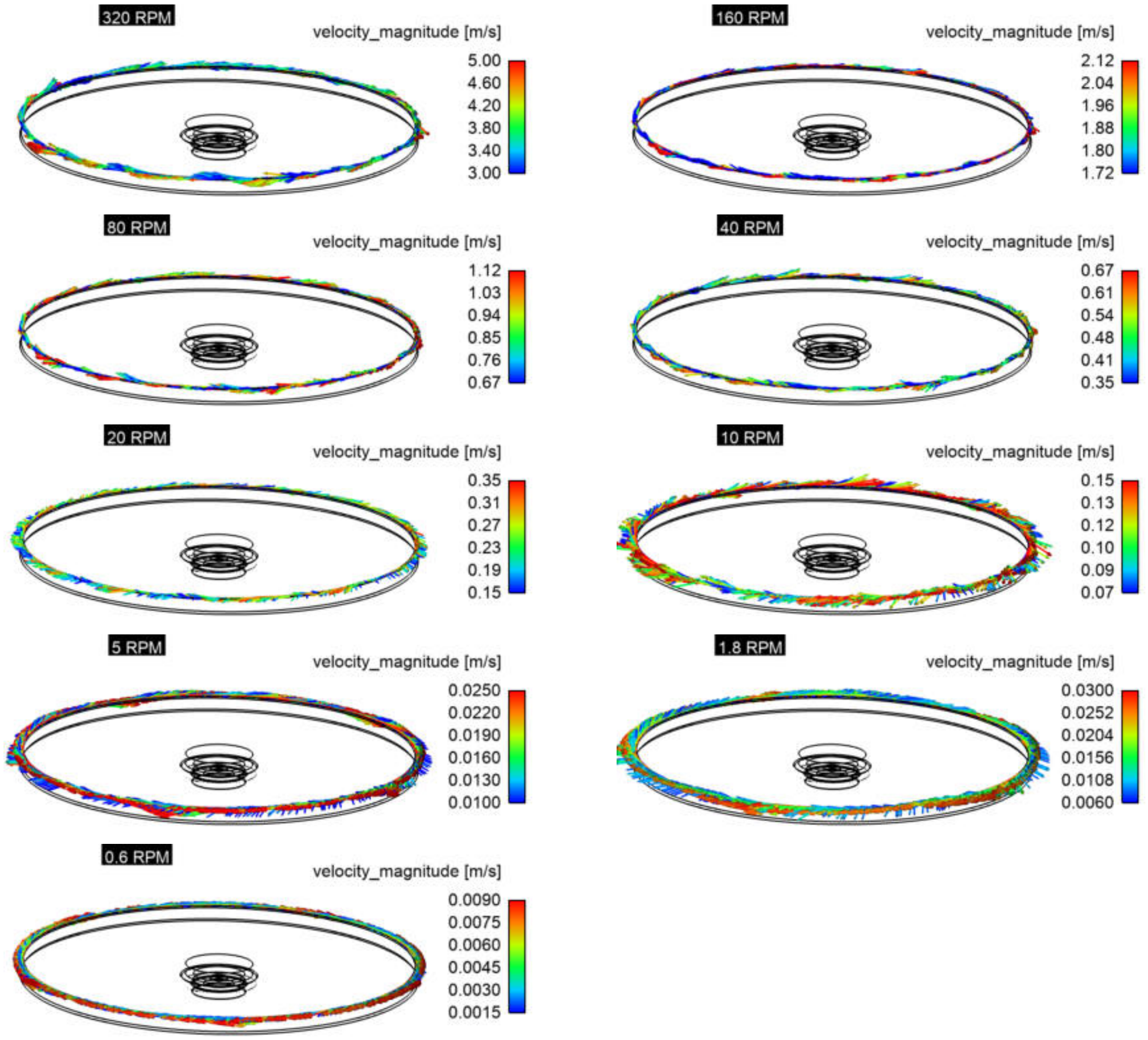
320 RPM
velocity_magnitude [m/s]
5.00
4.60
4.20
3.80
3.40
3.00
160 RPM
velocity_magnitude [m/s]
2.12
2.04
1.96
1.88
1.80
1.72
80 RPM
velocity_magnitude [m/s]
1.12
1.03
0.94
0.85
0.76
0.67
40 RPM
velocity_magnitude [m/s]
0.67
0.61
0.54
0.48
0.41
0.35
20 RPM
velocity_magnitude [m/s]
0.35
0.31
0.27
0.23
0.19
0.15
10 RPM
velocity_magnitude [m/s]
0.15
0.13
0.12
0.10
0.09
0.07
5 RPM
velocity_magnitude [m/s]
0.0250
0.0220
0.0190
0.0160
0.0130
0.0100
1.8 RPM
velocity_magnitude [m/s]
0.0300
0.0252
0.0204
0.0156
0.0108
0.0060
0.6 RPM
velocity_magnitude [m/s]
0.0090
0.0075
0.0060
0.0045
0.0030
0.0015

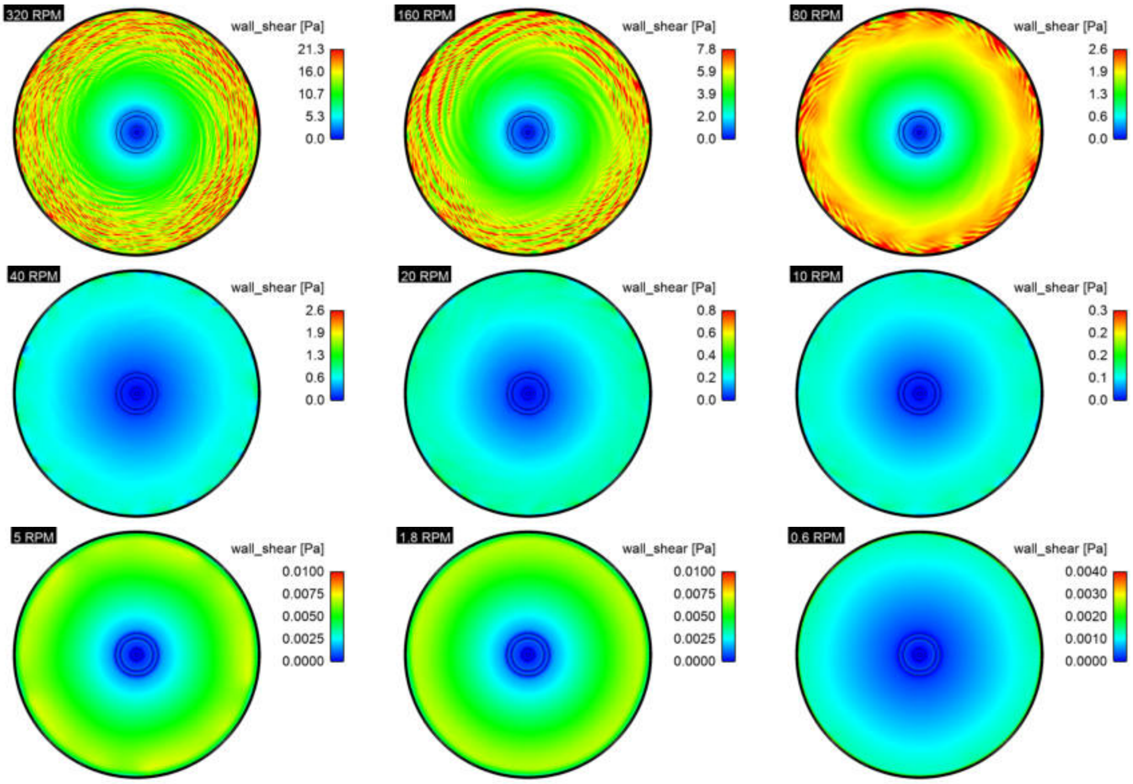
320 RPM
wall_shear [Pa]
21.3
16.0
10.7
5.3
0.0
160 RPM
wall_shear [Pa]
7.8
5.9
3.9
2.0
0.0
80 RPM
wall_shear [Pa]
2.6
1.9
1.3
0.6
0.0
40 RPM
wall_shear [Pa]
2.6
1.9
1.3
0.6
0.0
20 RPM
wall_shear [Pa]
0.8
0.6
0.4
0.2
0.0
10 RPM
wall_shear [Pa]
0.3
0.2
0.2
0.1
0.0
5 RPM
wall_shear [Pa]
0.0100
0.0075
0.0050
0.0025
0.0000
1.8 RPM
wall_shear [Pa]
0.0100
0.0075
0.0050
0.0025
0.0000
0.6 RPM
wall_shear [Pa]
0.0040
0.0030
0.0020
0.0010
0.0000

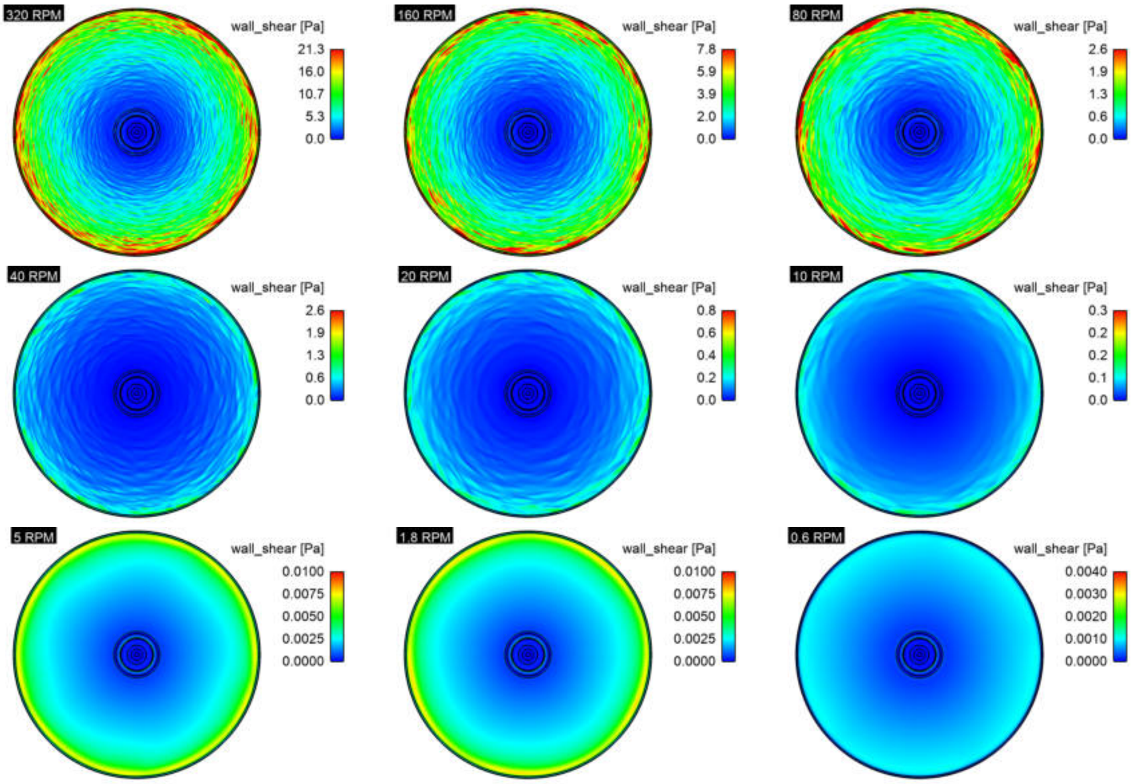
320 RPM
wall_shear [Pa]
21.3
16.0
10.7
5.3
0.0
160 RPM
wall_shear [Pa]
7.8
5.9
3.9
2.0
0.0
80 RPM
wall_shear [Pa]
2.6
1.9
1.3
0.6
0.0
40 RPM
wall_shear [Pa]
2.6
1.9
1.3
0.6
0.0
20 RPM
wall_shear [Pa]
0.8
0.6
0.4
0.2
0.0
10 RPM
wall_shear [Pa]
0.3
0.2
0.2
0.1
0.0
5 RPM
wall_shear [Pa]
0.0100
0.0075
0.0050
0.0025
0.0000
1.8 RPM
wall_shear [Pa]
0.0100
0.0075
0.0050
0.0025
0.0000
0.6 RPM
wall_shear [Pa]
0.0040
0.0030
0.0020
0.0010
0.0000

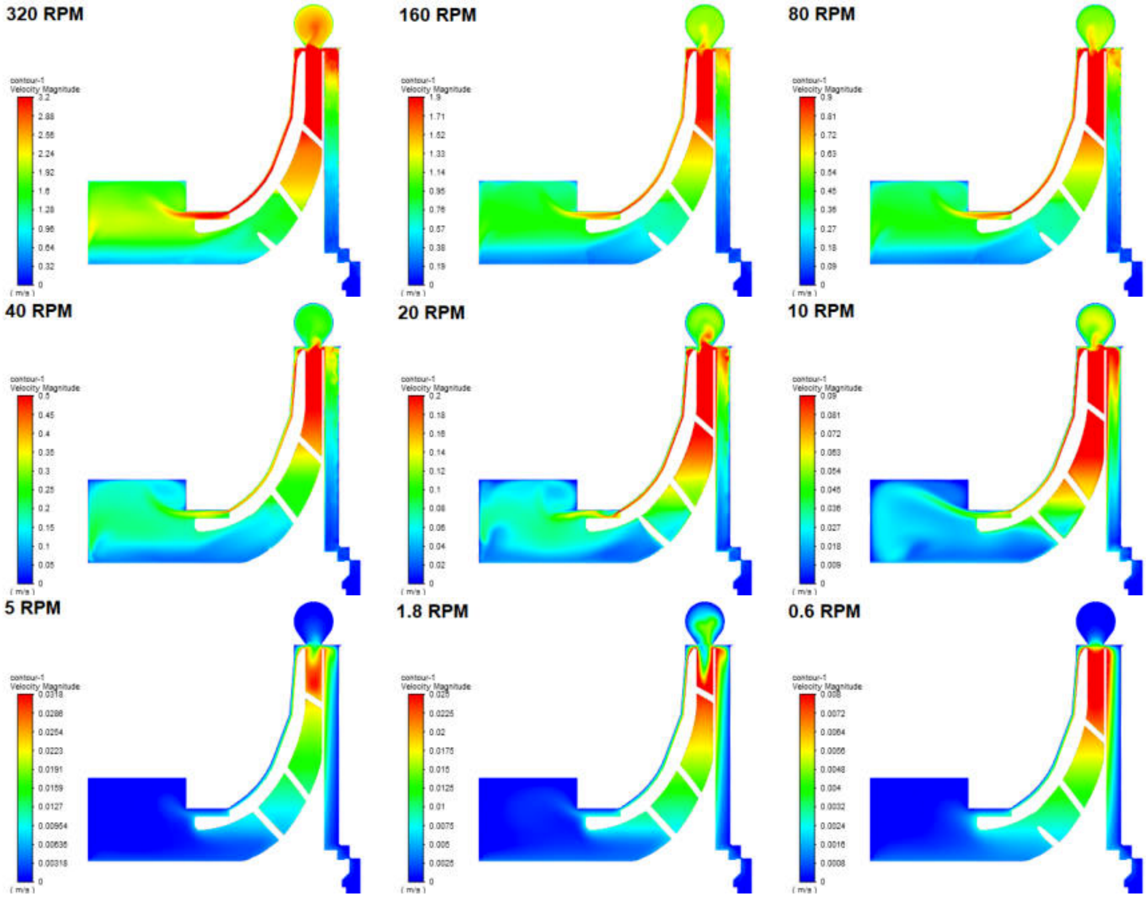
320 RPM
contour-1
Velocity Magnitude
3.2
2.88
2.56
2.24
1.92
1.6
1.28
0.96
0.64
0.32
0
(m/s)
160 RPM
contour-1
Velocity Magnitude
1.9
1.71
1.52
1.33
1.14
0.95
0.76
0.57
0.38
0.19
0
(m/s)
80 RPM
contour-1
Velocity Magnitude
0.9
0.81
0.72
0.63
0.54
0.45
0.36
0.27
0.18
0.09
0
(m/s)
40 RPM
contour-1
Velocity Magnitude
0.5
0.45
0.4
0.35
0.3
0.25
0.2
0.15
0.1
0.05
0
(m/s)
20 RPM
contour-1
Velocity Magnitude
0.2
0.18
0.16
0.14
0.12
0.1
0.08
0.06
0.04
0.02
0
(m/s)
10 RPM
contour-1
Velocity Magnitude
0.09
0.081
0.072
0.063
0.054
0.045
0.036
0.027
0.018
0.009
0
(m/s)
5 RPM
contour-1
Velocity Magnitude
0.0318
0.0286
0.0254
0.0223
0.0191
0.0159
0.0127
0.00954
0.00636
0.00318
0
(m/s)
1.8 RPM
contour-1
Velocity Magnitude
0.025
0.0225
0.02
0.0175
0.015
0.0125
0.01
0.0075
0.005
0.0025
0
(m/s)
0.6 RPM
contour-1
Velocity Magnitude
0.008
0.0072
0.0064
0.0056
0.0048
0.004
0.0032
0.0024
0.0016
0.0008
0
(m/s)

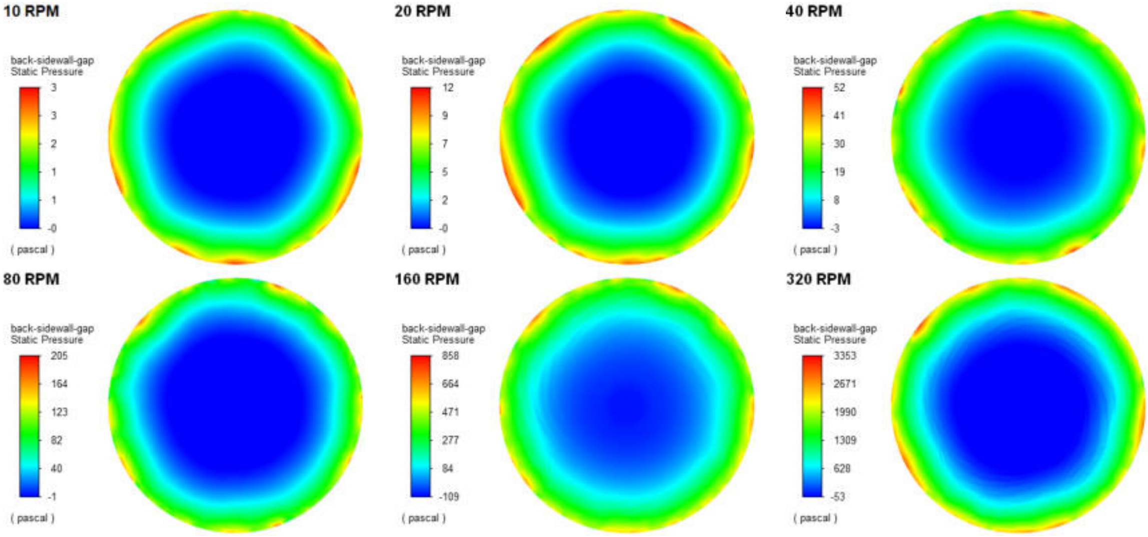
10 RPM
back-sidewall-gap
Static Pressure
3
3
2
1
1
-0
(pascal)
20 RPM
back-sidewall-gap
Static Pressure
12
9
7
5
2
-0
(pascal)
40 RPM
back-sidewall-gap
Static Pressure
52
41
30
19
8
-3
(pascal)
80 RPM
back-sidewall-gap
Static Pressure
205
164
123
82
40
-1
(pascal)
160 RPM
back-sidewall-gap
Static Pressure
858
664
471
277
84
-109
(pascal)
320 RPM
back-sidewall-gap
Static Pressure
3353
2671
1990
1309
628
-53
(pascal)

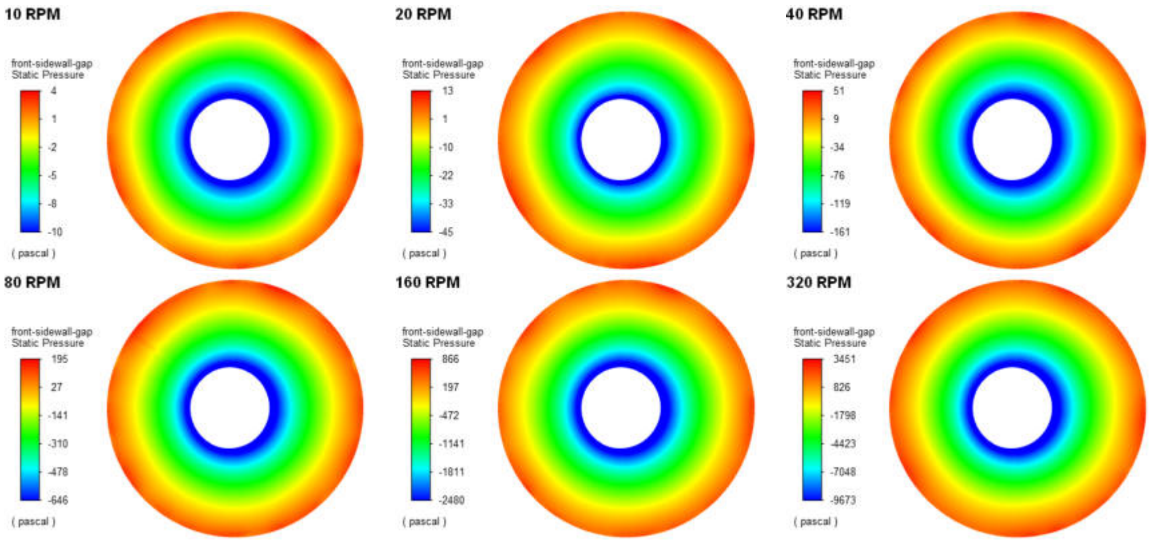
10 RPM
front-sidewall-gap Static Pressure
4
1
-2
-5
-8
-10
(pascal)
20 RPM
front-sidewall-gap Static Pressure
13
1
-10
-22
-33
-45
(pascal)
40 RPM
front-sidewall-gap Static Pressure
51
9
-34
-76
-119
-161
(pascal)
80 RPM
front-sidewall-gap Static Pressure
195
27
-141
-310
-478
-646
(pascal)
160 RPM
front-sidewall-gap Static Pressure
866
197
-472
-1141
-1811
-2480
(pascal)
320 RPM
front-sidewall-gap Static Pressure
3451
826
-1798
-4423
-7048
-9673
(pascal)

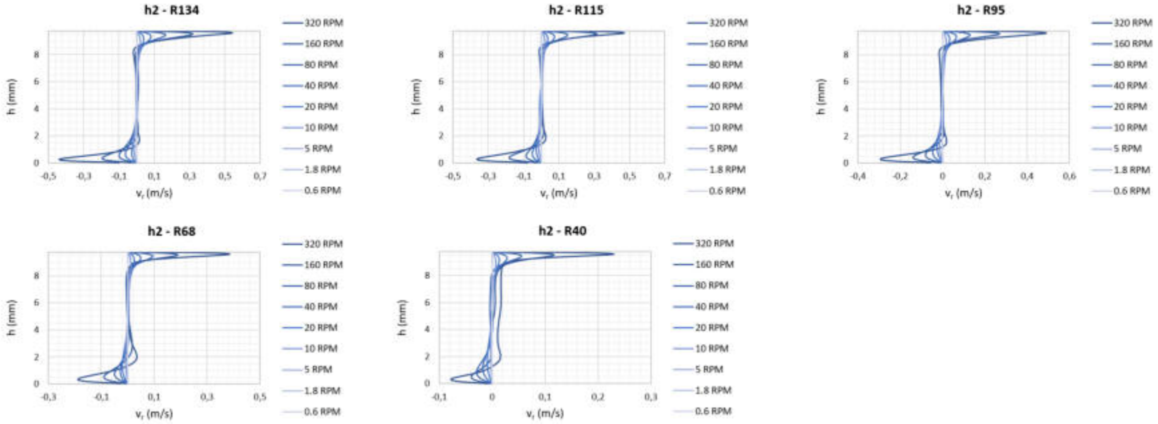
h2 - R134
h (mm)
0
2
4
6
8
-0,5
-0,3
-0,1
0,1
0,3
0,5
0,7
v_r (m/s)
h2 - R115
h (mm)
-0,5
-0,3
-0,1
0,1
0,3
0,5
0,7
v_r (m/s)
h2 - R95
h (mm)
-0,4
-0,2
0
0,2
0,4
0,6
v_r (m/s)
h2 - R68
h (mm)
-0,3
-0,1
0,1
0,3
0,5
v_r (m/s)
h2 - R40
h (mm)
-0,1
0
0,1
0,2
0,3
v_r (m/s)
320 RPM
160 RPM
80 RPM
40 RPM
20 RPM
10 RPM
5 RPM
1.8 RPM
0.6 RPM

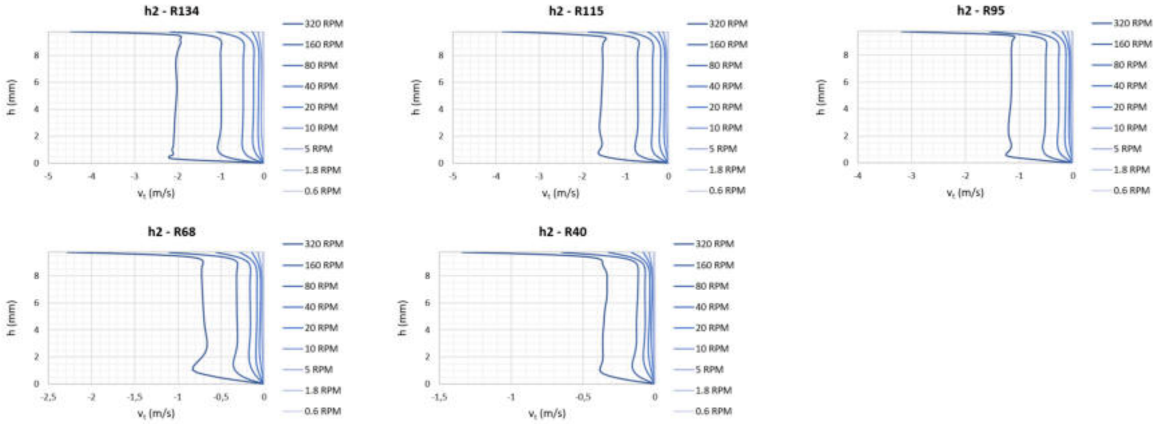
h2 - R134
h (mm)
0
2
4
6
8
-5
-4
-3
-2
-1
0
v_t (m/s)
h2 - R115
h (mm)
-5
-4
-3
-2
-1
0
v_t (m/s)
h2 - R95
h (mm)
-4
-3
-2
-1
0
v_t (m/s)
h2 - R68
h (mm)
-2,5
-2
-1,5
-1
-0,5
0
v_t (m/s)
h2 - R40
h (mm)
-1,5
-1
-0,5
0
v_t (m/s)
320 RPM
160 RPM
80 RPM
40 RPM
20 RPM
10 RPM
5 RPM
1.8 RPM
0.6 RPM

Gap width h_1

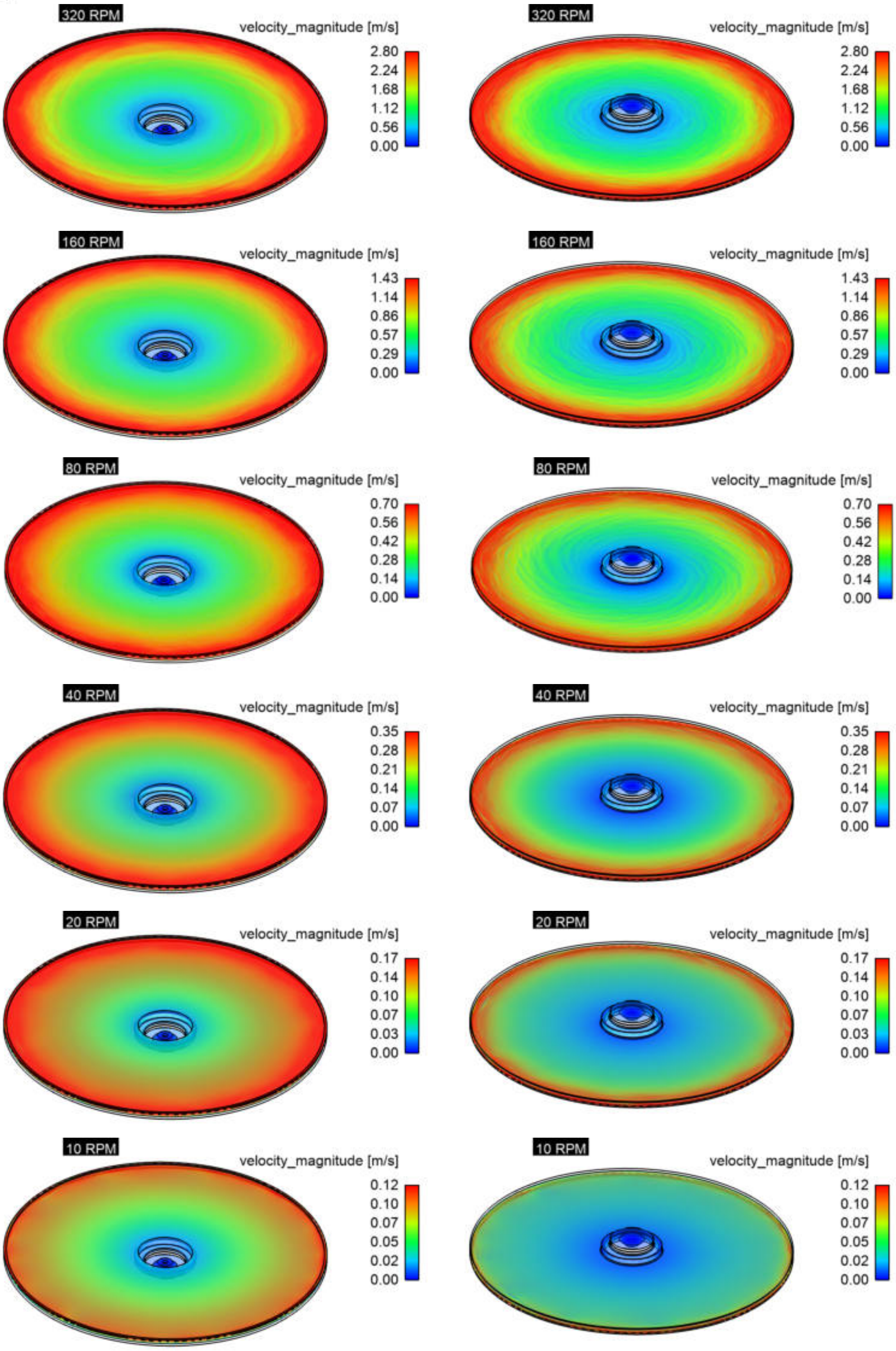
320 RPM
velocity_magnitude [m/s]
2.80
2.24
1.68
1.12
0.56
0.00
320 RPM
velocity_magnitude [m/s]
2.80
2.24
1.68
1.12
0.56
0.00
160 RPM
velocity_magnitude [m/s]
1.43
1.14
0.86
0.57
0.29
0.00
160 RPM
velocity_magnitude [m/s]
1.43
1.14
0.86
0.57
0.29
0.00
80 RPM
velocity_magnitude [m/s]
0.70
0.56
0.42
0.28
0.14
0.00
80 RPM
velocity_magnitude [m/s]
0.70
0.56
0.42
0.28
0.14
0.00
40 RPM
velocity_magnitude [m/s]
0.35
0.28
0.21
0.14
0.07
0.00
40 RPM
velocity_magnitude [m/s]
0.35
0.28
0.21
0.14
0.07
0.00
20 RPM
velocity_magnitude [m/s]
0.17
0.14
0.10
0.07
0.03
0.00
20 RPM
velocity_magnitude [m/s]
0.17
0.14
0.10
0.07
0.03
0.00
10 RPM
velocity_magnitude [m/s]
0.12
0.10
0.07
0.05
0.02
0.00
10 RPM
velocity_magnitude [m/s]
0.12
0.10
0.07
0.05
0.02
0.00

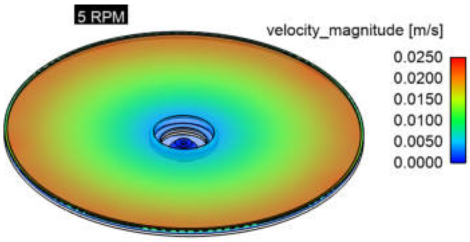
5 RPM
velocity_magnitude [m/s]
0.0250
0.0200
0.0150
0.0100
0.0050
0.0000

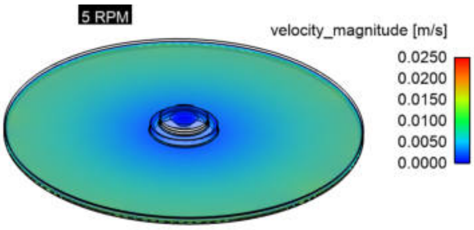
5 RPM
velocity_magnitude [m/s]
0.0250
0.0200
0.0150
0.0100
0.0050
0.0000

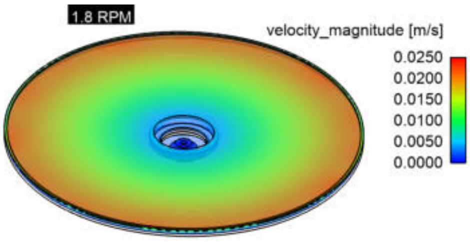
1.8 RPM
velocity_magnitude [m/s]
0.0250
0.0200
0.0150
0.0100
0.0050
0.0000

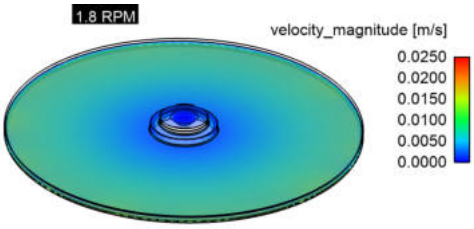
1.8 RPM
velocity_magnitude [m/s]
0.0250
0.0200
0.0150
0.0100
0.0050
0.0000

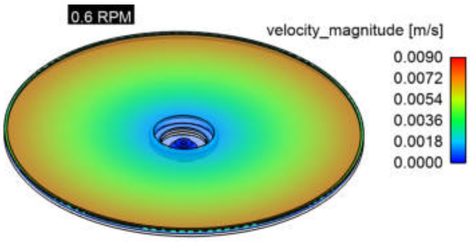
0.6 RPM
velocity_magnitude [m/s]
0.0090
0.0072
0.0054
0.0036
0.0018
0.0000

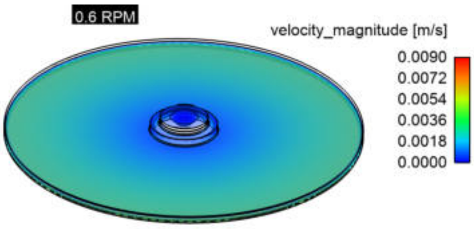
0.6 RPM
velocity_magnitude [m/s]
0.0090
0.0072
0.0054
0.0036
0.0018
0.0000

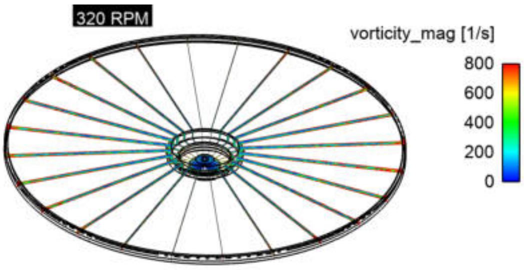
320 RPM
vorticity_mag [1/s]
800
600
400
200
0

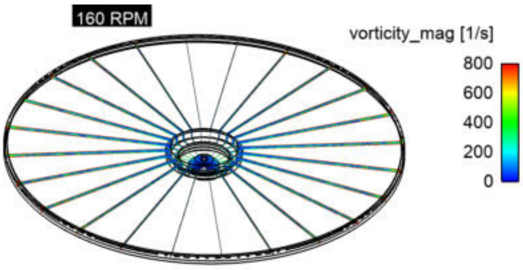
160 RPM
vorticity_mag [1/s]
800
600
400
200
0

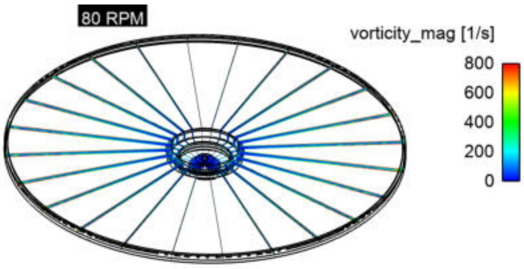
80 RPM
vorticity_mag [1/s]
800
600
400
200
0

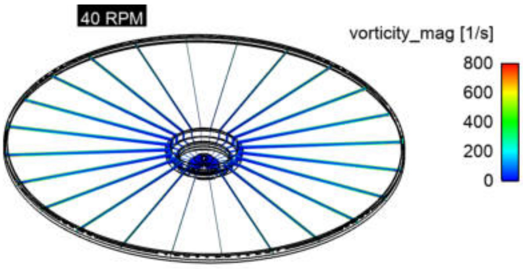
40 RPM
vorticity_mag [1/s]
800
600
400
200
0

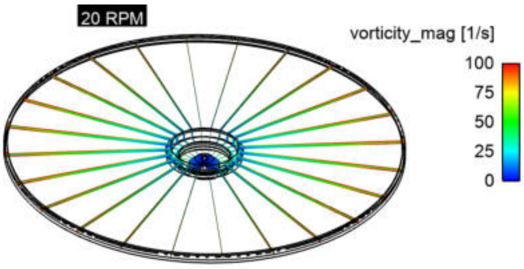
20 RPM
vorticity_mag [1/s]
100
75
50
25
0

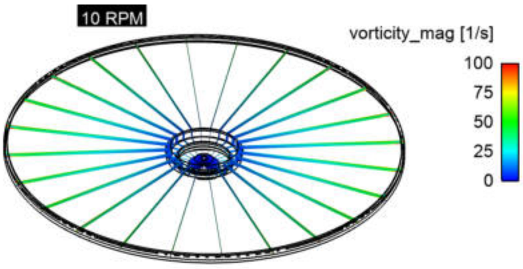
10 RPM
vorticity_mag [1/s]
100
75
50
25
0

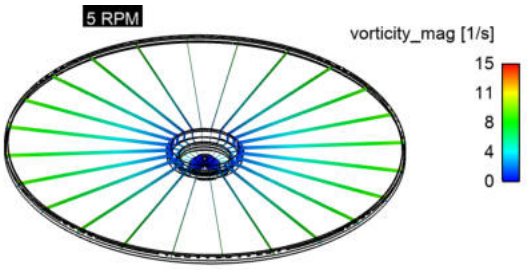
5 RPM
vorticity_mag [1/s]
15
11
8
4
0

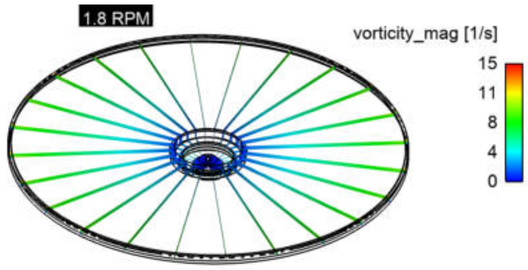
1.8 RPM
vorticity_mag [1/s]
15
11
8
4
0

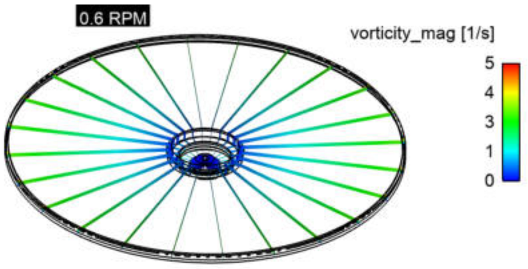
0.6 RPM
vorticity_mag [1/s]
5
4
3
1
0

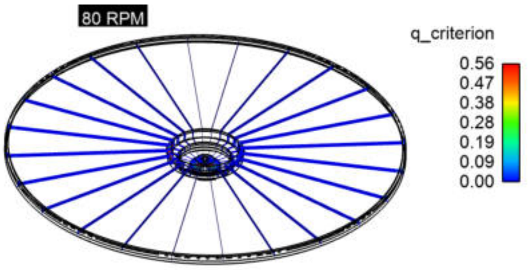
80 RPM
q_criterion
0.56
0.47
0.38
0.28
0.19
0.09
0.00


40 RPM
q_criterion
0.56
0.47
0.38
0.28
0.19
0.09
0.00

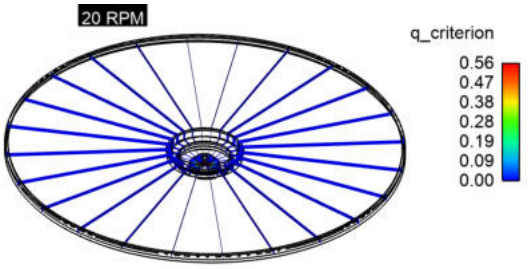
20 RPM
q_criterion
0.56
0.47
0.38
0.28
0.19
0.09
0.00


10 RPM
q_criterion
0.56
0.47
0.38
0.28
0.19
0.09
0.00

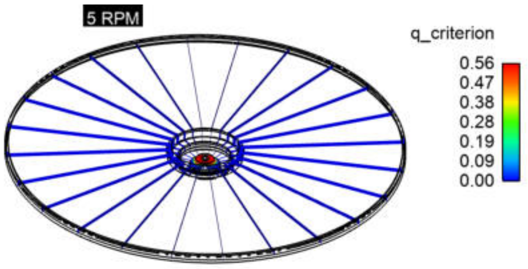
5 RPM
q_criterion
0.56
0.47
0.38
0.28
0.19
0.09
0.00


1.8 RPM
q_criterion
0.56
0.47
0.38
0.28
0.19
0.09
0.00

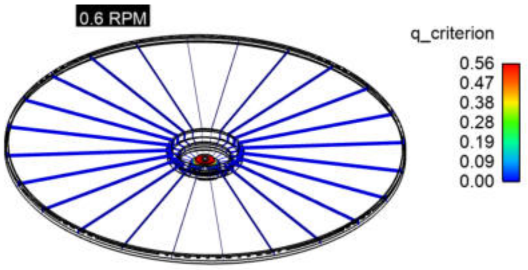
0.6 RPM
q_criterion
0.56
0.47
0.38
0.28
0.19
0.09
0.00

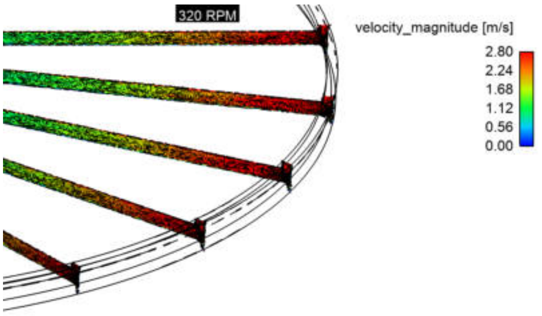
320 RPM
velocity_magnitude [m/s]
2.80
2.24
1.68
1.12
0.56
0.00

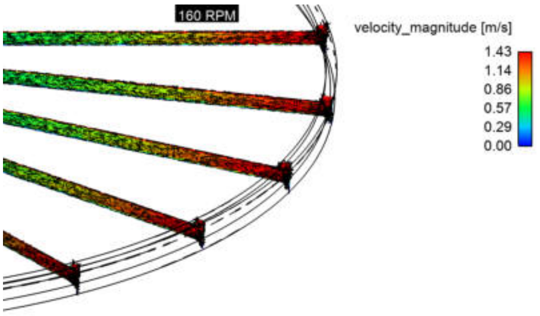
160 RPM
velocity_magnitude [m/s]
1.43
1.14
0.86
0.57
0.29
0.00

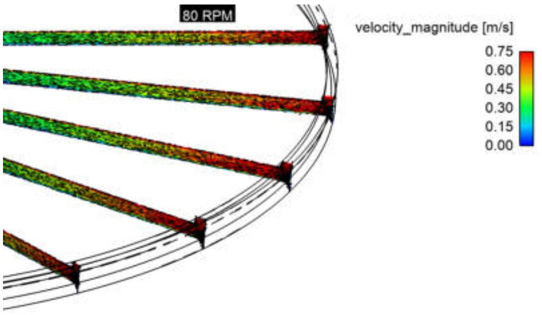
80 RPM
velocity_magnitude [m/s]
0.75
0.60
0.45
0.30
0.15
0.00

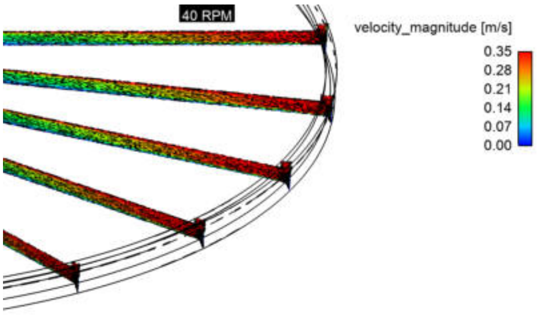
40 RPM
velocity_magnitude [m/s]
0.35
0.28
0.21
0.14
0.07
0.00

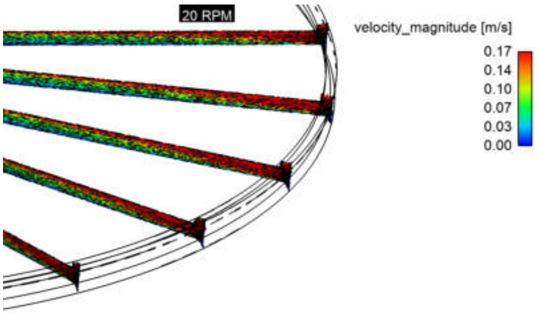
20 RPM
velocity_magnitude [m/s]
0.17
0.14
0.10
0.07
0.03
0.00

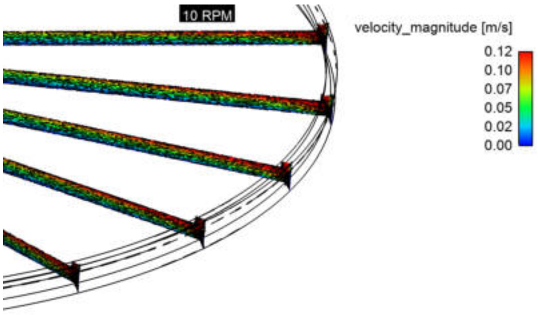
10 RPM
velocity_magnitude [m/s]
0.12
0.10
0.07
0.05
0.02
0.00

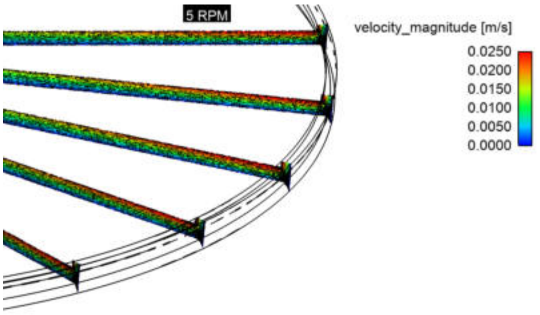
5 RPM
velocity_magnitude [m/s]
0.0250
0.0200
0.0150
0.0100
0.0050
0.0000

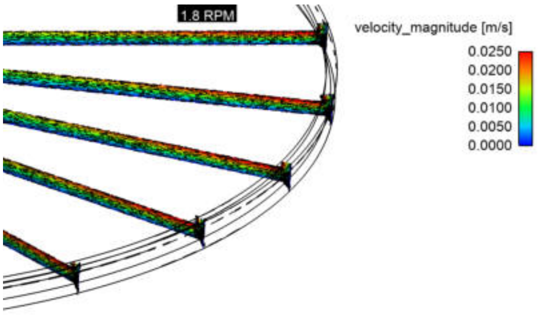
1.8 RPM
velocity_magnitude [m/s]
0.0250
0.0200
0.0150
0.0100
0.0050
0.0000

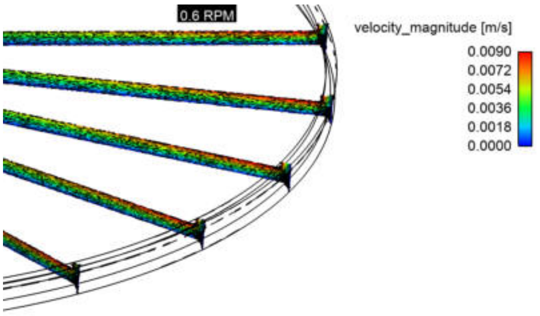
0.6 RPM
velocity_magnitude [m/s]
0.0090
0.0072
0.0054
0.0036
0.0018
0.0000

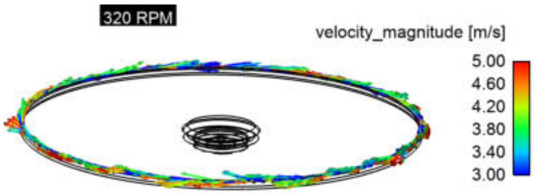
320 RPM
velocity_magnitude [m/s]
5.00
4.60
4.20
3.80
3.40
3.00

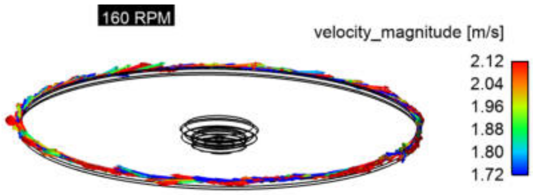
160 RPM
velocity_magnitude [m/s]
2.12
2.04
1.96
1.88
1.80
1.72

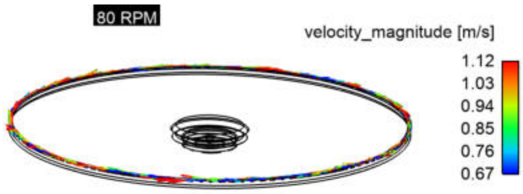
80 RPM
velocity_magnitude [m/s]
1.12
1.03
0.94
0.85
0.76
0.67

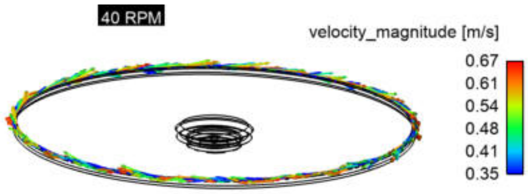
40 RPM
velocity_magnitude [m/s]
0.67
0.61
0.54
0.48
0.41
0.35

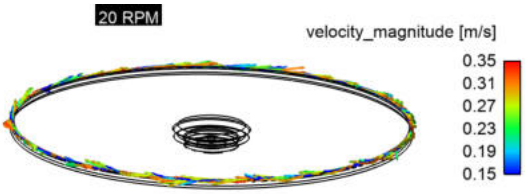
20 RPM
velocity_magnitude [m/s]
0.35
0.31
0.27
0.23
0.19
0.15

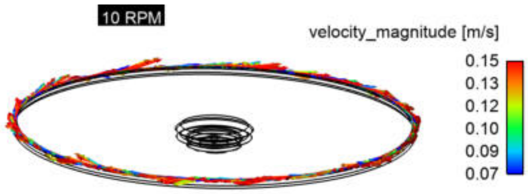
10 RPM
velocity_magnitude [m/s]
0.15
0.13
0.12
0.10
0.09
0.07

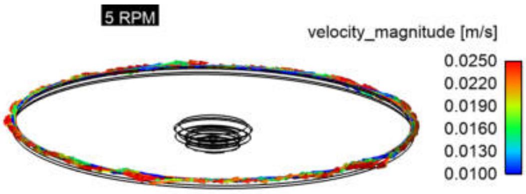
5 RPM
velocity_magnitude [m/s]
0.0250
0.0220
0.0190
0.0160
0.0130
0.0100

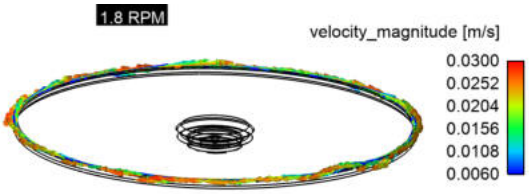
1.8 RPM
velocity_magnitude [m/s]
0.0300
0.0252
0.0204
0.0156
0.0108
0.0060

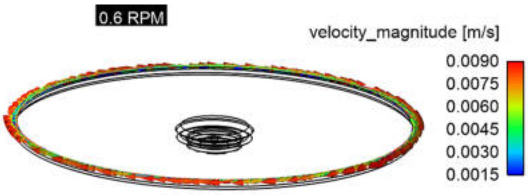
0.6 RPM
velocity_magnitude [m/s]
0.0090
0.0075
0.0060
0.0045
0.0030
0.0015

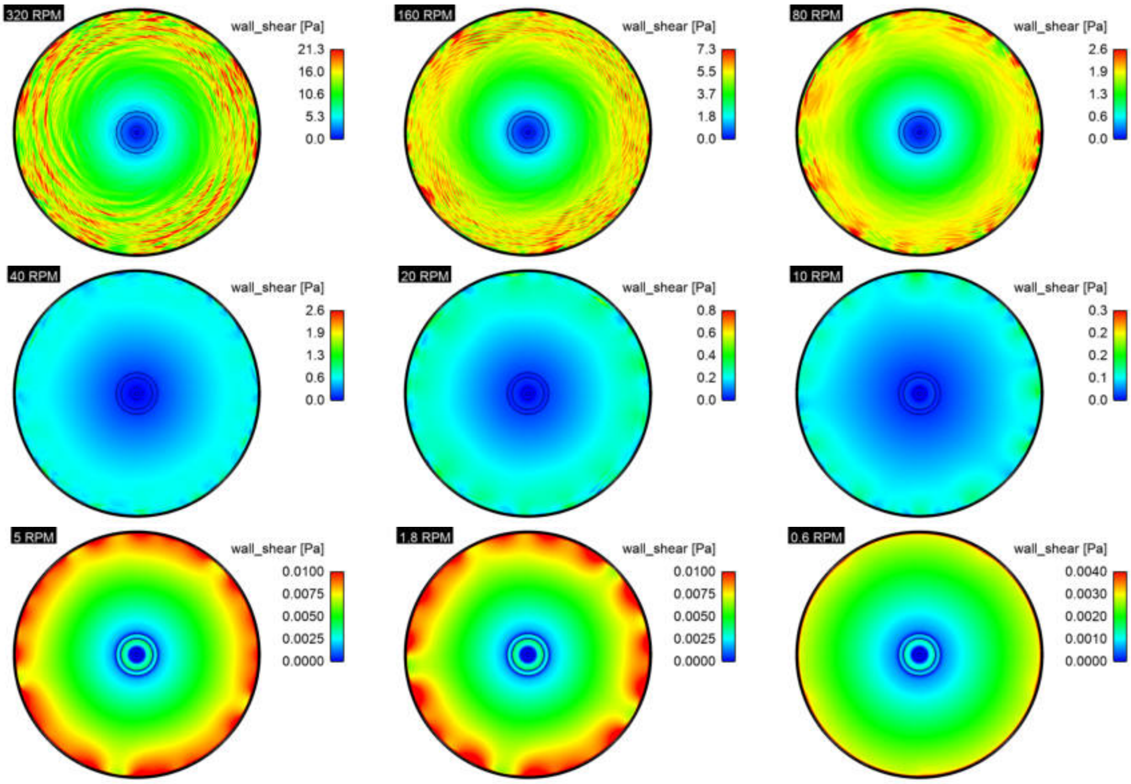
320 RPM
wall_shear [Pa]
21.3
16.0
10.6
5.3
0.0
160 RPM
wall_shear [Pa]
7.3
5.5
3.7
1.8
0.0
80 RPM
wall_shear [Pa]
2.6
1.9
1.3
0.6
0.0
40 RPM
wall_shear [Pa]
2.6
1.9
1.3
0.6
0.0
20 RPM
wall_shear [Pa]
0.8
0.6
0.4
0.2
0.0
10 RPM
wall_shear [Pa]
0.3
0.2
0.2
0.1
0.0
5 RPM
wall_shear [Pa]
0.0100
0.0075
0.0050
0.0025
0.0000
1.8 RPM
wall_shear [Pa]
0.0100
0.0075
0.0050
0.0025
0.0000
0.6 RPM
wall_shear [Pa]
0.0040
0.0030
0.0020
0.0010
0.0000

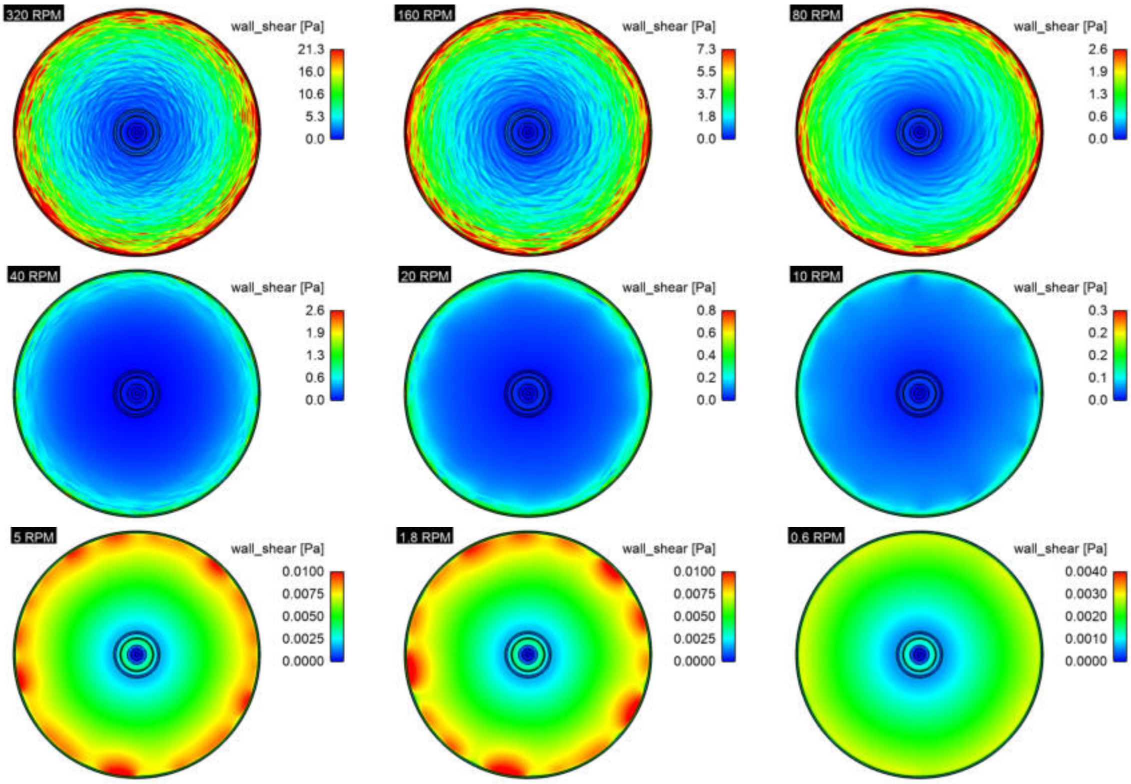
320 RPM
wall_shear [Pa]
21.3
16.0
10.6
5.3
0.0
160 RPM
wall_shear [Pa]
7.3
5.5
3.7
1.8
0.0
80 RPM
wall_shear [Pa]
2.6
1.9
1.3
0.6
0.0
40 RPM
wall_shear [Pa]
2.6
1.9
1.3
0.6
0.0
20 RPM
wall_shear [Pa]
0.8
0.6
0.4
0.2
0.0
10 RPM
wall_shear [Pa]
0.3
0.2
0.2
0.1
0.0
5 RPM
wall_shear [Pa]
0.0100
0.0075
0.0050
0.0025
0.0000
1.8 RPM
wall_shear [Pa]
0.0100
0.0075
0.0050
0.0025
0.0000
0.6 RPM
wall_shear [Pa]
0.0040
0.0030
0.0020
0.0010
0.0000

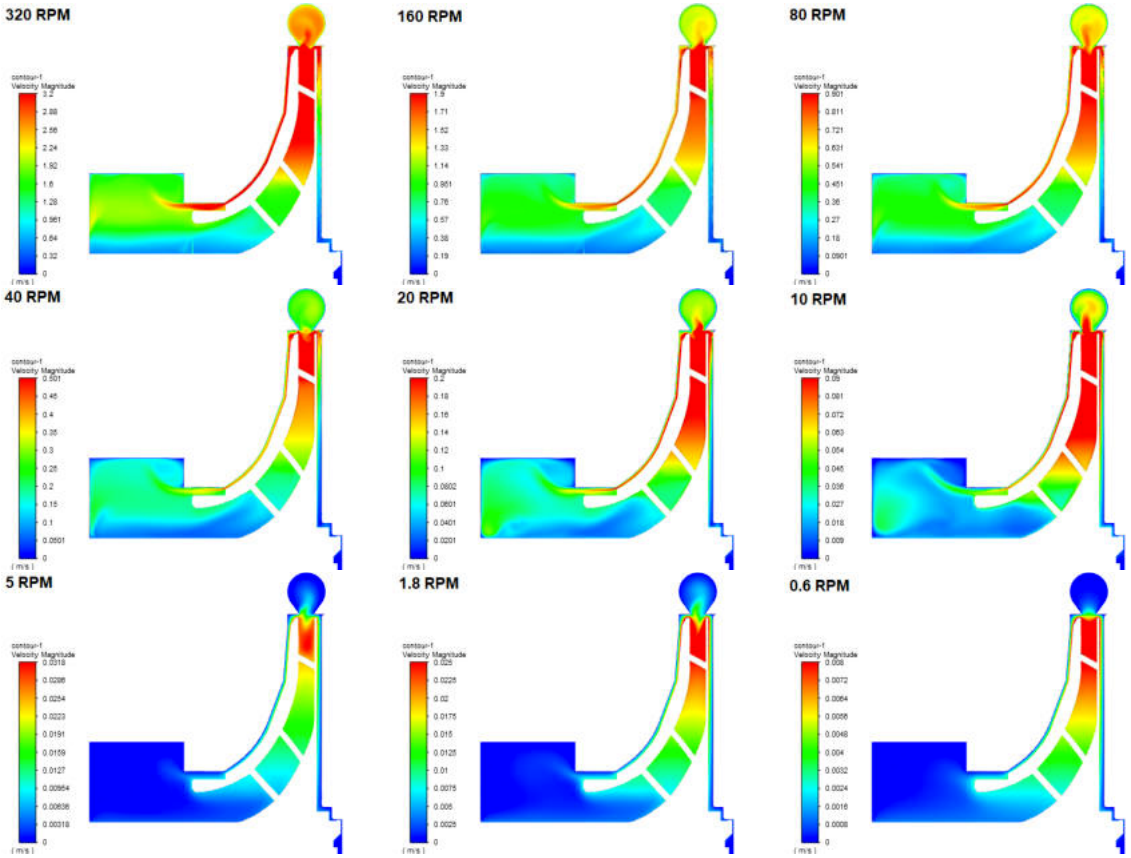
320 RPM
contour-1
Velocity Magnitude
3.2
2.88
2.56
2.24
1.92
1.6
1.28
0.961
0.64
0.32
0
(m/s)
160 RPM
contour-1
Velocity Magnitude
1.9
1.71
1.52
1.33
1.14
0.951
0.76
0.57
0.38
0.19
0
(m/s)
80 RPM
contour-1
Velocity Magnitude
0.901
0.811
0.721
0.631
0.541
0.451
0.36
0.27
0.18
0.0901
0
(m/s)
40 RPM
contour-1
Velocity Magnitude
0.501
0.45
0.4
0.35
0.3
0.25
0.2
0.15
0.1
0.0501
0
(m/s)
20 RPM
contour-1
Velocity Magnitude
0.2
0.18
0.16
0.14
0.12
0.1
0.0802
0.0601
0.0401
0.0201
0
(m/s)
10 RPM
contour-1
Velocity Magnitude
0.09
0.081
0.072
0.063
0.054
0.045
0.036
0.027
0.018
0.009
0
(m/s)
5 RPM
contour-1
Velocity Magnitude
0.0318
0.0286
0.0254
0.0223
0.0191
0.0159
0.0127
0.00954
0.00636
0.00318
0
(m/s)
1.8 RPM
contour-1
Velocity Magnitude
0.025
0.0225
0.02
0.0175
0.015
0.0125
0.01
0.0075
0.005
0.0025
0
(m/s)
0.6 RPM
contour-1
Velocity Magnitude
0.008
0.0072
0.0064
0.0056
0.0048
0.004
0.0032
0.0024
0.0016
0.0008
0
(m/s)

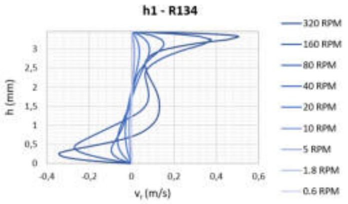
h1 - R134
h (mm)
3
2,5
2
1,5
1
0,5
0
-0,4
-0,2
0
0,2
0,4
0,6
v_r (m/s)
320 RPM
160 RPM
80 RPM
40 RPM
20 RPM
10 RPM
5 RPM
1.8 RPM
0.6 RPM

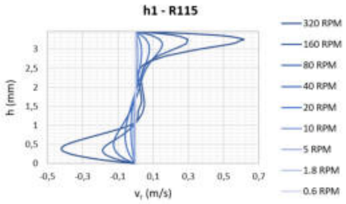
h1 - R115
h (mm)
3
2,5
2
1,5
1
0,5
0
-0,5
-0,3
-0,1
0,1
0,3
0,5
0,7
v_r (m/s)
320 RPM
160 RPM
80 RPM
40 RPM
20 RPM
10 RPM
5 RPM
1.8 RPM
0.6 RPM

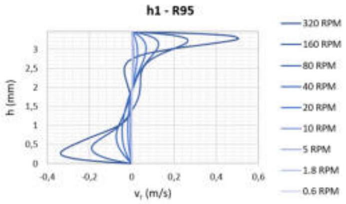
h1 - R95
h (mm)
3
2,5
2
1,5
1
0,5
0
-0,4
-0,2
0
0,2
0,4
0,6
v_r (m/s)
320 RPM
160 RPM
80 RPM
40 RPM
20 RPM
10 RPM
5 RPM
1.8 RPM
0.6 RPM

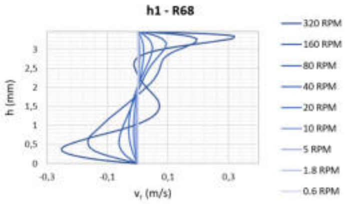
h1 - R68
h (mm)
3
2,5
2
1,5
1
0,5
0
-0,3
-0,1
0,1
0,3
v_r (m/s)
320 RPM
160 RPM
80 RPM
40 RPM
20 RPM
10 RPM
5 RPM
1.8 RPM
0.6 RPM

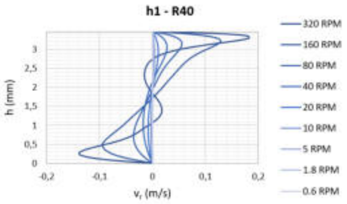
h1 - R40
h (mm)
3
2,5
2
1,5
1
0,5
0
-0,2
-0,1
0
0,1
0,2
v_r (m/s)
320 RPM
160 RPM
80 RPM
40 RPM
20 RPM
10 RPM
5 RPM
1.8 RPM
0.6 RPM

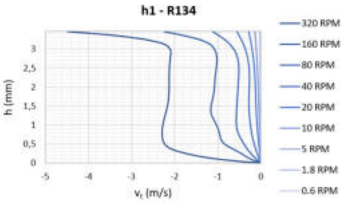
h1 - R134
h (mm)
3
2,5
2
1,5
1
0,5
0
-5
-4
-3
-2
-1
0
v_t (m/s)
320 RPM
160 RPM
80 RPM
40 RPM
20 RPM
10 RPM
5 RPM
1.8 RPM
0.6 RPM

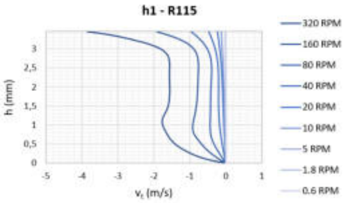
h1 - R115
h (mm)
3
2,5
2
1,5
1
0,5
0
-5
-4
-3
-2
-1
0
1
v_t (m/s)
320 RPM
160 RPM
80 RPM
40 RPM
20 RPM
10 RPM
5 RPM
1.8 RPM
0.6 RPM

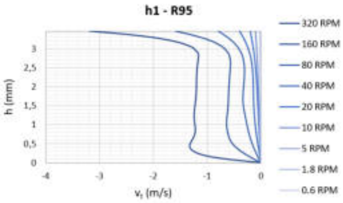
h1 - R95
h (mm)
3
2,5
2
1,5
1
0,5
0
-4
-3
-2
-1
0
v_t (m/s)
320 RPM
160 RPM
80 RPM
40 RPM
20 RPM
10 RPM
5 RPM
1.8 RPM
0.6 RPM

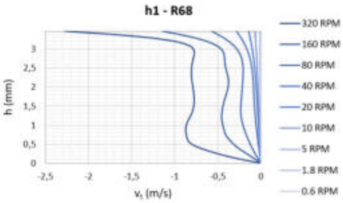
h1 - R68
h (mm)
3
2,5
2
1,5
1
0,5
0
-2,5
-2
-1,5
-1
-0,5
0
v_t (m/s)
320 RPM
160 RPM
80 RPM
40 RPM
20 RPM
10 RPM
5 RPM
1.8 RPM
0.6 RPM

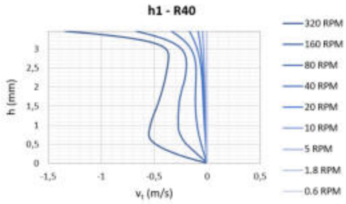
h1 - R40
h (mm)
3
2,5
2
1,5
1
0,5
0
-1,5
-1
-0,5
0
0,5
v_t (m/s)
320 RPM
160 RPM
80 RPM
40 RPM
20 RPM
10 RPM
5 RPM
1.8 RPM
0.6 RPM

Gap width h_3

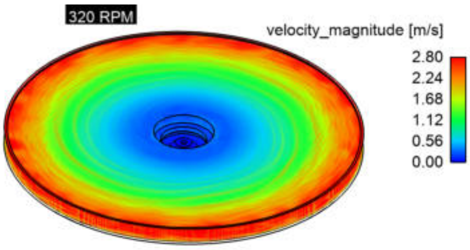
320 RPM
velocity_magnitude [m/s]
2.80
2.24
1.68
1.12
0.56
0.00

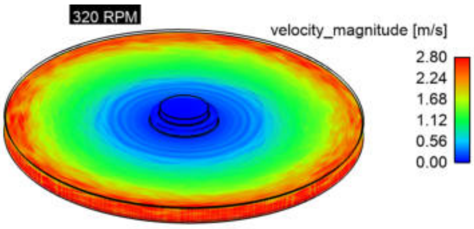
320 RPM
velocity_magnitude [m/s]
2.80
2.24
1.68
1.12
0.56
0.00

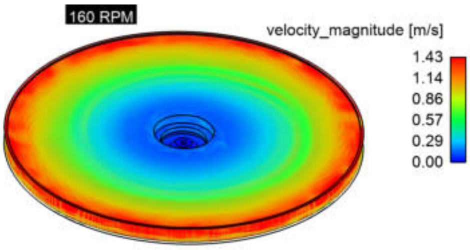
160 RPM
velocity_magnitude [m/s]
1.43
1.14
0.86
0.57
0.29
0.00

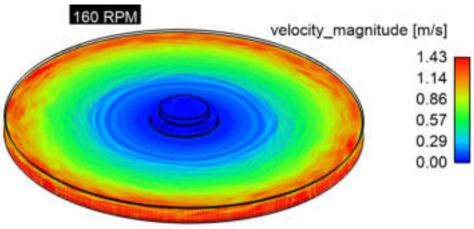
160 RPM
velocity_magnitude [m/s]
1.43
1.14
0.86
0.57
0.29
0.00

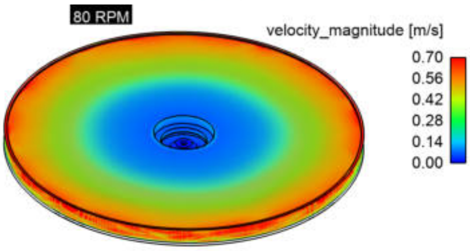
80 RPM
velocity_magnitude [m/s]
0.70
0.56
0.42
0.28
0.14
0.00

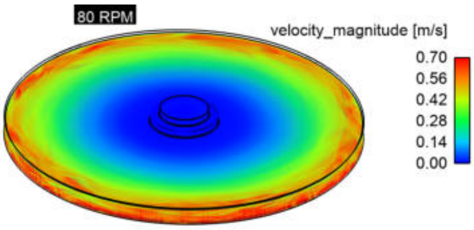
80 RPM
velocity_magnitude [m/s]
0.70
0.56
0.42
0.28
0.14
0.00

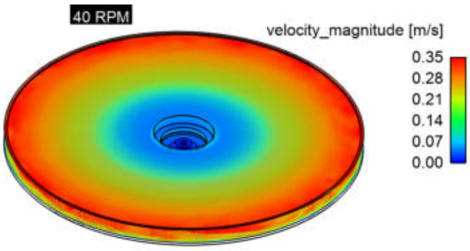
40 RPM
velocity_magnitude [m/s]
0.35
0.28
0.21
0.14
0.07
0.00

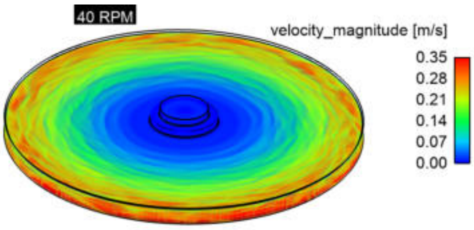
40 RPM
velocity_magnitude [m/s]
0.35
0.28
0.21
0.14
0.07
0.00

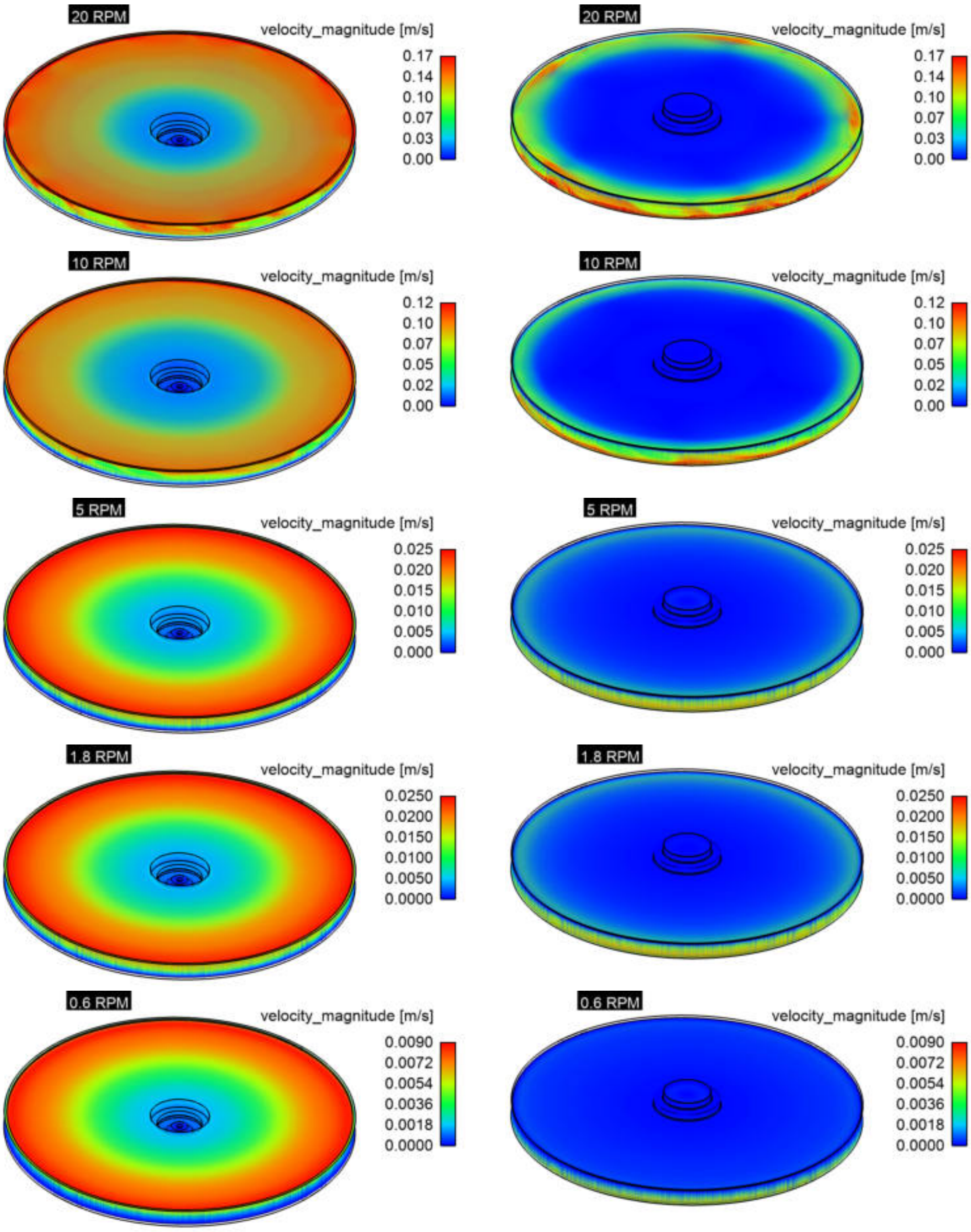
20 RPM
velocity_magnitude [m/s]
0.17
0.14
0.10
0.07
0.03
0.00
20 RPM
velocity_magnitude [m/s]
0.17
0.14
0.10
0.07
0.03
0.00
10 RPM
velocity_magnitude [m/s]
0.12
0.10
0.07
0.05
0.02
0.00
10 RPM
velocity_magnitude [m/s]
0.12
0.10
0.07
0.05
0.02
0.00
5 RPM
velocity_magnitude [m/s]
0.025
0.020
0.015
0.010
0.005
0.000
5 RPM
velocity_magnitude [m/s]
0.025
0.020
0.015
0.010
0.005
0.000
1.8 RPM
velocity_magnitude [m/s]
0.0250
0.0200
0.0150
0.0100
0.0050
0.0000
1.8 RPM
velocity_magnitude [m/s]
0.0250
0.0200
0.0150
0.0100
0.0050
0.0000
0.6 RPM
velocity_magnitude [m/s]
0.0090
0.0072
0.0054
0.0036
0.0018
0.0000
0.6 RPM
velocity_magnitude [m/s]
0.0090
0.0072
0.0054
0.0036
0.0018
0.0000

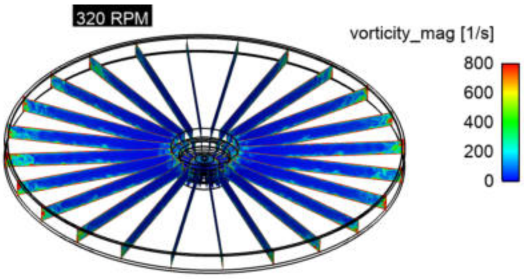
320 RPM
vorticity_mag [1/s]
800
600
400
200
0

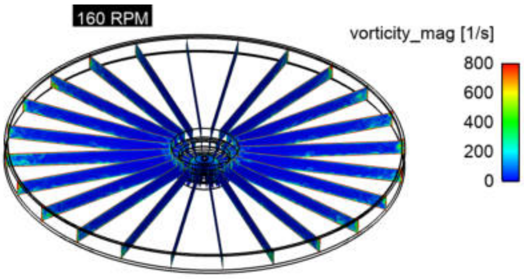
160 RPM
vorticity_mag [1/s]
800
600
400
200
0

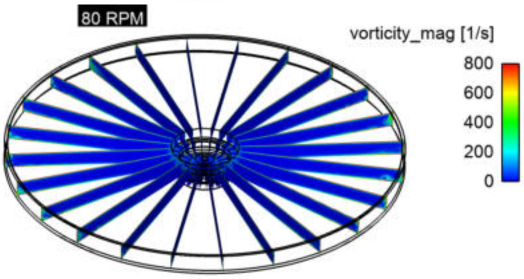
80 RPM
vorticity_mag [1/s]
800
600
400
200
0

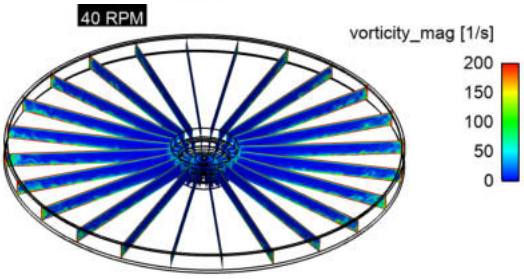
40 RPM
vorticity_mag [1/s]
200
150
100
50
0

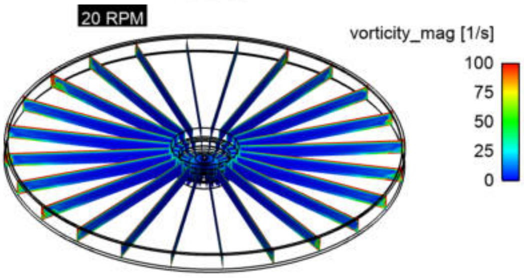
20 RPM
vorticity_mag [1/s]
100
75
50
25
0

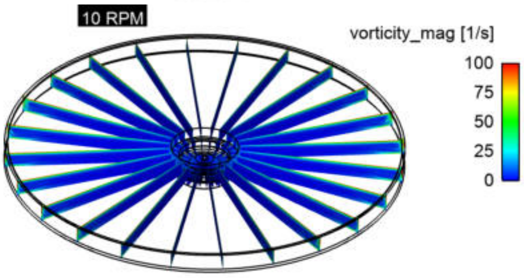
10 RPM
vorticity_mag [1/s]
100
75
50
25
0

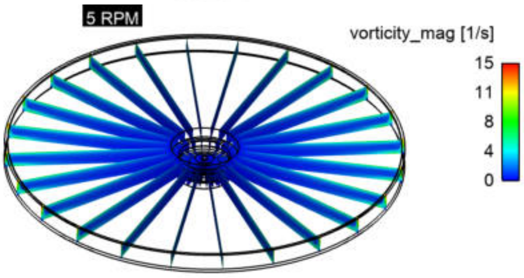
5 RPM
vorticity_mag [1/s]
15
11
8
4
0

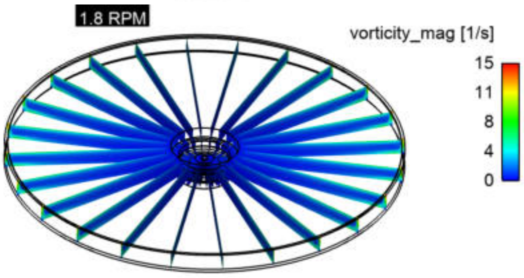
1.8 RPM
vorticity_mag [1/s]
15
11
8
4
0

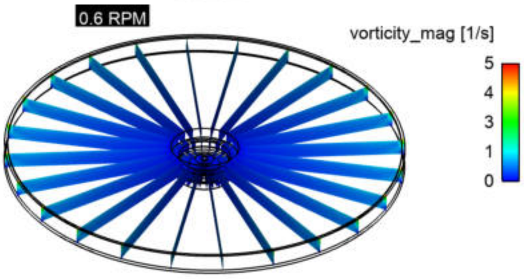
0.6 RPM
vorticity_mag [1/s]
5
4
3
1
0

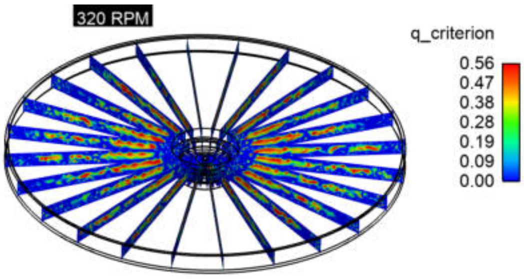
320 RPM
q_criterion
0.56
0.47
0.38
0.28
0.19
0.09
0.00

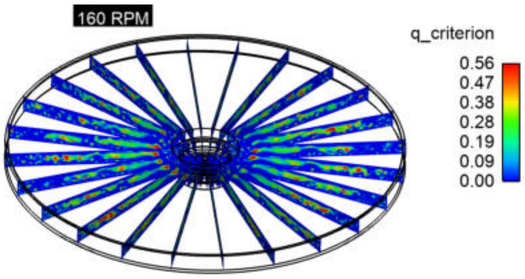
160 RPM
q_criterion
0.56
0.47
0.38
0.28
0.19
0.09
0.00

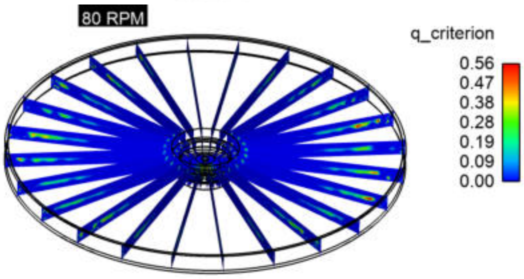
80 RPM
q_criterion
0.56
0.47
0.38
0.28
0.19
0.09
0.00

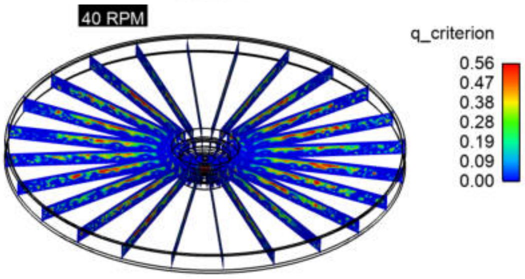
40 RPM
q_criterion
0.56
0.47
0.38
0.28
0.19
0.09
0.00

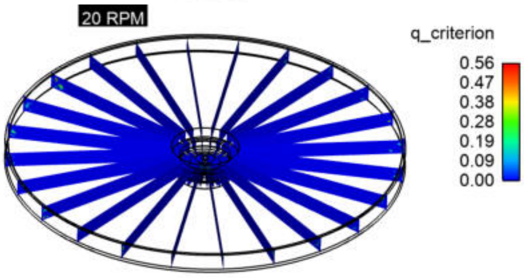
20 RPM
q_criterion
0.56
0.47
0.38
0.28
0.19
0.09
0.00

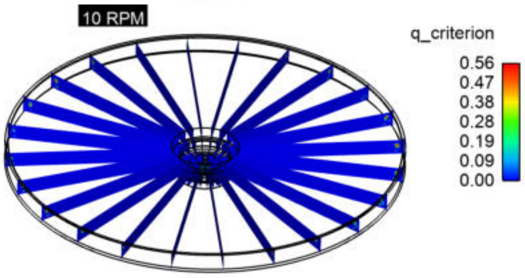
10 RPM
q_criterion
0.56
0.47
0.38
0.28
0.19
0.09
0.00

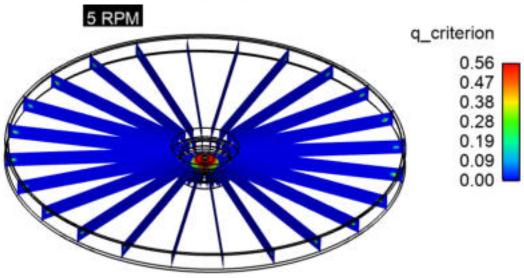
5 RPM
q_criterion
0.56
0.47
0.38
0.28
0.19
0.09
0.00

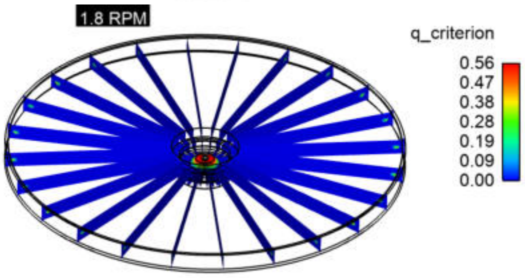
1.8 RPM
q_criterion
0.56
0.47
0.38
0.28
0.19
0.09
0.00

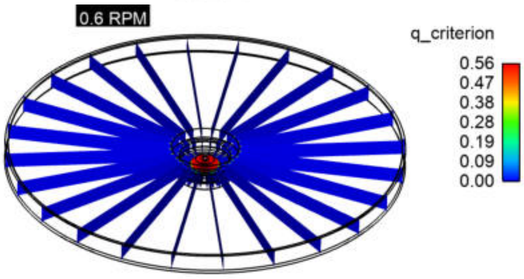
0.6 RPM
q_criterion
0.56
0.47
0.38
0.28
0.19
0.09
0.00

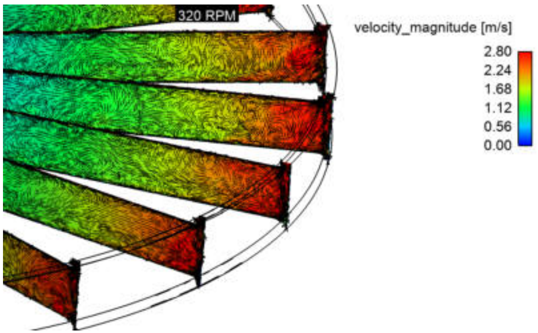
320 RPM
velocity_magnitude [m/s]
2.80
2.24
1.68
1.12
0.56
0.00

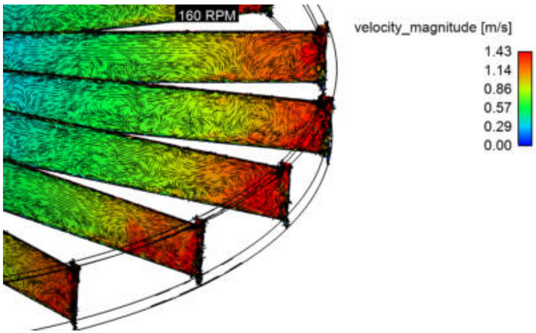
160 RPM
velocity_magnitude [m/s]
1.43
1.14
0.86
0.57
0.29
0.00

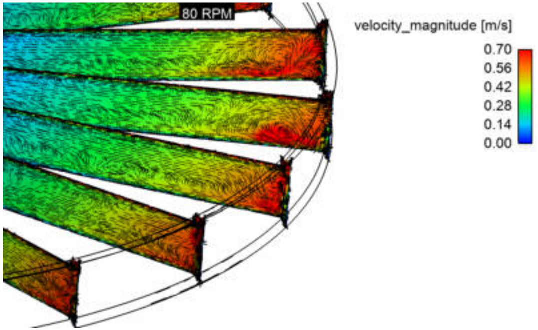
80 RPM
velocity_magnitude [m/s]
0.70
0.56
0.42
0.28
0.14
0.00

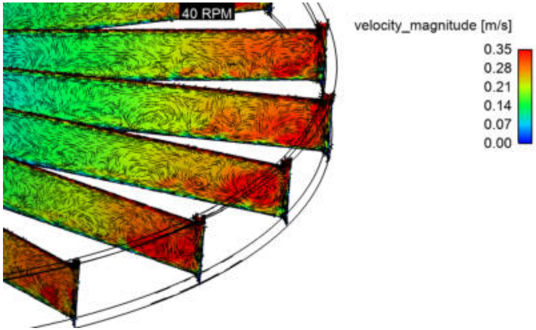
40 RPM
velocity_magnitude [m/s]
0.35
0.28
0.21
0.14
0.07
0.00

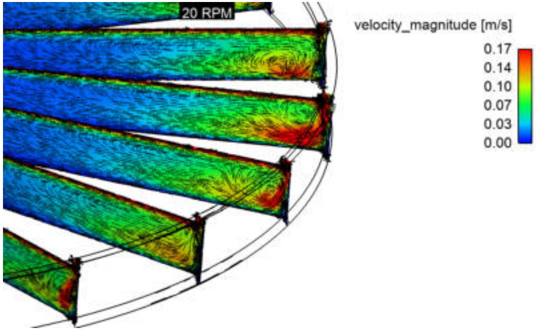
20 RPM
velocity_magnitude [m/s]
0.17
0.14
0.10
0.07
0.03
0.00

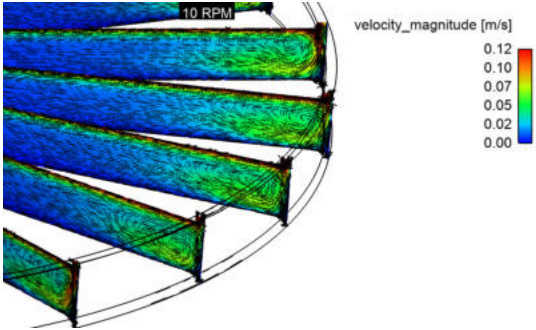
10 RPM
velocity_magnitude [m/s]
0.12
0.10
0.07
0.05
0.02
0.00

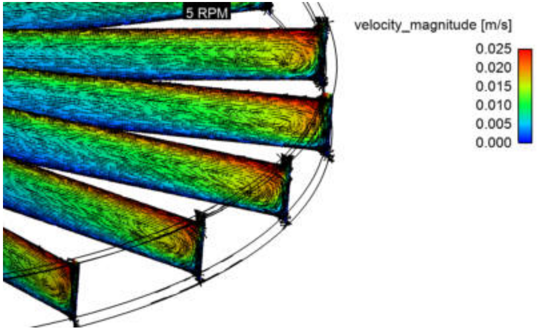
5 RPM
velocity_magnitude [m/s]
0.025
0.020
0.015
0.010
0.005
0.000

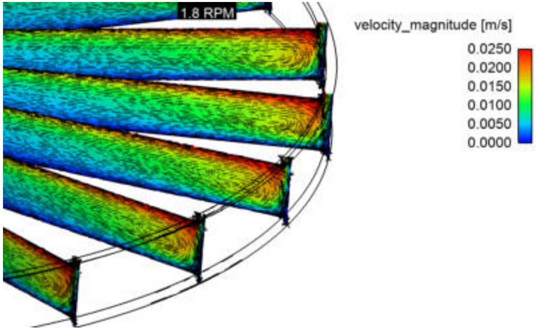
1.8 RPM
velocity_magnitude [m/s]
0.0250
0.0200
0.0150
0.0100
0.0050
0.0000

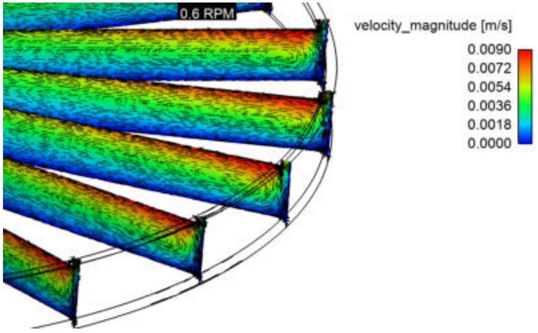
0.6 RPM
velocity_magnitude [m/s]
0.0090
0.0072
0.0054
0.0036
0.0018
0.0000

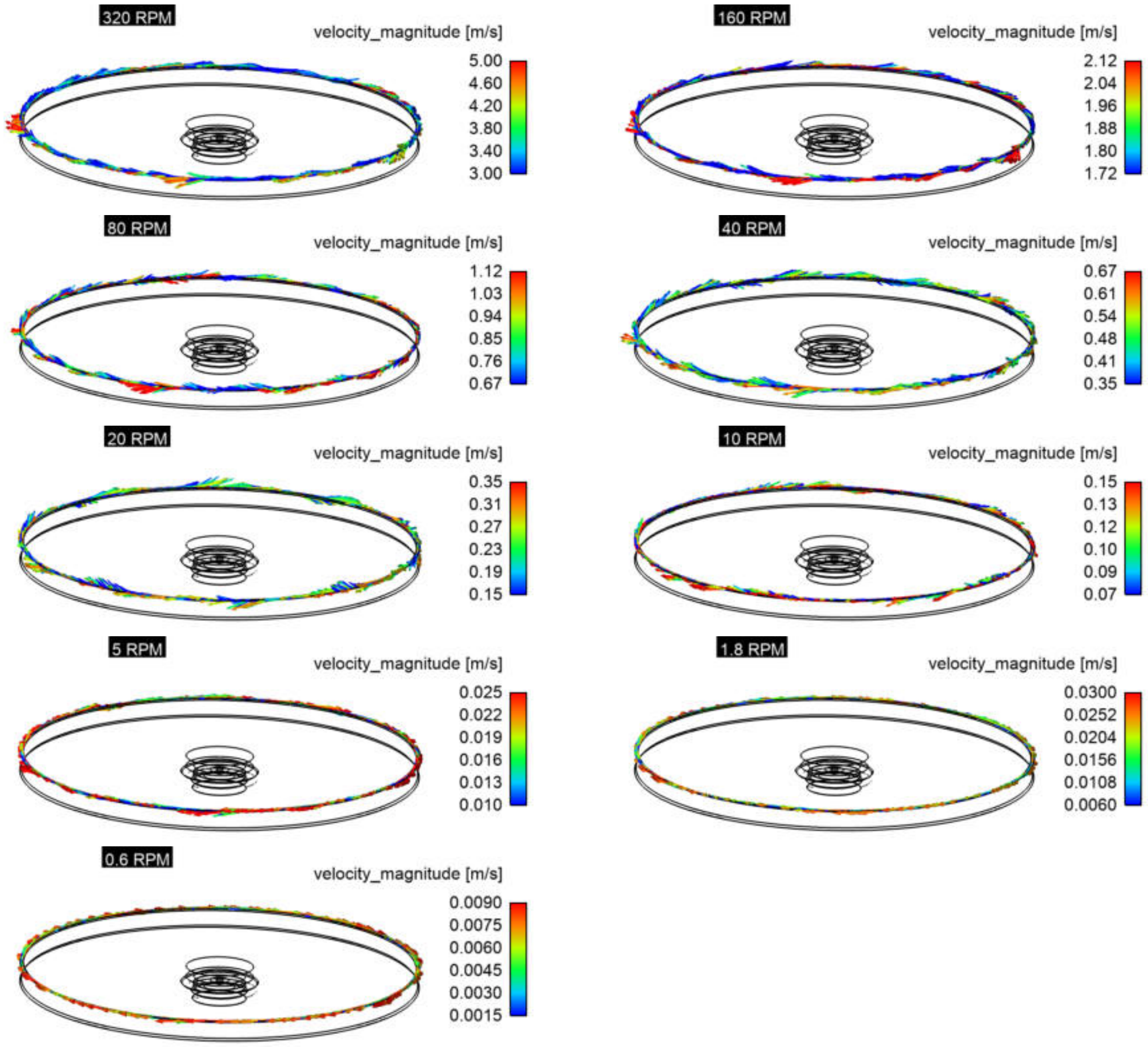
320 RPM
velocity_magnitude [m/s]
5.00
4.60
4.20
3.80
3.40
3.00
160 RPM
velocity_magnitude [m/s]
2.12
2.04
1.96
1.88
1.80
1.72
80 RPM
velocity_magnitude [m/s]
1.12
1.03
0.94
0.85
0.76
0.67
40 RPM
velocity_magnitude [m/s]
0.67
0.61
0.54
0.48
0.41
0.35
20 RPM
velocity_magnitude [m/s]
0.35
0.31
0.27
0.23
0.19
0.15
10 RPM
velocity_magnitude [m/s]
0.15
0.13
0.12
0.10
0.09
0.07
5 RPM
velocity_magnitude [m/s]
0.025
0.022
0.019
0.016
0.013
0.010
1.8 RPM
velocity_magnitude [m/s]
0.0300
0.0252
0.0204
0.0156
0.0108
0.0060
0.6 RPM
velocity_magnitude [m/s]
0.0090
0.0075
0.0060
0.0045
0.0030
0.0015

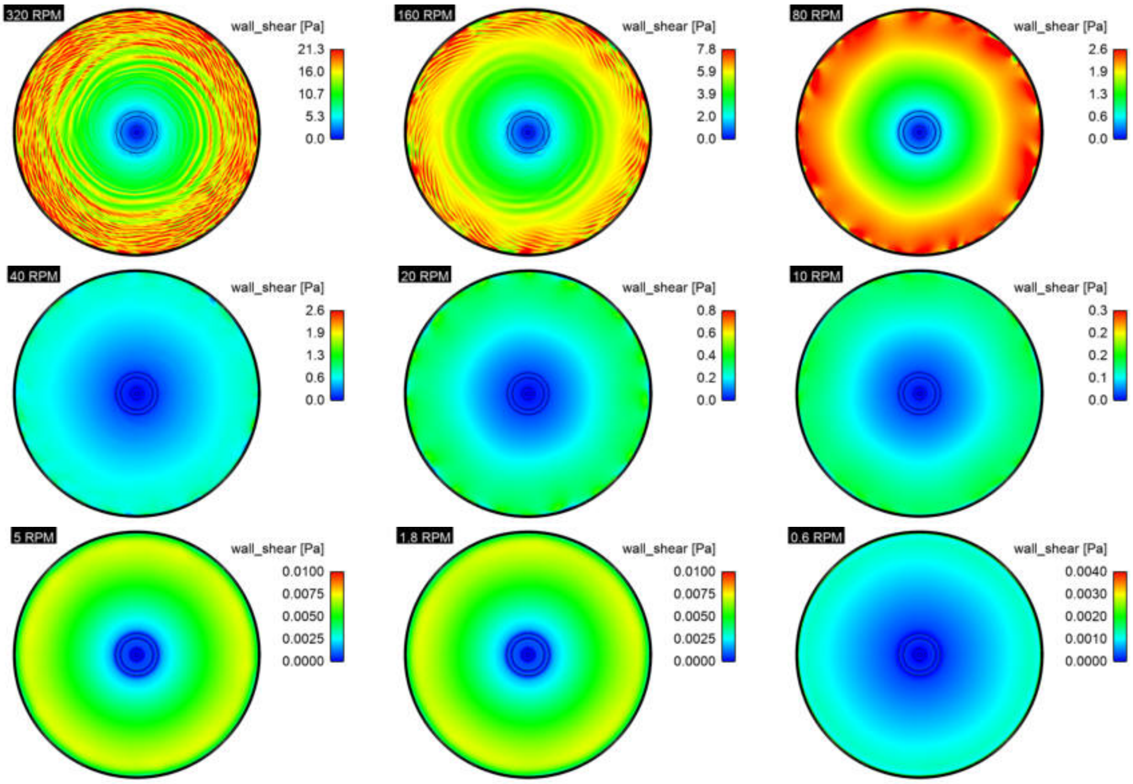
320 RPM
wall_shear [Pa]
21.3
16.0
10.7
5.3
0.0
160 RPM
wall_shear [Pa]
7.8
5.9
3.9
2.0
0.0
80 RPM
wall_shear [Pa]
2.6
1.9
1.3
0.6
0.0
40 RPM
wall_shear [Pa]
2.6
1.9
1.3
0.6
0.0
20 RPM
wall_shear [Pa]
0.8
0.6
0.4
0.2
0.0
10 RPM
wall_shear [Pa]
0.3
0.2
0.2
0.1
0.0
5 RPM
wall_shear [Pa]
0.0100
0.0075
0.0050
0.0025
0.0000
1.8 RPM
wall_shear [Pa]
0.0100
0.0075
0.0050
0.0025
0.0000
0.6 RPM
wall_shear [Pa]
0.0040
0.0030
0.0020
0.0010
0.0000

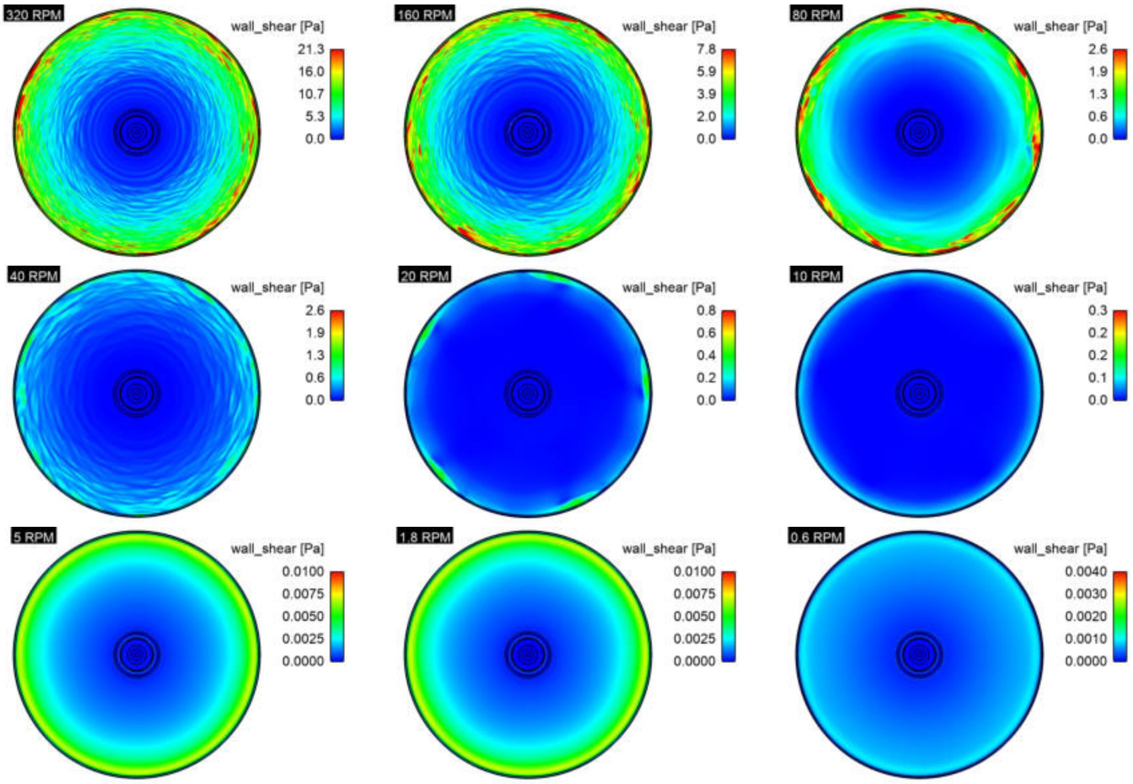
320 RPM
wall_shear [Pa]
21.3
16.0
10.7
5.3
0.0
160 RPM
wall_shear [Pa]
7.8
5.9
3.9
2.0
0.0
80 RPM
wall_shear [Pa]
2.6
1.9
1.3
0.6
0.0
40 RPM
wall_shear [Pa]
2.6
1.9
1.3
0.6
0.0
20 RPM
wall_shear [Pa]
0.8
0.6
0.4
0.2
0.0
10 RPM
wall_shear [Pa]
0.3
0.2
0.2
0.1
0.0
5 RPM
wall_shear [Pa]
0.0100
0.0075
0.0050
0.0025
0.0000
1.8 RPM
wall_shear [Pa]
0.0100
0.0075
0.0050
0.0025
0.0000
0.6 RPM
wall_shear [Pa]
0.0040
0.0030
0.0020
0.0010
0.0000

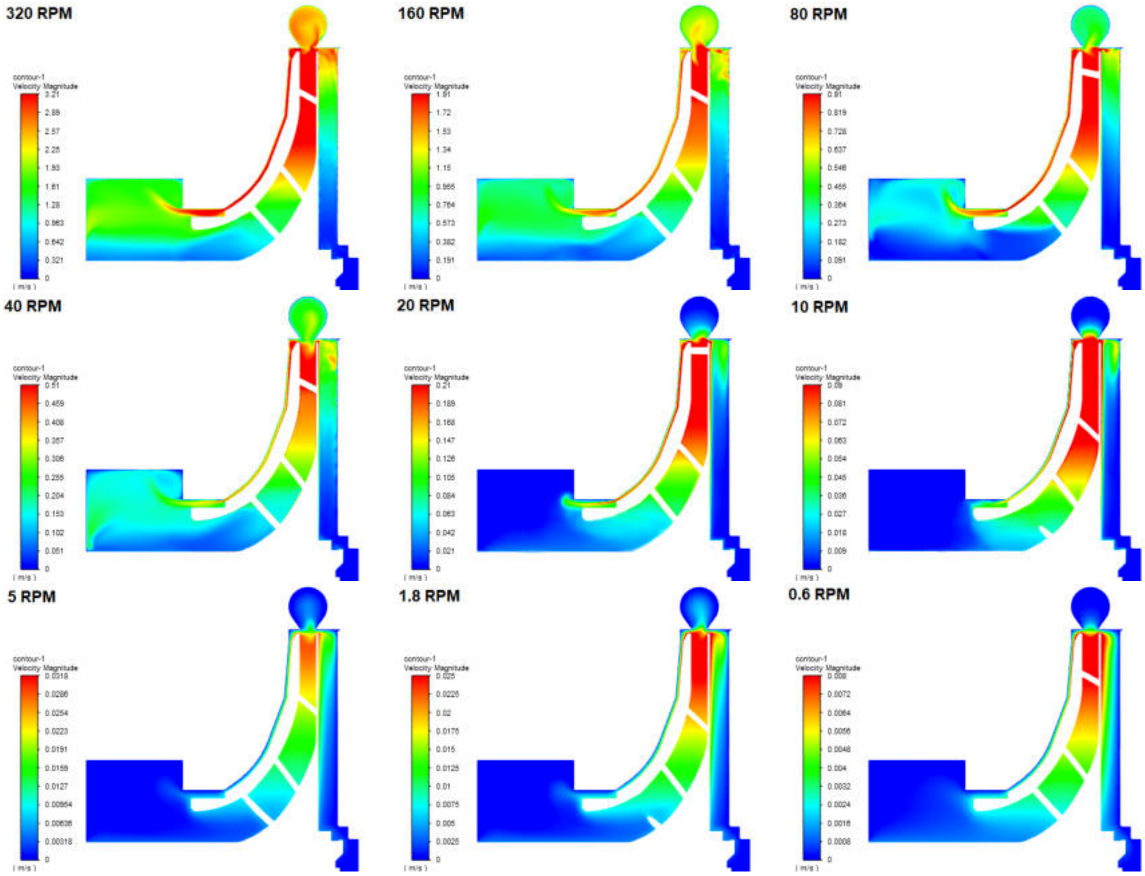
320 RPM
contour-1
Velocity Magnitude
3.21
2.89
2.57
2.25
1.93
1.61
1.28
0.963
0.642
0.321
0
(m/s)
160 RPM
contour-1
Velocity Magnitude
1.91
1.72
1.53
1.34
1.15
0.955
0.764
0.573
0.382
0.191
0
(m/s)
80 RPM
contour-1
Velocity Magnitude
0.91
0.819
0.728
0.637
0.546
0.455
0.364
0.273
0.182
0.091
0
(m/s)
40 RPM
contour-1
Velocity Magnitude
0.51
0.459
0.408
0.357
0.306
0.255
0.204
0.153
0.102
0.051
0
(m/s)
20 RPM
contour-1
Velocity Magnitude
0.21
0.189
0.168
0.147
0.126
0.105
0.084
0.063
0.042
0.021
0
(m/s)
10 RPM
contour-1
Velocity Magnitude
0.09
0.081
0.072
0.063
0.054
0.045
0.036
0.027
0.018
0.009
0
(m/s)
5 RPM
contour-1
Velocity Magnitude
0.0318
0.0286
0.0254
0.0223
0.0191
0.0159
0.0127
0.00954
0.00636
0.00318
0
(m/s)
1.8 RPM
contour-1
Velocity Magnitude
0.025
0.0225
0.02
0.0175
0.015
0.0125
0.01
0.0075
0.005
0.0025
0
(m/s)
0.6 RPM
contour-1
Velocity Magnitude
0.008
0.0072
0.0064
0.0056
0.0048
0.004
0.0032
0.0024
0.0016
0.0008
0
(m/s)

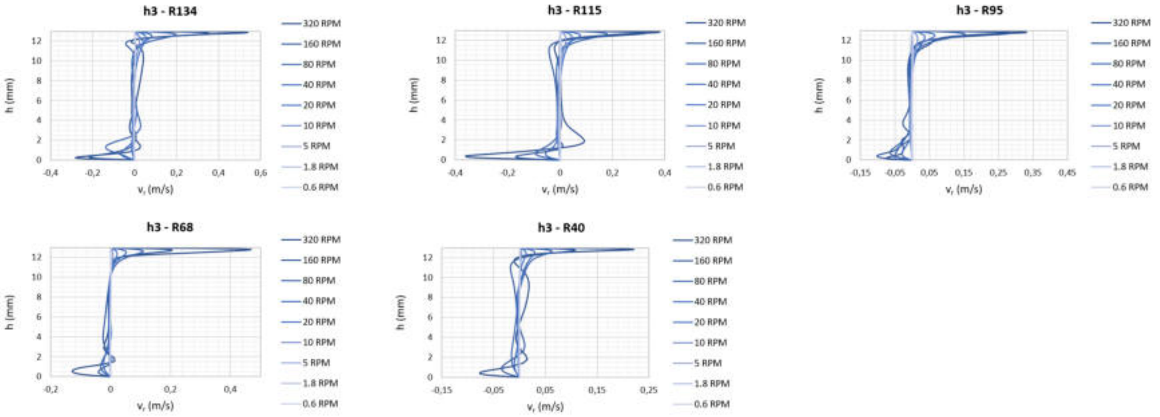
h3 - R134
h (mm)
12
10
8
6
4
2
0
-0,4
-0,2
0
0,2
0,4
0,6
v_r (m/s)
320 RPM
160 RPM
80 RPM
40 RPM
20 RPM
10 RPM
5 RPM
1.8 RPM
0.6 RPM
h3 - R115
h (mm)
-0,4
-0,2
0
0,2
0,4
v_r (m/s)
h3 - R95
h (mm)
-0,15
-0,05
0,05
0,15
0,25
0,35
0,45
v_r (m/s)
h3 - R68
h (mm)
-0,2
0
0,2
0,4
v_r (m/s)
h3 - R40
h (mm)
-0,15
-0,05
0,05
0,15
0,25
v_r (m/s)

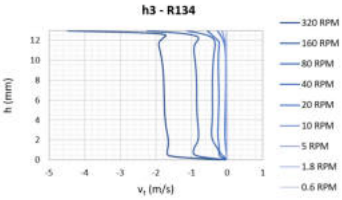

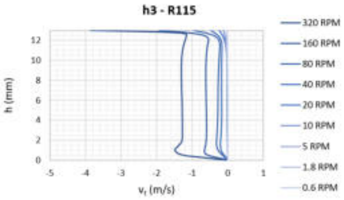

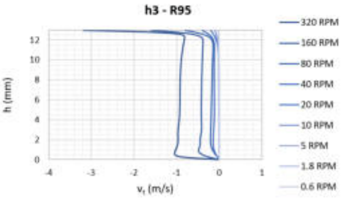

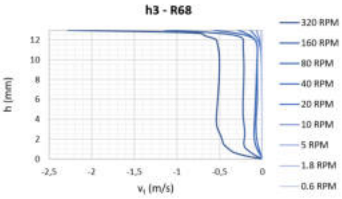

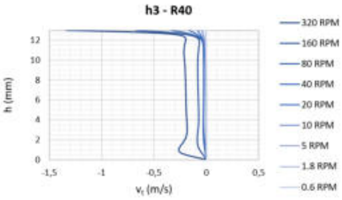

Gap width h_2 - with throughflow

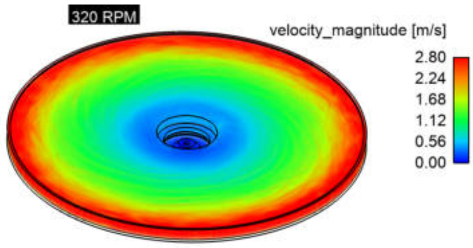

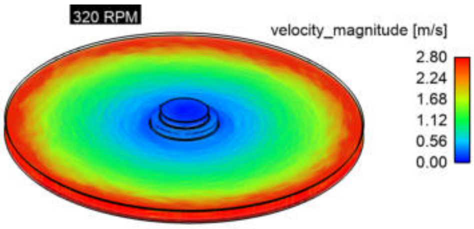

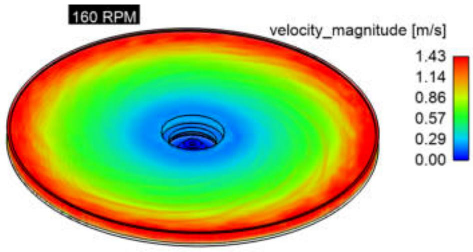

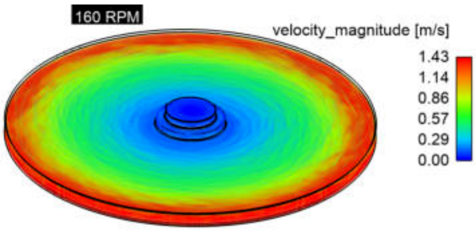

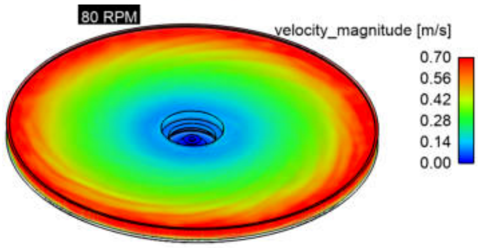

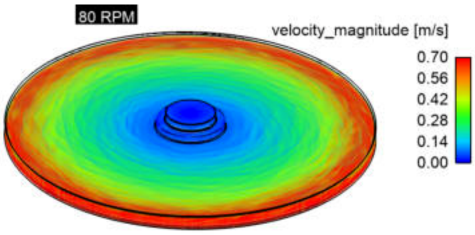

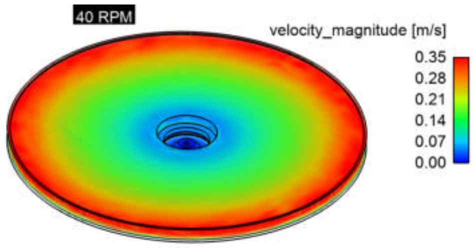

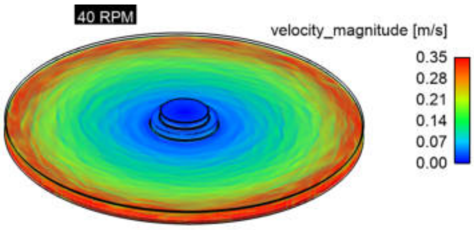

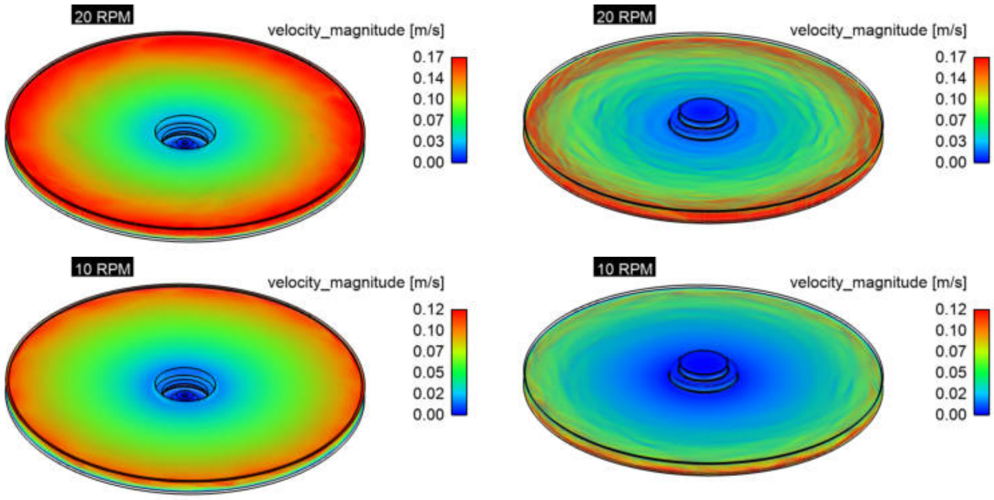
20 RPM
velocity_magnitude [m/s]
0.17
0.14
0.10
0.07
0.03
0.00
20 RPM
velocity_magnitude [m/s]
0.17
0.14
0.10
0.07
0.03
0.00
10 RPM
velocity_magnitude [m/s]
0.12
0.10
0.07
0.05
0.02
0.00
10 RPM
velocity_magnitude [m/s]
0.12
0.10
0.07
0.05
0.02
0.00

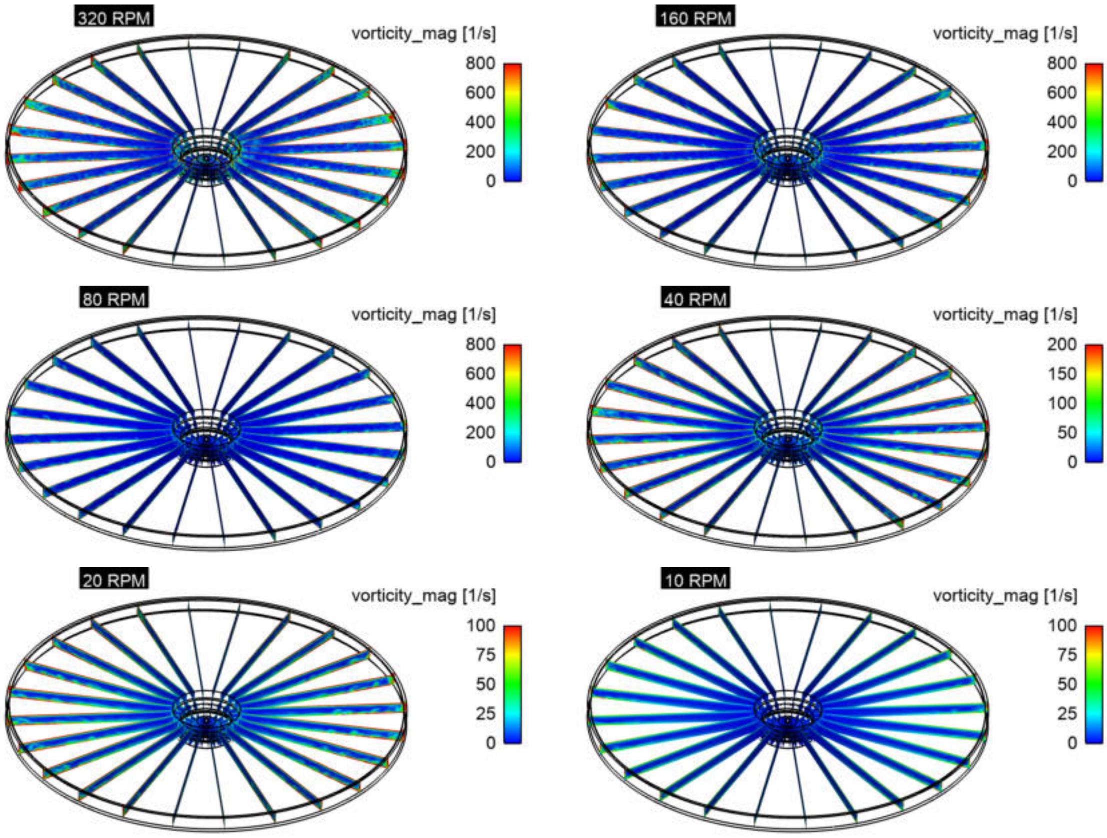
320 RPM
vorticity_mag [1/s]
800
600
400
200
0
160 RPM
vorticity_mag [1/s]
800
600
400
200
0
80 RPM
vorticity_mag [1/s]
800
600
400
200
0
40 RPM
vorticity_mag [1/s]
200
150
100
50
0
20 RPM
vorticity_mag [1/s]
100
75
50
25
0
10 RPM
vorticity_mag [1/s]
100
75
50
25
0

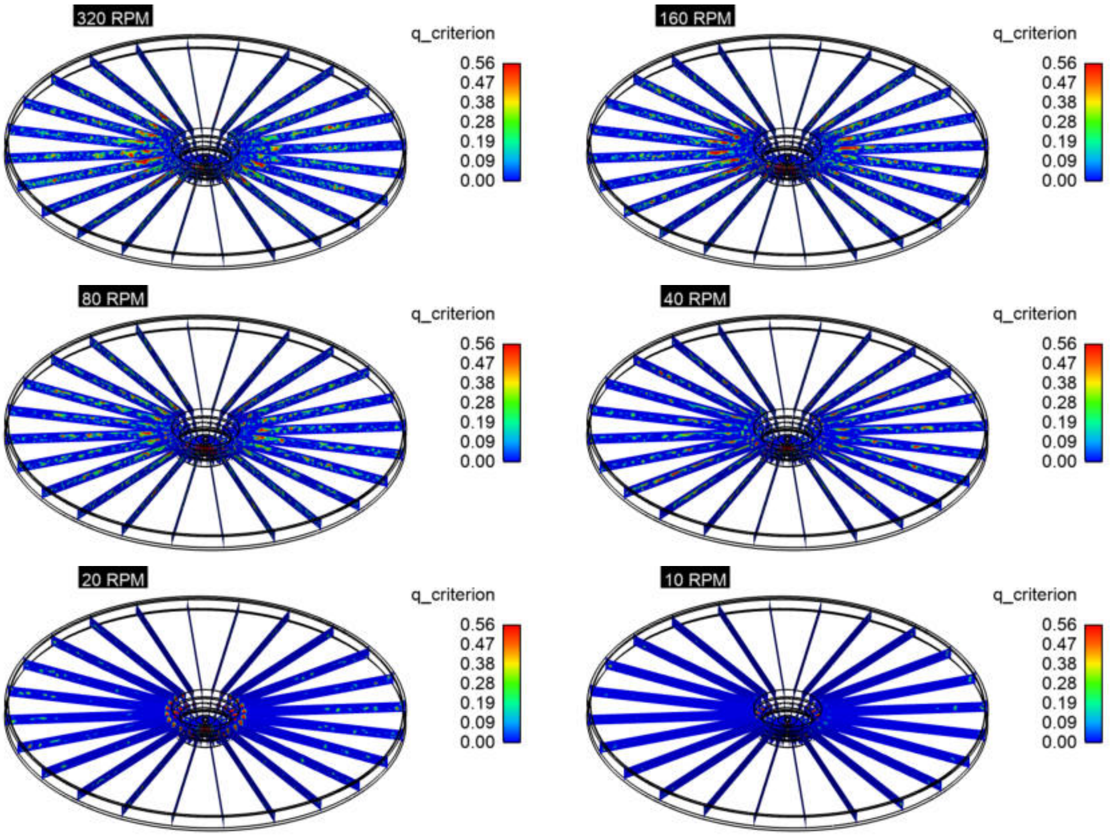
320 RPM
q_criterion
0.56
0.47
0.38
0.28
0.19
0.09
0.00
160 RPM
q_criterion
0.56
0.47
0.38
0.28
0.19
0.09
0.00
80 RPM
q_criterion
0.56
0.47
0.38
0.28
0.19
0.09
0.00
40 RPM
q_criterion
0.56
0.47
0.38
0.28
0.19
0.09
0.00
20 RPM
q_criterion
0.56
0.47
0.38
0.28
0.19
0.09
0.00
10 RPM
q_criterion
0.56
0.47
0.38
0.28
0.19
0.09
0.00

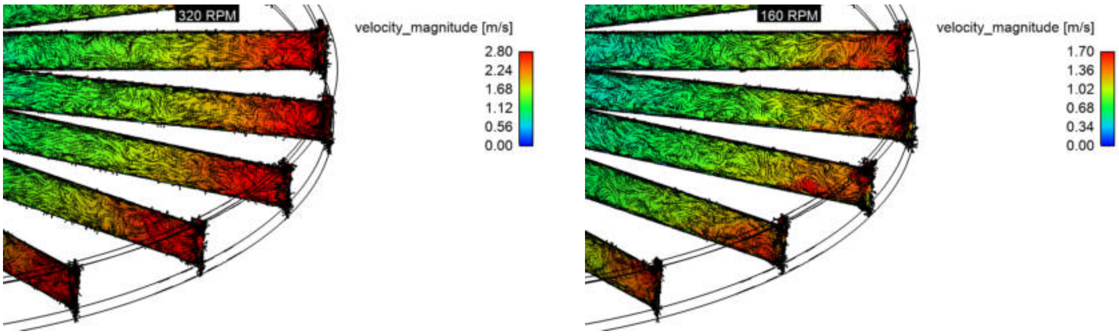
320 RPM
velocity_magnitude [m/s]
2.80
2.24
1.68
1.12
0.56
0.00
160 RPM
velocity_magnitude [m/s]
1.70
1.36
1.02
0.68
0.34
0.00

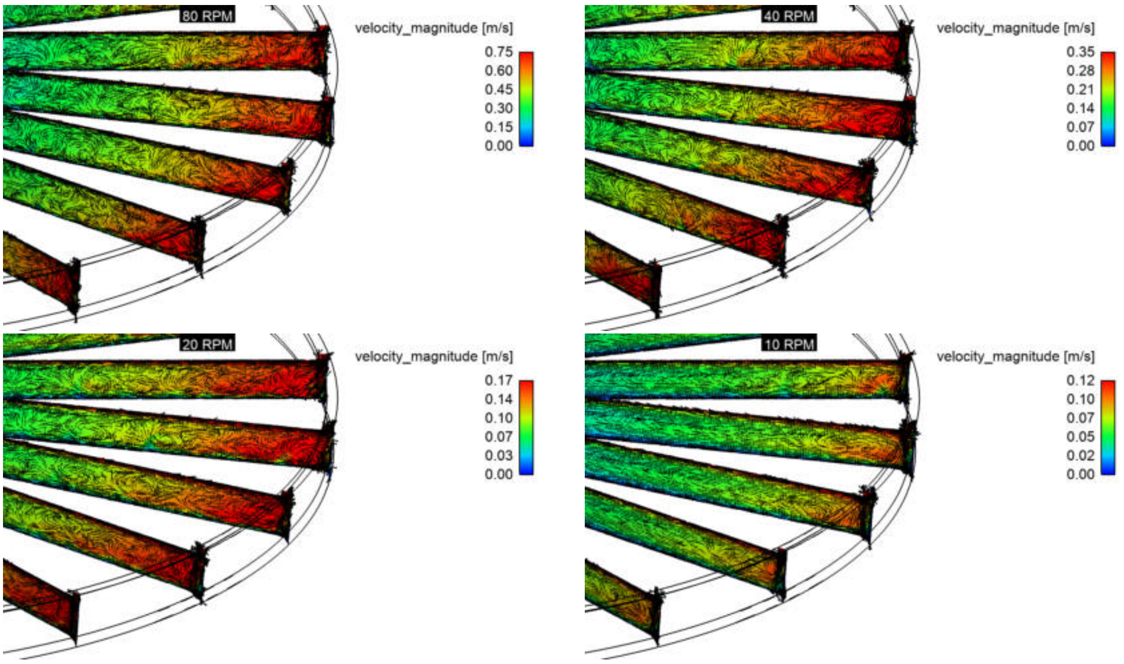
80 RPM
velocity_magnitude [m/s]
0.75
0.60
0.45
0.30
0.15
0.00
40 RPM
velocity_magnitude [m/s]
0.35
0.28
0.21
0.14
0.07
0.00
20 RPM
velocity_magnitude [m/s]
0.17
0.14
0.10
0.07
0.03
0.00
10 RPM
velocity_magnitude [m/s]
0.12
0.10
0.07
0.05
0.02
0.00

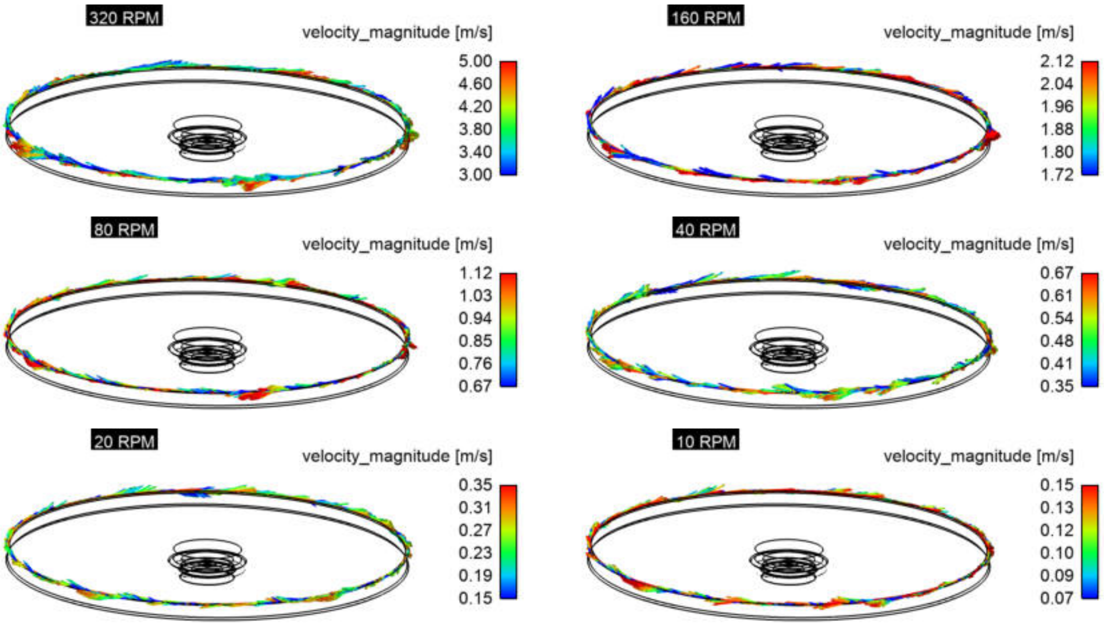
320 RPM
velocity_magnitude [m/s]
5.00
4.60
4.20
3.80
3.40
3.00
160 RPM
velocity_magnitude [m/s]
2.12
2.04
1.96
1.88
1.80
1.72
80 RPM
velocity_magnitude [m/s]
1.12
1.03
0.94
0.85
0.76
0.67
40 RPM
velocity_magnitude [m/s]
0.67
0.61
0.54
0.48
0.41
0.35
20 RPM
velocity_magnitude [m/s]
0.35
0.31
0.27
0.23
0.19
0.15
10 RPM
velocity_magnitude [m/s]
0.15
0.13
0.12
0.10
0.09
0.07

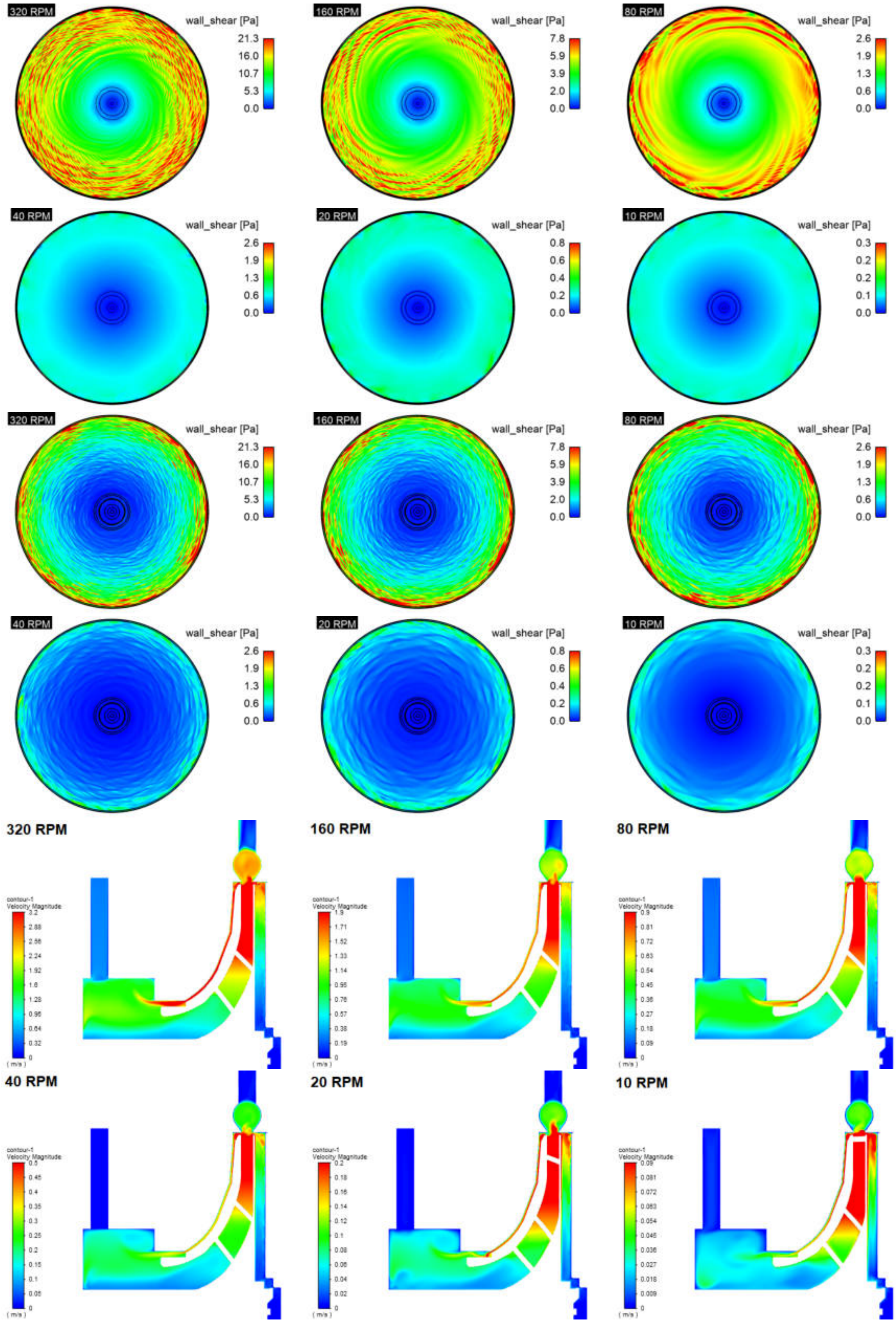
320 RPM
wall_shear [Pa]
21.3
16.0
10.7
5.3
0.0
160 RPM
wall_shear [Pa]
7.8
5.9
3.9
2.0
0.0
80 RPM
wall_shear [Pa]
2.6
1.9
1.3
0.6
0.0
40 RPM
wall_shear [Pa]
2.6
1.9
1.3
0.6
0.0
20 RPM
wall_shear [Pa]
0.8
0.6
0.4
0.2
0.0
10 RPM
wall_shear [Pa]
0.3
0.2
0.2
0.1
0.0
320 RPM
wall_shear [Pa]
21.3
16.0
10.7
5.3
0.0
160 RPM
wall_shear [Pa]
7.8
5.9
3.9
2.0
0.0
80 RPM
wall_shear [Pa]
2.6
1.9
1.3
0.6
0.0
40 RPM
wall_shear [Pa]
2.6
1.9
1.3
0.6
0.0
20 RPM
wall_shear [Pa]
0.8
0.6
0.4
0.2
0.0
10 RPM
wall_shear [Pa]
0.3
0.2
0.2
0.1
0.0
320 RPM
contour-1
Velocity Magnitude
3.2
2.88
2.56
2.24
1.92
1.6
1.28
0.96
0.64
0.32
0
(m/s)
160 RPM
contour-1
Velocity Magnitude
1.9
1.71
1.52
1.33
1.14
0.95
0.76
0.57
0.38
0.19
0
(m/s)
80 RPM
contour-1
Velocity Magnitude
0.9
0.81
0.72
0.63
0.54
0.45
0.36
0.27
0.18
0.09
0
(m/s)
40 RPM
contour-1
Velocity Magnitude
0.5
0.45
0.4
0.35
0.3
0.25
0.2
0.15
0.1
0.05
0
(m/s)
20 RPM
contour-1
Velocity Magnitude
0.2
0.18
0.16
0.14
0.12
0.1
0.08
0.06
0.04
0.02
0
(m/s)
10 RPM
contour-1
Velocity Magnitude
0.09
0.081
0.072
0.063
0.054
0.045
0.036
0.027
0.018
0.009
0
(m/s)

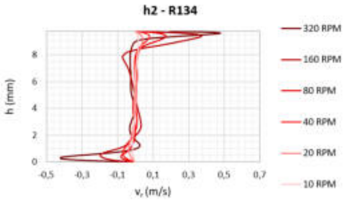
h2 - R134
h (mm)
0
2
4
6
8
-0,5
-0,3
-0,1
0,1
0,3
0,5
0,7
v_r (m/s)
320 RPM
160 RPM
80 RPM
40 RPM
20 RPM
10 RPM

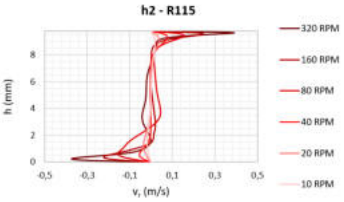
h2 - R115
h (mm)
0
2
4
6
8
-0,5
-0,3
-0,1
0,1
0,3
0,5
v_r (m/s)
320 RPM
160 RPM
80 RPM
40 RPM
20 RPM
10 RPM

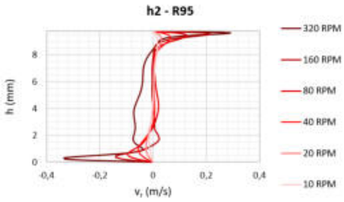
h2 - R95
h (mm)
0
2
4
6
8
-0,4
-0,2
0
0,2
0,4
v_r (m/s)
320 RPM
160 RPM
80 RPM
40 RPM
20 RPM
10 RPM

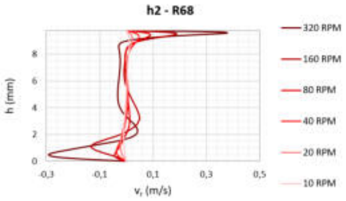
h2 - R68
h (mm)
0
2
4
6
8
-0,3
-0,1
0,1
0,3
0,5
v_r (m/s)
320 RPM
160 RPM
80 RPM
40 RPM
20 RPM
10 RPM

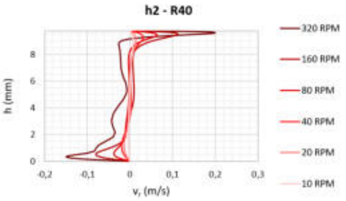
h2 - R40
h (mm)
0
2
4
6
8
-0,2
-0,1
0
0,1
0,2
0,3
v_r (m/s)
320 RPM
160 RPM
80 RPM
40 RPM
20 RPM
10 RPM

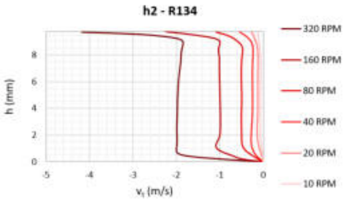
h2 - R134
h (mm)
0
2
4
6
8
-5
-4
-3
-2
-1
0
v_t (m/s)
320 RPM
160 RPM
80 RPM
40 RPM
20 RPM
10 RPM

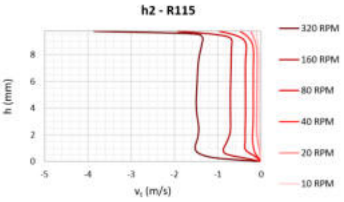
h2 - R115
h (mm)
0
2
4
6
8
-5
-4
-3
-2
-1
0
v_t (m/s)
320 RPM
160 RPM
80 RPM
40 RPM
20 RPM
10 RPM

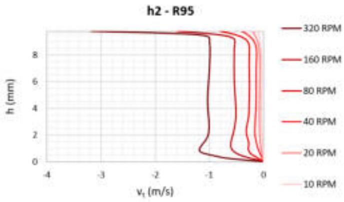
h2 - R95
h (mm)
0
2
4
6
8
-4
-3
-2
-1
0
v_t (m/s)
320 RPM
160 RPM
80 RPM
40 RPM
20 RPM
10 RPM

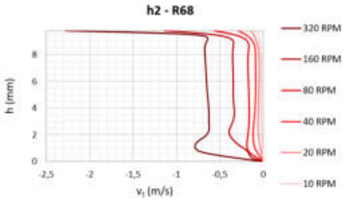
h2 - R68
h (mm)
0
2
4
6
8
-2,5
-2
-1,5
-1
-0,5
0
v_t (m/s)
320 RPM
160 RPM
80 RPM
40 RPM
20 RPM
10 RPM

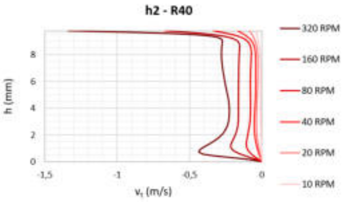
h2 - R40
h (mm)
0
2
4
6
8
-1,5
-1
-0,5
0
v_t (m/s)
320 RPM
160 RPM
80 RPM
40 RPM
20 RPM
10 RPM

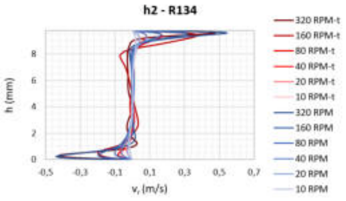
h2 - R134
h (mm)
0
2
4
6
8
-0,5
-0,3
-0,1
0,1
0,3
0,5
0,7
v_r (m/s)
320 RPM-t
160 RPM-t
80 RPM-t
40 RPM-t
20 RPM-t
10 RPM-t
320 RPM
160 RPM
80 RPM
40 RPM
20 RPM
10 RPM

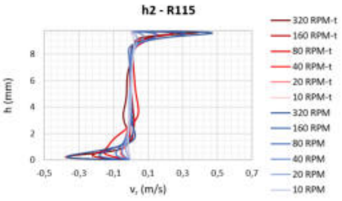
h2 - R115
h (mm)
0
2
4
6
8
-0,5
-0,3
-0,1
0,1
0,3
0,5
0,7
v_r (m/s)
320 RPM-t
160 RPM-t
80 RPM-t
40 RPM-t
20 RPM-t
10 RPM-t
320 RPM
160 RPM
80 RPM
40 RPM
20 RPM
10 RPM

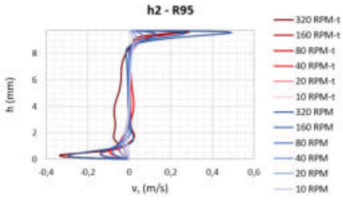
h2 - R95
h (mm)
0
2
4
6
8
-0,4
-0,2
0
0,2
0,4
0,6
v_r (m/s)
320 RPM-t
160 RPM-t
80 RPM-t
40 RPM-t
20 RPM-t
10 RPM-t
320 RPM
160 RPM
80 RPM
40 RPM
20 RPM
10 RPM

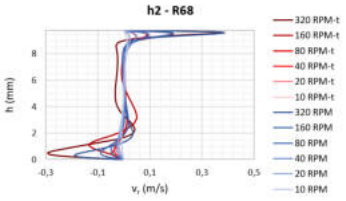
h2 - R68
h (mm)
0
2
4
6
8
-0,3
-0,1
0,1
0,3
0,5
v_r (m/s)
320 RPM-t
160 RPM-t
80 RPM-t
40 RPM-t
20 RPM-t
10 RPM-t
320 RPM
160 RPM
80 RPM
40 RPM
20 RPM
10 RPM

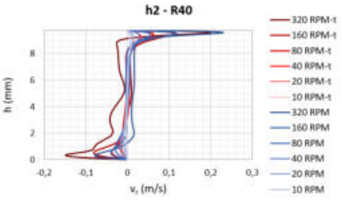
h2 - R40
h (mm)
0
2
4
6
8
-0,2
-0,1
0
0,1
0,2
0,3
v_r (m/s)
320 RPM-t
160 RPM-t
80 RPM-t
40 RPM-t
20 RPM-t
10 RPM-t
320 RPM
160 RPM
80 RPM
40 RPM
20 RPM
10 RPM

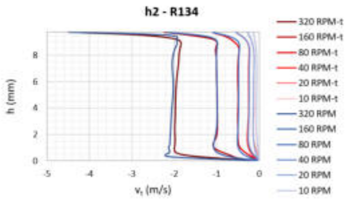
h2 - R134
h (mm)
0
2
4
6
8
-5
-4
-3
-2
-1
0
v_t (m/s)
320 RPM-t
160 RPM-t
80 RPM-t
40 RPM-t
20 RPM-t
10 RPM-t
320 RPM
160 RPM
80 RPM
40 RPM
20 RPM
10 RPM

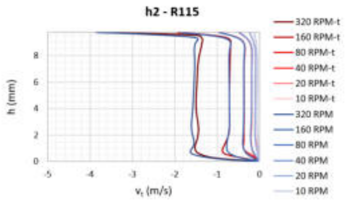
h2 - R115
h (mm)
0
2
4
6
8
-5
-4
-3
-2
-1
0
v_t (m/s)
320 RPM-t
160 RPM-t
80 RPM-t
40 RPM-t
20 RPM-t
10 RPM-t
320 RPM
160 RPM
80 RPM
40 RPM
20 RPM
10 RPM

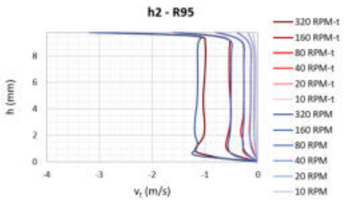
h2 - R95
h (mm)
0
2
4
6
8
-4
-3
-2
-1
0
v_t (m/s)
320 RPM-t
160 RPM-t
80 RPM-t
40 RPM-t
20 RPM-t
10 RPM-t
320 RPM
160 RPM
80 RPM
40 RPM
20 RPM
10 RPM

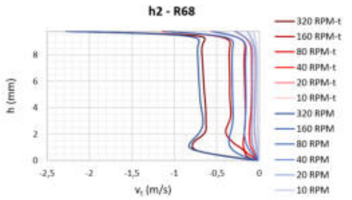
h2 - R68
h (mm)
0
2
4
6
8
-2,5
-2
-1,5
-1
-0,5
0
v_t (m/s)
320 RPM-t
160 RPM-t
80 RPM-t
40 RPM-t
20 RPM-t
10 RPM-t
320 RPM
160 RPM
80 RPM
40 RPM
20 RPM
10 RPM

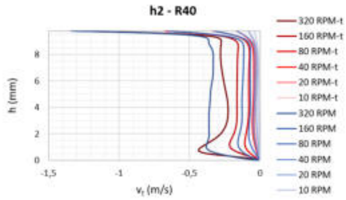
h2 - R40
h (mm)
0
2
4
6
8
-1,5
-1
-0,5
0
v_t (m/s)
320 RPM-t
160 RPM-t
80 RPM-t
40 RPM-t
20 RPM-t
10 RPM-t
320 RPM
160 RPM
80 RPM
40 RPM
20 RPM
10 RPM

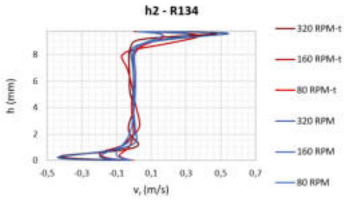
h2 - R134
h (mm)
0
2
4
6
8
-0,5
-0,3
-0,1
0,1
0,3
0,5
0,7
v_r (m/s)
320 RPM-t
160 RPM-t
80 RPM-t
320 RPM
160 RPM
80 RPM

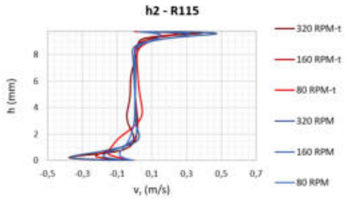
h2 - R115
h (mm)
0
2
4
6
8
-0,5
-0,3
-0,1
0,1
0,3
0,5
0,7
v_r (m/s)
320 RPM-t
160 RPM-t
80 RPM-t
320 RPM
160 RPM
80 RPM

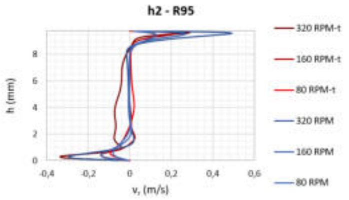
h2 - R95
h (mm)
0
2
4
6
8
-0,4
-0,2
0
0,2
0,4
0,6
v_r (m/s)
320 RPM-t
160 RPM-t
80 RPM-t
320 RPM
160 RPM
80 RPM

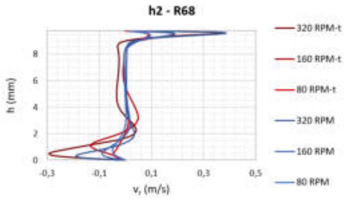
h2 - R68
h (mm)
0
2
4
6
8
-0,3
-0,1
0,1
0,3
0,5
v_r (m/s)
320 RPM-t
160 RPM-t
80 RPM-t
320 RPM
160 RPM
80 RPM

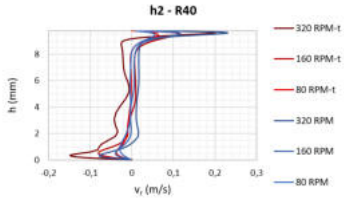
h2 - R40
h (mm)
0
2
4
6
8
-0,2
-0,1
0
0,1
0,2
0,3
v_r (m/s)
320 RPM-t
160 RPM-t
80 RPM-t
320 RPM
160 RPM
80 RPM

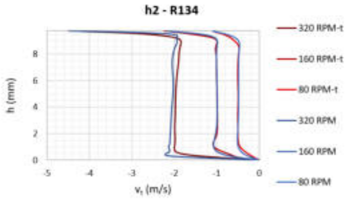
h2 - R134
h (mm)
0
2
4
6
8
-5
-4
-3
-2
-1
0
v_t (m/s)
320 RPM-t
160 RPM-t
80 RPM-t
320 RPM
160 RPM
80 RPM

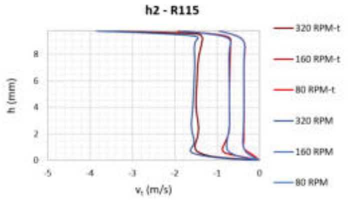
h2 - R115
h (mm)
0
2
4
6
8
-5
-4
-3
-2
-1
0
v_t (m/s)
320 RPM-t
160 RPM-t
80 RPM-t
320 RPM
160 RPM
80 RPM

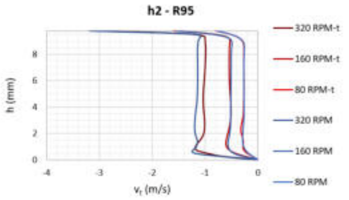
h2 - R95
h (mm)
0
2
4
6
8
-4
-3
-2
-1
0
v_t (m/s)
320 RPM-t
160 RPM-t
80 RPM-t
320 RPM
160 RPM
80 RPM

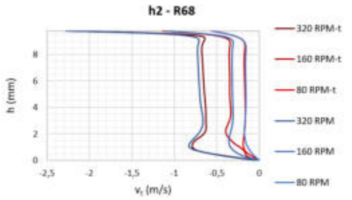
h2 - R68
h (mm)
0
2
4
6
8
-2,5
-2
-1,5
-1
-0,5
0
v_t (m/s)
320 RPM-t
160 RPM-t
80 RPM-t
320 RPM
160 RPM
80 RPM

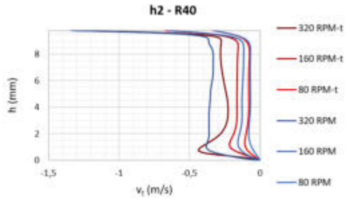
h2 - R40
h (mm)
0
2
4
6
8
-1,5
-1
-0,5
0
v_t (m/s)
320 RPM-t
160 RPM-t
80 RPM-t
320 RPM
160 RPM
80 RPM

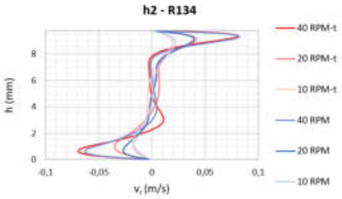
h2 - R134

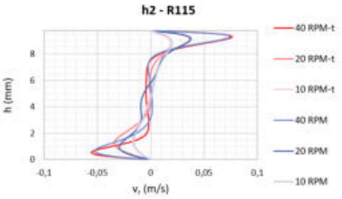
h2 - R115

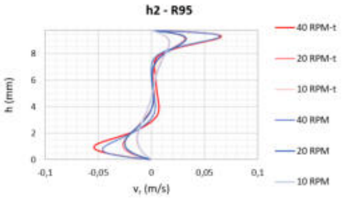
h2 - R95

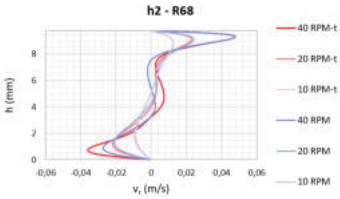
h2 - R68

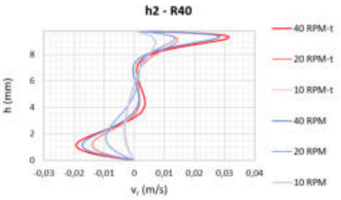
h2 - R40

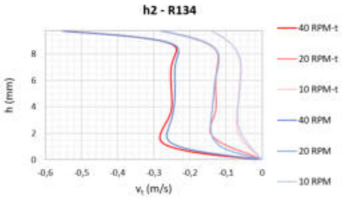
h2 - R134

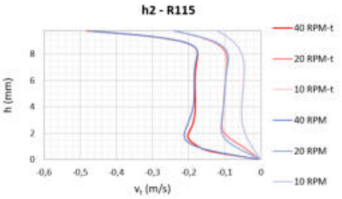
h2 - R115

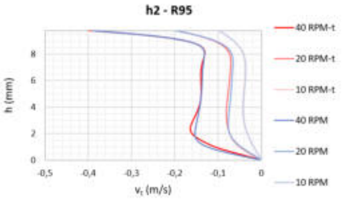
h2 - R95

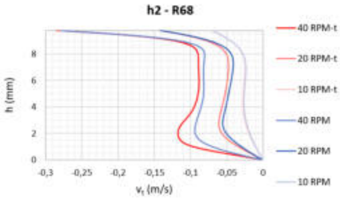
h2 - R68

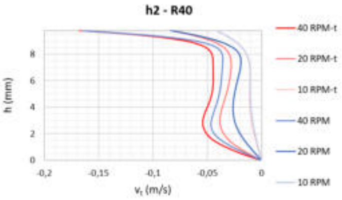
h2 - R40

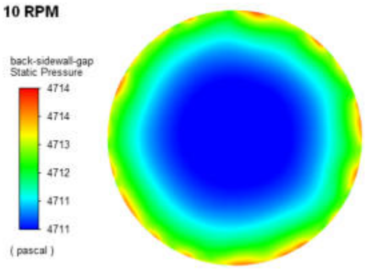
10 RPM

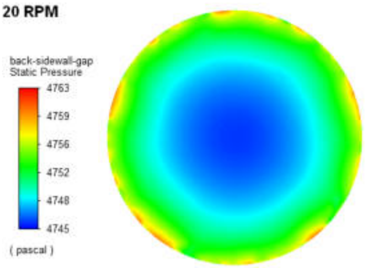
20 RPM

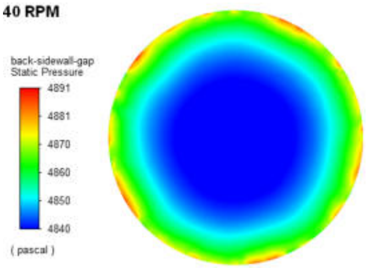
40 RPM

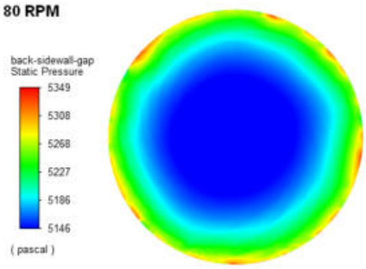
80 RPM

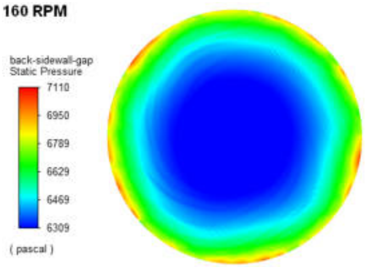
160 RPM

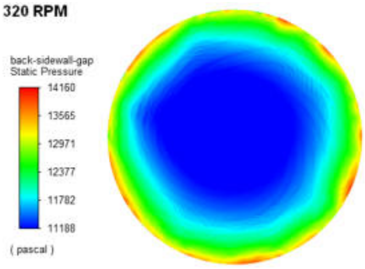
320 RPM

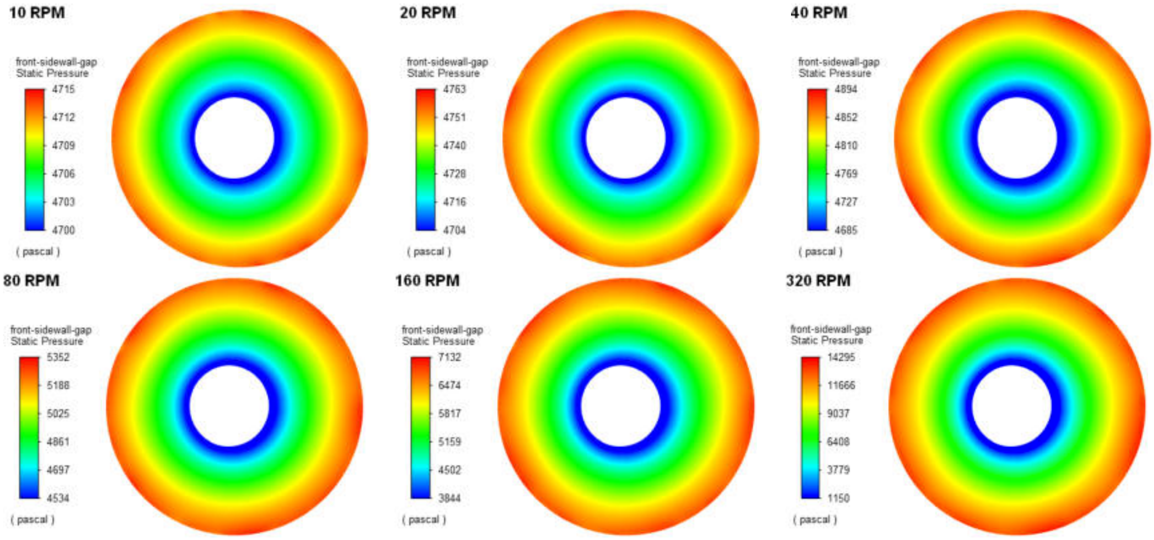
10 RPM
front-sidewall-gap
Static Pressure
4715
4712
4709
4706
4703
4700
(pascal)
20 RPM
front-sidewall-gap
Static Pressure
4763
4751
4740
4728
4716
4704
(pascal)
40 RPM
front-sidewall-gap
Static Pressure
4894
4852
4810
4769
4727
4685
(pascal)
80 RPM
front-sidewall-gap
Static Pressure
5352
5188
5025
4861
4697
4534
(pascal)
160 RPM
front-sidewall-gap
Static Pressure
7132
6474
5817
5159
4502
3844
(pascal)
320 RPM
front-sidewall-gap
Static Pressure
14295
11666
9037
6408
3779
1150
(pascal)